Structure-Activity Effects in Self-Assembled Multivalent (SAMul) Polyanion Binding

Buthaina Abdulmohsen M Albanyan

PhD

University of York
Chemistry
September 2016

Abstract

We have synthesized several self-assembled multivalent (SAMul) systems based on two parts; a hydrophobic part as the driving force for self-assembly, and a cationic hydrophilic part as the binding site for polyanions. A number of modified ligand displays were synthesized in order to investigate structure-activity relationship and their effects on self-assembly of such systems as well as their selectivities towards binding different polyanions (heparin and DNA).

The first three systems were synthesized using unsaturated fatty acids (containing alkene groups), this resulted in different self-assembly abilities, in addition to different selectivities towards the biological polyanions (heparin and DNA). In an attempt to stabilize those systems, we cross-linked the alkene groups – however the binding did not improve. We modified the ligand binding sites, using different amines. This also resulted in different self-assembly preferences in addition to selectivities for binding heparin and DNA. Alternative approaches to stabilizing displays of heparin-binding ligands were tested using a branched scaffold with a high density of positive charges on the surface groups, gold nanoparticles and a ligand-polymer conjugate approach. Finally, a multicomponent approach was employed in this work. PEG-lipid additives, were introduced to our SAMul systems to test their impact on binding heparin and DNA. Adding PEG-lipids to our SAMul demonstrated that a simple uncharged species can have an influence on binding strength in the clinically relevant serum medium. In addition, the multicomponent approach was also performed on two compounds using a multi component MalB assay. This showed that this approach may in the future help rapidly identify mixtures of self-assembling components which have positive synergistic effects.

In each study we have learned more about the structural impact of ligand designed display in polyanion binding – information which should prove useful in the future design of systems with clinical relevance.

Table of Contents

Lists of Figures

List of Tables

List of Schemes

List of Equations

Acknowledgements

I would like to begin by thanking Allah (God) for his blessings on me, then to thank my supervisor Professor David Smith for all his guidance and encouragement throughout the past four years and for being a constant source of inspiration. I am grateful for his support and understanding of my obligations to my family, by allowing me of working with a flexible schedule. I am also so grateful to the Ministry of Education in Saudi Arabia for their generous funding by granting me a full scholarship. I must also acknowledge our international collaborators who have contributed to this project; Professor Sabrina Pricl and her group for their work on ITC and the multiscale modelling of some of the compounds presented in this thesis.

I have also been fortunate to have worked with some excellent colleagues within the Smith group who have created a friendly and supportive working environment throughout my time at York. In particular, I would like to thank Stephen Bromfield for his initial contributions to this work during his PhD at York by synthesising the novel dye; Mallard Blue. I also would like to thank the Erasmus student Loryn Fechner for her work on the ligand effects on polyanion binding in terms of synthesis and some analysis in addition of publishing a paper together. Also, I would like thank Babatunde Okesola for his guidance on the gold nanoparticles synthesis, Ching Wan Chan (Rex) for his NMR tips, my talented MChem student Constantin Voll and excellent post-doc Ana Campo-Rodrigo for their contribution to the multicomponent chapter of this thesis. Finally, I am grateful to have worked alongside Jorge Ruiz-Olles who has always been there for all the group members when they needed him and Vania Vieira who has not only contributed to a comparison study in this work but also been a good friend.

I would also like to extend my gratitude towards all of the technical staff at University of York who have helped me with various experiments; Dr Karl Heaton (MS), Heather Fish for NMR, Meg Stark (TEM), Ian Wright (EDX and SEM) imaging, Dr Graeme McAllister for elemental analysis and Mike Dunn for his extraordinary IT support.

Lastly, but most importantly, I would not be able to reach this stage without my loving and supporting husband Mohammed and my three lovely children; Abdullah, Maha and Rand who have been my companions and my rock during this journey. I can only hope that the achievements in this volume would have make them proud.

Declaration

I declare that the work presented within this thesis is entirely my own, except where otherwise acknowledged. Aspects of this work have been published in the following journal article: *Chem. Sci*., 2016, **7**, 4653-4659. This work has not been submitted in part or fully for examination towards any other degrees or qualifications.

1 Introduction

1.1 Nanomedicine

Biological systems – proteins, nucleic acids, membranes etc. – all have nanoscale dimensions. This has increasingly driven the attention of chemists towards working in the 1-100 nanometre length scale in order to intervene in new ways in biomedical processes. This has led to the development of nanoscale interactions which are widely investigated and used in all aspects of science. Indeed, the prediction of the famed Richard Feynman[1] "There is plenty of room at the bottom"[2], has been proven as scientists have designed systems which inhabit the nanoscale world in order to develop new technologies.

In the last two decades, there has been a revolution in nanotechnology; the science of engineering particles 1-100 nanometre in diameter. This revolution is rapidly having increasing impact in the pharmaceutical industry. Nowadays, drugs can be designed on the nanoscale level in order to achieve the best results, accomplish improved delivery of poorly soluble materials and facilitate them to reach specific targets.[3] Pharmaceutical nanotechnology has two basic types; nanomaterials and nanodevices (Fig. 1-1). Nanodevices such as microelectromechanical (MEMS) and nanoelectromechanical (NEMS) systems can integrate electrical and mechanical functionality on the micro and nanoscale, respectively.[4] Nanomaterials such as polymer nanostructures; nanoparticles, micelles, dendrimers and drug conjugates, have great potential importance for biomedical use.[5]

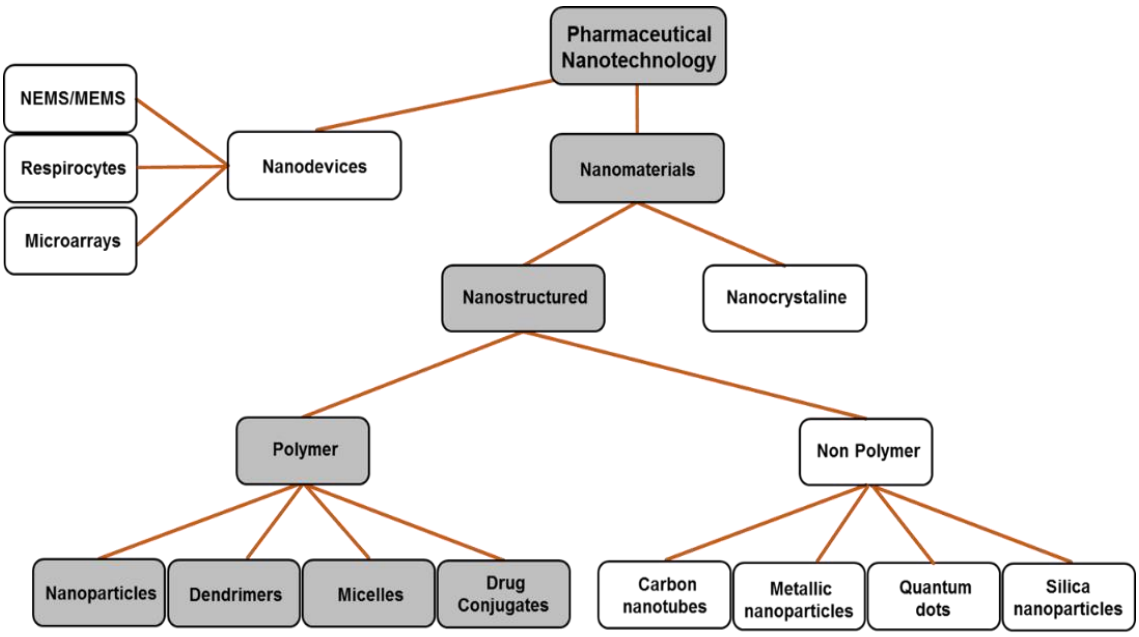

Fig. 1-1 Schematic diagram of nanotechnology types of pharmaceutical nano systems, reproduced from reference.[5]

So far, there are few nanomedicines that have been approved by the U.S. Food and Drug Administration (FDA).[6-8] The first nano-drug to be approved by FDA in 1995 was Doxil®; a liposomal doxorubicin product (Fig. 1-2) in which hydrophobic doxorubicin is incorporated within a liposome (vesicle).[9,10] It targeted tumours and its doxorubicin is released and becomes available to kill tumour cells. It is reasoned that the nanoscale size led to tumour targeting through the enhanced penetration and retention effect which means tumour tissue is more accessible to drugs in this size range – hence limiting off-target toxicity effects associated with the drug.[10]

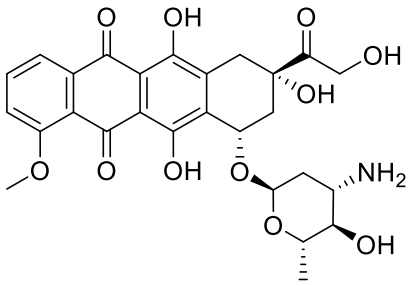

Fig. 1-2 Doxorubicin structure (Doxil®).

Some other nanoscale drugs have been tested in mice and showed good results but are awaiting testing in human trials.[5] For example, gold nanoshells; are proposed for use to

diagnose and cure cancer.[11] Sokolov et al.[12] demonstrated the use of gold colloids, as scattering contrast agents, conjugated to antibodies to the epidermal growth factor receptor (EGFR) and used for biomolecular optical imaging *in vivo* of cervical cancer cells and tissues. They showed that gold bio-conjugates can be delivered topically in order to image the whole epithelium.[11,12] Also, liposomes were used as vaccine adjuvants as well as vehicles for drug transport.[5,13,14] Liposome formulations were used for reducing toxicity as well as increasing accumulation at targeted sites.[15] Preparation methods of liposomes were based on lipid drug interactions and the mechanism of disposition liposome which was achieved by controlling particle size charge and surface hydration, hence inhibiting the rapid clearance of the liposome.[16]

Biodegradable polymers are still under investigation as drug nano-carriers.[17] They attracted researchers because of their non-toxicity and complete elimination from the body[18,19] as well as low side effects.[20,21] For example, poly(lactic-co-glycolic acid), poly(lactic acid) and poly(glycolic acid) have been approved by FDA for specific medical applications, such as treatment of neurodegenerative diseases[22] and to diagnose and treat cardiovascular disease.[23] These polymers can be degraded and eliminated from the body as carbon dioxide and water.[24]

Another class of nano-drugs is dendrimers, which offer a new approach compared with traditional linear polymer architecture classes. Dendrimers are based on repetitive branched structures.[25] Synthetic dendrimers offer the chance to generate monodisperse nanoscale structures, similar to those observed in biological systems such as proteins.[26,27] Over one hundred families of different dendrimer have been synthesized as well as >1000 reported significant chemical surface modifications.[26,28,29] In general, the design of dendrimers is based on three parts; inner scaffold, terminal groups and linkers[5,29] (Fig. 1-3).[5] Increasing the generation, molecular size and terminal groups of a dendrimer

increases the potential for varies of interactions, as such, the dendrimer would be considered as highly functional.[30]

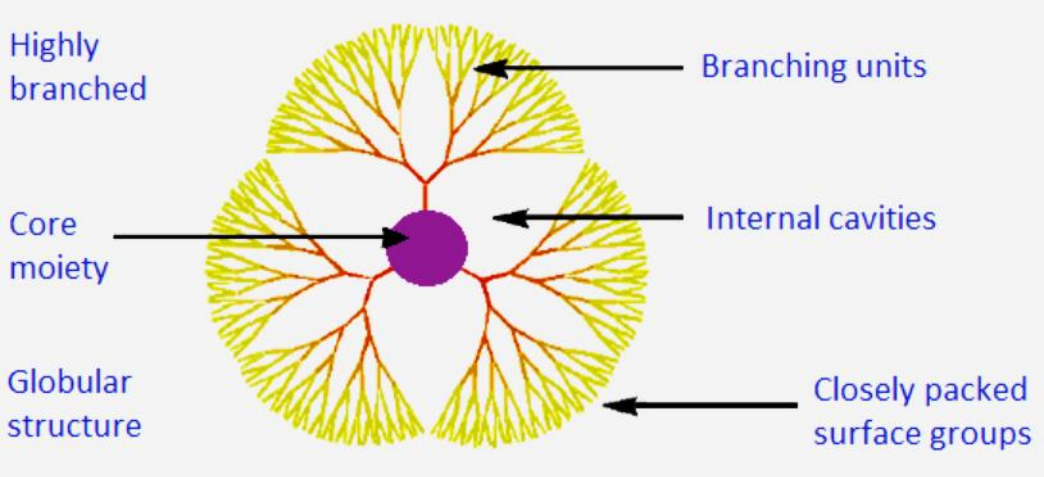

Fig. 1-3 Schematic representation of a dendrimer showing core, branches, and surface. Figure adapted from reference.[5]

Overall, novel functional nanomaterials with special physical properties are being designed to deliver significant improvements to current medicines. They have been developed with the intention to avoid significant side effects to patients (toxicity). However, many nanomaterials, in preclinical assessment, face problems by either having high toxicities during *in vitro* or *in vivo* testing, or failing to have the minimum bioavailability according to their adsorption, distribution, metabolism, and excretion (ADME) profile. These challenges created a need to develop alternative methods for producing such systems.[31]

1.2 Self-Assembled Multivalent (SAMul) Nanostructures

1.2.1 Multivalency

Multivalency is the concept of a molecule having multiple binding groups/sites. Although the term 'multivalency' is most used by macromolecular chemists, it is widely applied across a range of scientific disciplines.[32-34] An effective way of binding nanoscale biopolymers is to use multivalent interactions where multiple ligands cooperate in the binding process.[35,36] On the molecular level, multivalent interactions should be defined with care. For instance, a multivalent host, that has two or more binding sites, interacting with two or more monomeric guest molecules does not count as a multivalent interaction, because each individual guest will only form a single interaction with the host. However, these interactions can be described as multivalent when the guest become larger – when interactions are occurring between the guest, at multiple binding sites, and different receptor groups on the same molecule (host).[33]

Multivalent ligands can have enhanced binding through a number of different mechanisms as shown in Figure 1-4. In general, after the binding of the first ligand an entropic effect will allow subsequent binding events to occur more easily, for example at; an additional binding site **(a)** or a sub binding site **(b)**. In addition, multiple ligands can enhance binding by clustering the receptors together facilitating the binding **(c)** – this type of effect frequently occurs in biological membranes. There can also be an effect of local concentration, in which rebinding of a ligand has a greater chance once it has dissociated from a receptor due to a high local concentration **(d)**.[37] some, or all, of these mechanisms can be operating in a multivalent binding event.

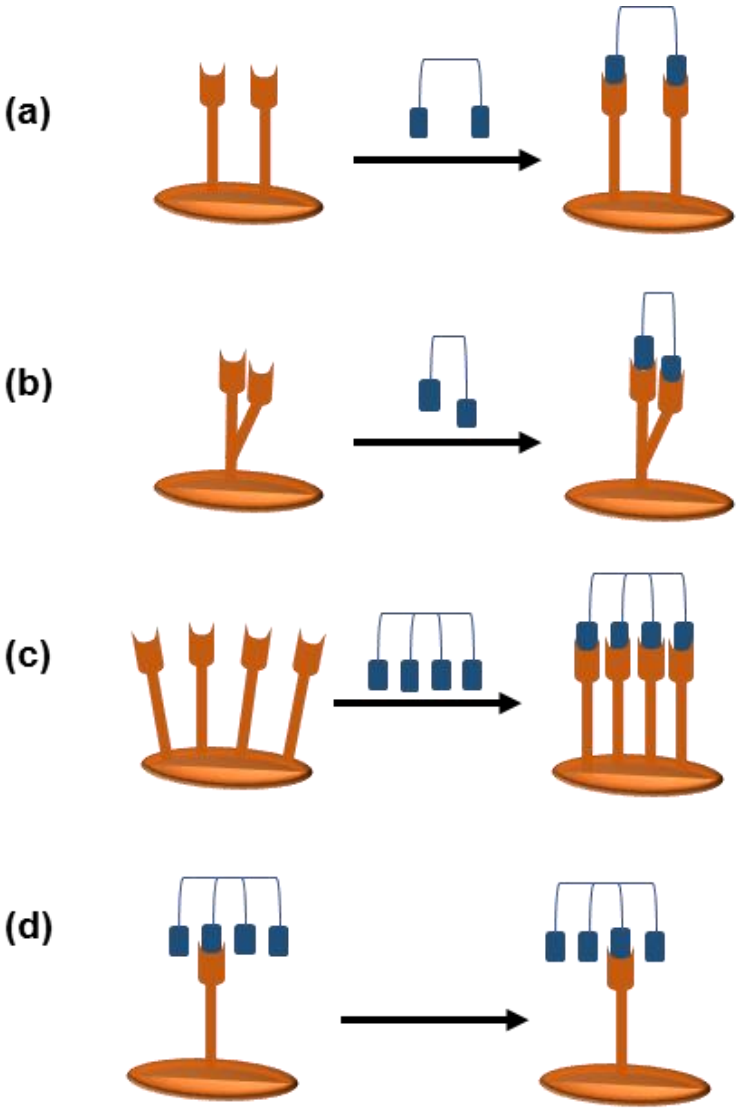

Fig. 1-4 Different binding modes displayed by multivalent ligands; additional binding site **(a)**, sub binding site **(b)**, clustering of multiple ligands **(c)** and high local concentration **(d)**. cartoon reproduced from reference.[37]

The calculation of the free energy of multivalent interactions (ΔG_{multi}) can be achieved in a similar way to calculating monovalent interactions.[38] Such calculations were done in a study by Whitesides et al.[32] to determine the degree of cooperativity associated with a multivalent interaction. This study provided a comparison between the changes in the free energy of multivalent interactions and monovalent interactions in order to determine the binding enhancement factor, α, which is described as the degree of cooperativity (Eq. 1.1), where N is the number of ligand-receptor pairs, ΔG_{multi} is the free energy associated with the interaction between N receptors and N ligands, ΔG_{mono} is the free energy change

from the corresponding monovalent interaction and K_{multi} and K_{mono} are the affinities resulting from multivalent and monovalent binding events, respectively.

$$\alpha = \frac{\Delta G_{multi}}{N\,\Delta G_{mono}} = \frac{\ln (K_{multi})}{\ln (K_{mono})^{N}}$$

Eq. 1-1 Calculation of changes in the free energy of a multivalent interaction, by Whitesides.[32]

In general, the α value can be employed to define three types of multivalent interaction. The first is when $\alpha > 1$, which means that for binding events, the second binding is more favourable than the first, which can be defined as positive cooperativity or a synergistic interaction. When $\alpha = 1$, the binding events are non-cooperative; each subsequent binding event has the same affinity as the previous one. The final type, when $\alpha < 1$ indicates that the interaction of the second ligand with the receptor is inhibited due to the presence of the first one; this means the interaction can be described as negatively cooperative.[39,40]

However, it is worth noting that it is not strictly necessary that a multivalent interaction requires a positively cooperative synergistic effect. Simply it requires a higher affinity for the whole system towards the target than when it is just a monovalent system.[40] In this way, binding affinity can be boosted – a particularly valuable effect for useful interactions in highly competitive biological media.

Multivalent binding can be employed across a wide range of biological and chemical systems. Examples of such processes in nature[32] can be found when a virus is attached to a cell surface wall (Fig. 1-5). The attachment of a virus on a host cell is mediated by several surface components, with the virion protein(s) binding either to specific host surface molecule(s) such as membrane proteins, lipids, or to the carbohydrate moieties present either on glycoproteins or glycolipids.[41] An example for such processes is when virus membrane glycoproteins attach to a target cell surface by binding to heparan sulfate proteoglycans.[42] These first interactions between a target cell surface and a virus are

usually electrostatic and facilitate virus attachment to a specific receptor.[43] There are two types of cell receptors; adhesion and entry receptors. The adhesion receptors attach to a virus in a reversible manner to target cells or organ but do not trigger entry. However, the adhesion receptors facilitate more concentration of the virus in the vicinity of the entry receptors. Once a virus is attached to the entry receptors, the receptors trigger virus entry by endocytosis or by inducing fusion (penetration), which is an irreversible process.[44]

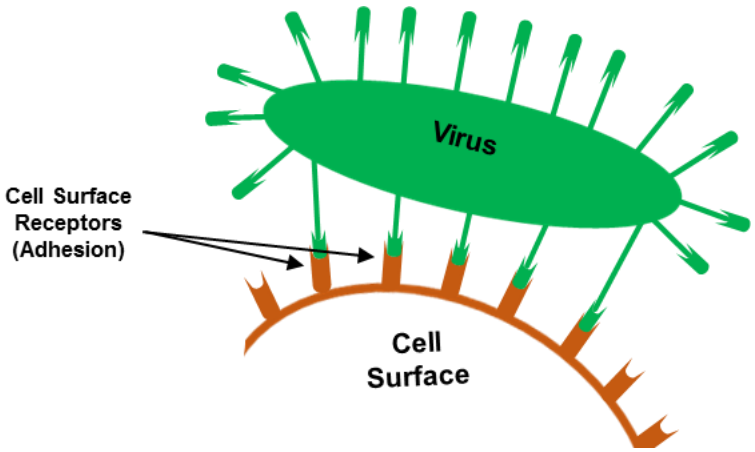

Fig. 1-5 Schematic cartoon of virus binding to cell surface adhesion receptor.

Another example of multivalent binding in nature is when a dendritic polymer interacts with DNA as shown in Figure 1-6. Polyamidoamine (PAMAM) dendrimers can achieve targeted gene delivery,[45,46] and have multivalent binding to DNA. PAMAM dendrimers have a well-defined spherical cationic structure consisting of primary amines on the surface and tertiary amines in the interior (Fig. 1-6) this allows them to bind electrostatically to DNA.[47] In particular, for effective gene delivery, highly multivalent larger fifth generation PAMAM dendrimers are required.[48]

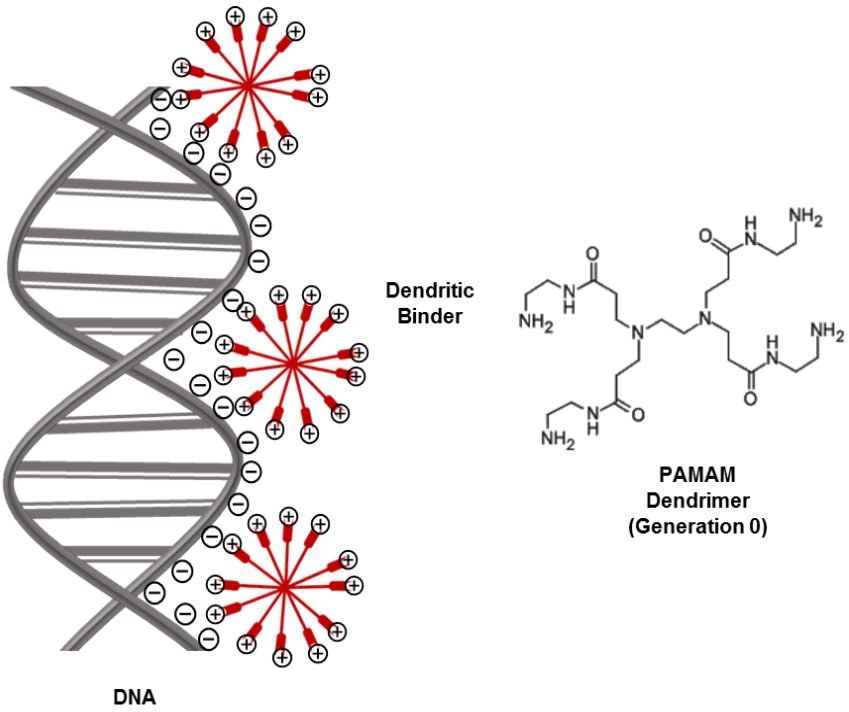

Fig. 1-6 Schematic cartoon of a dendritic polymer, such as PAMAM, multivalent binding to DNA through surface electrostatic interactions.

Supramolecular chemists have studied many varieties of multivalent binding system, from systems designed for biological applications to templates for assisting covalent synthesis. For example, synthetic multivalent inhibitors were designed for inhibiting viruses,[49-52] bacterial toxins,[53-55] and for promoting required cellular responses.[37,56,57] Multivalency can also be used for controlling recognition events at surfaces.[34,58] Understanding the multivalent attachment processes of viruses on cell surfaces, led medicinal approaches to develop viral inhibitors that are capable of multivalent interactions. Haag[59] and co-workers developed a range of multivalent antiviral ligands by focusing on the use of synthetic dendritic polyglycerol sulphates (dPGS) (Fig. 1-7). dPGS operates via a multivalent binding mechanism mimicking naturally occurring ligands and proved to inhibit both leukocytic L-selectin and endothelial P-selectin with high efficacy.[59]

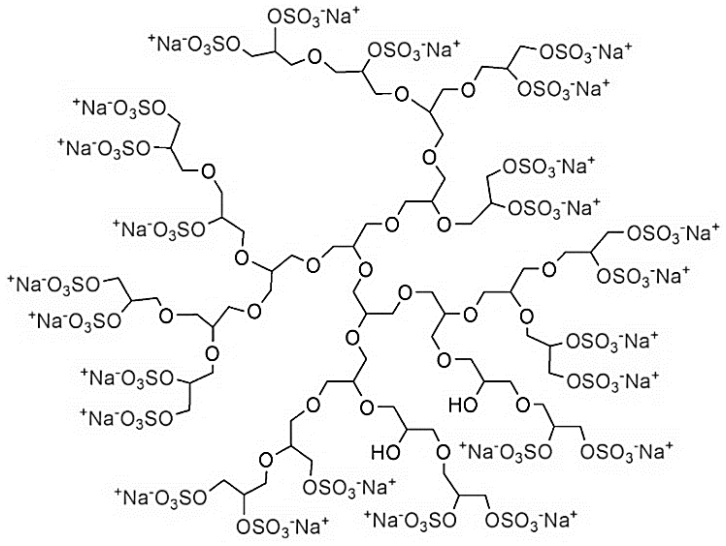

Fig. 1-7 Dendritic polyglycerol sulphate structure, by Haag.[59]

Other synthetic multivalent inhibitors were reported by Whitesides and co-workers. They synthesized polymers of sialic acid in multiple copies; which are approximately 109-fold stronger than monovalent sialic acid when blocking the adhesion of influenza virus particles to erythrocytes.[60] Also, Kitov et al.[61] designed oligo-valent inhibitors of Shiga-like toxin 1 which were 1–10 million-fold more active than the monovalent ligands.

As a further example, Gestwicki[56] and co-workers synthesized multivalent derivatives of the chemo-attractant galactose (Fig. 1-8a) in order to create reagents that stabilize the cell inter-receptor interactions. They investigated the impact of ligand multivalency on bacterial behaviour especially *Escherichia coli (E. coli*). They observed that *E. coli* mutants and wild-type *E. coli*, after pre-treatment by monovalent ligand were unaffected when adding serine. However, when they were pre-treated by multivalent ligands, they showed more stabilized inter-receptor contact, when adding serine; the response to serine was amplified by at least 100-fold from motion analysis results (Fig. 1-8b).[56]

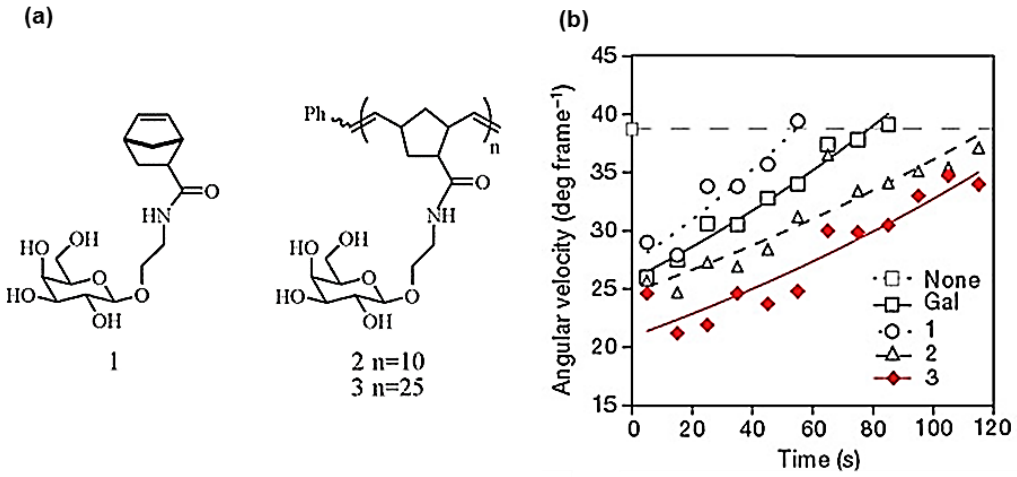

Fig. 1-8 Structure of the galactose monomer 1 and the multivalent arrays displaying galactose 2–3 **(a)** and motion analysis showing a plot of average angular velocity versus time for *E. coli* AW405 treated with chemoattractant (galactose or ligands 1-3) **(b)**. Figure adapted from reference.[56]

1.2.2 Ligand Display

1.2.2.1 Cationic Lipids

Generally, cationic lipids consist of three parts; a head group (cationic), a tail (hydrophobic) and a linker between the two parts. Modification of each of these parts have developed a wide range of vectors for gene delivery in addition to many studies of structure-activity relationships. Cationic lipids were used for gene transfection in pioneering work by Felgner et al.,[62] who developed the lipid *N*-[1(2,3-dioleyloxy)propyl]-*N*,*N*,*N*-trimethylammonium chloride (DOTMA) (Fig. 1-9).[62-64] After that, they performed another study to uncover more details of structure-activity relationships in order to enhance the performance of their systems. This initial effort was followed by several attempts to develop other cationic lipids such as 1,2-dioleyloxypropyl-3-dimethyl-hydroxyethyl ammonium bromide (DORIE) and 1,2-dimyristyloxypropyl-3-dimethyl-hydroxyethyl ammonium bromide (DMRIE) (Fig. 1-9)[65] which have later been employed by other research groups.

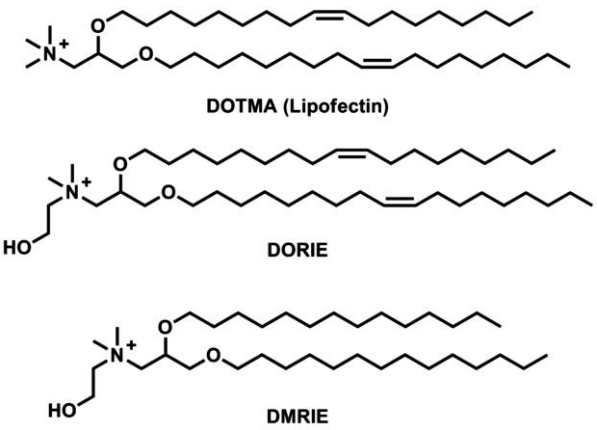

Fig. 1-9 Structure of cationic lipids DOTMA, DORIE and DMRIE.by Felgner.[62]

Several developments followed that initial effort by Felgner and co-workers in which the ligand or linker were modified to produce commercially available cationic lipids including DOTMA, sold under the name Lipofectin™.[62] A derivative product from DOTMA known as 2,3-dioleyloxy-*N*-[2(sperminecarboxamido)ethyl]-*N*,*N*-dimethyl-1 propanaminiumtrifluoroacetate (DOSPA), is sold under the name Lipofectamine 2000™.[66] In addition, two more products were developed; 1,2-dioleoyl-3-trimethylammoniumpropane (DOTAP)[67] and dioctadecylamido-glycylspermine (DOGS) or Transfectam®[68] (Figure 1-10).

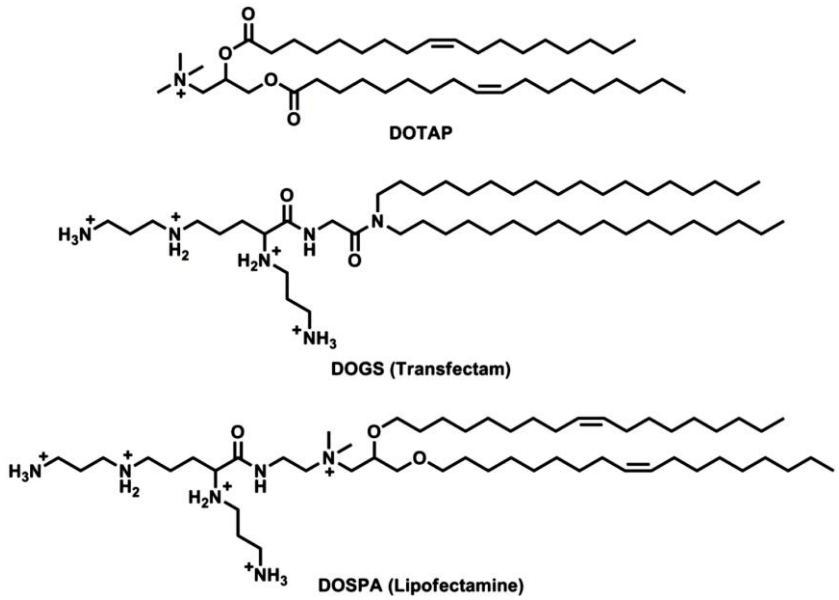

Fig. 1-10 Structure of cationic lipids DOTAP, DOGS and DOSPA, all of which are commercially available as transfection agents.

1.2.2.2 Gold Nanoparticles (AuNPs)

Gold Nanoparticles (AuNPs) have attracted the attention of researchers due to their unique properties and multi-applications.[69,70] AuNPs are used as biomarkers and bio-delivery vehicles in medicine and pharmacy.[71,72] The unique optical properties of AuNPs, their size dependent properties and their high chemical stability have made them an ideal system for exploring many aspects including self-assembly, bio-labelling, catalysis, etc., These nanoparticles when stabilized or protected by a shell of thiolate ligands,[70] display good stability toward aggregation and other modes of decay.[73]

There are two methods to synthesise such thiolate-protected nanoparticles; the top-down approach and the bottom-up technique. The second method is more common and effective. Gold ions are reduced, from their salt, by a reducing reagent. They then start to nucleate to form nanoparticles while in the presence of protective ligands which prevent uncontrolled growth of gold metal.[70] "Brust synthesis" [74,75] has been thoroughly explored (Fig. 1-11). This method has enabled the synthesis of a great variety of functionalized noble metal nanoparticles over the years.[75,76,77] Their high stability is due to the passivation property that alkanethiols cause, which form a strong bond with the particle surface.[75,78]

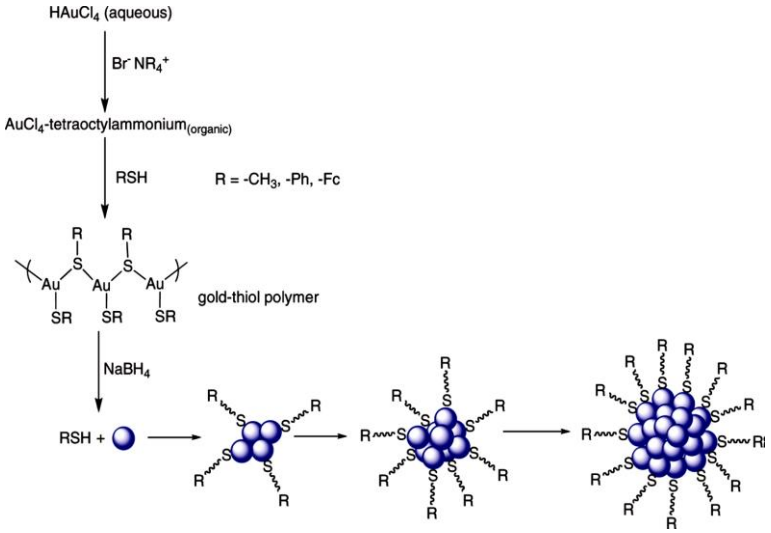

Fig. 1-11 Scheme for gold nanoparticle synthesis by Brust Two-Phase Approach, cartoon adapted from reference.[75]

Another method was introduced by Turkevich et al.[79-81] as a single phase synthesis. This method is water based reduction of a gold salt by citrate. Later, Frens[81,82] improved this method to produce almost spherical particles with controllable range of sizes.[83] These nanoparticles, when stabilized or protected by a shell of thiolate ligands,[70] display good stability toward aggregation and other modes of decay.[73]

In the development of therapeutics, Melander[84] and co-workers constructed a platform for their multivalent therapeutic by employing 2.0 nm diameter, mercaptobenzoic acid modified gold nanoparticles. These mercaptobenzoic acid coated gold nanoparticles were conjugated to SDC-1721, a derivative of TAK-779, a known CCR5 antagonist (Fig. 1-12).[84] They demonstrated that when gold nanoparticles are conjugated to a weakly binding and biologically inactive small molecule they transform it into a multivalent array that has the ability to inhibit HIV-1 fusion to human T cells (Fig. 1-13).[84]

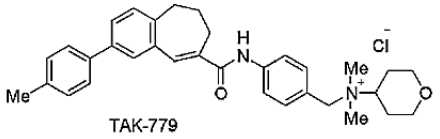

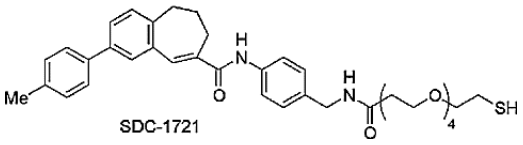

Fig. 1-12 TAK-779 and SDC-1721.[84]

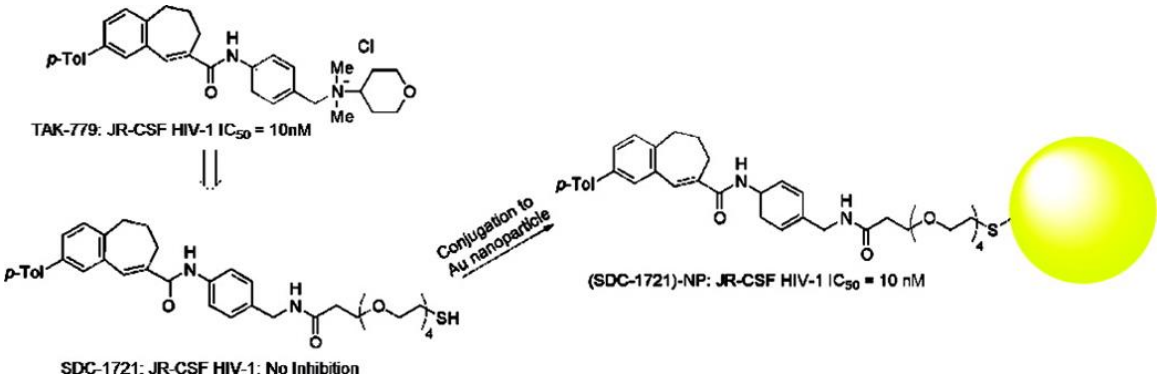

Fig. 1-13 Synthesis of a multivalent gold nanoparticle therapeutic; multivalent presentation of small molecules on gold nanoparticle surfaces can convert inactive drugs into potent therapeutics. Adapted from reference.[84]

Gold nanoparticles have been employed in many studies to mimic the multivalent presentation of cell surface carbohydrates and have been used in applications such as drug delivery systems, sensors, bioimaging reagents and affinity probes.[85-88] In recent work from Okada and co-workers,[89] they developed multivalent carbohydrate photoaffinity probes based on gold nanoparticles as an approach for the identification of carbohydrate-binding proteins. They designed their systems to be capable of removing non-specific proteins by covalent cross-linking as well as promoting affinity enhancement to achieve efficiency and selectivity of capturing specific carbohydrate-binding proteins. This work presented novel bifunctional chemical tools, which can perform a one-pot photoaffinity labelling and affinity purification (Fig. 1-14).[89]

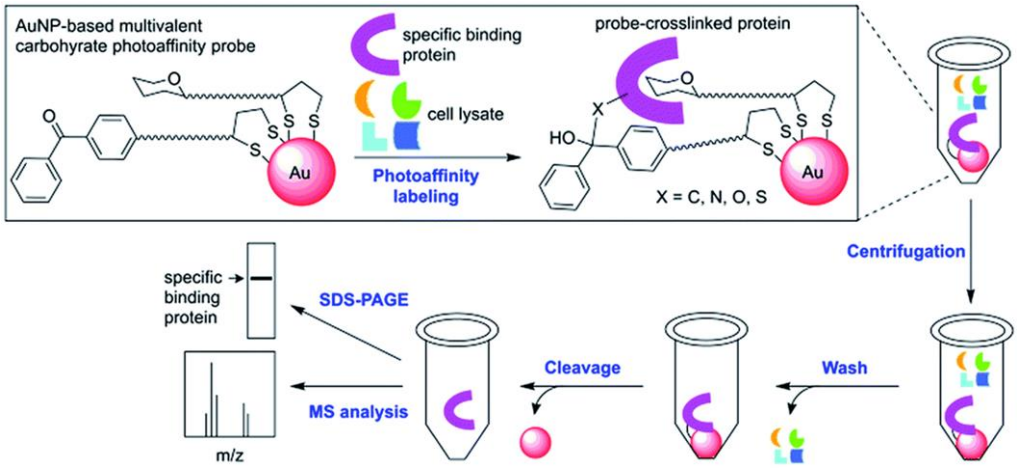

Fig. 1-14 A streamlined photoaffinity labelling approach toward identification of carbohydrate-binding proteins by using AuNP-based multivalent carbohydrate probes by Okada and co-workers. Figure adapted from reference.[89]

1.2.2.3 Drug-Polymer Conjugates

In the 1960s, initial work on employing polymers, as pharmaceutical drugs, was using them as blood plasma expanders, for wound bandages and as injectable depots.[90,91] In 1975, Helmut Ringsdorf[92] proposed the first coherent model for pharmacologically active polymers (Fig. 1-15). The concept he proposed, of covalently bound polymer-drug conjugates, is still employed for most of the performed work in this area to date. This model attracted drug delivery scientists, as it offered a practical way of achieving the

specific delivery of therapeutic agents to their desired site as well as improving efficacy and decreasing toxicity.

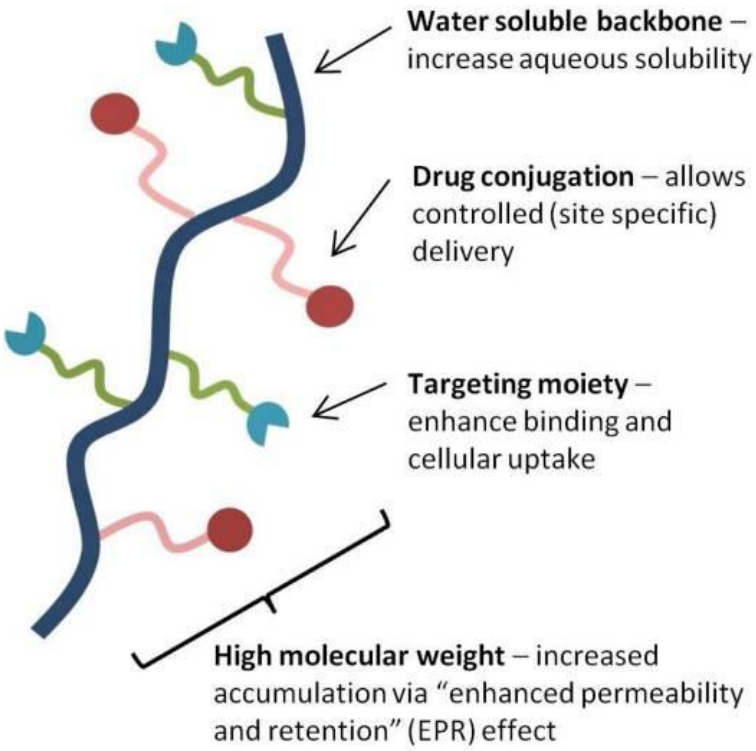

Fig. 1-15 The first proposed model for pharmacologically active polymers, Ringsdorf, 1975, figure adapted from reference.[93]

Cell–cell recognition and the initiation of signal transduction processes often depend on the formation of the multiple receptor-ligand complexes at cell surfaces. These complex events of cell surface-binding could benefit from a multivalent ligand approach.[94] Ligand architectures have effects on inhibitory activity and specificity, these effects were explored by Reuter et al. with series of polymeric synthetic inhibitors of hemagglutination.[95] They generated a number of ligands, with distinct structures such as sialic acid (SA) residues conjugated to be tested *in vitro* for their ability to inhibit hemagglutinin binding and viral infection (Fig. 1- 16). The polymer-conjugates were shown to be more effective than monomeric SA after testing on four viruses; influenza A H2N2 (selectively propagated two ways), X-31 influenza A H3N2, and sendai.[95]

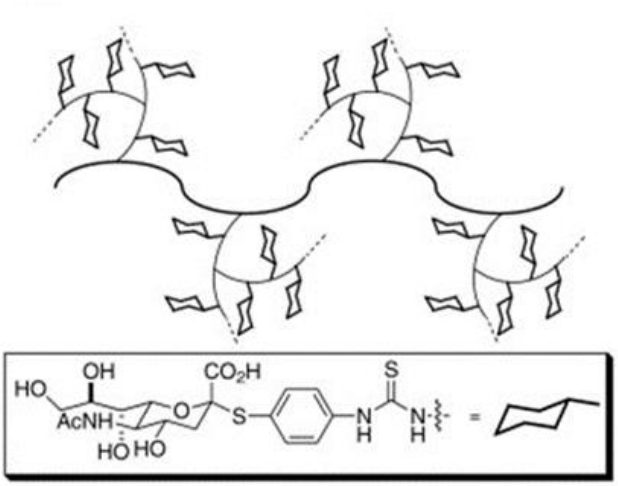

Fig. 1-16 Structure of sialic-acid-conjugated polymeric inhibitor subunits. Adapted from reference.[95]

Schaffer[96] and co-workers designed multivalent conjugates with the ability to organize stem cell receptors into nanoscale clusters in addition to controlling behaviour of stem cells *in vitro* and *in vivo*. They conjugated an integral membrane protein ligand, ectodomain of ephrin-B2, to a soluble biopolymer (Fig. 1-17). The results were multivalent nanoscale conjugates that have the potential to induce signals in the neural stem cells as well as promoting neuronal differentiation; both in culture and within the brain.

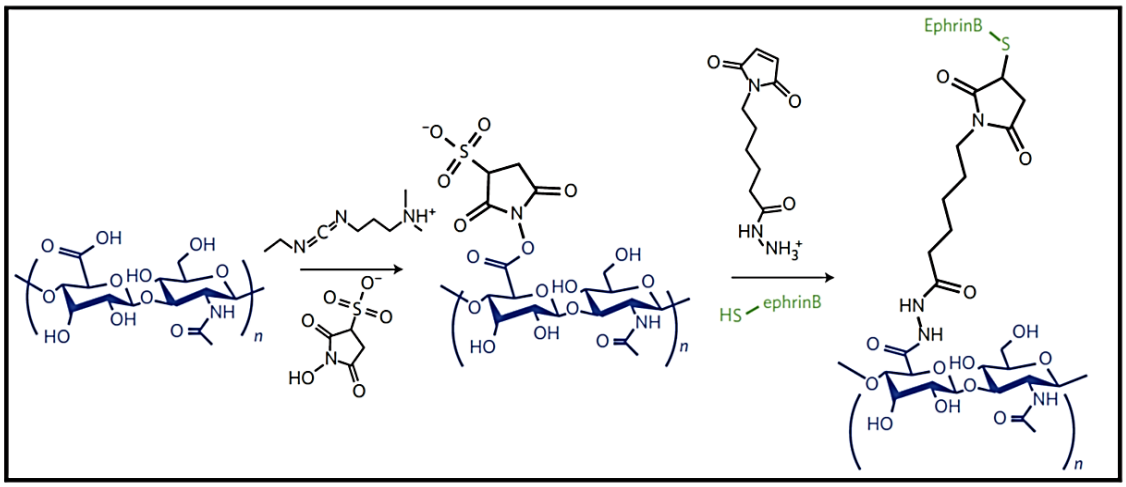

Fig.1-17 Synthesis of multivalent ephrin-B2. Scheme adapted from reference.[96]

1.2.3 Self-Assembly

The spontaneous aggregation of molecules into well-defined structures held together by non-covalent interactions is known as self-assembly. One example of self-assembly is provided by surfactants which contain both hydrophobic and hydrophilic regions.[97] For simple amphiphilic molecules, when the concentration of a monomer molecules increases (in solution), the hydrophobic groups aggregate to minimize contact with water and surface groups (hydrophilic) are displayed on the periphery.[98] This process is reversible and there are a number of factors that affect the overall aggregate's structure, such as, the monomer concentration and its morphology.[99]

Israelachvili et al. published a discussion in 1976 of the monomer geometry effects and the degree to which hydrophobicity influences the subsequent self-assembly mode.[100] They introduced a definition of a critical packing parameter, P, which allowed a prediction of the morphology of such aggregate. This P value was based on the volumes of both hydrophobic and hydrophilic groups within the assembly. As shown in Figure 1-18, the relative sizes of hydrophilic and hydrophobic groups of a monomer affect the overall shape of the nanoscale assembly. As the hydrophobic group size increases compared to the hydrophilic surface group, the morphology changes so that more geometric space is provided to incorporate it. At low P values, spheres are favoured **(a)** – maximizing surface area but as P increases cylindrical morphologies occur, reducing unfavourable interactions with the aqueous solvent **(b)**. With an increase in hydrophobicity (e.g. presence of a second aliphatic tail) vesicles or liposomes become the preferred mode of self-assembly **(c)**. When hydrophilic and hydrophobic groups are of similar size, a planar bilayer structure will form **(d)**. Once the hydrophobicity is significantly increased and becomes much bigger than the hydrophilic surface group, an inversion will occur and the micelle non-polar groups will be at the surface and the

hydrophilic groups in the core **(e)**. Such systems form these reverse micelles in organic media.

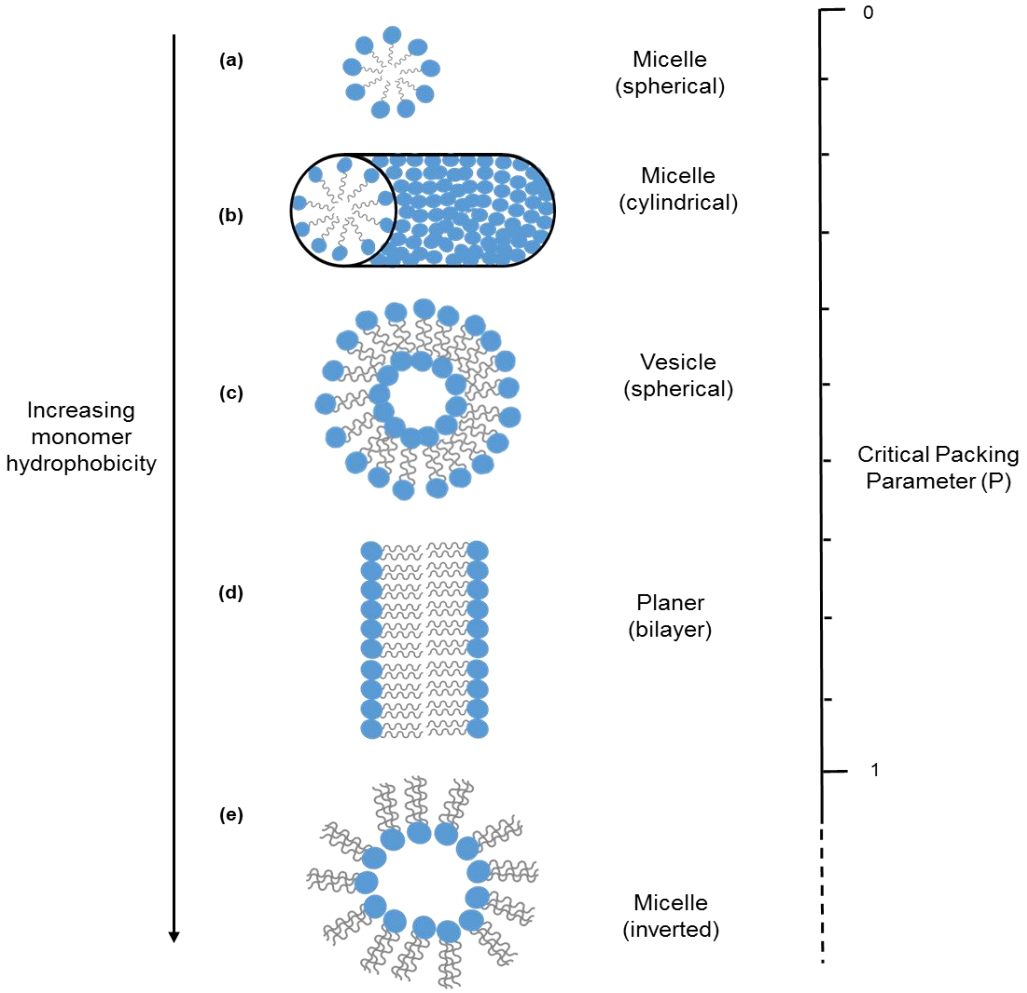

Fig. 1-18 Critical packing parameter (P); prediction of aggregate morphology in aqueous solution by Israelachvili.[100]

In the early 1990s, Whitesides[97] and co-workers presented an example of self-assembly. The strategy that they outlined proved to be a successful one. This strategy was based on reversible, noncovalent interactions to assemble nanostructures aggregates. They achieved that by synthesizing nanostructures (solid 1:1) complex formed by mixing melamine (M) and cyanuric acid (CA) in aqueous solution to form CA-M lattice; each CA and M units were connected by benzene ring, as a linker (Fig. 1-19), to minimize the entropic cost of self-assembly and to control the assembled nanostructure shape.

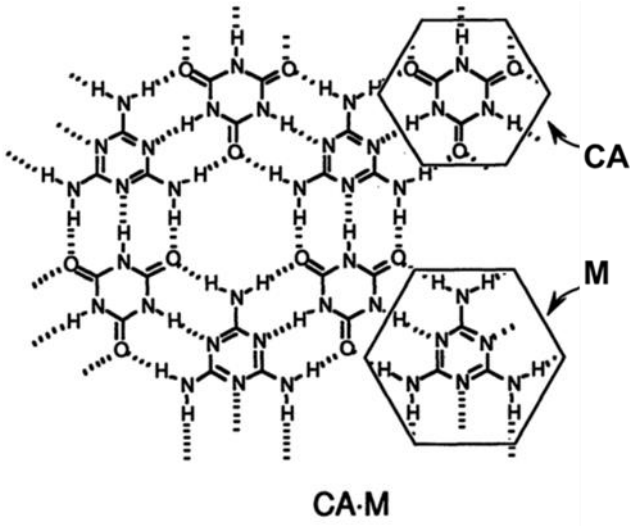

Fig. 1-19 Melamine cyanuric acid synthesized self-assembled nanostructures (CA-M lattice), by Whistsides.[97]

1.2.4 Self-Assembled Multivalent (SAMul) Approaches

Self-assembly has significant power in the solution-phase and readily allows multiple monovalent non-assembled ligands to potentially cooperate in binding to a target. This can allow high-affinity multivalent binding (Fig. 1-20).[101] This area was first conceptualized as a distinct approach in a key review by Barnard and Smith.[101] The ease of synthesis (assembly) and tunability of nanostructure morphology and ligands, in addition to the potential to incorporate multiple active units as well as the responsive nature of self-assembly, mean this is a powerful and general tool for generating synthetic multivalent nanoscale binding arrays with potential biomolecular applications.[101]

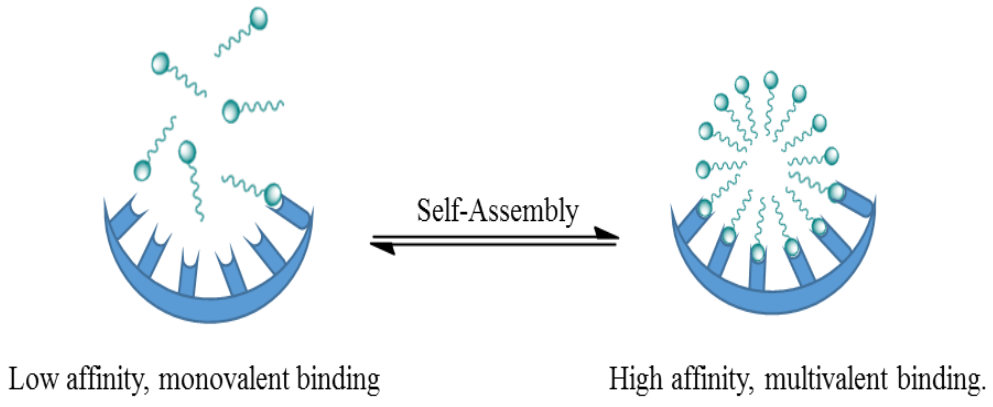

Fig. 1-20 Self-assembly enables high-affinity multivalent binding.

The biological and medicinal applications of self-assembled multivalent (SAMul) nanostructures are currently being developed.[102] DNA has been a target for several research groups who have employed self-assembled binding approaches for develop potential medicinal drugs of genetic diseases[103] as well as cancer treatments.[104] Yadav[105] and co-workers synthesized a conjugated system of branched hydrophilic oligosaccharide structure neomycin with a hydrophobic modified dipeptide to result an amphiphilic self-assembled nanostructure (Pep–Neo conjugate) (Fig. 1-21). This system has cationic charges on the surface that would facilitate entry into the cells after interaction with negatively charged DNA.

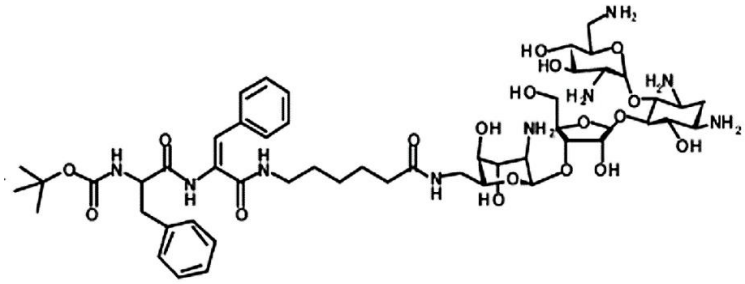

Fig. 1-21 Structure of Pep–Neo conjugate, by Yadav.[105]

The naturally occurring DNA-binding ligand spermine is one of the most employed surface groups in SAMul systems and was featured in notable work from both Cheng[106] and Smith[107] group. Cheng and co-workers used two oleyl hydrophobes to directly functionalize spermine (Fig. 1-22). Whereas Smith used Newkome[108,109] low-generation amphiphilic dendron (cholesterol) and decorated its surface with spermine[107] (Fig. 1-23), then reasoned that more lipidic character better promoted self-assembly.

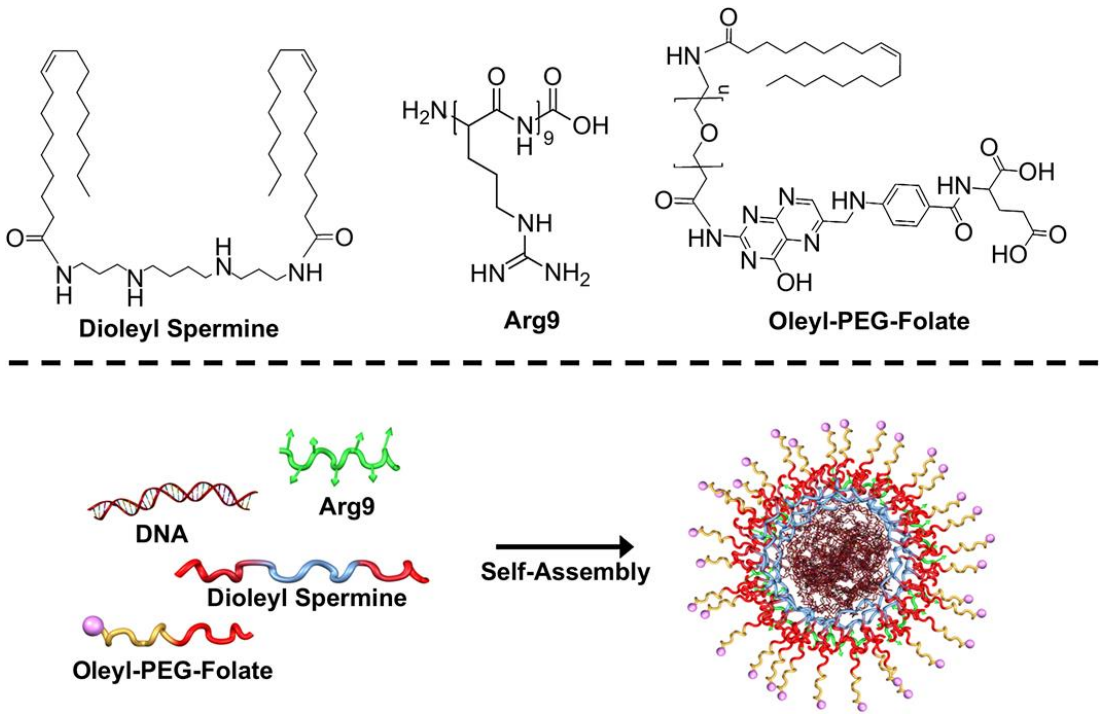

Fig. 1-22 Schematic representation of the supramolecular self-assembly of individual vector components with plasmid DNA, by Cheng. Figure adapted from reference.[106]

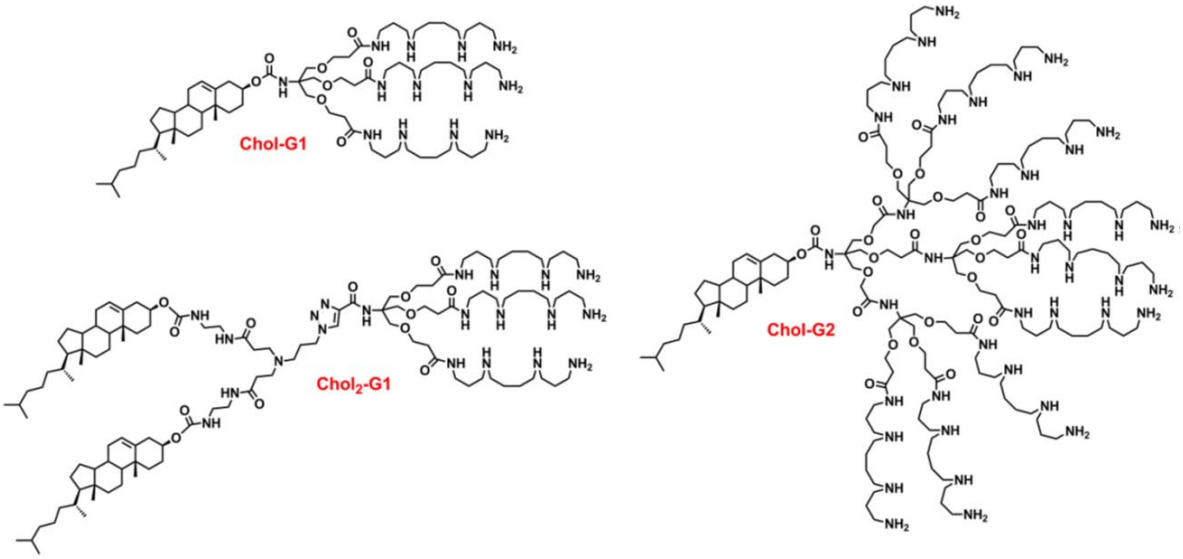

Fig. 1-23 Structure of cholesterol functionalised Newkome dendrons with spermine ligands on their surface.[107,110]

Smith and co-workers have investigated their systems through several structural modifications; on the monomer surface,[39] within the scaffolds of the dendritic branches[110,111] and modifications to the hydrophobic part.[112] Also, they examined the effects of co-assembling PEG-additives into the self-assembled DNA-binding

nanostructures.[113] Overall, the potential gene delivery vehicle they worked to develop, contained a DAPMA binding group, a degradable scaffold (polyester) and a cholesterol hydrophobe as well as a cleavable disulphide-containing linker to enable breakdown of the SAMul array. They developed this system to bind DNA, then release it from the complex as the self-assembled system degraded into small components, that individually have low affinity towards binding DNA.[112] In collaboration with the Haag group, they also synthesized low-molecular-weight dendritic polyglycerol-based amphiphiles with *N*,*N*-di-(3-aminopropyl)-*N*-(methyl)amine (DAPMA) on their surfaces (Fig. 1-24).[114] They suggested that these structures have a prospective application *in vivo* as new promising alternatives for nonviral siRNA delivery systems in addition of great potential for further synthetic modifications.[114] It was demonstrated that such self-assembled vehicles did not induce any immune response in an animal model.

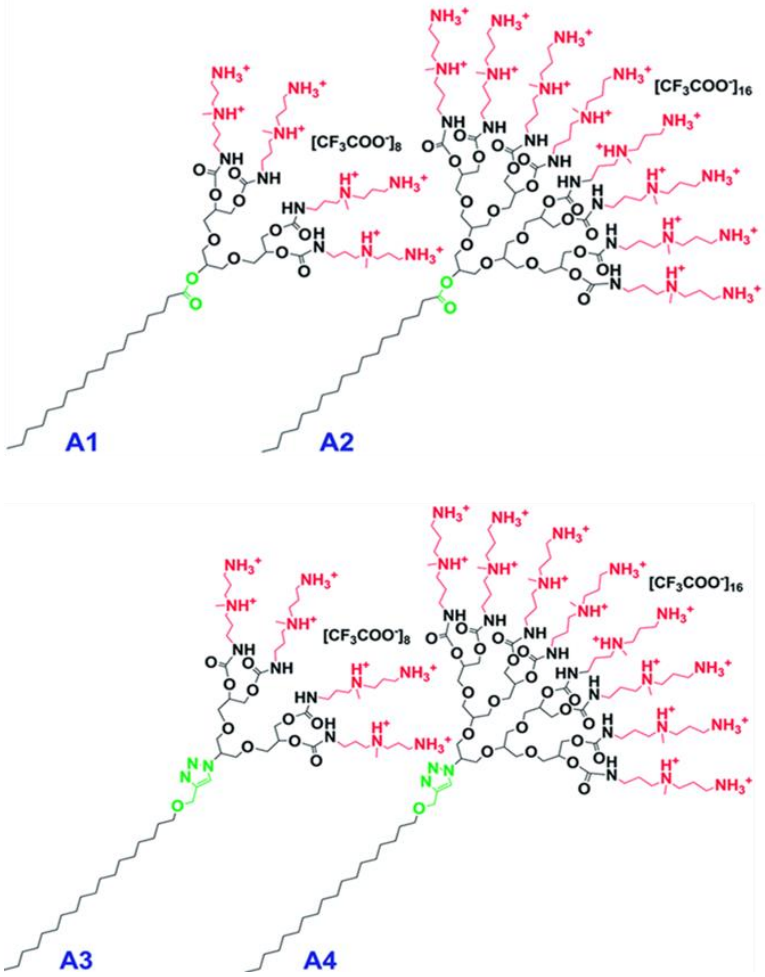

Fig. 1-24 Synthetic low-molecular-weight dendritic amphiphiles, reported by Haag and Smith.[114]

Stupp and co-workers employed self-assembly using isoleucine-lysine-valine-alanine-valine (IKVAV). IKVAV, is a vital pentapeptide sequence for cell attachment, migration, and neurite outgrowth.[115,116] They used it to synthesize nanofiber peptides[117] as bioactive sequence for neural applications.[118-120] They designed these IKVAV-containing peptide amphiphiles to contain four regions; hydrophobic tail, beta-sheet forming segment, charged groups and bioactive epitope (Fig. 1-25).

Fig. 1-25 IKVAV-containing peptide amphiphile molecule and its self-assembly into nanofibers, by Stupp.[117]

Another study was performed by Ravoo and co-workers[121] to develop switchable SAMul DNA binders. Their work was based on using an azobenzene moiety to functionalize spermine, this moiety has the ability to be encapsulated within cyclodextrins (CD) α and β (α-CD and β-CD) at the surface of CD-vesicles (Fig. 1-26). They found that this self-assembled multivalent approach enhanced DNA binding, and could be switched by light as the azobenzene unit converted from trans to cis.

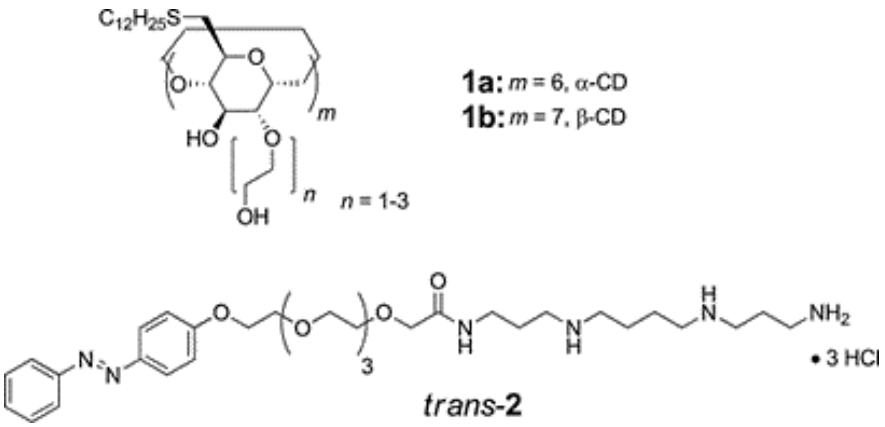

Fig. 1-26 Ravoo and co-workers self-assmbled systems; functionalized spermine by azobenzene at CD-vesicles surface. Structures adapted from reference.[121]

1.3 Heparin

1.3.1 Heparin Therapy

Heparin (Fig. 1-27), from mast cells, is an anionic sulphated polysaccharide that is considered the most highly charged anionic biological polymer.[122-124] It has a heterogeneous chain consisting of different repeating monomers (copolymers).[123,125] The molecular weight of heparin varies between 3,000 and 30,000 kDa, the mean being around 15,000, which represents 45 saccharide units (Fig. 1-27).[126] In practical terms, only about one third of those units consist of the functional active pentasaccharide that binds specifically to its target-antithrombin.[127,128,123]

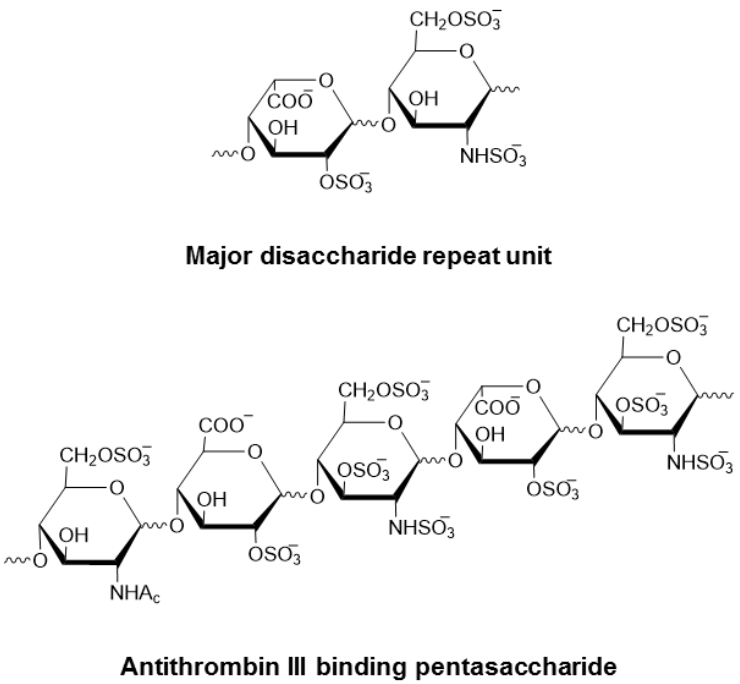

Fig. 1-27 Major heparin disaccharide repeated unit and the active antithrombin III binding pentasaccharide, reproduced from reference.[126]

In nature, heparin exists as part of the heparans in the inner walls of the microvascular system.[129] Heparin is extracted from animals as a heterogeneous drug, and injected into the blood stream to circulate during surgical procedures.[130,131] It is considered the only choice to treat and prevent thromboembolic disease.[129] It acts as, and can be considered

as, the only anticoagulant drug during surgery by binding to antithrombin and has been in use since 1935.[132-134] There are two major forms of heparin in current use; unfractionated heparin (UFH) and the fractionated heparin; low-molecular-weight-heparin (LMWH), which mainly consists of polysaccharides with *M*r typically between 4000 – 6000 Da. Both work as indirect anti-coagulants, where plasma cofactors play a mediation role.[135] However, LMWH has a metabolism half-life of 3-6 hours, whereas UFH is removed rapidly in *ca*. 30 minutes.[136] The normal concentration of heparin, during clinical procedures, is between 1.2 and 48 μg/ml (0.2–8 international unit (IU) /ml).[137] For estimation of heparin *in vivo*, a method of activated clotting time is commonly used.[137,138]

Despite the fact that heparin is widely used in open heart surgery and other major operations, heparin sodium causes a low platelet count in patients (thrombocytopenia).[125,135] Therefore, complications such as severe bleeding can lead to postoperative mortality.[139] As such, it is necessary to reverse the effects of heparin once surgery is complete (see below).

1.3.2 Heparin Replacements

Heparin alternatives such as Warfarin (Fig. 1-28); a synthetic derivative of coumarin have been used as anticoagulants by reducing all four dependent coagulation factors of vitamin K. Warfarin produces its anticoagulant effect by interfering with the vitamin K interconversion cycle and its epoxide (2,3 epoxide).[140] It blocks the formation of vitamin K1 and vitamin KH2 by inhibiting vitamin KO reductase, which stops the carboxylation of glutamate residues of vitamin K–dependent proteins (Fig. 1-29).[141] Nonetheless, its function in blood is slower than heparin. In addition, it causes bleeding, headache,

dizziness and difficulty breathing.[142] Typically, it is used as a long-term blood-thinner in patients as risk of stroke, rather than in critical care and during surgical intervention.

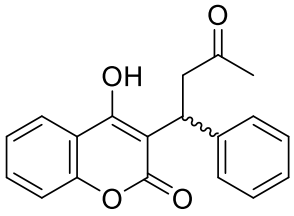

Fig. 1-28 Warfarin Structure.

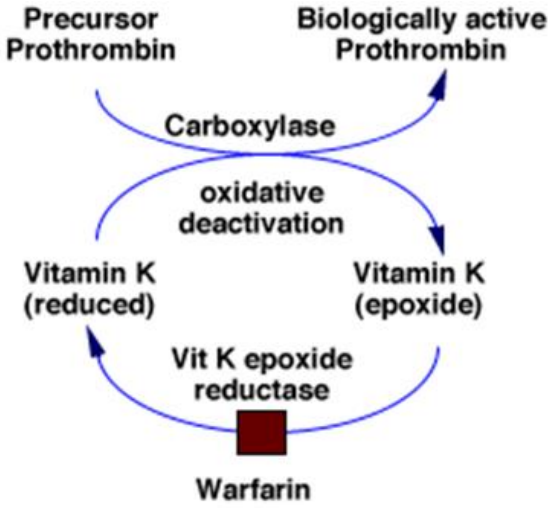

Fig. 1-29 Warfarin inhibition of the vitamin K interconversion cycle and its epoxides. Adapted from reference.[141]

Ancrod[143] from the venom of the Malayan pit viper, was another candidate to replace heparin, but it causes skin reactions, pain at the injection site, splenomegaly, and some systemic bleeding.[143,144] Lepirudin[145] which was extracted from yeast cells (in the past, saliva of leeches), also has major side effects such as numbness, weakness, headache, confusion, problems with vision and speech, and bleeding (haemorrhage). In addition, when excreted through the renal system (90%) it affects kidney function.[145,146] Another example of a heparin replacement is Fondaparinux[147] a synthetic pentasaccharide factor Xa inhibitor but this has no antidote, is expensive, causes skin rashes and has renal excretion problems which prevent its use in patients with renal dysfunction. Overall, all

of these alternative compounds have more critical side effects than heparin[147] and as such, heparin remains the only clinically used anticoagulant during major surgery.

1.3.3 Protamine

The removal of excess heparin from the blood system after surgery is essential in order to rapidly limit excess bleeding during patient recovery. Protamine, an arginine-rich protein[123,128] (Fig. 1-30),[148] derived from salmon sperm,[147] has been used for heparin removal after surgical intervention for decades.[149] Protamine is used in its sulphate form: it is a polyarginine polypeptide (positively charged) and can reverse heparin anticoagulant effects. After it is injected through the intravenous route, protamine (cationic) binds with heparin (anionic) to produce a salt (neutral).[149,150] The complex is excreted, and hence, protamine eliminates heparin's anticoagulation effects.[151] Although the mechanism of protamine appears to be a straight-forward cation-anion binding interaction, it is not well defined as both components are polydisperse.[152]

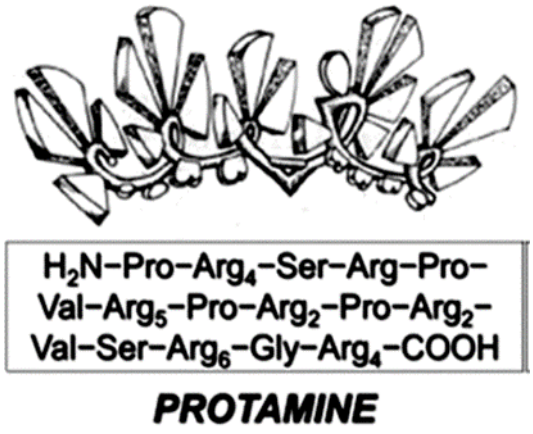

Fig. 1-30 An example of protamine (e.g. Arg_4 = Arg-Arg-Arg-Arg), adapted from reference.[148]

Protamine also inhibits the inactivation of thrombin by antithrombin III (AT III).[152,153] Moreover, clotting assays showed that the inhibition of thrombin by converting fibrinogen to fibrin depends on concentration. Although this conversion is partial and reversible,[154,155] protamine has complications by inhibiting factor V activation which leads to "hidden hemorrhage".[153,156]

In addition, studies of cardiac contractility showed that injection of protamine sulphate is followed by systemic pulmonary hypotension in patients.[157,158] Other major side effects such as allergy and anaphylaxis were also reported.[149] The demand for a simple non-toxic protamine replacement has therefore increased.

1.3.4 Protamine Replacements

There have been a number of attempts to replace protamine in order to prevent the toxic side effects in 10% of the treated patients.[152,158] However; none of those attempts were successful due to their critical side effects or lack of efficiency.[159] Polybrene; polycationic hexadimethrine bromide; a positively charged polymer[160,161] (Fig. 1-31), was investigated as early as 1950s. It was 70% effective at removing heparin by producing non-specific agglutination of red blood cells, to neutralize the negative charge of the red blood cells caused by heparin.[160,162,163] However, it has side effects such as hemodynamic, hematologic, and renal problems.[164]

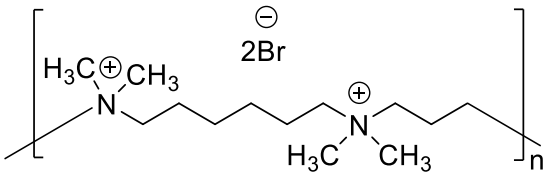

Fig. 1-31. Polybrene structure; rich positively charged molecule.

Another compound tested as a protamine replacement was toluidine blue (tolunium chloride,[160,165] (tolunium chloride).[166] Although it has a reversal effect on heparin, it caused disagreeable side-effects; methemoglobinemia and hypoxia were seen after the treatment of 23 heparinized dogs.[160] Heparinase 1 enzyme[167] is a naturally occurring enzyme which can degrade heparin into less active fragments to neutralize the anticoagulant effects. It was tested clinically, but was not applied directly and has been used via dialysis through a blood filter containing immobilized heparinase. This method required a blood transfusion and was time consuming.[168]

The most recent clinical attempt was Delparantag,[169] initially reported as PMX 60056.[170] This is a chiral peptide consisting of salicylamide units and lysine groups (Fig. 1-32).

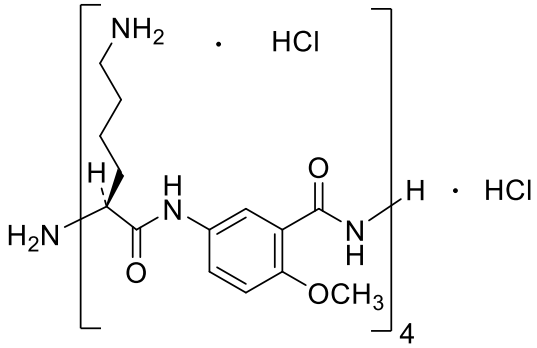

Fig. 1-32. Delparantag structure; lysine group with aromatic core.

Although the mechanism of action of Delparantag was not reported in the literature, from its structure it is obvious that it is positively charged (5 +ve) and can bind with heparin, with the aromatic part possibly enhancing stability or providing structural organization. However, this compound has failed to replace protamine due to "funding problems".[169]

The search for a heparin binder through the development of protamine replacement(s) is now a hot topic in the field of nanomedicine. A self-assembling mimetic for the protamine structure was reported by Smith et al. This was a spherical self-assembled protamine mimic formed from **C_{22}-G1** (Fig. 1-33). The focal hydrophobic chain provided the driving

force for the assembly of this supermolecule. The positively charged amines were the cationic part that binds heparin.[171]

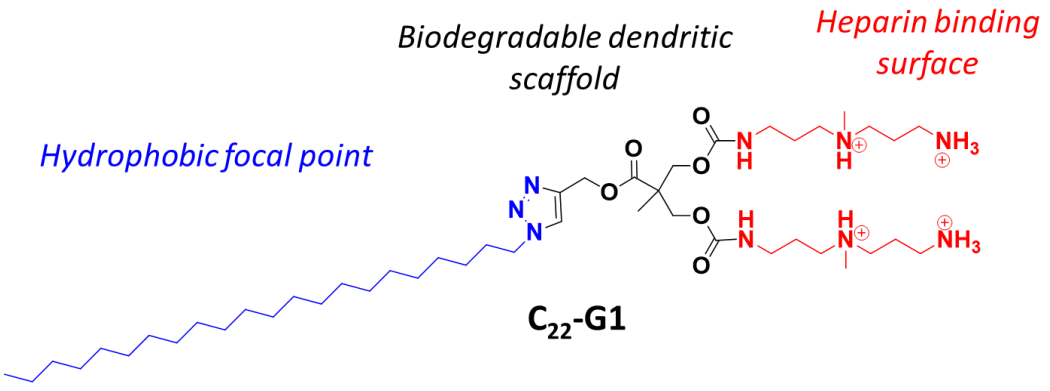

Fig. 1-33 Self-assembling ligand **C_{22}-G1**.[171]

Although the binding of this system along the heparin polymer chains was successful and has been proven by electron microscopy and a solution phase binding assay, unfortunately, it was relatively unstable in blood serum.[171,172]

1.4 Project Aims

The aim of this project is to gain a fundamental insight into structure-activity relationships in self-assembled multivalent polyanion binding. This will be achieved by building a self-assembling supramolecular system consisting of an amine as the positively charged binding site and a hydrophobic part that has the force to drive the assembly**.** Importantly, we then aim to stabilize the self-assembled structure by stabilization of the hydrophobic part of the molecule; for example, by cross-linking. In addition, several modifications will be made to the hydrophobic tail and/or the hydrophilic binding site to test the effect of such modifications on binding affinities towards different polyanions such as heparin and DNA. In addition, multi-component systems will be used to test their effects on the binding affinities.

2 Effect of Alkene Modified Hydrophobic Units on SAMul Binding of Biological Polyanions

2.1 Introduction

The search for a heparin binder through the development of protamine replacement(s) is now a hot topic in the field of nanomedicine as illustrated in detail in the previous chapter (1. 3. 4). A self-assembling mimetic for the protamine structure was reported by Smith et al.[171] This was a spherical self-assembled protamine mimic formed from **C_{22}G1** (Fig. 1-33). The hydrophobic chain at the focal point provided the driving force for the assembly of this supermolecule. The positively charged amines were the cationic part that binds heparin.[171] Although the binding to heparin polymer chains was successful and has been proven by electron microscopy and a solution phase binding assay, unfortunately, these self-assemblies were relatively unstable in human blood serum.[171,173]

Furthermore, there was significant interest in gaining further fundamental understanding of the binding process which underpin this kind of nanoscale recognition event. In addition, we wanted to understand the features that governed the binding of different polyanions, such as DNA and heparin. Little attention has been given to attempts to explore selectivity in binding between such highly charged polyanion targets. Therefore, we decided to continue the work of finding a biocompatible nanostructured heparin binder with potentially greater serum stability by building a self-assembling supramolecule(s) consisting of amine, with two positive charges, as the positively charged binding site and a naturally occurring fatty acid as the hydrophobic focal point that will drive the assembly (Fig. 2-1)**.** We proposed that geometric differences in the nanostructures should impact directly on the heparin and DNA binding abilities of self-assembled multivalent systems (SAMul). In this part of our work, we therefore decided to modify the hydrophobic tail

of the micelles, in an attempt to impact on their assembly, structural characterization and binding ability.

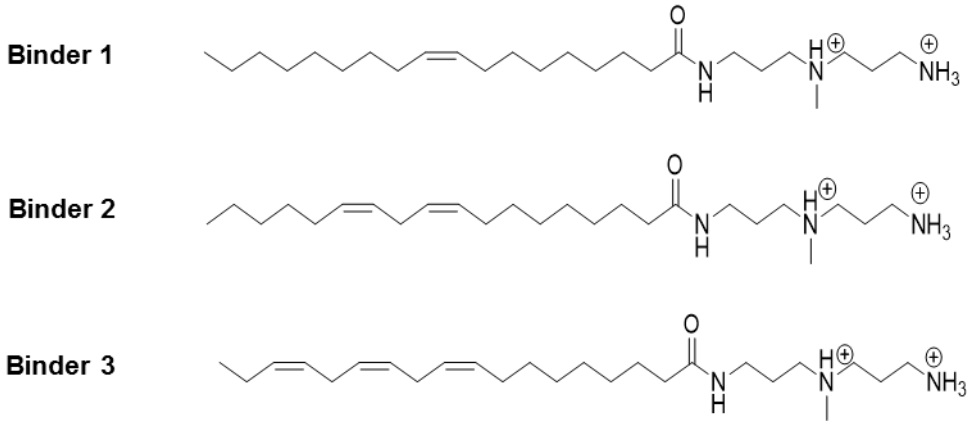

Fig. 2-1 Target compounds; consisting of amine, with two positive charges, as the positively charged binding site and a naturally occurring fatty acid as the hydrophobic focal point that will drive the assembly.

Importantly, we then hoped to stabilize the self-assembled structures by modification of the hydrophobic part of the molecule. It is known that micelles are unstable at lower concentrations than their critical micelle concentration (CMC), and in different solvents particularly competitive media such as human serum.[174] In an attempt to mimic natural ways of stabilizing self-assembled structures which is often achieved by covalent cross-links, we proposed to perform a polymerization reaction[175] to cross-link the alkene groups within the micelles. Such covalent cross-linking (C-L) should help to 'capture' and stabilize the self-assembled micelles in more competitive media. In recent years the researchers interest has been focused on cross-linking few polymer molecules within self-assembled structures.[176-178] Thurmond et al., had reported the stabilization of polymer micelles by cross-linking.[174,179] They demonstrated that incorporation of cross-linkable functional groups within the exterior of micelles allows polymerization to take place and gives stability to the micellar assembly.[179,180]

There are several locations for C-L within the micelle's domain; it could occur in the core chains or it could happen on the surface of the micelle, the shell. The location of C-L has a dramatic effect on the physical and chemical properties of the resultant products. In

addition, the extent of C-L could impact on the level of the stability and also the structure, hence modifying the binding abilities of such compounds.[174]

2.2 Alkene-Modified SAMul Nanostructures

The initial aim was to study the effect of alkene groups on self-assembly as well as binding affinities to heparin and DNA. We therefore started by building a self-assembled supramolecular system consisting of a positively charged binding site (amine) and hydrophobic focal point (naturally occurring unsaturated fatty acid). The unsaturated fatty acids were varied from mono-unsaturated to di- and tri-unsaturated fatty acid (Fig. 2-1).

2.3 Synthesis of Unsaturated-C_{18}-DAPMA

Three unsaturated-C_{18}-DAPMA compounds were synthesized with different alkene groups in the hydrophobic chain. Each of these were based on a naturally occurring unsaturated lipid. The synthesis of each of these compounds consisted of three key steps; the first step was the protection of *N*,*N*-di-(3-aminopropyl)-*N*-methylamine (DAPMA). The protection was a selective protection, as DAPMA contains relatively unreactive tertiary amine in addition to two primary amines. The mono-protection was achieved by using di-*tert*-butyl dicarbonate (Boc_2O) to produce mono-Boc-DAPMA or compound **1**[171] (Scheme 2-1). This was achieved by using an excess of DAPMA in the reaction; unreacted DAPMA could then be easily removed. This limited the formation of di-Boc-protected DAPMA, and the small amounts which did form could also easily be removed by washing. Although this step was straightforward, the yield was relatively low (39%).

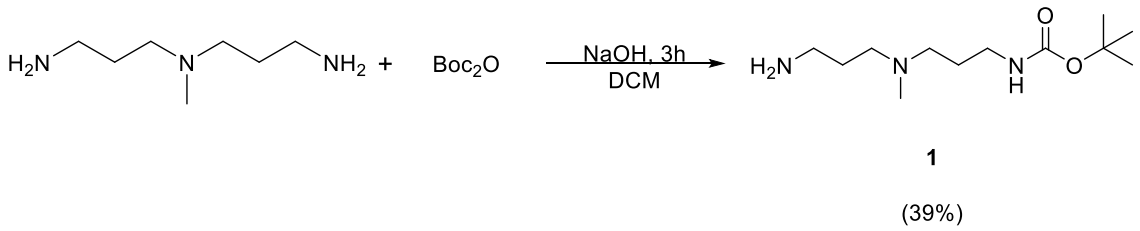

1

(39%)

Scheme 2-1 Protection of DAPMA by using Boc_2O (compound **1**).

Peptide coupling reaction was then performed between mono-Boc-protected DAPMA and the target hydrophobic units, each of which contained a different number of alkene groups. Firstly, to test the method, we synthesized potential binder (di-unsaturated C_{18}-DAPMA, **Binder 2**)**,** corresponding to two alkene groups within the hydrophobic tail**.** The protected *N*,*N*-di-(3-aminopropyl)-*N*-methylamine (Boc-DAPMA**, 1)** was reacted with naturally occurring linoleic acid (di-unsaturated fatty acid). The reaction was performed in the presence of *O*-(benzotriazol-1-yl)-*N*,*N*,*N*′,*N*′-tetramethyluronium tetrafluoroborate (TBTU) (Fig. 2-2) as coupling agent (Scheme 2-2).[181]

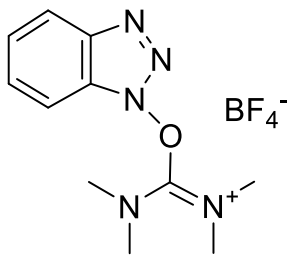

Fig. 2-2 *O*-(benzotriazol-1-yl)-*N*,*N*,*N*′,*N*′-tetramethyluronium tetrafluoroborate (TBTU).

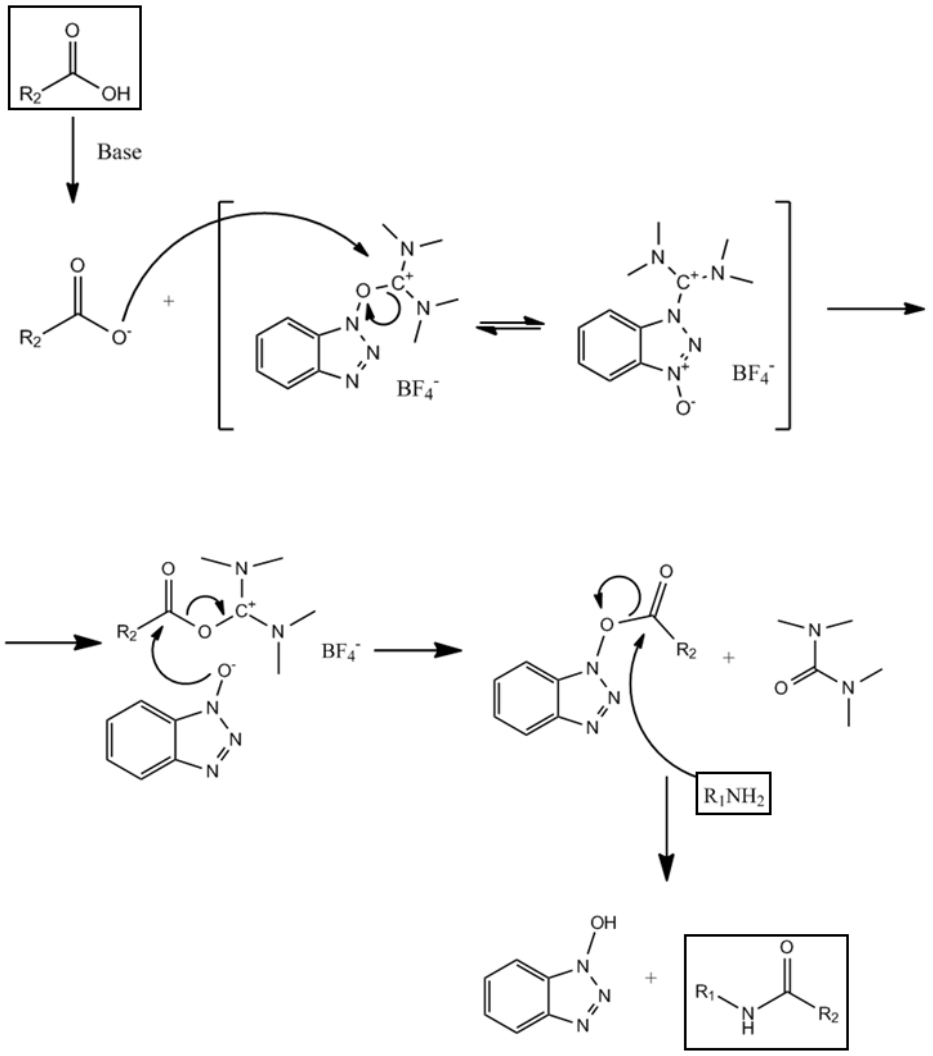

Scheme 2-2 TBTU coupling reaction mechanism.[181]

The product (di-unsaturated-C_{18}-Boc-DAPMA) was purified by using gel permeation chromatography (GPC) column (Bio-beads SX-1, 100% DCM) and gave 33% yield. The identity of the product was demonstrated using all key analytical techniques including mass spectrometry (MS); HRMS: Calc. $[M+H]^+$ ($C_{30}H_{58}N_3O_3$) m/z = 508.4473 Found $[M+H]^+$ = 508.4456. The third step was to remove the Boc group and hence produce **Binder 2**. To achieve that, the compound resulting from the previous step was dissolved in methanol and HCl gas was applied for 15-20 seconds then the mixture left to stir for 3 hours (Scheme 2-3). The solvent and excess HCl was then removed by evaporation to produce a product of 80% yield. The removal of the Boc group was demonstrated by the loss of the CH_3 protons at ca. 1.4 ppm in the ^1H NMR (Fig. 2-3). The shifts in other peak

positions are due to the different solvents that we have used; for the protected compound we used chloroform and due to solubility issues with the deprotected compound (**Binder 2**) we had to use methanol as the solvent.

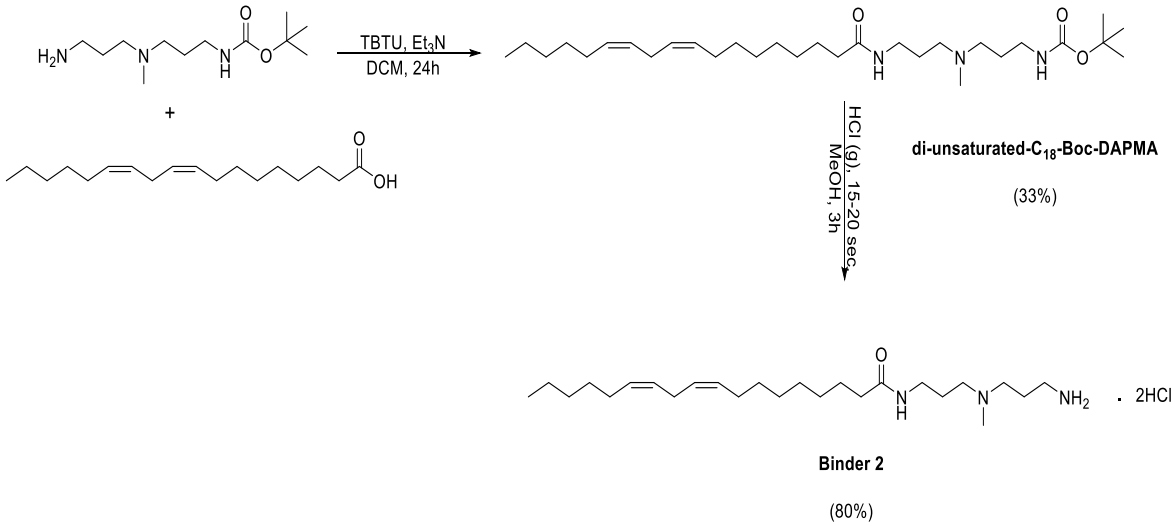

Scheme 2-3 Synthesis of di-unsaturated-C_{18}-Boc-DAPMA by coupling of compound **1** and the fatty acid (linoleic acid), then removing the Boc group to produce **Binder 2**.

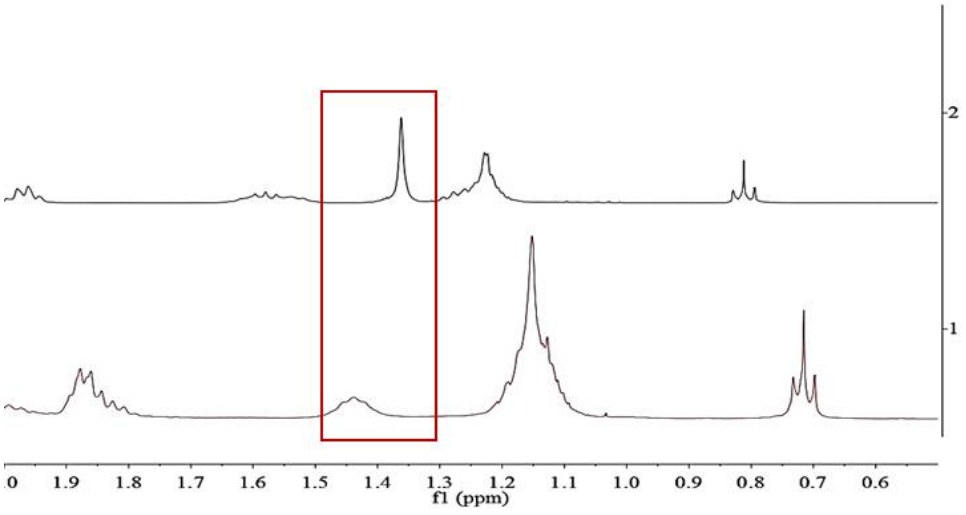

Fig. 2-3 NMR spectra for **Binder 2** before removing the Boc group (top) showing CH_3 protons around 1.35 ppm and (bottom) the spectra showing the loss of the peak after the deprotection reaction.

In addition, coupling reactions were performed between the other fatty acids and compound **1** to synthesize new potential heparin binders with different numbers of alkene groups. This was achieved using the same method described above for the synthesis of **Binder 2**. Oleic acid which has one alkene group (Fig. 2-4a) was used to synthesize mono-unsaturated-C_{18}-DAPMA or **Binder 1** with overall yield of 91% (Fig. 2-5a) and linolenic acid (Fig. 2-4b) which has three alkene groups was used to synthesize tri-unsaturated C_{18}-DAPMA or **Binder 3** (77%) (Fig. 2-5b). For simplicity, the binders were named according to the number of double bond(s) they have within the hydrophobic tail.

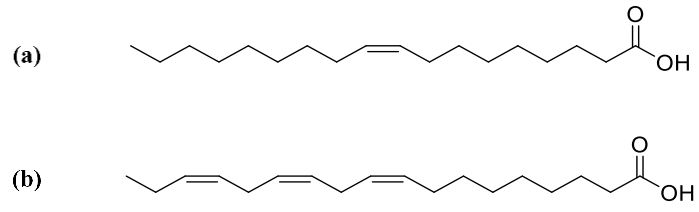

Fig. 2-4 (a) Oleic acid (one double bond) and **(b)** Linolenic acid (three double bonds).

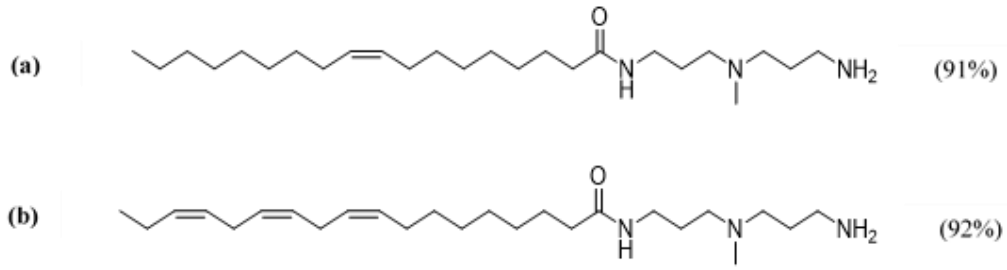

Fig. 2-5 (a) Binder 1 (one double bond) and **(b) Binder 3** (three double bonds).

All three binders, in the Boc protected form, were purified by size-exclusion method; gel permeation chromatography (GPC) column (Bio-beads, 100% DCM) then fully characterized by all analytical methods including mass spectrometry (MS) and NMR. Final binders were also fully characterized after the simple HCl-mediated deprotection step.

2.4 Self-Assembly Studies

2.4.1 Nile Red Assay

In order to determine the critical aggregation concentration (CAC) for the synthesized compounds, a Nile Red assay was performed. Nile Red dye **(**9-diethylamino-5-benzo[a]phenoxazinone)[182] (Fig. 2-6) is a hydrophobic compound that has a high fluorescence emission which is quenched when in the presence of water.[182,183] Nile Red has demonstrated its efficiency to measure the aggregation[183,184] of compounds that contain both hydrophilic and hydrophobic parts (i.e., amphiphiles). It begins to fluoresce (Fig. 2-7) when it is encapsulated within the hydrophobic interior of a self-assembled structure, as a result of its increased solubility and a decrease in quenching.[182,183] In this assay, Nile Red fluorescence excitation was achieved at 550 nm and its emission intensity was measured at 635 nm.[171] The ability of Nile Red to fluoresce is determined as a function of the concentration of the amphiphile. Once the critical aggregation concentration (CAC) is reached, Nile Red fluorescence gets switched on. Monitoring the emission intensity as a function of concentration therefore allows critical concentration to be determined.

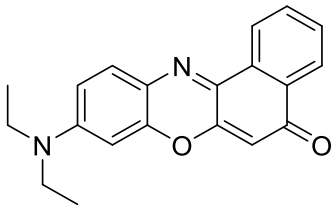

Fig. 2-6 9-Diethylamino-5-benzo[a]phenoxazinone (Nile Red).

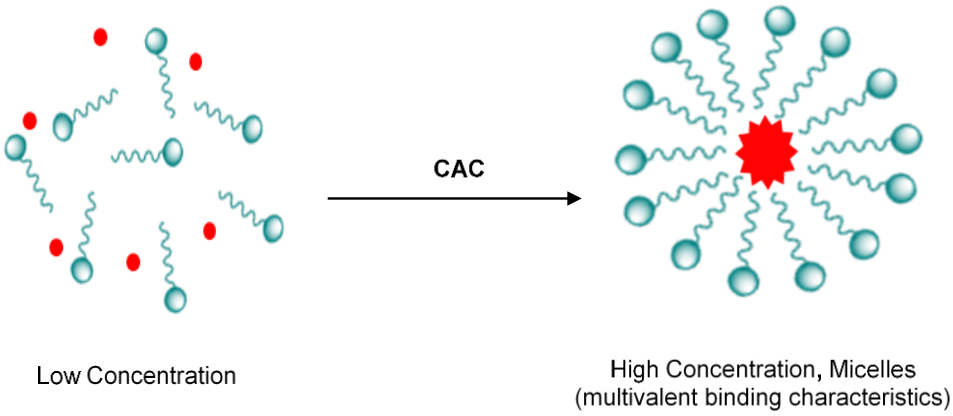

Fig. 2-7 Nile Red confined in the micelle's core at and above CAC provides evidence of self-assembly and allows quantification of the CAC.

The compounds stock solutions were prepared at a variety of concentrations starting from (200 µM) and less in disposable cuvettes. Samples of the stock solution were diluted by phosphate-buffered saline (PBS) to the required concentration in a 1 mL assay volume. Nile red (1 µL) was applied to each sample to give concentration of (2.5 µM).

The CAC for **Binder 2** was found to be around 82 (± 1.7) µM ($\log_{10}$ Concentration = 1.96) (Table. 2-1). This was calculated from Figure 2-8. This value indicates that this compound will only self-assemble at concentrations above 82 µM. This is a relatively high value compared to the previously reported heparin binder; **C_{22}-G1** (Fig. 1-33). which had a CAC of 4 µM. However, **Binder 2** is only a very simple self-assembling unit with two positive charges and the goal of the study here was not to form the best self-assembly but rather to determine the effect of changing the number of alkene groups on self-assembly and consequently on polyanion binding. Therefore, the CACs of the other two compounds (**Binders 1** and **Binder 3**) were also measured.

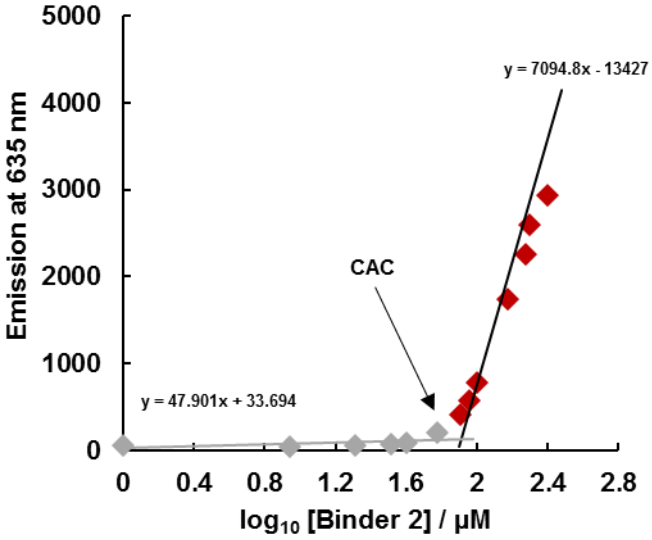

Fig. 2-8 Critical aggregation concentration (CAC) for **Binder 2** determined by Nile Red assay.

CACs for **Binder 1** and **Binder 3** were 42 (± 3.1) μM and 78 (± 9.8) μM respectively (Table 2-1), (Fig. 2-9 and 2-10). Clearly if only one alkene is present, the CAC is lower, whereas if 2 or 3 alkenes are present in the hydrophobic chain the CAC is elevated. This would suggest that the presence of alkene groups hinders self-assembly by distorting the extended conformation of the alkene chain. Fewer double bonds give more freedom for the compound (**Binder 1**) to self-assemble as the compound practically still has a linear shape. Double bonds enforce a geometric preference onto the hydrophobic group – in particular the cis alkenes found in these three examples. More than one double bond in a compound begins to enforce strongly nonlinear geometric onto the tail and can even cause a bend in the compound's structure to produce a semi-ring shaped tail[185] (Fig. 2-11). Similar disruption effects of alkenes on lipid self-assembly have been reported elsewhere and are known for example to introduce fluidity into cell membranes.[186,187] A double bond results in a bend of approximately 30 degrees in a chain of carbons,[188] therefore, it causes a space within the molecule. This space gives unsaturated fatty acids (lipids), on the molecular level, more fluidity than saturated lipids as they are unable to pack together as effectively.[189]

Binder	**1**	**2**	**3**
CAC (μM)	42 ± 3.1	82 ± 1.7	78 ± 9.8

Table 2-1 Critical aggregation concentration (CAC) for binders (**1** – **3**), in PBS buffer (pH = 7.4).

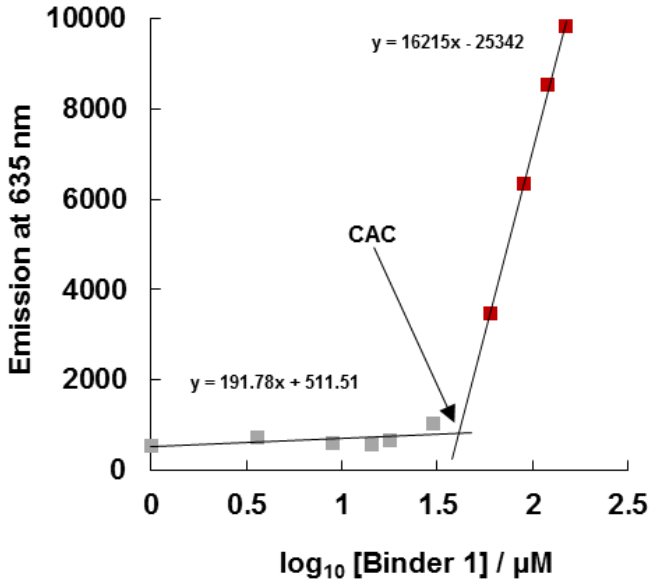

Fig. 2-9 Critical aggregation concentration (CAC) for **Binder 1** determined by Nile Red assay.

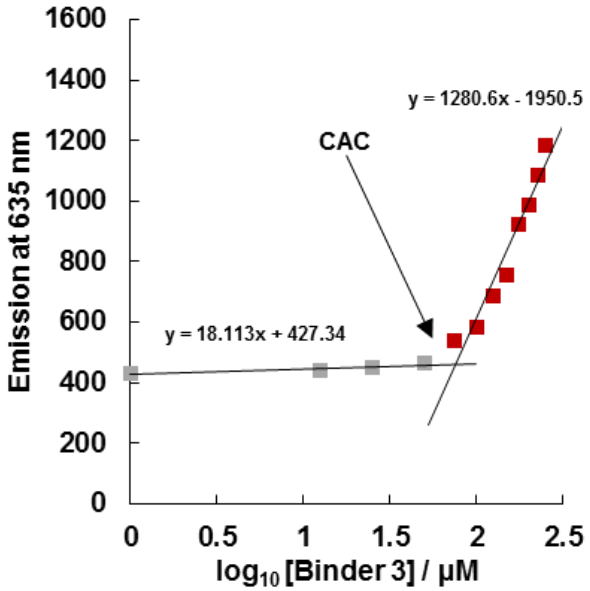

Fig. 2-10 Critical aggregation concentration (CAC) for **Binder 3** determined by Nile Red assay.

It is also worth noting that above the CAC, the emission intensity of Nile Red is greatest with **Binder 1** than for **Binder 2** and **Binder 3**. This would suggest the less-ordered hydrophobic domains formed by these more bent systems are less-able to protect the Nile Red from quenching by the surrounding water – indicative of 'looser' and more open self-assembled nanostructures.

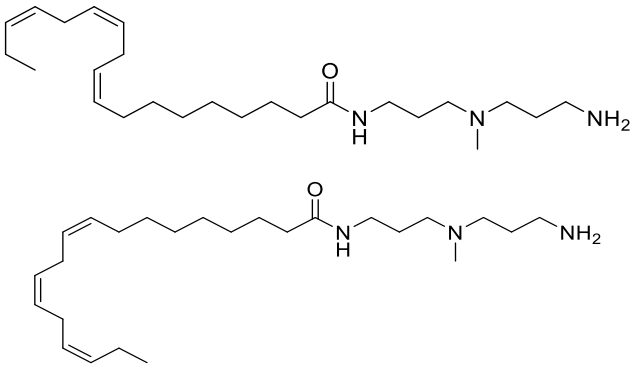

Fig. 2-11 Binder 3 possible semi-ring shapes of the hydrophobic unsaturated tail.

We were also interested in using mixtures of different compounds in the hope of combining (e. g.) the lower CAC of **Binder 1** with the greater alkene density of **Binder 3**. As such, a mixture of **Binder 1** and **Binder 3** (1:1) was prepared. The CAC for this mixture was measured and it was 88 (± 5) μM (Fig. 2-12). This CAC was closer to the CAC value of **Binder 3** than that of **Binder 1** and this demonstrated that the disruption effect of the other alkene groups on self-assembly dominates in the mixed system.

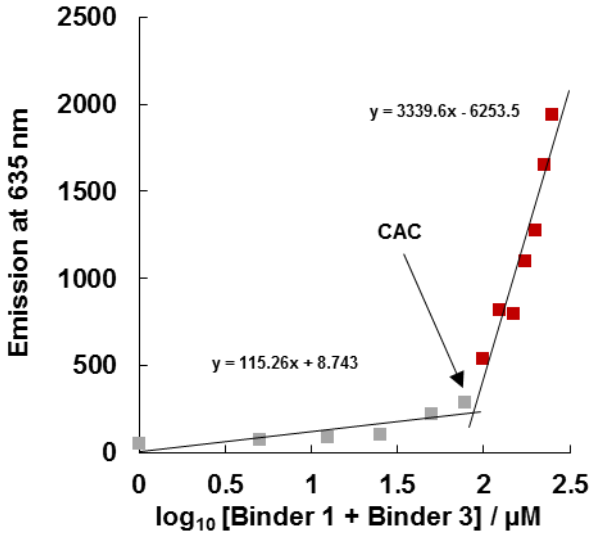

Fig. 2-12 Critical aggregation concentration (CAC) for **Binders 1** and **Binder 3** mixture (1:1).

2.4.2 Dynamic Light Scattering (DLS)

The synthesized binders were then characterized in terms of aggregate size in solution by dynamic light scattering (DLS). This provides a quantitative insight into the self-assembled nanostructures present in solution which is of key importance for understanding their preferences in (e. g.) heparin binding assays. The DLS technique uses a laser light beam and when the light shines onto a solution with spherical particles (in Brownian motion) the light hits the moving particle causing a change (scatter) in the wavelength of that incoming light.[190] This scattered light is related to the size of the particles and the sphere size distribution.[191] Particle size was calculated by the instrument's software in accordance with the Stokes-Einstein formula[192] (Eq. 2-1), which relates particle size to the diffusion coefficient and viscosity. Where N_A is the Avogadro number, T is the temperature and η is the viscosity of the solution, r_u is the solute radius assuming the solute has a spherical geometry (a reasonable assumption for these systems).

$$D = \frac{RT}{N_A} \quad \frac{1}{6\pi\eta r_u}$$

Eq. 2-1 Stokes-Einstein formula.

The self-assembly of the binders was measured under similar conditions to the heparin binding assay reported later (i.e., in buffer; 150 mM NaCl / 10 mM Tris HCl). In addition, the samples were prepared at concentrations above the CAC to guarantee the measurement of the self-assembled micelles. Diameters can either be calculated using a volume distribution (which reflects the amount of self-assembled volume) or an intensity distribution (which reflects the intensity of the scattered light).

Converting from intensity distribution to volume distribution lowers the contribution of larger aggregates which scatter light more significantly even at lower concentrations and emphasizes the contribution of the species which are present as the majority is solution.

As such, larger aggregates are often not observed in the volume distribution and all peaks are shifted to smaller diameters as the larger components have their larger contributions re-weighted (this is similar to the difference between M_w and M_n in polymers molecular mass distributions).[193] We therefore use volume distribution to characterize and report the size of the dominant species in solution. However, it is important not to ignore the contribution/presence of larger aggregates as minor component in solution and for this reason we also present intensity distribution data.

The results (Table 2-2) showed that the binders are dispersed in a moderate level; the poly-dispersity index (PDI) values were higher than 0.1-0.2, for a perfectly uniform sample the PDI would be 0.0.[194] This is a consequence of the intensity distribution data which indicates the presence of a larger aggregate (>100) (Fig. 2-13). It is noteworthy that going from **Binder 1** to **2** to **3**, the intensity distribution indicates that the relative amount of light scattered from larger aggregates increases. This would suggest that the controlled assembly into smaller micelles is most favoured by 1 > 2 > 3. This would be in agreement with the CAC values described earlier and may suggest that **Binder 2** and **Binder 3** have a greater propensity to assemble into less well-defined, larger aggregates in addition to well-defined smaller micelles. This would support the view that the more alkene groups are present, the more the self-assembly of these systems is disrupted owing to the distorted structures of the hydrophobic chains limiting effective packing.

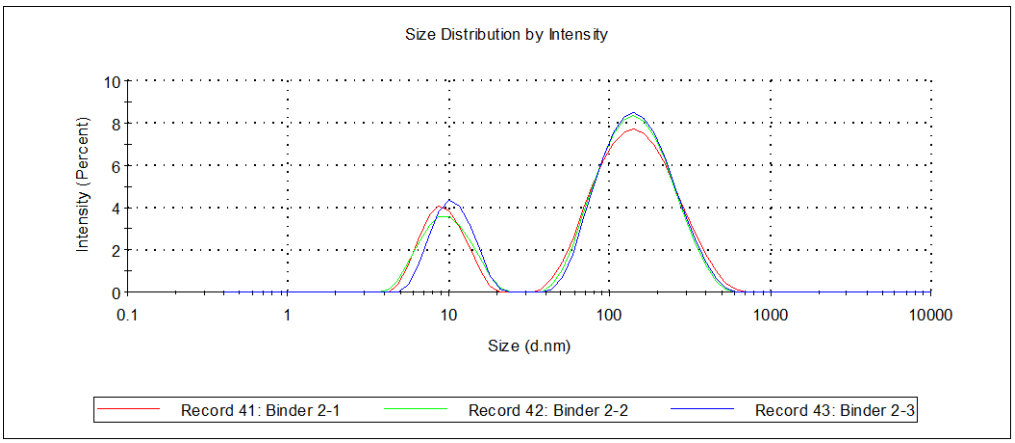

Fig. 2-13 Size distribution by intensity from DLS analysis of **Binder 2** in buffer (150 mM NaCl / 10 mM Tris HCl) showing the contribution of larger aggregates which scatter light more significantly even at low concentrations.

Sample in NaCl (150 mM) / Tris HCl (10 mM)	Diameter (Intensity distribution) / nm	Diameter (Volume distribution) / nm	PDI
Binder 1	Pk1: 10.5 (38%) Pk2: 167.4 (62%)	5.2 ± 0.51	0.344 ± 0.004
Binder 2	Pk1: 9.6 (27%) Pk2: 156.3 (73%)	6.4 ± 0.41	0.365 ± 0.002
Binder 3	Pk1: 10.6 (45%) Pk2: 203.1 (55%)	7.6 ± 0.27	0.697 ± 0.012

Table 2-2 Size Analysis by DLS for the three synthesized binders in NaCl (150 mM) / Tris HCl (10 mM).

When considering the volume distribution to focus on the major species presence (Fig. 2-14), the average diameter for **Binder 1** micelles was around 5.2 (± 0.5) nm. Comparing with the other two compounds (**Binder 2** and **Binder 3**), **Binder 1**'s micelles are smaller. The average diameter for **Binder 2** micelles was around 6.4 ± (0.41) nm and for **Binder 3** was 7.6 (± 0.27) nm (Table 2-2). We suggest that these size differences reflect the number of the double bonds in the hydrophobic tail. **Binder 1**, which has one double bond, has a linear hydrophobic tail that packs effectively and allows relatively small micelles to assemble. Conversely**, Binder 2** and **Binder 3**, which have two and three

double bonds, respectively, form larger micelles. We suggest that more double bonds adversely affect the shape of the molecules and the self-assembly gives larger and looser micelles. This supports the Nile Red assay (2. 4. 1), when the CAC values for **Binders 2** and **Binders 3** were higher than **Binder 1**, and the observed emission intensities were lower.

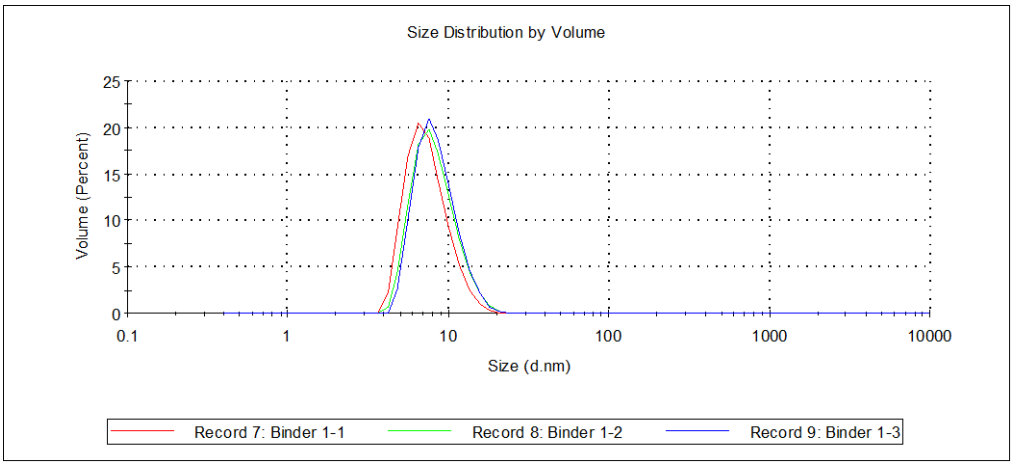

Fig. 2-14 Size distribution by volume from DLS analysis of **Binder 1** in buffer (150 mM NaCl / 10 mM Tris HCl) showing that larger aggregates not observed and all peaks are shifted to smaller diameters as the larger components have their larger contributions re-weighted.

In addition, DLS data showed that the self-assembled nanostructures were highly positively charged. Zeta potentials for **Binders 1-3**, which reflect surface charge density, were between 64 and 73 mV (Table 2-3). These high positive charges assure that the potential binders are suitable to bind heparin as it is known that binding to heparin, which is a highly negatively charged anion, will occur through electrostatic interactions.[195,196]

Sample in Buffer	Zeta potential (mV)
Binder 1	64.1 ± 0.6
Binder 2	72.9 ± 3.7
Binder 3	72.9 ± 2.5

Table 2-3 Zeta potential for binders **1-3** in buffer; NaCl (150 mM) / Tris HCl (10 mM), showing that they are highly positively charged.

2.4.3 TEM Images

Transmission electron microscopy (TEM) images were recorded for the three binders. The images were recorded both in the absence and the presence of heparin in order to characterize both the self-assembled nanostructures and the impact of heparin on them. The binder solutions were prepared in ultra-pure water at concentrations (200 μM), above the CAC values calculated from the Nile Red assay, in an effort to ensure that there would be self-assembled prior to sample preparation. The samples were then placed on a formvar grid, stained with uranyl acetate then left to dry for about 20 minutes prior to imaging. Electron microscopy is particularly subject to artifacts, and can be unable to differentiate between 'real' agglomerates and those formed upon deposition and drying.[197] However, the images showed approximate size and shape of the micelles, in particular in the presence of heparin (see below). This allows us to estimate a rough size of the micelles as well as visualizing them when bound to their polyanion targets.

In the absence of heparin, **Binder 1** showed some aggregates (Fig. 2-15a) but these were not particularly well-defined. This might suggest that the micelles, characterized by DLS, are not particularly stable when dried down on a TEM grid and imaged under the electron beam. Conversely, in the presence of heparin, micellar objects are clearly seen. We suggest that heparin binding plays a role in stabilizing the aggregates under imaging conditions. Furthermore, the micelles are organized into an effective (lattice-like) arrangements. A similar effect was previously reported by Smith and co-workers[171] for the binding of **C_{22}-G1** to heparin (Fig. 2-16), showing their self-assembled binder in the presence of heparin. We suggest that interactions between the polyanionic rods of heparin and the polycationic sphere of the binder leads to this degree of hierarchical assembled nanostructure within the overall aggregate. This organizational effect may play a role in enabling the better imaging of the micelles as they are more effectively immobilized on the grid. Comparing Binder 1's image (Fig. 2-15b) to the reported TEM images by Smith

et. al, Binder 1 was found to have similarity of forming organized nanostructured aggregates on the surface of heparin. Figure 20b shows the spherical micelles of Binder 1 deposited in organized linear arrays on the surface of heparin. The individual spherical structures of Binder 1 appeared to be less than 10 nm in diameter.

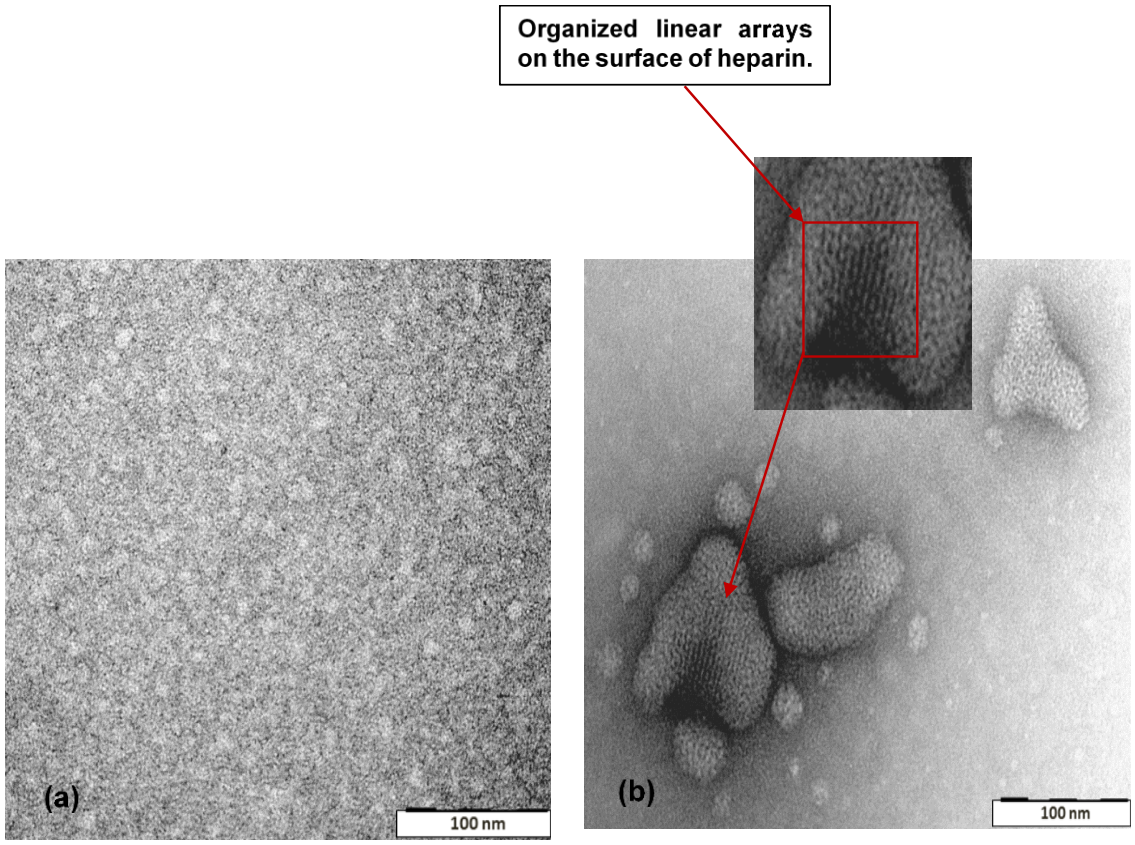

Fig. 2-15 TEM images of **Binder 1**, dried from aqueous solution (200 µM), in the absence of heparin (a); a spherical self-assembled nanostructure and in the presence of heparin (b), showing the organized linear nanostructured arrays, scale bar = 100 nm.

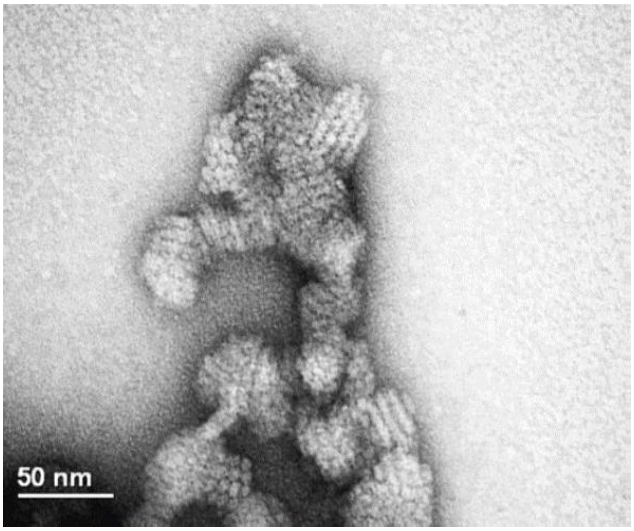

Fig. 2-16 TEM image of self-assembled spherical **C_{22}-G1** nanostructures in the presence of heparin, leading to linear organization of the nanostructures.[171]

A previous binder Mallard Blue (MalB), that has been synthesized by Smith group for heparin sensing showed that MalB does not form these notable aggregations by itself. In addition, when imaging heparin by itself (Fig. 2-17a), we found that it does not aggregate. Furthermore, on mixing MalB and heparin (Fig. 17b), MalB does not self-assemble and does not show hierarchical structure or patterning. As such, we are confident in assigning the hierarchical nanostructures to **Binder 1**:heparin assemblies.

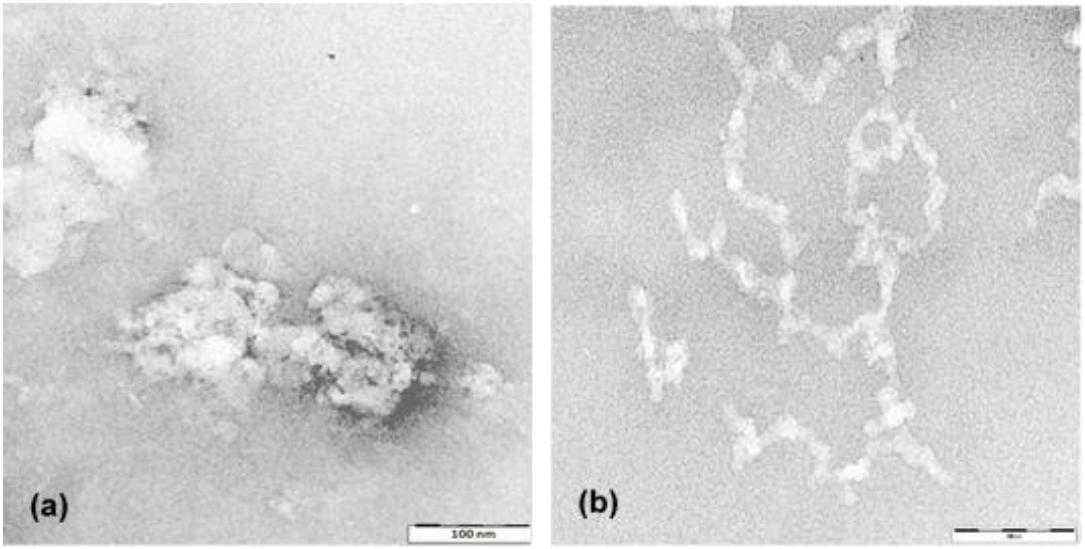

Fig. 2-17 TEM images dried from aqueous solution of: **(a)** MalB (25 μM) in the presence of heparin showing the less defined organized nanostructured on the surface of heparin and **(b)** heparin by itself in similar assay conditions (27 μM), scale bar = 100 nm.

In addition, TEM images of **Binder 2** and **Binder 3** showed similar characteristics (Fig. 2-18 and 2-19). Some self-assembly was observed in the absence of heparin but on binding of the nanostructures to heparin, these micelles could be much more clearly observed and furthermore the micelle-heparin aggregates had a degree of internal nanostructuring with effective close packing of cationic nanospheres presumably being meditated by interactions with the polyanionic heparin chain.

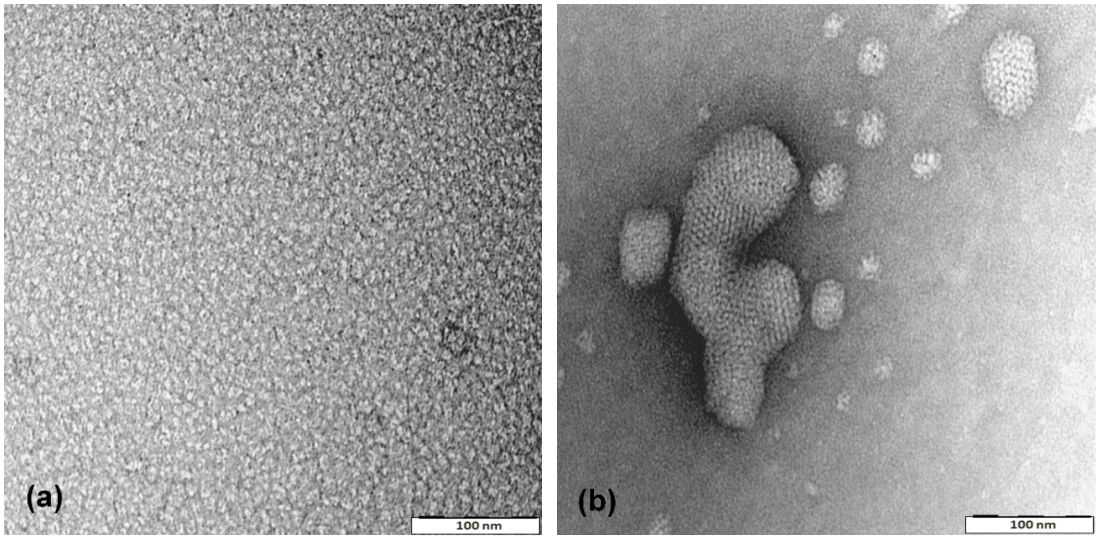

Fig. 2-18 TEM image of **Binder 2** dried from aqueous solution (200 µM), showing spherical self-assembled nanostructures; **(a)** before binding to heparin, **(b)** in the presence of heparin, scale bar = 100 nm.

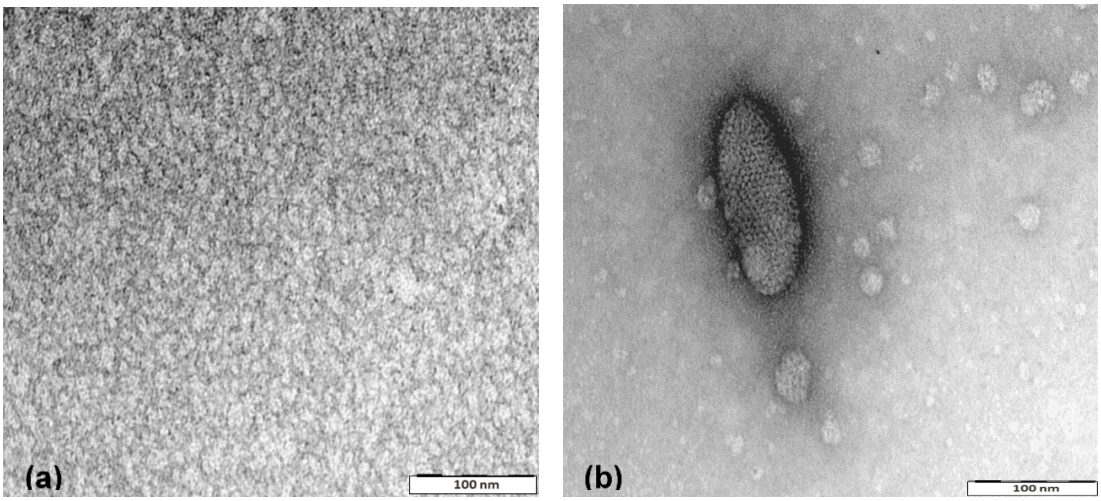

Fig. 2-19 TEM image of **Binder 3** dried from aqueous solution (200 µM), showing spherical self-assembled nanostructures; **(a)** before binding to heparin, **(b)** in the presence of heparin, scale bar = 100 nm.

Nevertheless, all binders' aggregates in TEM images showed that the micelles were aligned in an organized style. This nanoscale organization was induced by heparin, as it is considered to be a relatively rigid polymer, which led the micelles to be organized along its backbone. This way of binding, known as "beads on a string" has been observed when spherical cationic systems bind to DNA.[198]

2.5 Binding Data

2.5.1 Heparin Binding

2.5.1.1 Mallard Blue

The detection of heparin binding in serum has recently been achieved by the Smith group[199] through the development of a novel cationic dye "Mallard Blue" (MalB); an arginine-functionalized thionine (Fig. 2-20), which has a high affinity for heparin and works as a sensor for the anionic polysaccharide.

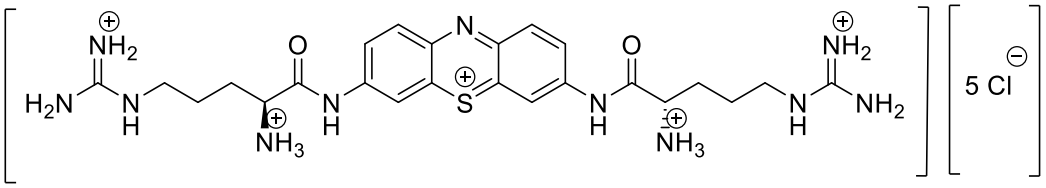

Fig. 2-20 Mallard Blue (MalB); a dye with five positive charges designed to bind to polyanionic heparin.[14]

Monitoring heparin binding with this dye was performed by UV-Vis spectroscopy.[199] The dye showed a high efficiency as the binding was detectable at low concentrations of heparin in serum; as low as 1 IU/mL in 100% human serum.[123,199] Mallard Blue showed much better detection levels for heparin compared with other heparin sensing dyes such as Azure A.[200] Currently, in the research group, a MalB competition assay, as discussed below, is used to screen new potential therapeutic candidates for non-toxic protamine

replacements to bind with heparin in order to remove it from patients' blood after surgeries.[123]

Heparin binding affinities for the synthesized compounds were tested in competitive conditions such as buffer (pH 7.4), salt and human serum. The maximum UV-Vis absorbance at 615 nm for MalB was recorded. When initially dissolved in buffer at room temperature (20 -22 ºC) the color develops when the solution is incubated at 50 °C for 24 hours (Fig. 2-21). This incubation process is essential to prevent the aggregation or to un-stack the tri-cyclic aromatic cores of this dye. In addition, the binding of this dye to heparin has proven to be more efficient after the incubation process. The incubation is done prior to any binding assay, the flasks were wrapped with foil to ensure that the dye was not exposed to direct light as it has been reported to be light-sensitive.[123]

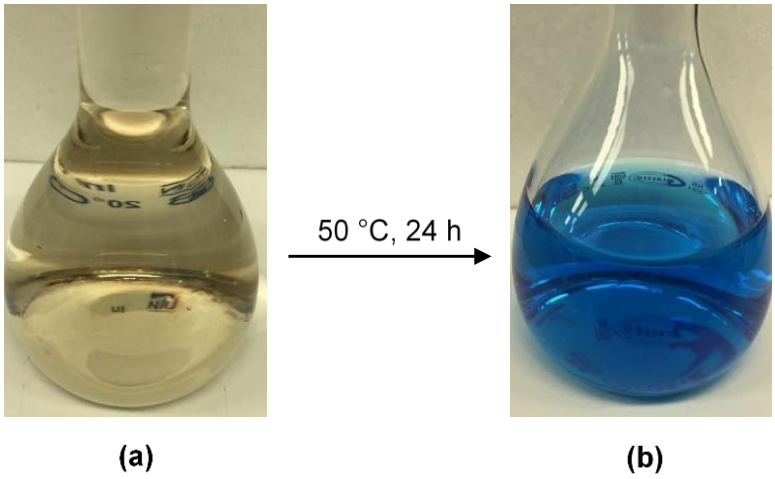

Fig. 2-21 MalB (25μM) before incubation **(a)** and after the incubation for 24 h at 50 °C **(b)**.

On binding to heparin, the MalB absorbance peak at 615 nm dropped in intensity (Fig. 2-22), also, the solution color changed to a darker shade of blue. On the addition of any compound's (binder's) stock solution, the binder then replaced MalB gradually (Fig. 2-23) in the competition assay and as a result the intensity increases. This demonstrates that these compounds (binders) can effectively bind heparin under these assay conditions.

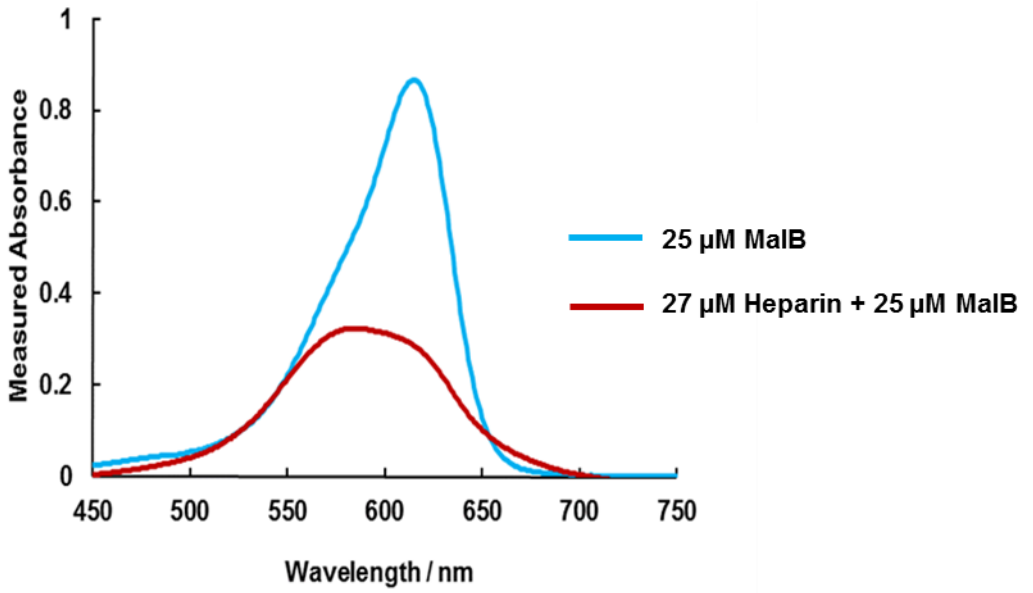

Fig. 2-22 UV-Vis spectra showing mallard blue (MalB) maximum absorbance at 615 nm binding to heparin (blue line) and after binding to heparin (red line).

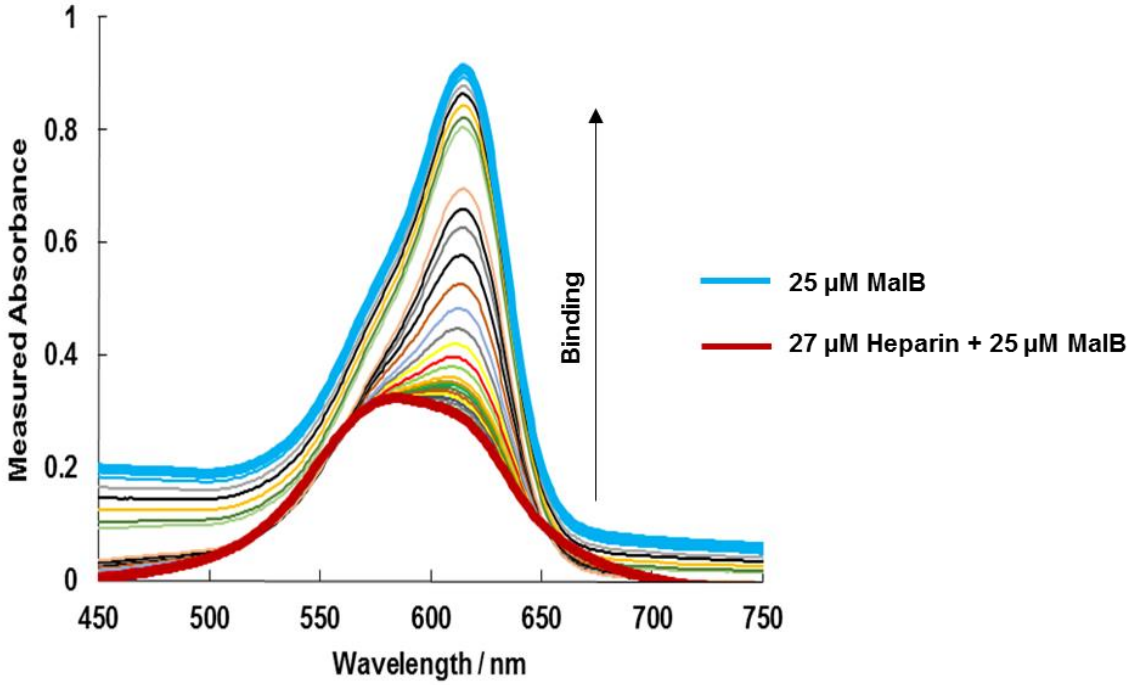

Fig. 2-23 UV-Vis spectra showing a binder replacing mallard blue (MalB) in the titration competition experiment.

a. MalB Assay in Buffer

The MalB competition assay, in buffer, was performed for each binder individually. The assay was carried out under optimized conditions of 25 µM MalB, 27 µM heparin, 150 mM NaCl and 10 mM Tris HCl. Each titration was carried out in triplicate and the results, are presented below (Fig. 2-24, Table 2-4). For each compound, the charge ratio in the cuvette was calculated after every addition and was plotted against the normalized absorbance value at 615 nm for each reading. The charge ratio at the point when normalized absorbance = 0.5 was estimated by plotting a linear graph of the data around this value. The effective concentration at 50% binding (EC_{50}) and the charge excess at 50% binding (CE_{50}) were calculated from the plotted graph as well as the required dose in mg/100 IU of heparin (Table 2-4).

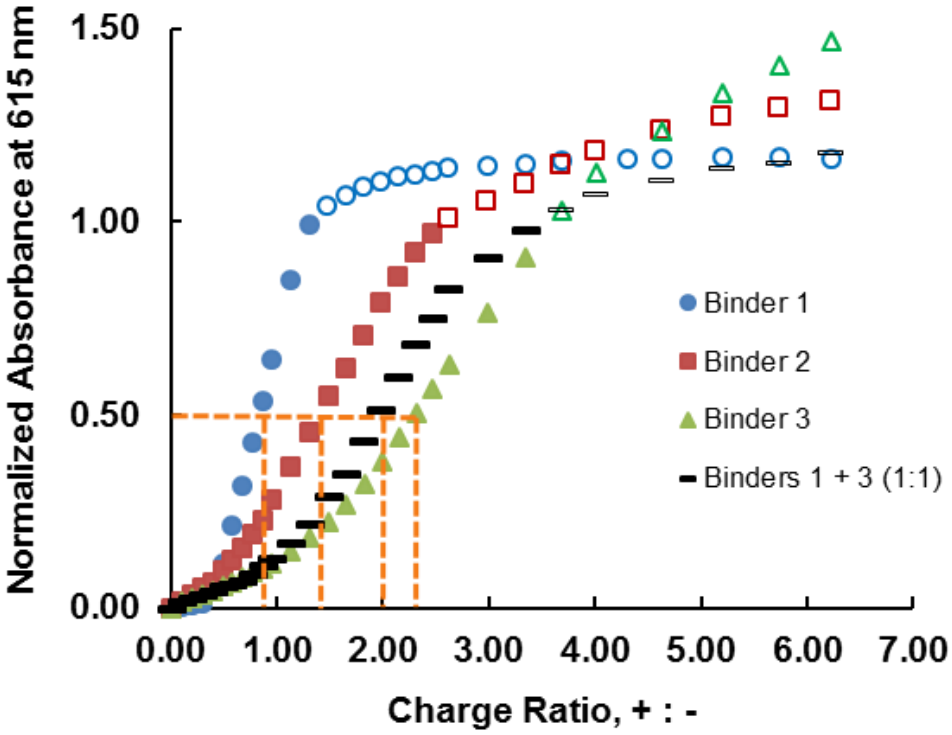

Fig. 2-24 Charge ratio against normalized absorbance at 615 nm of **Binders 1 - 3** and a mixture of **Binder 1** and **Binder 3** (1:1), in buffer, showing the effect of alkene variation on binding to heparin, 'open' markers represent points in the titration affected by aggregation and light scattering.

The charge excess is a useful tool to consider the binding ability normalized per charge of the binder, a lower charge excess means more binding. Therefore, CE_{50} values are used to indicate the efficiency of a binder to bind heparin. Also, these values are used in comparison terms between different binders especially where theses binders have different number of charges, such as the drug; protamine. Protamine's CE_{50} has been reported to be 0.52 using this assay.[123,126,128]

Table 4 also shows the effect of alkene groups on heparin binding ability. Clearly the system with most alkenes (**Binder 3**) is least able to bind to heparin with a CE_{50} of 2.3 (± 0.18). whereas that with the fewest (**Binder 1**) is the most effective heparin binder with a much lower CE_{50} of 0.8 (± 0.05). **Binder 2** is intermediate in value with CE_{50} of 1.8 (± 0.1). This would suggest that the alkenes, which hinder the self-assembly of these nanostructures as discussed above, also limit their ability to bind to polyanionic heparin. These differences are significant and are well beyond errors associated with this assay.

We also monitored the ability of co-assembled **Binder 1** and **Binder 3** to bind heparin and found that the CE_{50} value of 2.0 (± 0.3) was more similar to the performance of **Binder 3** than the performance of **Binder 1**. This agrees with our previous hypothesis that the presence of **Binder 3**, and the multiple alkene groups within it, significantly disrupt the self-assembly process, and hence the ability of the SAMul nanostructures to bind to heparin.

Compound	**Binder 1**	**Binder 2**	**Binder 3**	**Binder 1 + Binder 3 (1:1)**
CE_{50}	0.8 ± 0.05	1.8 ± 0.1	2.3 ± 0.18	2.0 ± 0.3
EC_{50} (μM)	45 ± 3.0	76 ± 7.0	125 ± 9.9	107 ± 16.2
Dose (mg) / 100 IU	0.6 ± 0.04	1.1 ± 0.01	1.7 ± 0.13	1.5 ± 0.22

Table 2-4 Calculated CE_{50}, EC_{50}, required dose (in buffer) and the CAC of the synthesized binders showing the effect of the alkene group(s) on self-assembly and binding abilities comparing to compounds with saturated hydrophobic tails.

It should be noted that in some cases the final normalized absorbance is > 1.0, Figure 2.25 demonstrates this effect. As can be seen, on titration, the absorbance at 615 nm becomes higher than that of Mallard Blue alone. However, looking at intensity at 500 nm also shows that in the later part of the titration intensity begins to increase at this wavelength. For this reason, we assign the increase of intensity > 1.0 as due to light scattering associated with aggregates between heparin and the SAMul binder which impacts across the whole spectrum. We Note that in early stages of the titration, light scattering effects are not seen significantly at 500 nm and we therefore reason that the determination of the CE_{50}, which lies in the early part of the titration is sound. As a result, we did not attempt to correct data for this aggregation effect. We also note that for **Binders 1-3**, the largest absorbance are observed for **Binder 3 > Binder 2** > **Binder 1**. This is in agreement with DLS studies on the binders above which suggested that aggregation was less controlled for **Binder 3** because of the alkene units inserted in the structure. As such, the observation of uncontrolled aggregation in the MalB titration would seem to match the preference of the binder.

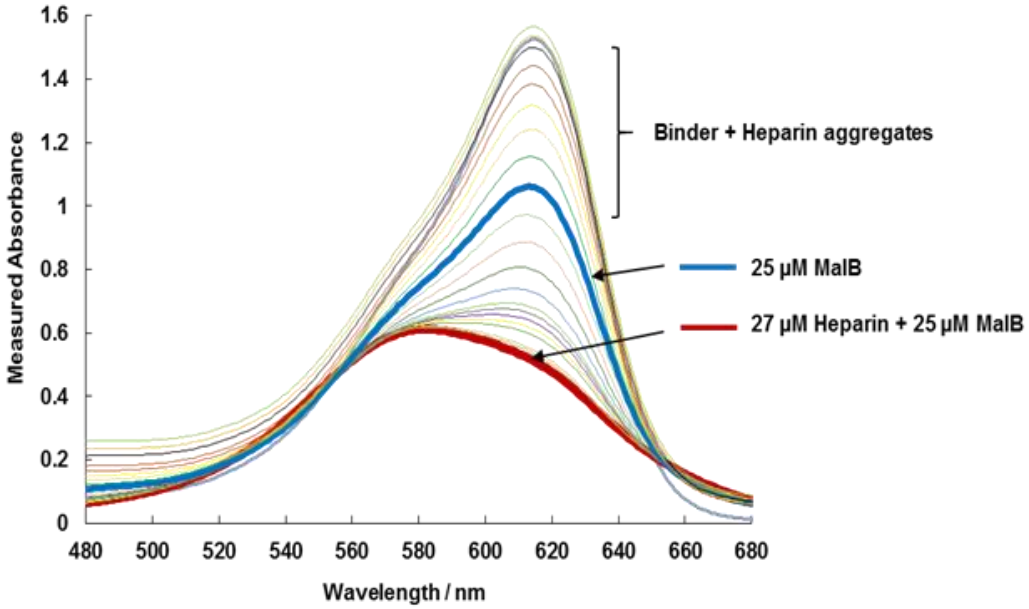

Fig. 2-25 UV spectra for the MalB assay of **Binder 3** showing the aggregation effect that increase absorbance at higher charge ratios towards the end of the titration.

b. MalB Assay in Human Serum

Human serum has an extraordinary binding ability for a wide range of ligands; endogenous and exogenous. This binding ability makes it significant to determine the pharmacokinetic behavior of many drugs.[201-203] Human serum does not contain white or red blood cells nor a clotting factor; it is basically plasma without fibrinogens.[201,204,205] However, human serum albumin (HSA), a spherical protein that consists of 585 amino acids, constitutes 60% of the total protein in blood serum.[202,205] It is known that HSA can interact with a wide range of different molecular species – in particular those with significant hydrophobic surfaces.[206] Therefore, testing the synthesized compounds, in such conditions, was the next step in this work.

After testing the synthesized binders' abilities to bind heparin in 150 mM NaCl and 10 mM Tris HCl, we decided to investigate the stability of these systems in more challenging conditions. Biologically relevant media, such as human serum is recognized as suitable and challenging biological conditions. This type of testing will allow more insight to the binding behavior of these compounds and allow them to be considered as potential candidates for future trials in even more challenging conditions, such as blood plasma.

The ability of the synthesized compounds (**Binders 1**-**3**) to bind heparin in human serum was therefore tested. Binding data were recorded by measuring MalB absorbance by UV-Vis spectroscopy at 615 nm as described in the buffer procedure above. Binders (**1-3**) showed binding to heparin and the charge ratio at the point when normalized absorbance = 0.5 was estimated by plotting a graph of the data around this value. EC_{50} and CE_{50} values as well as the required dose were calculated from the plotted graphs in a similar method to that described above. While the binders showed stable binding to heparin in human serum, the binding abilities were relatively rather weaker than those in buffer; less competitive conditions. The **Binder 1** CE_{50} value in human serum (Fig. 2-26) was high

(2.5 ± 0.2) (Table 2-5), compared to the value in buffer (0.8 ± 0.05) suggesting significant disruption of the binding.

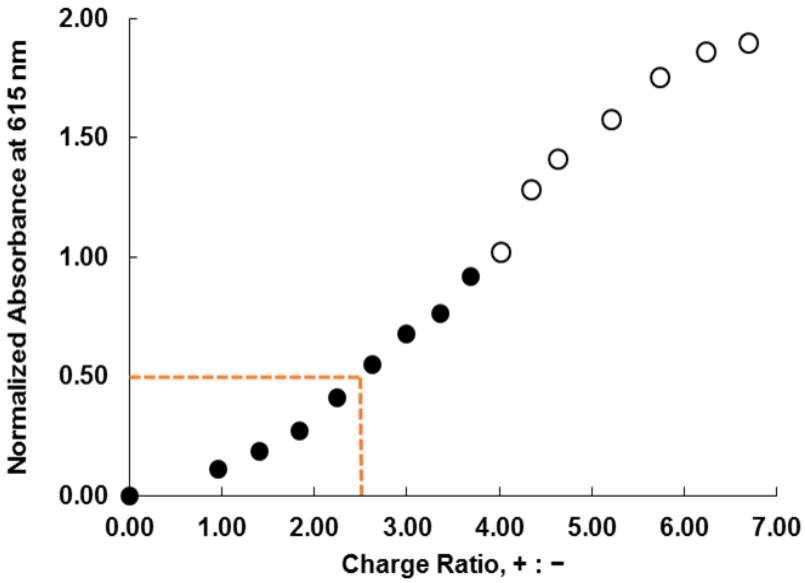

Fig. 2-26 Charge ratio against normalized absorbance at 615 nm of **Binder 1** in human serum, showing high values of CE_{50} which indicates less binding to heparin, 'open' markers represent points in the titration affected by aggregation and light scattering.

Binder 1 in Human Serum	
CE_{50}	2.5 ± 0.2
EC_{50} (µM)	133.5 ± 10.0
Dose (mg) / 100 IU	1.86 ± 0.13

Table 2-5 Calculated CE_{50}, EC_{50} and required dose (in human serum) of **Binder 1**, showing the weaker binding abilities than in buffer.

Binder 2 (Fig. 2-27 and Table. 2-6) showed some binding to heparin in human serum, but again this binding ability was weaker than its ability to perform in buffer, with a CE_{50} value in serum (3.4 ± 0.1) higher than that in buffer (1.8 ± 0.1).

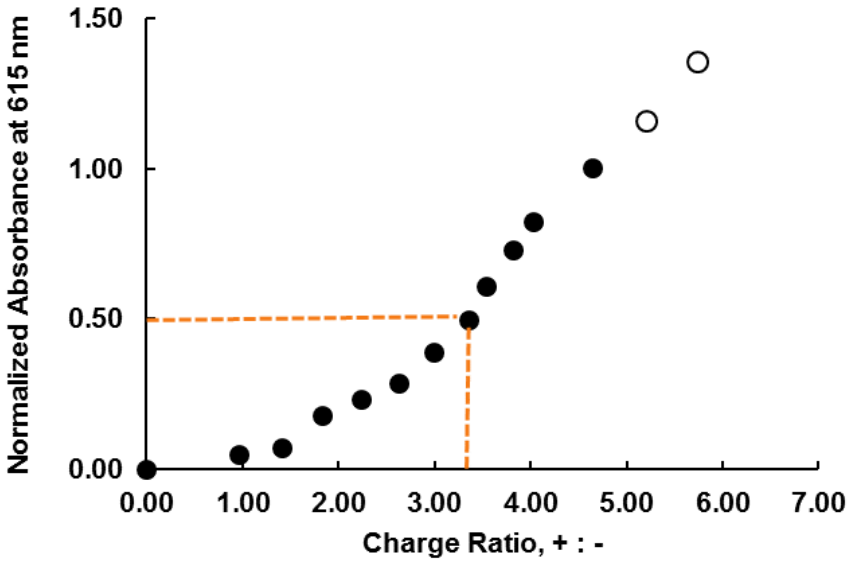

Figure 2-27 Charge ratio against normalized absorbance at 615 nm of **Binder 2** in human serum, showing high values of CE_{50} suggesting significant disruption of the binding, 'open' markers represent points in the titration affected by aggregation and light scattering.

Binder 2 in Human Serum	
CE_{50}	3.4 ± 0.1
EC_{50} (μM)	182 ± 14
Dose (mg) / 100 IU	2.5 ± 0.2

Table 2-6 Calculated CE_{50}, EC_{50} and required dose (in human serum) of **Binder 2**, showing the weaker binding abilities than in buffer.

Binder 3 (Fig. 2-28 and Table 2-7) was also adversely affected by human serum although less so than **Binder 1** and **Binder 2** as the binding was already relatively weak even in buffer. The CE_{50} rises from 2.3 (± 0.18) in buffer to 3.1 (± 0.1) in serum. Interestingly, this might suggest that human serum is less-able to adversely affect the self-assembly of **Binder 3** than it does to **Binder 1** and **Binder 2**. It is known that HSA has a preference for binding long chain aliphatic compounds which would lead to disruption of self-

assembly and hence SAMul binding. However, for **Binder 3**, which has the most distorted chain (Fig. 2-11), perhaps this binds less effectively to HSA and hence the relative degree of disruption is less.

It is worth noting that the binding of MalB (the competitive species) to heparin is relatively un influenced by the presence of human serum, presumably because it does not have a hydrophobic unit capable of interaction with (and competition from) HSA.

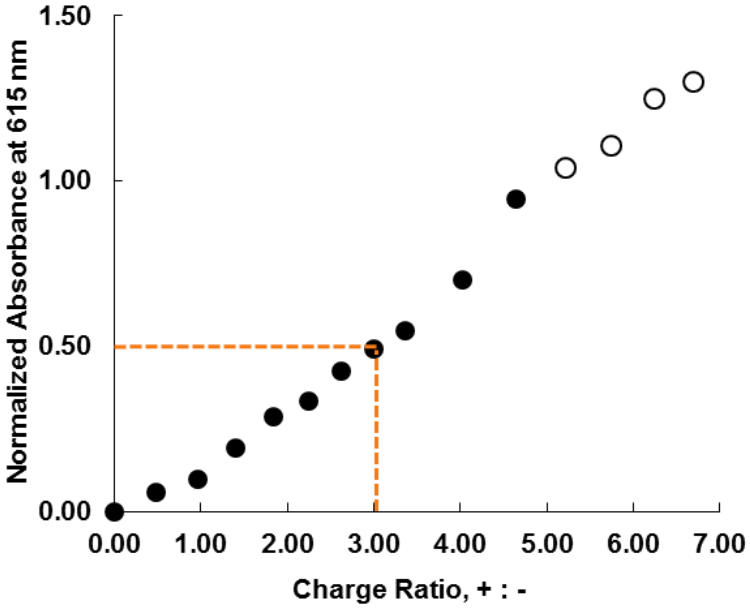

Fig. 2-28 Charge ratio against normalized absorbance at 615 nm of **Binder 3** in human serum, showing no significant differences in CE_{50} values in buffer, 'open' markers represent points in the titration affected by aggregation and light scattering.

Binder 3 in Human Serum	
CE_{50}	3.1 ± 0.1
EC_{50} (µM)	166 ± 1.9
Dose (mg) / 100 IU	2.3 ± 0.01

Table 2-7 Calculated CE_{50}, EC_{50} and required dose (in human serum) of **Binder 3**, showing no significant differences in those values in buffer.

2.5.2 DNA Binding

We were then interested in the relative ability of these compounds to bind to different polyanionic targets. As such, we went on to study the binding of these compounds to DNA. We were interested to know the impact of modifying the hydrophobic group on selectivity between different biological polyanions. The biological world is highly rich in polyanions and understanding theses selectivities in this process is of key importance, yet surprisingly selective binding of such species is rarely addressed. We discussed DNA binding[207] to self-assembled amphiphilic peptides in the introduction chapter (1. 2. 4). In order to perform such a study, we also selected a competition assay. Calf-thymus DNA was mixed with a known concentration of ethidium bromide (EthBr). EthBr (Fig. 2-29); a well-known DNA stain,[208,209] is a flat molecule that fits between adjacent base pairs (intercalates) in the DNA double helix.[210,211] On the addition of increasing amounts of binder, the EthBr is displaced from the DNA causing a reduction in fluorescence. The fluorescence of EthBr is significantly higher when intercalated than it is in aqueous solution.[211,212] Competitive displacement studies with EthBr showed that complexes compete for the DNA binding sites with EthBr and displaces the molecule.[211,212] This method can be used to quantify interactions between DNA and different binding molecules and is a very useful comparative technique, although it does not give any data on the binding mode.

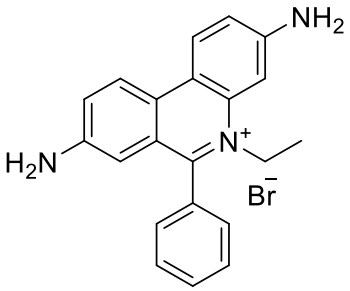

Fig. 2-29 8-Diamino-5-ethyl-6-phenylphenanthridinium bromide (EthBr).

The studies of the synthesized binders were carried out in HEPES buffer at pH 7.4 and at physiological salt concentrations, 150 mM NaCl. At this pH value the amine groups (binding site) on the binder are protonated and can thus form interactions with the negatively charged phosphate backbone of the DNA via electrostatic binding. The concentration of calf-thymus DNA was 4.0 μM with respect to an individual nucleotide base, with a molecular weight assumed to be 330 $gmol^{-1}$. The concentration of EthBr in solution was 5.07 μM. The maximum EthBr emission was measured at 595 nm. The fluorescence measurements were normalized to a value of 0.0, with respect to a solution of EthBr alone, and to a value of 1.0 for the starting solution containing both EthBr and DNA.

EthBr displacement assays were performed on all the binders (**Binders 1**-**3**) to assess their relative binding abilities to DNA.[213] In addition, a DNA assay was performed on a mixture of **Binders 1** and **Binders 3** (1:1). The assay results, for each binder, indicated different DNA binding affinities (Fig. 2-30, Table 2-8). Interestingly, in this case, there was an apparent decrease of CE_{50} values with an increasing number of alkene groups on the hydrophobic tail. This decrease was from = 5.0 ± 0.7, in the case of **Binder 1**, to 4.3 ± 0.5 and 3.5 ± 0.4 for **Binder 2** and **Binder 3**, respectively (Table 2-8). It should be noted that these differences are somewhat smaller than observed for heparin binding and **Binder 1** and **Binder 2** have DNA affinities within error of one another, but most remarkably, and contrary to our initial expectations **Binder 1**, with the smallest number of alkenes and the best ability to self-assemble, was no longer the most effective binder, and appeared to be the least able to bind DNA.

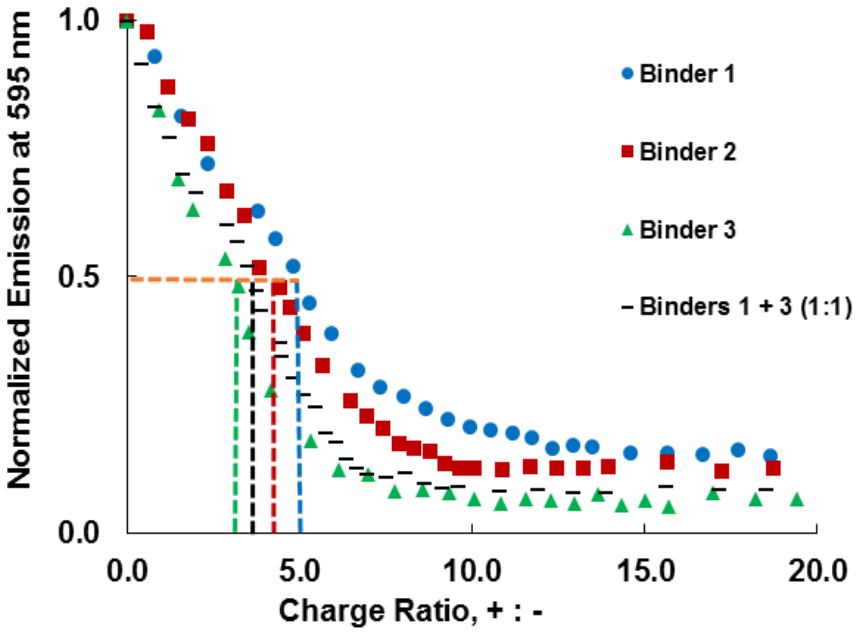

Fig. 2-30 Charge ratio against normalized emission at 595 nm from EthBr assay for all the synthesized binders.

.

Binder	**1**	**2**	**3**	**1 + 3 (1:1)**
CE_{50} in DNA	5.0 ± 0.7	4.3 ± 0.5	3.5 ± 0.4	3.2 ± 0.2
CE_{50} in Heparin	0.8 ± 0.1	1.8 ± 0.2	2.3 ± 0.2	2.0 ± 0.3

Table 2-8 CE_{50} of the binders **1-3** (in buffer) after binding to DNA and heparin showing the binding selectivity caused by differences in alkene groups density.

In other words, **Binder 3** is better for binding DNA than **Binder 1**. This is clearly in contrast to the CE_{50} values for binding to heparin which were much better for **Binder 1** than **Binder 3** (Table 2-8). This would suggest that DNA and heparin, at least in the assays performed here, have different requirements in terms of compounds which will exhibit optimal binding profiles towards them. We suggest that the looser aggregates formed by **Binder 3** may be more effective for DNA binding as the ligands may be more freely able to insert into the minor groove and bind to the phosphate groups, whereas for heparin binding we suggest that the most densely packed best organized charged assemblies are optimal – more for a pure charge-charge interaction with less influence of

ligand organization. We come back to this concept in a later chapter (Chapter 3) dealing with the impact of ligand structure on polyanion binding process.

The mixture of **Binders 1** and **Binder 3** (1:1) was closer to **Binder 3**'s values, for DNA binding, which indicated that, once again, **Binder 3** dominates the self-assembly and also indicates that the loosening effect on the self-assembly of incorporating the lipid with these double bonds is significant and is the key factor influencing polyanion recognition.[214]

The observation of different binding preferences for heparin and DNA induced by a simple change in the hydrophobic unit is a very significant observation. In both cases, cation-anion interactions are responsible for binding and it might be expected that simple change density will dominate and control the binding interaction. The fact that heparin and DNA show different responses indicates that the morphology of the nanostructure can significantly influence the binding event. This result overthrows many preconceptions about electrostatic ion-ion interactions which are usually considered to be difficult to have control, and demonstrates that by modulating the self-assembly of multivalent systems, we can have direct influence on the preferences of the SAMul array (Fig. 2-31). This shows how versatile this approach to biological binding really is.

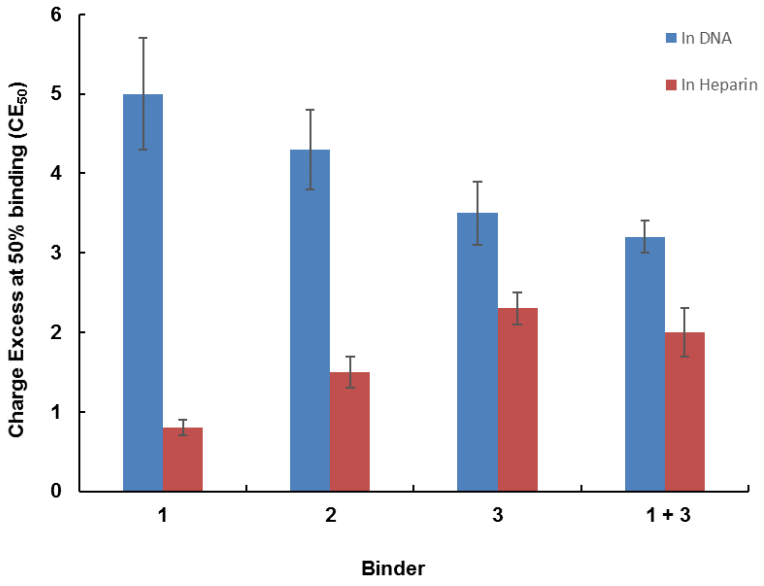

Fig. 2-31 CE_{50} values showing binding selectivity of **Binders 1-3** between different biological polyanions; heparin and DNA**.**

2.6 Alkene Groups Cross-linking (C-L)

The goal of this step was to enhance the stability of the self-assembled micelles of each binder in serum as micelle stability has been previously reported to be improved after cross-linking.[174,215] We tested the cross-linking of **Binders 1-3** using 2,2-azo-bis(isobutyronitrile) (AIBN)[175] (Fig. 2-32) as a radical polymerization initiator (Fig. 2-33); each binder was cross-linked individually. Polymerization of the alkene groups should act to link each binder together covalently and within the confined environment of the micelle interior might be expected to hence covalently 'capture' the self-assembled nanostructure. The mechanism of AIBN initiation and alkene polymerization is shown in Scheme 2-4.

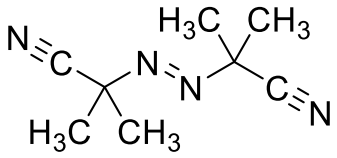

Fig. 2-32 2,2-azo-bis(isobutyronitrile) (AIBN) as the radical initiator in the polymerization reaction of the alkene groups or cross-linking (C-L) reaction.

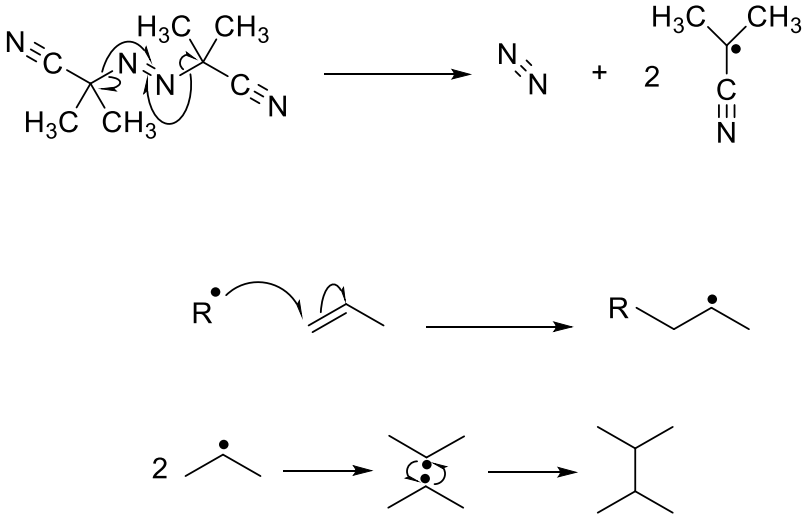

Scheme 2-4 Proposed mechanism of AIBN initiation and the alkene polymerization (cross-linking).

Water was used as the reaction medium of choice in order to enable the binders to form a self-assembled nanostructure. Tetrahydrofuran (THF) was then used as a co-solvent to ensure the total solubility of AIBN which should partition inside the self-assembled nanostructures prior to thermal activation. The self-assembled nanostructures should be stable at these elevated temperatures as the entropically driven hydrophobic effect is usually favoured as temperature increases ($\Delta G = \Delta H - T\Delta S$). It is well-known, for example, that detergent micelles, used in cleaning applications have greater stability at elevated temperatures.

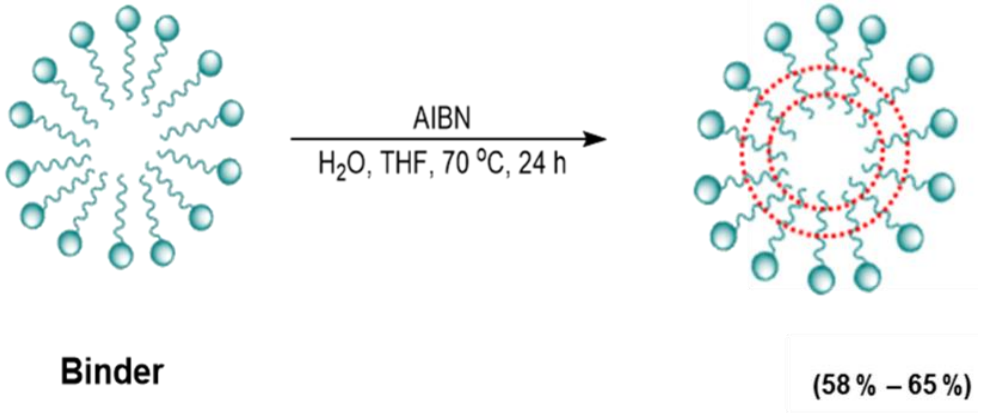

Fig. 2-33 Cross-linking the reactive alkene groups of binders using AIBN as a radical polymerization initiator. The red dotted red line indicates the proposed cross-linking within the nanostructures.

It is clear that the number of alkenes may impact on the potential for cross-linking. Furthermore, it is possible that either intramolecular reaction (undesired) or intermolecular cross-linking (desired) may occur for the systems which have more than one alkene group. After the cross-linking reaction of **Binder 1**, there was still a presence of the alkene groups at 5.10-5.24 ppm in the ^{1}H NMR (Fig. 2-34). The integral had decreased by 20% relative to other peaks. This would suggest that some reaction is occurring but that any polymerization is incomplete.

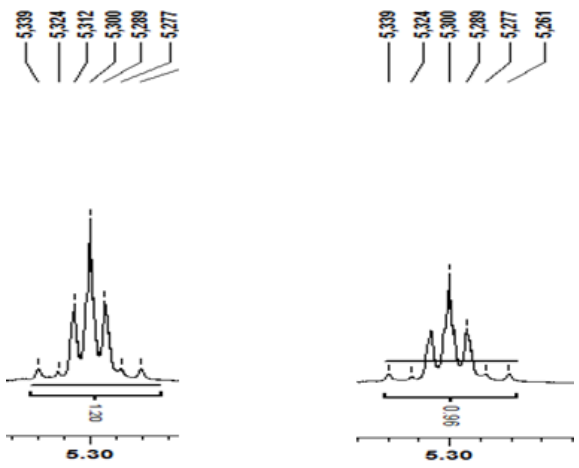

Fig. 2-34 NMR spectra of **Binder 1** before cross-linking alkene groups (left) and (right) after the cross-linking reaction, showing the presence of the alkene protons multi peaks at 5.10-5.24 ppm.

In addition, mass spectrometry (MS) of **Binder 1** after polymerization showed the clear presence of the monomer (Fig. 2-35), HRMS: Calc. $[M+H]^+$ ($C_{25}H_{52}N_3O$) m/z = 410.4105 Found $[M+H]^+$ = 410.4097. This supports the NMR data to indicate that the cross-linking was not complete. We suggest that with just one alkene self-assembled within the micelle interior, these groups are unable to effectively come into contact with one another and hence polymerization is relatively ineffective.

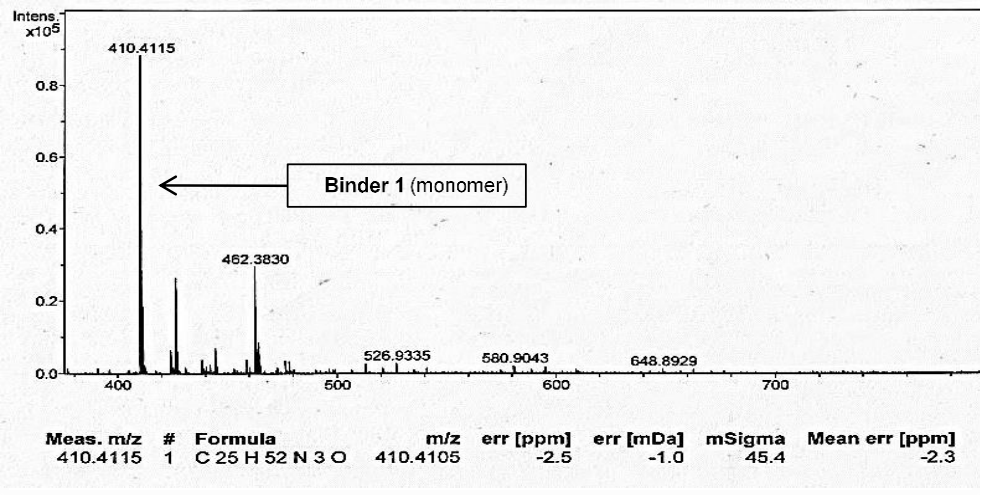

Fig. 2-35 MS spectra showing the presence of **Binder 1**'s monomer, indicating the unsuccessful C-L.

In contrast, after the cross-linking reaction of **Binder 2** the alkene groups multiplet peak at 5.10-5.24 ppm in the ^{1}H NMR had a significantly lower intensity (Fig. 2-36); a decrease

of 76% was recorded. Further, the alkene group multiplet peak for **Binder 3** was negligible after cross-linking (Fig. 2-37), decreasing to just 19%. This would suggest when more alkenes are present a greater degree of alkene cross-linking can occur. This may be a result of enhanced intermolecular cross-linking as a result of the greater density of alkenes in the micelle interior, or may result from intramolecular alkene-alkene reactions.

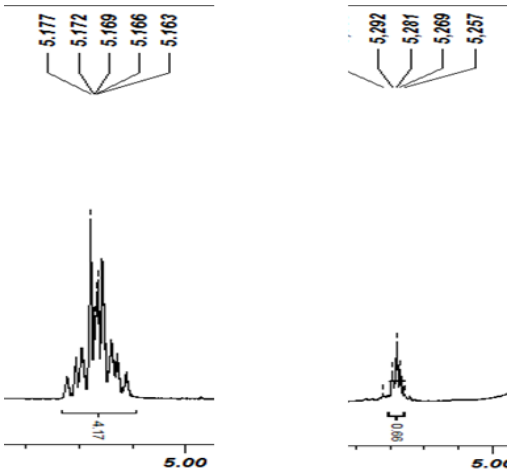

Fig. 2-36 NMR spectra of **Binder 2** before cross-linking alkene groups (left) showing the presence of the alkene protons multi peaks at 5.10-5.24 ppm and (right) after the cross-linking reaction the peaks had a lower intensity.

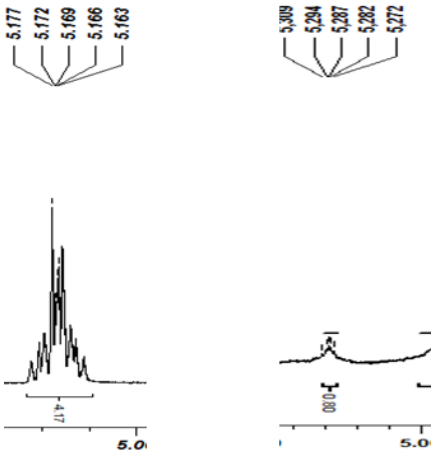

Fig. 2-37 NMR spectra of **Binder 3** before cross-linking alkene groups (left) showing the presence of the alkene protons multi peaks at 5.10-5.24 ppm and (right) after the cross-linking reaction the peaks are negligible.

In order to determine whether the reaction between alkenes was intra or inter molecular, we employed mass spectrometric analysis of the products from these cross-linking

reactions. The mass spectra for **Binder 2 and Binder 3** (Fig. 2-38 and Fig. 2-39) supported the NMR results by showing a distribution of several peaks at higher masses than that expected for the monomer (m/z = 408 and 406 for **Binder 2** and **Binder 3** respectively). We suggest that these peaks represent multiply charged ions resulting from oligomerization of the binders induced by the AIBN cross-linking conditions, although they were difficult to fully assign.

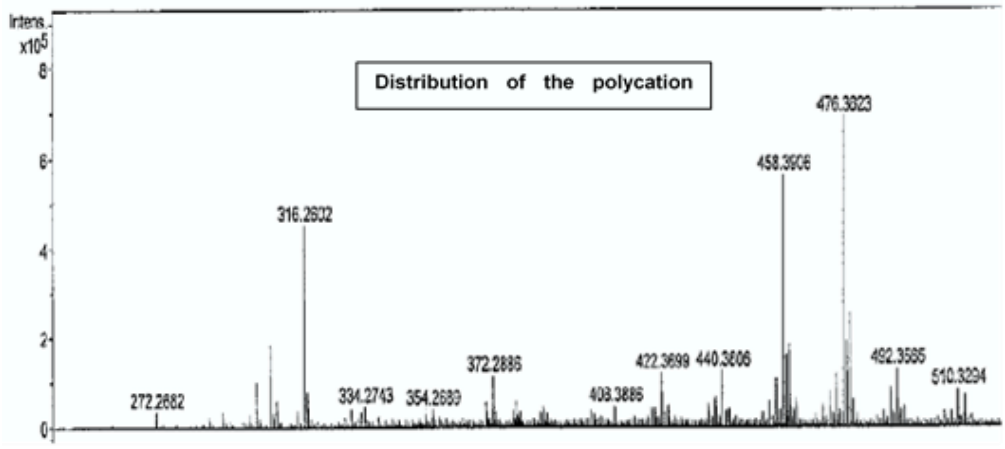

Fig. 2-38 MS spectra of **Binder 2** after C-L showing distribution of the polycation ions.

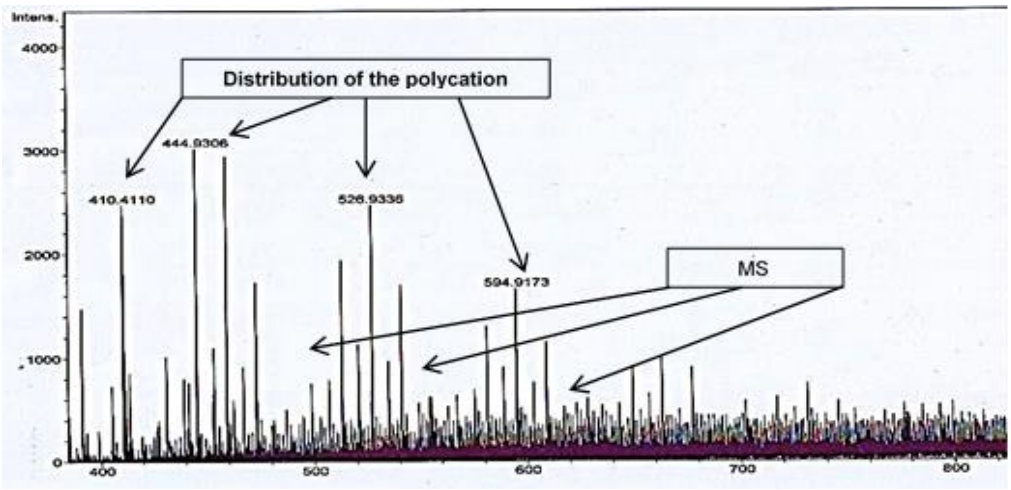

Fig. 2-39 MS spectra of **Binder 3** after C-L showing distribution of the polycation ions.

The differences in alkene reactivity between **Binders 1**,**2** and **3** lead us to suggest that the higher density of alkenes in self-assembled nanostructures formed by **Binder 3** leads to far more effective intermolecular cross-linking (C-L) and capture. On the other hand, the

relatively low density of alkenes in **Binder 1** means that the alkenes are more difficult to react with one another within the self-assembled nanostructure and, as such, we suggest that cross-linking does not occur successfully. We then went on to test the performance of these cross-linked systems.

2.6.1 Characterization of the Cross-linked Systems

2.6.1.1 Nile Red Assay

The Nile Red assay was used to determine CAC for the cross-linked systems. This assay was performed as described above (2. 4. 1). CACs for **Binder 1** before and after C-L (Fig. 2-40, Table 2-9) were similar (42 µM). The stability of the CAC values is a result of the presence of the alkene groups after the C-L reaction indicating unsuccessful C-L and/or capture of the nanostructure in this case.

Compound	**Binder 1** Before C-L	**Binder 1** After C-L	**Binder 2** Before C-L	**Binder 2** After C-L	**Binder 3** Before C-L	**Binder 3** After C-L
CAC (µM)	42 ± 3.1	42 ± 1.8	82 ± 1.7	90 ± 2.7	78 ± 9.8	151 ± 10

Table 2-9 Critical aggregation concentration (CAC) for **Binders** (**1** – **3**) before and after C-L.

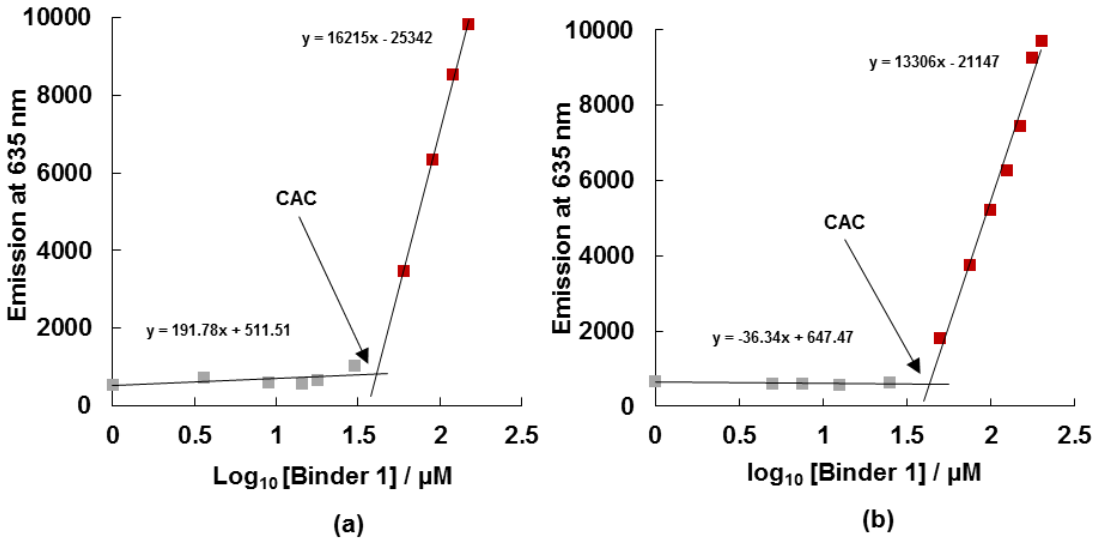

Fig. 2-40 Critical aggregation concentration (CAC) for **Binder 1** before C-L **(a)** and after C-L **(b)**; **Binder 1** micelles showed similar aggregation behavior before and after C-L.

The CAC value (Table 2-9) of **Binder 2** after the C-L reaction was determined as 90 ± 2.7µM, similar to the value before C-L (82 ± 1.7 µM). This would suggest that the reaction of the alkenes is not significantly impacting on the concentration at which Nile Red is fluorescing which would suggest that self-assembly is similar both before and after our C-L reaction. It was, however, noted that there was some difference in the line-shape for **Binder 2** after C-L compared with before (Fig. 2-41) with more Nile Red being solubilized at lower concentrations (i.e. the grey line is less horizontal). This may suggest some more nanostructure stabilization after C-L allowing Nile Red to be solubilized below the CAC of the binder alone.

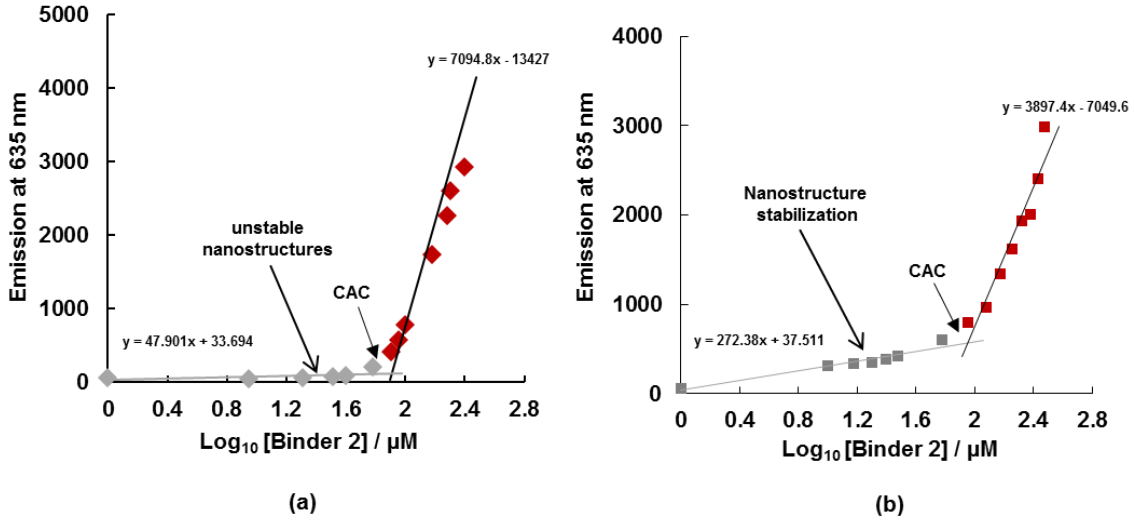

Fig. 2-41 Critical aggregation concentration (CAC) for **Binder 2** before C-L **(a)** and after C-L **(b)** showing the difference in the grey line shape which might indicate some stabilization.

Binder **3**'s CAC values, however, had changed (151 µM) after the C-L reaction (Fig. 2-42b) comparing to the values before the C-L reaction (78.0 µM) (Fig. 2-42a). It was, somewhat, surprising that the CAC had increased (Table 2-9) as we had been hoping to stabilize the nanostructure, which should mean it forms at lower concentrations. We discuss this further below.

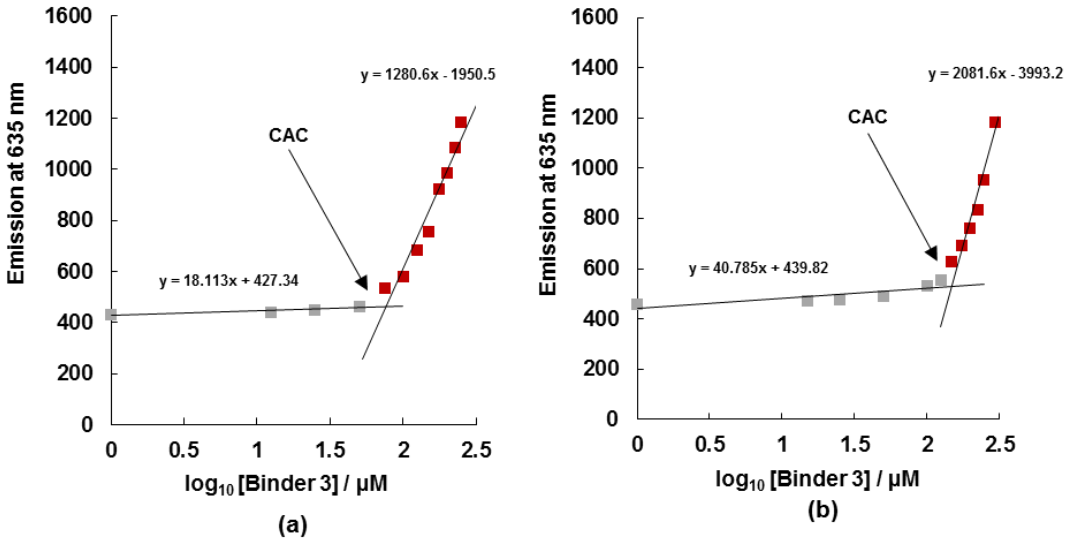

Fig. 2-42 Critical aggregation concentration (CAC) for **Binder 3** before C-L **(a)** and after C-L **(b)**.

2.6.1.2 Dynamic Light Scattering (DLS)

The cross-linked systems of **Binder 2** and **Binder 3** were characterized by DLS in order to obtain an insight into the micelle size after the C-L reaction. The samples were prepared as described above (2. 4. 2). After the C-L reaction, **Binder 2** (Table 2-10) maintained the same size average (around 7 nm). However, **Binder 3** average diameter by volume distribution before C-L was around 7 nm (Table 2-10), while after C-L the average was bigger; around 9 nm. An explanation to the size increase after C-L is that only parts of the structure are cross-linked which then still need to self-assemble, a process which gives an even less well-defined aggregate. Interestingly, the data support our hypothesis that **Binder 3** assembles into a large and looser nanostructure than **Binder 2**, presumably as a consequence of the additional alkene group which for geometric reasons prevents effective packing of the hydrophobic tails (Fig 2-11).

Sample in NaCl (150 mM) / Tris HCl (10 mM)	**Diameter (Intensity distribution) / nm**	**Diameter (Volume distribution) / nm**	**PDI**
Binder 2	Pk1: 7.80 (75%) Pk2: 143.8 (25%)	6.36 ± 0.41	0.365 ± 0.002
Cross-linked Binder 2	Pk1: 8.20 (25%) Pk2: 168.6 (75%)	7.08 ± 0.05	0.981 ± 0.032
Binder 3	Pk1: 10.69 (45%) Pk2: 203.1 (55%)	7.58 ± 0.27	0.697 ± 0.012
Cross-linked Binder 3	Pk1: 17.21 (66%) Pk2: 159.8 (34%)	8.87 ± 0.09	0.438 ± 0.011

Table 2-10 Size Analysis by DLS for **Binder 2** and **Binder 3** (before and after C-L), in NaCl (150 mM) / Tris HCl (10 mM).

It is also important to note that zeta potential values for **Binder 2** and **Binder 3** after C-L were similar to the values before C-L (Table 2-11); this is an indication that performing the C-L reaction has not affected the surface charges of those two compounds.

Sample in Buffer	**Zeta potential (mV)**
Cross-linked **Binder 2**	69.4 ± 1.0
Cross-linked **Binder 3**	75.6 ± 2.7

Table 2-11 Zeta potential values of **Binder 2** and **Binder 3** in buffer; NaCl (150 mM) / Tris HCl (10 mM), showing that the cross-linked systems were highly positively charged.

2.6.1.3 TEM Images

Transmission electron microscopy (TEM) images were recorded for the cross-linked systems of **Binder 2** and **Binder 3** in a similar method to that described above (2. 4. 3). TEM images of **Binder 2** after C-L (Fig. 2-43), showed that, in the presence of heparin after C-L the micelles have similar shape yet smaller in size than those before C-L (Fig. 18). Furthermore, TEM images of **Binder 3** after C-L (Fig. 2-44) gave smaller aggregates than before C-L (Fig. 2-19). This might be reflective of less organized system being present after C-L has taken place.

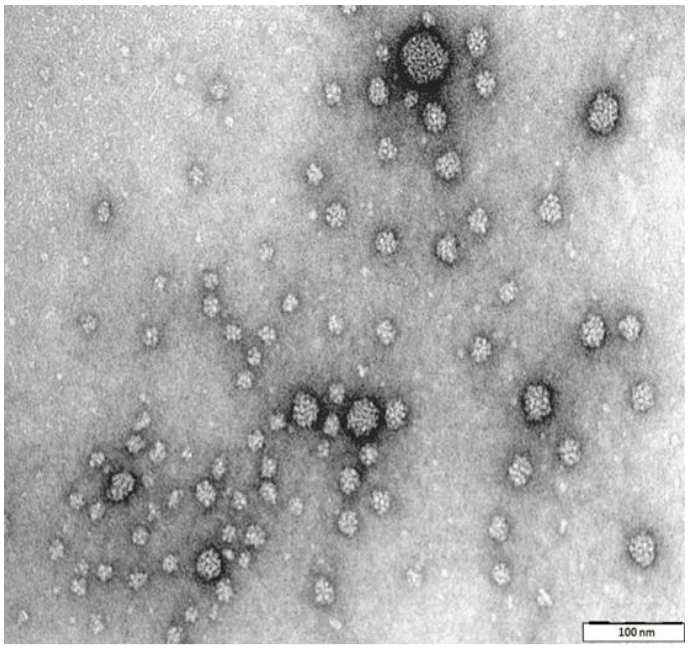

Fig. 2-43 TEM images of **Binder 2** dried from aqueous solution (200 µM), showing spherical self-assembled nanostructures in the presence of heparin; after C-L, scale bar = 100 nm.

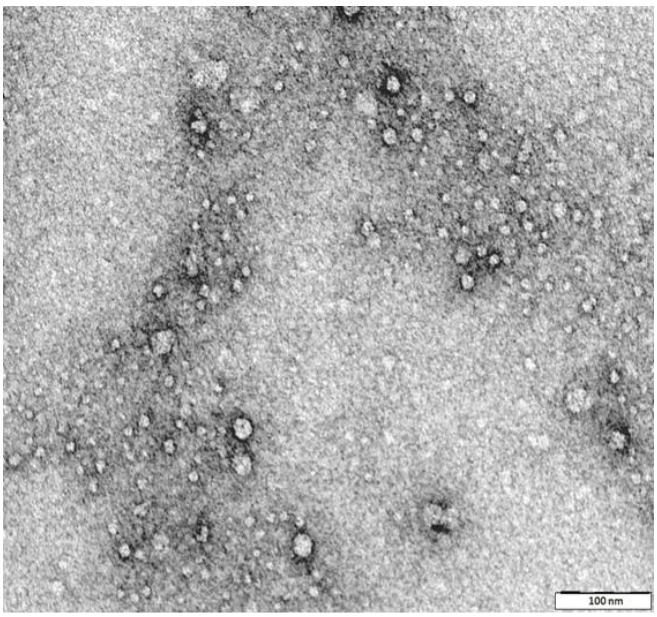

Fig. 2-44 TEM images of **Binder 3** dried from aqueous solution (200 µM), showing spherical self-assembled nanostructures in the presence of heparin; after C-L, scale bar = 100 nm.

2.6.2 Heparin Binding

2.6.2.1 Mallard Blue

a. MalB Assay in Buffer

Binding abilities of the cross-linked systems were tested using MalB assay; **Binder 2** and **Binder 3** were tested individually. The assay was performed as described above. After C-L the alkene groups in **Binder 2**, the binding ability has improved slightly. This improvement was shown in the values of EC_{50} and CE_{50} (Table 2-12), which was calculated from the graph below (Fig. 2-45). The CE_{50} was 1.5 ± 0.19 which is lower than the value before C-L (1.8 ± 0.1) and may suggest that C-L has tightened the self-assembly and strengthened its binding ability. However, it should be noted that differences are very close to error range. We now needed to test this system in serum, where competition was stronger. However, although the C-L reaction appeared to be more successful in the case of **Binder 3**, CE_{50} values were higher after C-L; 2.6 (Table 2-12). By looking at the graph below (Fig. 2-46), we could see a clear difference between these values.

Compound in buffer	Binder 2 Before C-L	Binder 2 After C-L	Binder 3 Before C-L	Binder 3 After C-L
CE_{50}	1.8 ± 0.1	1.5 ± 0.19	2.3 ± 0.18	2.6 ± 0.03
EC_{50} (μM)	76 ± 7.0	64 ± 10.7	125 ± 9.9	142 ± 5.8
Dose (mg) / 100 IU	1.1 ± 0.01	0.9 ± 0.14	1.7 ± 0.13	1.9 ± 0.01

Table 2-12 Calculated CE_{50}, EC_{50} and required dose (in buffer) of synthesized binders, before and after C-L, showing the effect of the density of alkene groups on self-assembly and binding abilities.

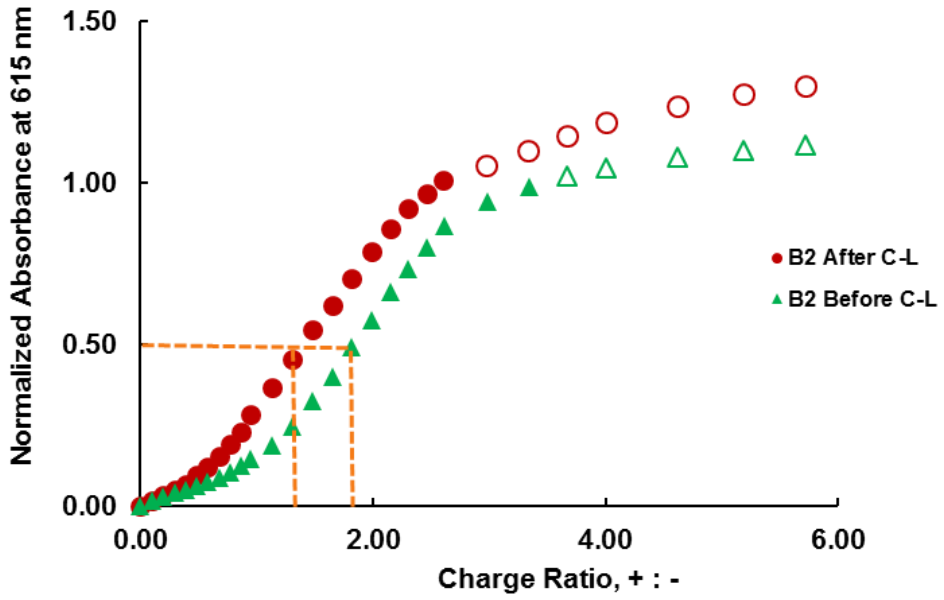

Fig. 2-45 Charge ratio against normalized absorbance at 615 nm of **Binder 2**, in buffer**,** before and after C-L, showing a slight improvement in CE_{50} values, 'open' markers represent points in the titration affected by aggregation and light scattering.

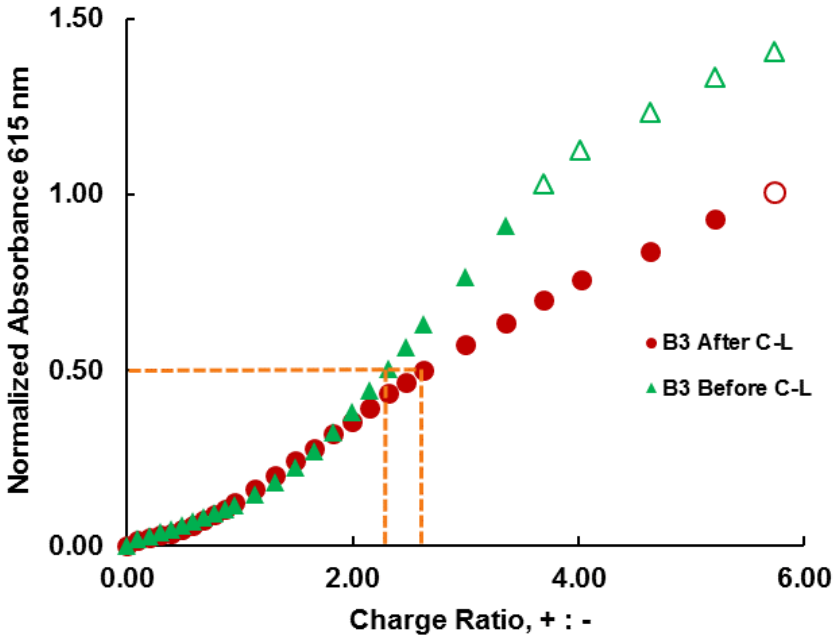

Fig. 2-46 Charge ratio against normalized absorbance at 615 nm of **Binder 3**, in buffer, before and after C-L, showing a slight difference in CE_{50} values, 'open' markers represent points in the titration affected by aggregation and light scattering.

On cross-linking, there is no significant improvement in heparin binding. This suggests that cross-linking is either incomplete or does not significantly change the ability of these compounds to bind under these conditions. We considered that in serum, which is much more competitive, the advantages of cross-linking should become more apparent and we therefore went on to study the heparin binding event in serum.

b. MalB Assay in Human Serum

After testing the cross-linked systems, abilities to bind heparin in 150 mM NaCl and 10 mM Tris HCl, we decided to investigate the stability of these systems in more challenging conditions; human serum. The assay was carried out as described above. **Binder 2** CE_{50} values in serum (3.4 ± 0.1) were higher than the values in buffer (1.8 ± 0.1). After C-L (Fig. 2-47) **Binder 2** showed some improvement but not significantly more than error (3.1 ± 0.3).

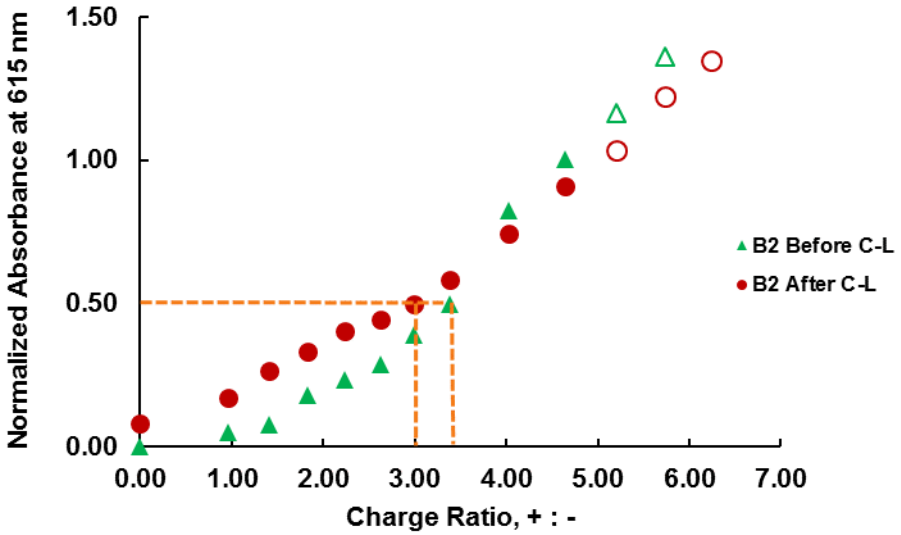

Fig. 2-47 Charge ratio against normalized absorbance at 615 nm of **Binder 2** before and after C-L, in human serum, showing no significant differences in CE_{50} values more than error might suggest, 'open' markers represent points in the titration affected by aggregation and light scattering.

Considering the data from the table below (Table 2-13), it was clear that **Binder 3**'s binding ability to bind heparin in human serum after C-L did not change significantly CE_{50} values before and after C-L were about 3.0 (± 0.1) (Fig. 2-48). We believe that overall, the reaction of the alkenes is not significantly enhancing the polyanion binding performance of these nanostructures.

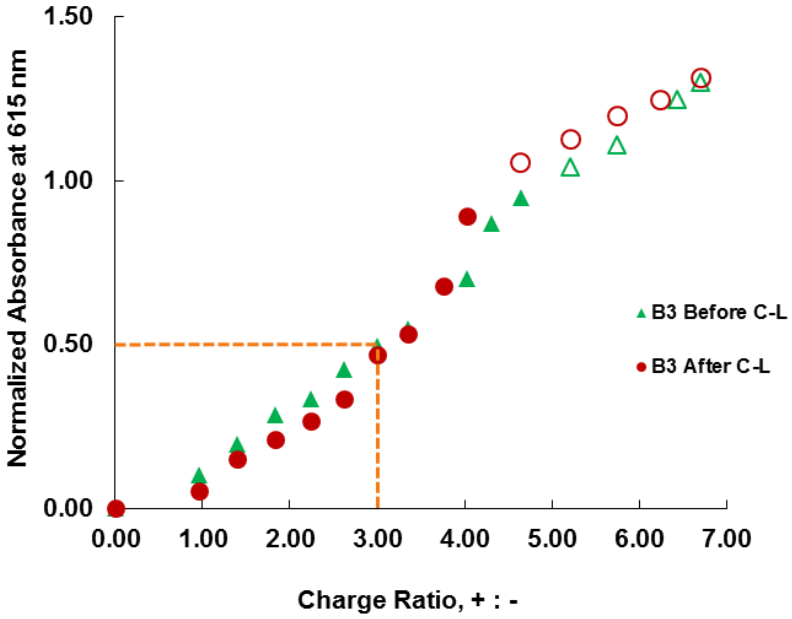

Fig. 2-48 Charge ratio against normalized absorbance at 615 nm of **Binder 3** before and after C-L, in human serum, showing total similarity of binding behavior; no significant differences in CE_{50} values, 'open' markers represent points in the titration affected by aggregation and light scattering.

Compound	**Binder 2** Before C-L	**Binder 2** After C-L	**Binder 3** Before C-L	**Binder 3** After C-L
in Buffer				
CE_{50}	1.8 ± 0.1	1.50 ± 0.19	2.30 ± 0.18	2.60 ± 0.03
EC_{50} (μM)	76.0 ± 7.0	64.0 ± 10.7	125.0 ± 9.9	142.0 ± 5.8
Dose (mg) / 100 IU	1.10 ± 0.01	0.90 ± 0.14	1.70 ± 0.13	1.90 ± 0.01
in Human Serum				
CE_{50}	3.4 ± 0.1	3.0 ± 0.3	3.1 ± 0.1	3.2 ± 0.1
EC_{50} (μM)	182.0 ± 14.0	150.0 ± 12.0	166.0 ± 1.9.0	168.0 ± 0.7
Dose (mg) / 100 IU	2.5 ± 0.2	2.0 ± 0.4	2.30 ± 0.01	2.40 ± 0.02

Table 2-13 Calculated CE_{50}, EC_{50} and required dose (in buffer and human serum) of **Binder 2** and **Binder 3**, before and after C-L.

2.7 Comparison Study

Finally, we compared the results collected here with those for two analogue compounds synthesized by Vieira, Smith et al. These two compounds' hydrophobic tails were modified using saturated fatty acids with different lengths; palmitic acid to produce (**C_{16}-DAPMA**) and stearic acid to produce (**C_{18}-DAPMA**) (Fig. 2-49).

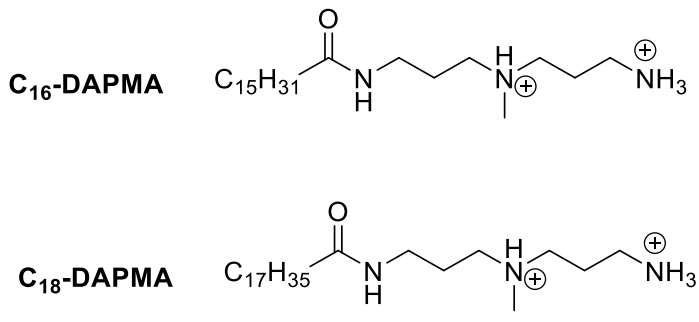

Fig. 2-49 C_{16}-DAPMA and **C_{18}-DAPMA**; saturated hydrophobic tails.

The saturated hydrophobic tails yield assemblies which had lower CE_{50}, and EC_{50} values indicating the adverse effect of the alkene group(s) on nanostructures packing and on the binding abilities. A slight solubility problem occurred with **C_{18}-DAPMA**, due to the chain length, this hydrophobic behavior resulted in high aggregation values, CAC at 75 μM. it is interesting to note that the alkene-containing analogues studied in this chapter do not suffer from this solubility problem – mainly because the hydrophobic chains are distorted and pack less well. Furthermore, the low CACs of those compounds with saturated hydrophobic chains, supported the effect the alkene group have on self-assembly and hence heparin binding. It is clear from our proposal that the lower CE_{50} values of the saturated systems, that they had better binding to heparin (0.6 and 0.7).

Compound (in buffer)	**Binder 1**	**Binder 2**	**Binder 3**	**C_{16}-DAPMA**	**C_{18}-DAPMA**
Fatty Acid	Oleic ($C_{18}H_{34}O_2$)	Linoleic ($C_{18}H_{32}O_2$)	Linolenic ($C_{18}H_{30}O_2$)	Palmitic ($C_{16}H_{32}O_2$)	Stearic ($C_{18}H_{36}O_2$)
CE_{50}	0.8	1.8	2.3	0.6	0.7
EC_{50} (μM)	45.0	76.0	125.0	35.0	37.0
Dose (mg) / 100 IU	0.6	1.1	1.7	0.5	0.5
CAC (μM)	41.0	82.0	77.0	38.0	75.0

Table 2-14 Calculated CE_{50}, $EC_{50,}$ required dose (in buffer) and the CAC of the synthesized binders showing the effect of the alkene group(s) on self-assembly and binding abilities comparing to compounds with saturated hydrophobic tails.

2.8 Conclusions and Future Work

This project continues the investigations of a biocompatible nanostructured heparin binders with by building a self-assembling supramolecule consisting of an amine group as the positively charged binding site and a naturally occurring fatty acid as the hydrophobic focal point that will drive the assembly**.** The synthesis of these compounds was relatively straightforward and the target compounds were fully characterized. The amphiphilic synthesized compounds were successfully self-assembled into micelles and bonded to large polyanionic targets (heparin and DNA) electrostatically (Fig. 2-50). The binding was monitored using Mallard Blue dye as a sensor which allowed us to determine heparin binding affinities and the ability to bind in competitive media, such as human serum. Ethidium bromide displacement was used to monitor DNA binding. We found that human serum disrupted self-assembly and heparin binding. Moreover, the binders showed intriguing different binding affinity to heparin and DNA which we believe are controlled by the alkene modified self-assembly and nanostructured morphology of the SAMul systems. We suggested that the more organized nanostructures are better able to bind to heparin while the looser ones are preferentially bound by DNA.

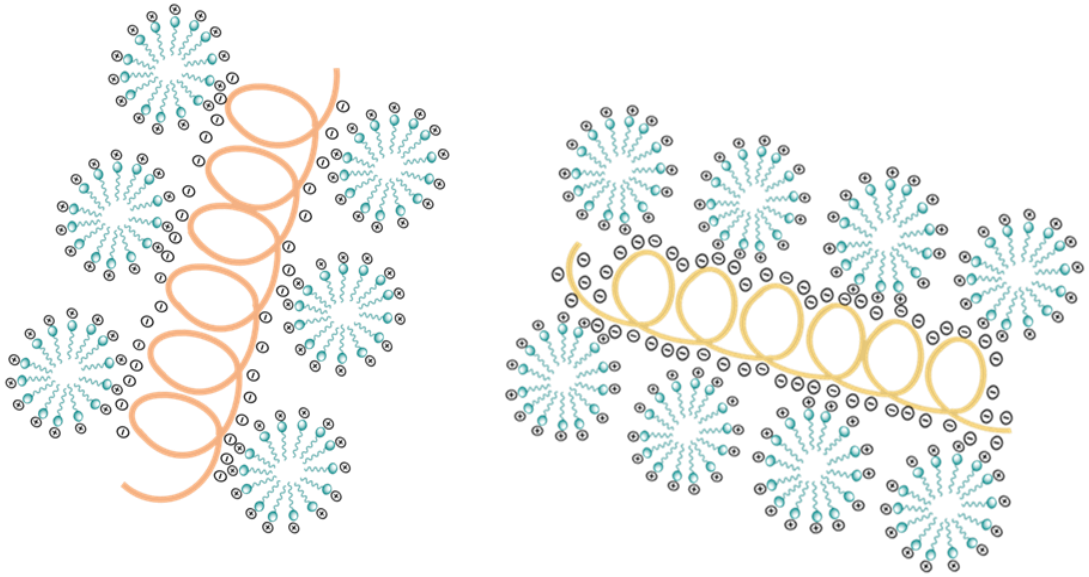

Fig. 2-50 Amphiphilic micelles bind to large polyanionic targets (heparin and DNA) electrostatically.

The alkene group cross-linking reaction which was performed for all three binders went to highest conversion for **Binder 3** with the most alkene groups and was unsuccessful for **Binder 1**. Cross-linking proved not to significantly enhance binding affinity. In addition, the cross-linking reaction appeared to increase the size of the binder micelles suggesting that cross-linking may be only partial and that some reorganization may occur during self-assembly. Nonetheless, this size enhancement means an increase of the core size; this may be a useful tool to load a greater amount of (e. g) drug inside such systems.

In future work, other compounds (binders) could be synthesized to be tested for both heparin and DNA binding. These compounds could consist of the same hydrophobic tail bonded to different ligands or similar ligands bonded to a different hydrophobic tail. Also, using two hydrophobic tails could be considered to enhance the self-assembly which would lead to a better binding. By tuning these head groups and tails, we can modify the binding abilities of the SAMul nanostructures to heparin and DNA; nanoscale biological polyanions. Ion-ion binding is often considered as non-directional and as such only depends on the charge density of the species involved – however, this study clearly demonstrates that under competitive biological conditions, the choice of hydrophobic group and its capacity to display and orientate the ligands has a major role in tuning the binding affinity (such effects will be discussed in further detail in the following chapter).

3 Effects of Modifying Ligands of Polycationic SAMul Nanostructures on Binding Affinities to Different Polyanions

Some of the results in this chapter have been reported in: L. E. Fechner, B. Albanyan, V. M. P. Vieira, E. Laurini, P. Posocco, S. Pricl and D. K. Smith, *Chem. Sci*., 2016, **7**, 4653-4659.

3.1 Introduction

The selectivity between different polyanions, in terms of electrostatic binding, that we observed in the previous chapter led us to be more curious to understand the factors behind the preferences of self-assembled displays of receptors to bind to one polyanion over another. In addition, we wanted to address a genuine challenge in supramolecular design by developing systems that would be able to intervene more precisely in biomedical processes and would be better optimised for specific clinical applications.[126,216] Self-assembled multivalent (SAMul) ligands are small molecules with a highly tunable strategy due to their simple synthesis. Therefore, it is easy to vary their structures and hence explore structure–activity relationships.[217]

It is known that to bind polyanions such as DNA or heparin, cationic ligands are required and that binding is established via multiple electrostatic ion–ion interactions.[102,107,110,114,218-220] Recently, Smith and co-workers, have reported that ligand chirality could have an influence on heparin/DNA binding selectivity,[221] but selective polyanion binding induced by structural ligand differences is rarely explored, and hence a challenging target. Although charge density has the major role in binding, other interactions can have an influence on selectivity, however, there are relatively few examples of such experimental studies.[222-224] In this chapter we determine the effect of

ligand modifications in our SAMul nanostructures on observed selectivities of different biological polyanions; DNA and heparin. In addition, we used multiscale modelling methods in collaboration with Pricl group (Trieste) in order to provide further insight into such complexes, and the interdependent, hierarchical self-assembly and nanoscale binding processes.

We selected palmitic acid (C_{16}), as the hydrophobic unit, coupled with different amines as ligands to study this structure–activity effect. The synthesised compounds had nominal ligand charges of +1, +2, +2 and +3 (Fig. 3-1). This work was carried out by visiting undergraduate student Loryn E. Fechner; under my guidance she performed the synthesis and some of the analytical studies and I completed the analytical work ready for publication.

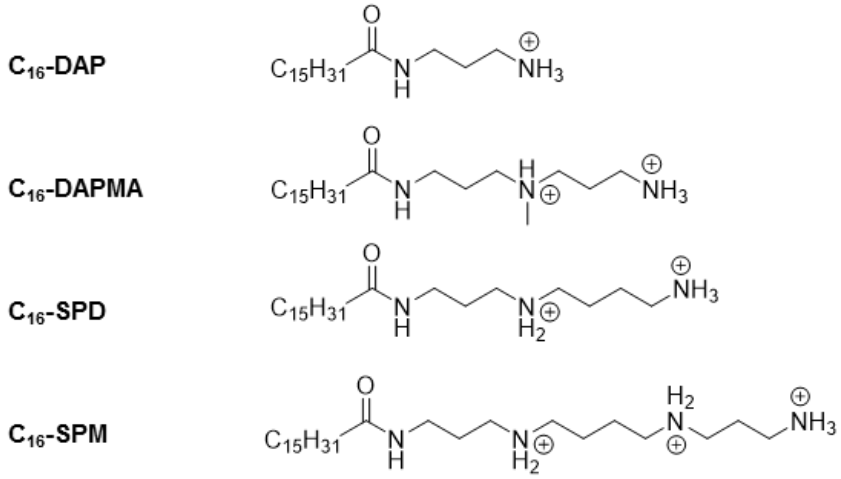

Fig. 3-1 C_{16}-ligands; compounds investigated in this chapter.

3.2 Synthesis of C_{16}-Ligands

Four binders containing a hydrophobic tail and a positively charged polyamine head group were synthesized to investigate the influence of structural differences on the self-assembly and binding affinities to heparin and DNA. The hydrophobic tail used for this work was palmitic acid ($C_{16}H_{32}O_2$), a C_{16} saturated chain.[217] The synthesized C_{16}-ligands were designed to have different positively charged head groups (Fig. 3-1). The first

compound was synthesized using 1,3-propanediamine (DAP) which after coupling contains one primary amine group. It was synthesized using a TBTU-mediated coupling strategy with Boc protecting groups (Scheme 3-1). All the compounds in each step, including the final product, were characterized by ^{1}H and ^{13}C NMR, MS and IR.

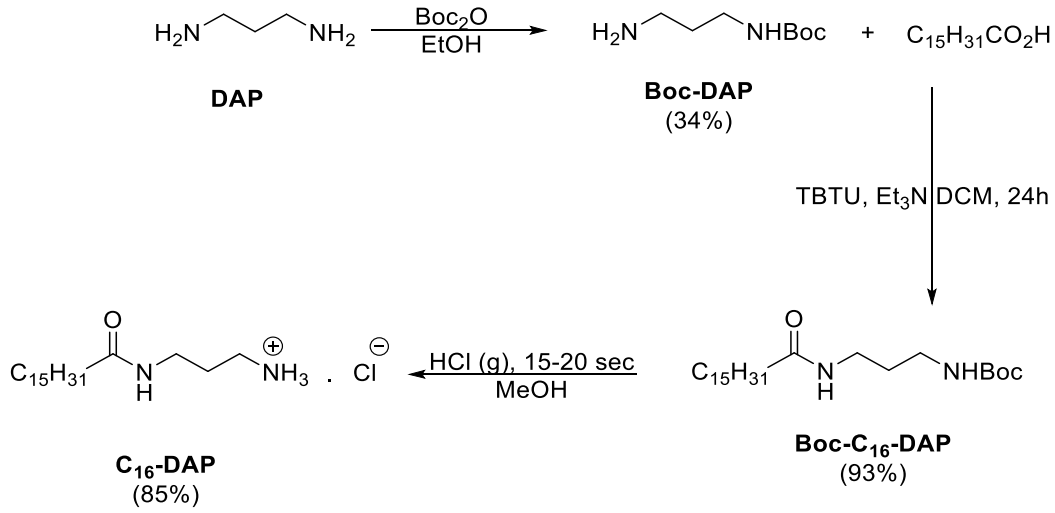

Scheme 3-1 Synthesis of **C_{16}-DAP**.

DAPMA and spermidine (SPD), both contain, after coupling, two free amine groups which can be positively charged, and were used to synthesized two more compounds; **C_{16}-DAPMA** and **C_{16}-SPD** (Fig. 3-1). **C_{16}-SPD** possesses a secondary amine in the middle whereas **C_{16}-DAPMA** contains a tertiary amine.

C_{16}-DAPMA was simply synthesized using TBTU-mediated coupling of compound **1** (reported in chapter 2) with palmitic acid to produce Boc-C_{16}-DAPMA in 90% yield, followed by deprotection with HCl gas (Scheme 3-2). The final product structure was confirmed by ^{1}H- and ^{13}C-NMR, MS and IR.

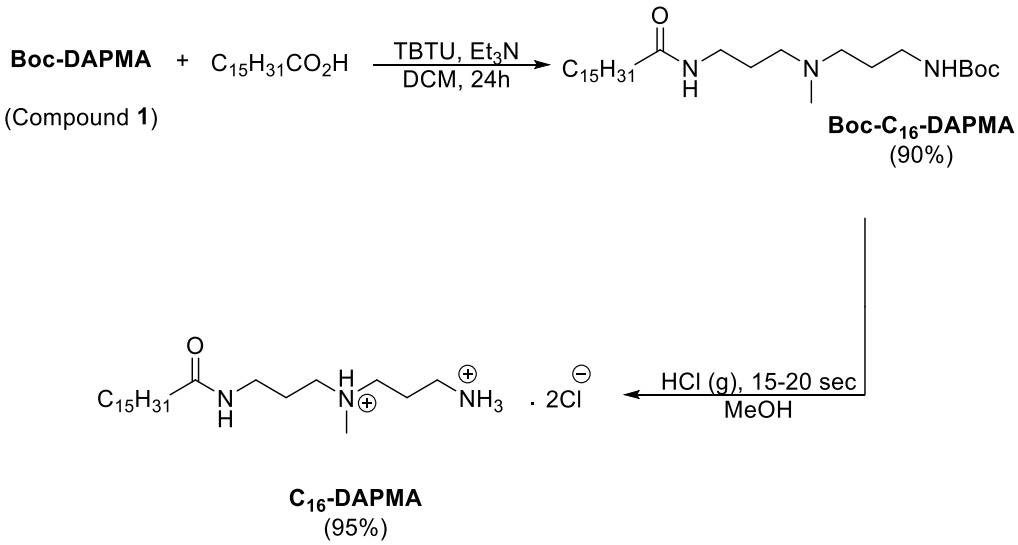

Scheme 3-2 Synthesis of **C_{16}-DAPMA**.

For the Synthesis of **C_{16}-SPM**, due to the asymmetry of the polyamine spermidine (Figure 3-1), the selective Boc-protection required a different approach. Instead of using spermidine as a starting material for selective protection, an alternative pathway starting from diamino butane (DAB) was employed.[225] This allowed stepwise construction of the protected spermidine. Similar reactions to form selectively protected spermidines and spermidine homologues have been described by Andruszkiewicz et al. in 2005.[226]

The first reaction was the mono-Boc-protection of DAB (Scheme 3-3) analogous to the protection of DAP in Scheme 3-1. The di-protected water-insoluble side product was separated by filtration and the product was extracted from the filtrate with DCM. The di-protected product was also isolated in 13% yield. Both structures were confirmed by ^{1}H- and ^{13}C-NMR, MS and IR. A Michael reaction between mono-Boc DAB and acrylonitrile then yielded compound cyanoethyl mono-Boc-DAB. This reaction proceded with simple heating in THF. After drying in vacuum, cyanoethyl mono-Boc-DAB was received as yellow oil in 84 % yield (Scheme 3-3). The secondary amine was then Boc-protected in a similar manner as the first protection (Scheme 3-3) to give compound cyanoethyl di-Boc-DAP in 92% yield. All structures were confirmed by ^{1}H and ^{13}C NMR, MS and IR.

Finally, the selectively – protected N^1,N^2-Bis-Boc-spermidine (Boc-SPD) was yielded by reduction of the cyano group to an amine with lithium aluminium hydride (LAH). The reaction conditions were chosen according to the description of Andruszkiewicz et al.[226] The product was extracted with ether, then with water in acidic conditions (pH = 3-4) then with DCM. After drying, the product was obtained as a slightly yellow oil in 62% yield (Scheme 3-3). The structure was confirmed by ^{1}H and ^{13}C NMR, MS and IR.

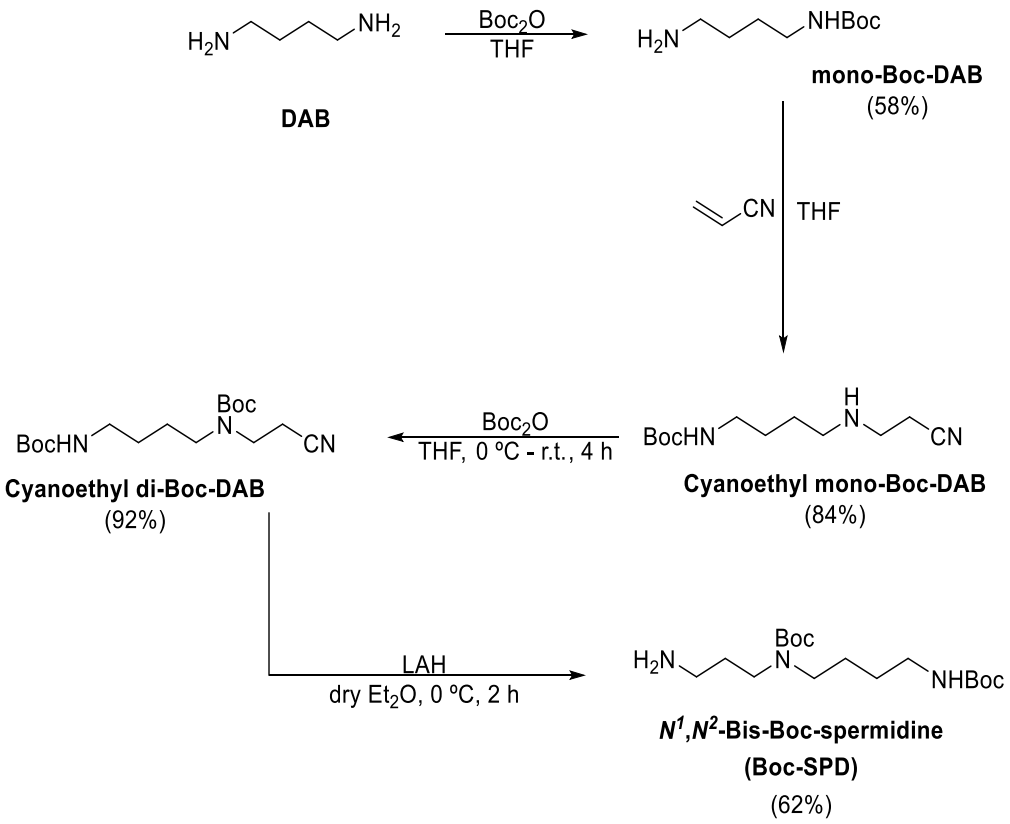

Scheme 3-3 Synthesis of Boc-SPD.

N^1,N^2-Bis-Boc-spermidine (Boc-SPD) was then coupled with palmitic acid by a standard TBTU-mediated coupling (Scheme 3-4) to yield 76%, and the product was deprotected by HCl gas to produce **C_{16}-SPD** as a white powder (81%). The structure was confirmed by ^{1}H and ^{13}C NMR, MS and IR.

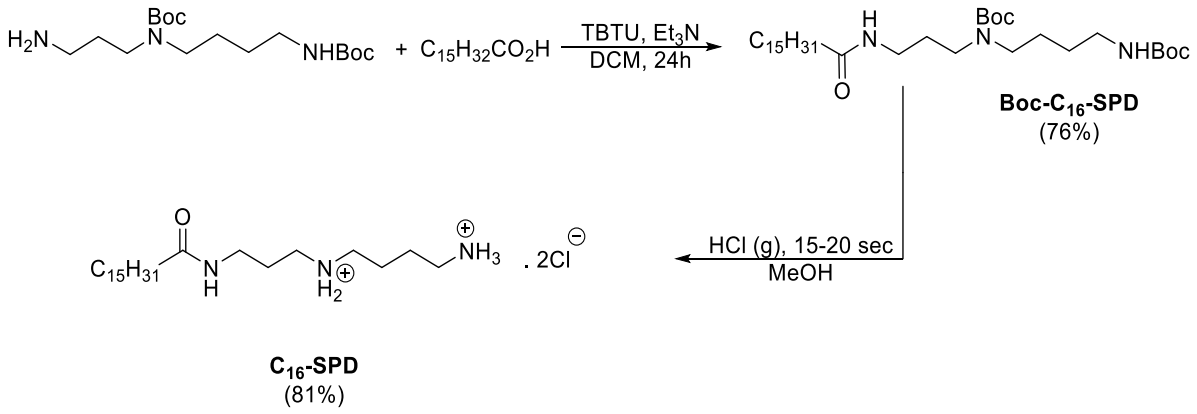

Scheme 3-4 Synthesis of **C_{16}-SPD**.

The final compound **C_{16}-SPM** was synthesized from spermine (SPM) (Fig. 3-1). The selective Boc-protection should be carried out in a way such that both of the secondary and one of the primary amine groups are protected. Due to the symmetry of the molecule, this can be achieved by doing firstly a mono-protection of one of the primary amines with an orthogonal protecting group to the Boc-groups, i.e., the protecting group used should be stable in acidic media and cleavable under basic conditions. In 1998, Blagbrough and Geall[227] described a one-pot procedure using trifluoroacetic acid as the orthogonal protection group (Scheme 3-5). Spermine was dissolved in MeOH and cooled to -78 °C. Ethyl trifluoroacetate was added slowly and the mixture was stirred for 1 h at -78 °C and for 75 minutes at 0 °C. Afterwards the remaining amines were all protected with Boc-groups by adding Boc_2O in excess. Finally, the trifluoroacetyl was removed by adding conc. NH_3(aq) until the pH was higher than 10. The crude product was a very sticky yellow oil (34%). Mass spectra indicated the desired product contaminated with tetra-Boc-spermine as side product. The tetra-Boc-spermine a side product should not react in the coupling reaction with palmitic acid due the lack of free amine groups, and as such the crude product was used in the following coupling reaction without further purification.

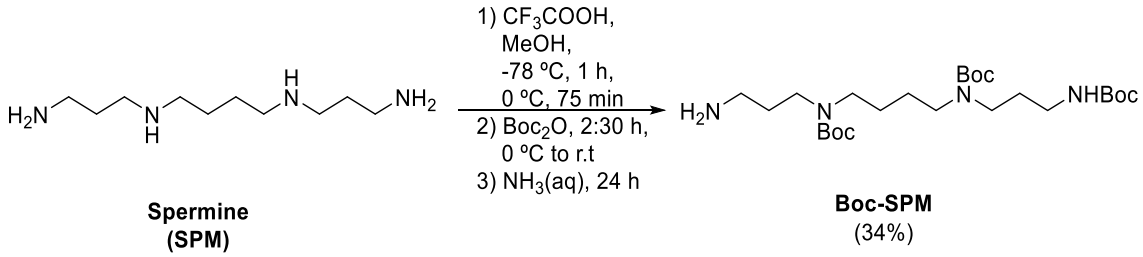

Scheme 3-5 Synthesis of protected spermine (Boc-SPM).

Boc-SPM was coupled with palmitic acid by standard TBTU-mediated coupling and after the solvent was evaporated the product was purified first by silica column chromatography in DCM/MeOH (1:0 to 9:1) then by a second column in Hex/EtOAc 2:1 to give a colourless oil (75%). The final step was deprotection of Boc groups by HCl gas to produce **C_{16}-SPM** in 97% yield as a white solid (Scheme 3-6). The structures were confirmed by ^{1}H and ^{13}C NMR, MS and IR.

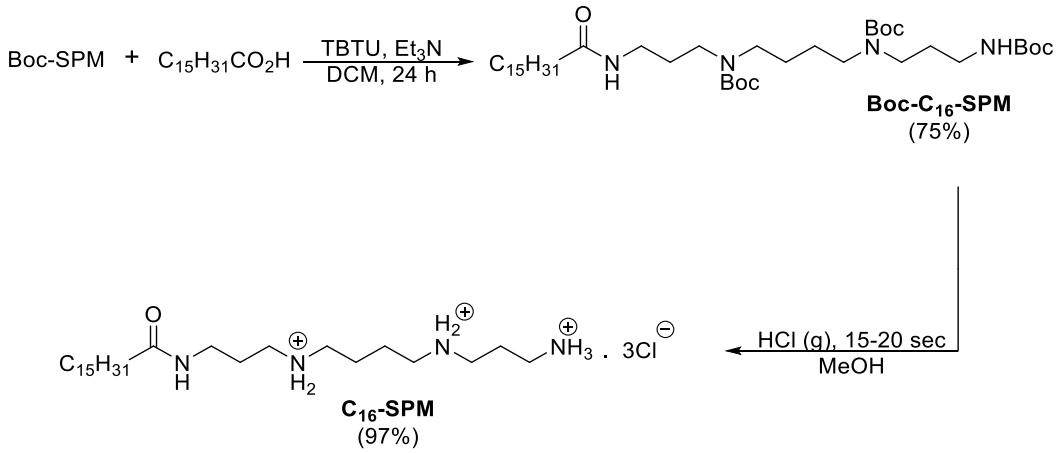

Scheme 3-6 Synthesis of **C_{16}-SPM**.

3.3 Self-Assembly Studies

3.3.1 Nile Red Assay

The Nile Red assay was performed on all four C_{16}-ligands, individually, in order to quantify their self-assembly and determine CAC values (Table 3-1).

Compound	**C_{16}-DAPMA**	**C_{16}-SPD**	**C_{16}-SPM**
CAC (μM)	40.0 ± 1.0	51.0 ± 2.0	65.0 ± 20.0

Table 3-1 CACs values for the synthesized binders from Nile red assay.

The standard assay procedure is usually to dissolve (dilute) the binders with phosphate-buffered saline (PBS) to the required concentrations – however, C_{16}-ligands had solubility difficulties, therefore, they were dissolved (diluted) in Tris HCl (10 mM) in the presence of NaCl (150 mM). It is worth noting that different solubilities in different buffers can results as a consequence of interactions between (e. g.) the cationic self-assembled structures and the anionic phosphate ions present in PBS. Even still, **C_{16}-DAP** (single charged) was largely insoluble in water/buffer – we reasoned that its +1 charge is insufficient to counterbalance the hydrophobicity, and it was not studied further.[217] Compound **C_{16}-DAPMA** (+2) was well-soluble in water/buffer, **C_{16}-SPD** (+2) was slightly less soluble, and **C_{16}-SPM** (+3) was more difficult to dissolve and heating was required to encourage solubility under the assay conditions. We suggest that the +3 charge of **C_{16}-SPM** hinders assembly, and hence solubility, the cation–cation repulsions on the micellar surface are not fully balanced by the hydrophobic driving force for assembly.[228] From the results shown in Table 3-1; **C_{16}-DAPMA** had the lowest CAC (40.0 ± 1.0) and **C_{16}-SPM** the highest. The latter also required heating to encourage solubility – this was in agreement with entropically-driven hydrophobic self-assembly. As $\Delta G = \Delta H - T\Delta S$,

increasing the temperature makes the ΔG value for assembly more favourable, as commonly seen for surfactant assembly.

3.3.2 Dynamic Light Scattering (DLS)

DLS analysis was performed on C_{16}-ligands with the same methods described before. The micelle size for all three binders was around 6 nm and the nanoparticles were all positively charged (Table 3-2). Interestingly the zeta potential was lowest for **C_{16}-SPM** in spite of the fact that the ligand itself can carry a higher charge. This is consistent with a view in which this compound struggles to assemble as a result of charge-charge repulsions at the micellar surface – hence leading to a looser, less well-packed assembly.

Sample in Buffer	Volume distribution (nm)	PdI	Zeta potential (mV)
C_{16}-DAPMA	6.2 ± 1.3	0.21 ± 0.01	+51.5 ± 3.1
C_{16}-SPD	6.6 ± 0.2	0.45 ± 0.09	+44.0 ± 1.7
C_{16}-SPM	6.2 ± 0.1	0.32 ± 0.09	+40.5 ± 0.9

Table 3-2 DLS analysis of C_{16}-ligands.

In addition, DLS analysis was performed in the presence of heparin and also in the presence of DNA. The aim of these measurements was to monitor the binders' behavior in terms of size and charge after binding to heparin or DNA. The results showed that the binders' zeta potential decreased and the particle size has increased after binding to heparin and DNA (Tables 3-3 and 3-4).

Sample in Buffer + Heparin (27 µM)	Volume distribution (nm)	PdI	Zeta potential (mV)
C_{16}-DAPMA	137 ± 4.0	0.87 ± 0.18	+38.1 ± 1.0
C_{16}-SPD	140 ± 50	0.24 ± 0.04	+9.8 ± 1.8
C_{16}-SPM	304 ± 55	0.52 ± 0.13	+21.3 ± 4.2

Table 3-3 DLS analysis for the C_{16}-ligands after binding to heparin showing an increase in the particles' size and a decrease in zeta potential values.

For **C_{16}-DAPMA** zeta potential before binding to heparin (27 µM) was +51.5 mV (Table 3-2), and after binding to heparin it was +38.1 mV (Table 3-3), showing that the binder is somewhat binding to heparin but not completely. In addition, the particle size increased after binding to heparin from 6.2 ± 1.3 nm to 137.0 ± 4.0 nm, indicating electrostatic binding and aggregation on the heparin surface which is supported by TEM images as will be discussed later. Notably, the decrease in zeta potential was much more significant for **C_{16}-SPD** after binding heparin; from +44.0 mV (Table 3-2) to ca. +10 mV (Table 3-3), suggesting that **C_{16}-SPD** is binding better than **C_{16}-DAPMA.** Once again, the size of **C_{16}-SPD** particles increased after binding to heparin to 140.0 nm (Table 3-3).

The third binder (**C_{16}-SPM**) particle size increased very significantly. The excess charge was expected to be less than the other two binders, due to its three positive charges. However, the zeta potential value for this binder was relatively high; before binding to heparin it was around +40.5 mV and after binding it was +21.3 mV. Unexpectedly, for a binder that has three positive charges, which was expected to bind better to heparin – however, probably due to the repulsion between the positive charges within its micelles, the binder was poorly organized and did not bind completely (see further evidence below).

Moreover, DLS analysis for the three binders on binding to DNA once again showed that the size increased (Table 3-4) consistent with aggregation on binding between nanoscale cations and anions. Zeta potential values were negative and we think that these negative charges are associated with the present unbound DNA. After binding to DNA, **C_{16}-DAPMA** and **C_{16}-SPD** zeta potential values were -24.6 mV and -21.1 mV respectively (Table 3-4). This shows that when these two compounds were presented to DNA, there was excess negative charge from DNA. However, the excess negative charge from DNA when it was mixed with **C_{16}-SPM** was significantly less (-11.2 mV). This suggests that it is binding better than the other compounds. These values support the results of Mallard Blue (MalB) and Ethidium Bromide (EthBr) displacement assays (Table 3-5), which we will discuss in more detail later in this chapter.

Sample in Buffer + DNA (4 µM)	Volume distribution (nm)	PdI	Zeta potential (mV)
C_{16}-DAPMA	152.8 ± 42.5	0.2 ± 0.07	-24.6 ± 0.3
C_{16}-SPD	209.8 ± 11.4	0.16 ± 0.01	-21.1 ± 2.1
C_{16}-SPM	192.4 ± 44.8	0.11 ± 0.06	-11.2 ± 0.5

Table 3-4 DLS analysis for the C_{16}-ligands after binding to DNA showing an increase in the particles' size and a major decrease in zeta potential values.

3.3.3 TEM Images

TEM images were recorded using standard methods for all C_{16}-ligands. The images (Fig. 3-2) were in agreement with similar reported studies on related systems[171,221] the micelles remained remarkably intact, and were organised into hierarchical nanoscale arrays. We suggest these is a result of close packing interactions between the spherical micellar polycations and the linear polyanions. As such, we are confident that the micelles do

indeed remain intact on binding, and this supports our suggested methodological approach for computational modelling (described in more detail below) in which the pre-formed micelle is brought into contact with a polyanion chain in order to determine the fundamental binding interactions. These images allow us to rule out a model in which micellar assembly is disrupted on addition of the polyanion, with individual surfactant coating the anionic surface and clearly shows the self-assemblies remain intact.

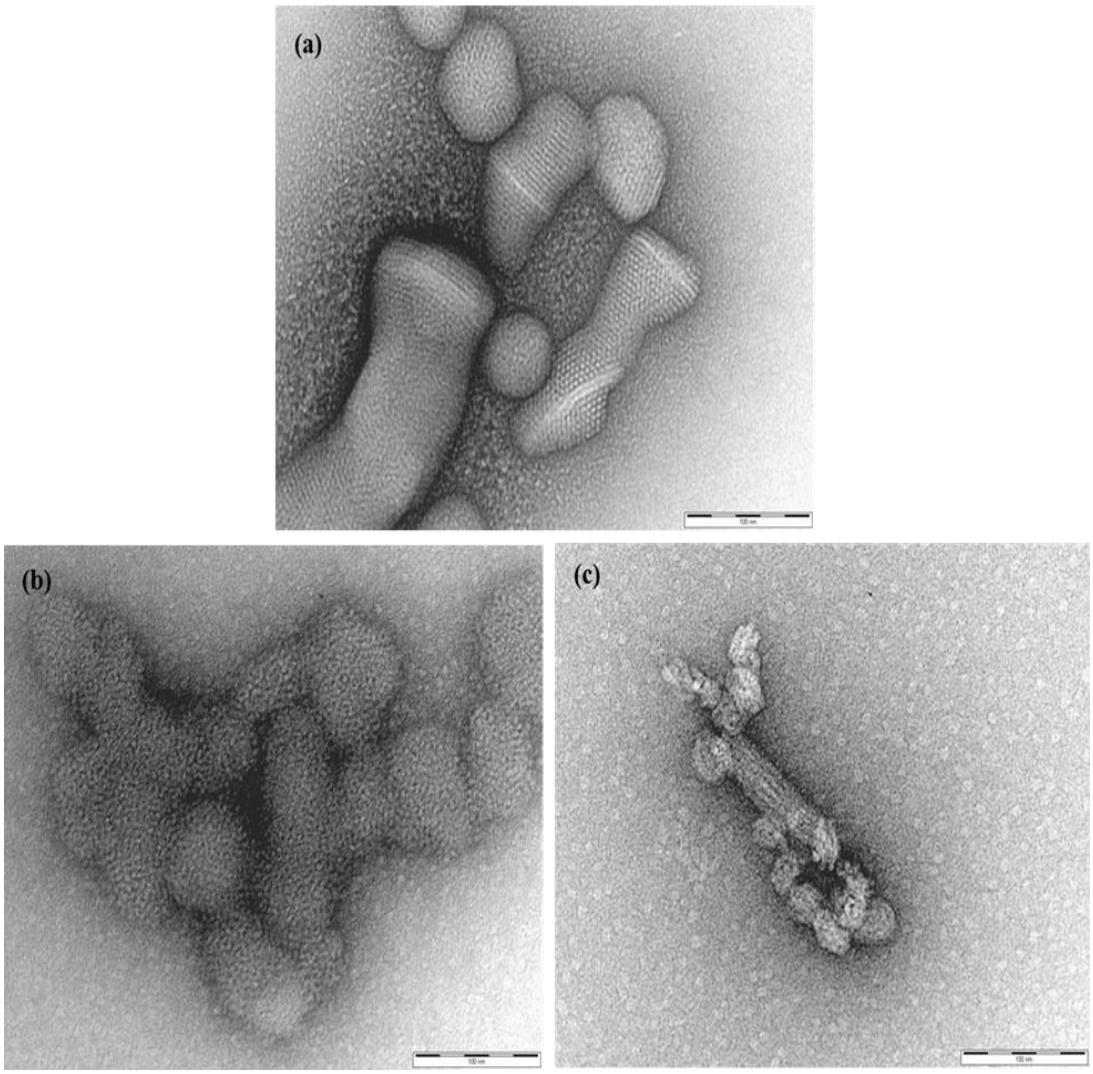

Fig. 3-2 TEM image of self-assembled micellar nanostructures in the presence of heparin showing self-assembled micellar nanostructures binding on its surface yielding a hierarchically organised self-assembled nanoscale aggregate, **(a) C_{16}-DAPMA**, **(b) C_{16}-SPD** and **(c) C_{16}-SPM**. All scale bars are 100 nm.

Although DLS analysis for **C_{16}-SPM** proved that the particles' size after binding to heparin has increased (Table 3-3), TEM images (Fig. 3-2) showed less aggregation of C_{16}-SPM on the surface of heparin than the images of the other two binders (**C_{16}-DAPMA**

and **C_{16}-SPD**) which supports the idea of less binding due to the repulsive forces between the positive charges of the micelles. Certainly, the organization of interactions between self-assembled micelles and heparin appears to be much less effective.

3.4 Binding Data

3.4.1 Polyanions Binding

C_{16}-ligands were then tested for heparin and DNA binding to compare the binding affinity of such systems between different biological polyanions. The results are shown in Figures 3-3, 3-4 and Table 3-5. It was found from Table 3-5 that the more highly charged **C_{16}-SPM** ligand appears to be the best DNA binder with a low CE_{50} value (4.3 ± 0.1). However, **C_{16}-SPD** and **C_{16}-DAPMA** were less effective with CE_{50} values of (6.0 ± 0.3) and (5.0 ± 0.1) respectively. Notably, although **C_{16}-DAPMA** and **C_{16}-SPD** have the same ligand charge (+2), **C_{16}-DAPMA** is a slightly better DNA binder.

Binder	**C_{16}-DAPMA**	**C_{16}-SPD**	**C_{16}-SPM**
CE_{50} with DNA	5.0 ± 0.1	6.0 ± 0.3	4.3 ± 0.1
CE_{50} with Heparin	0.70 ± 0.10	0.34 ± 0.05	0.49 ± 0.01

Table 3-5 CE_{50} values of C_{16}-ligands from Ethidium Bromide (EtBr) and MalB displacement assays.

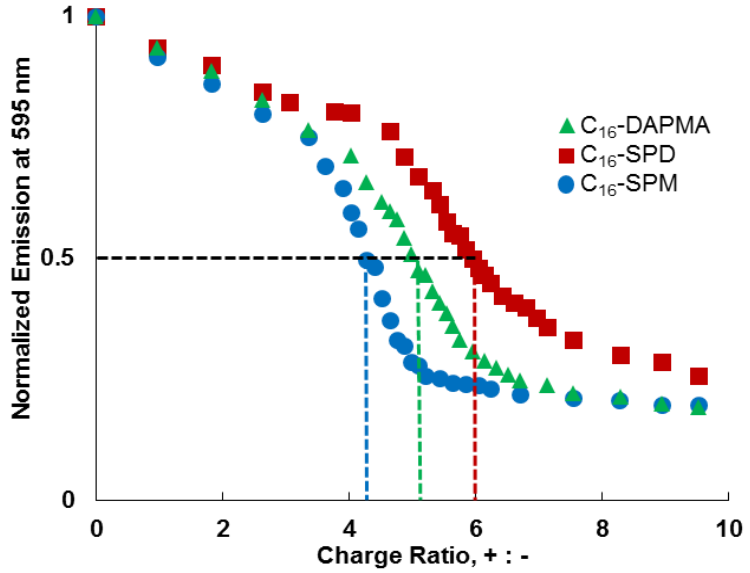

Fig. 3-3 Charge ratio against normalized emission at 595 nm from EthBr assay for all the C_{16}-ligands.

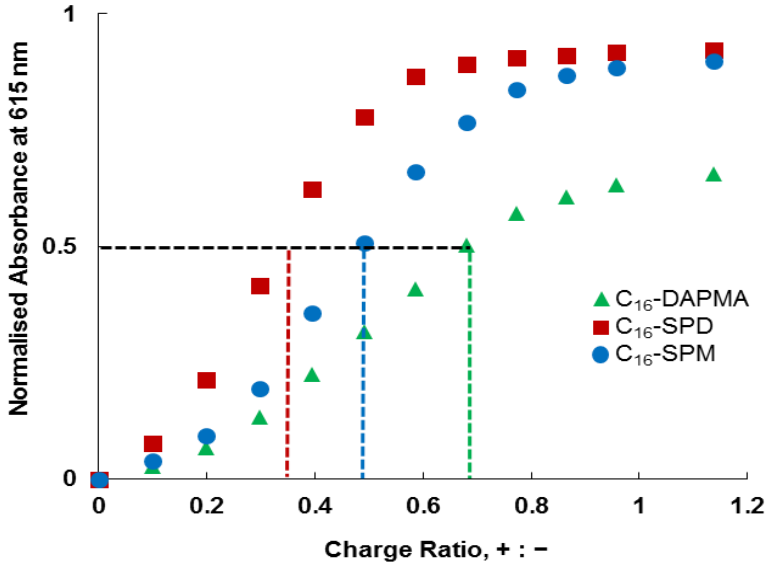

Fig. 3-4 Charge ratio against normalized absorbance at 615 nm of C_{16}-liganda in buffer, showing the effect of ligand variation on binding heparin.

In contrast, although **C_{16}-DAPMA** was the slightly better DNA binder and has the same surface charge as **C_{16}-SPD**, the latter compound, for heparin binding, was by some margin the most charge-efficient binder as measured by its CE_{50} value. In addition to significantly outperforming **C_{16}-DAPMA**, **C_{16}-SPD** also performs better than more highly charged **C_{16}-SPM** in terms of its CE_{50} value. Although these differences are relatively small, they were reproducible and outside of error range – as such, they provide a hint that DNA (Fig. 3-5) and heparin (Fig. 3-6) behave differently in these assays when faced with these SAMul nanostructures as binders.

All of the reported EC_{50} values (Table 3-5) were below the CAC values of these compounds (Table 3-1). It is well-known that polyanions can assist self-assembly by limiting electrostatic repulsion on the cationic SAMul surface.[229,230] As such, the competition assay suggests different polyanion preferences dependent on ligand choice. In order to ensure this was not an artefact of our choice of assays, we wanted to collect data using a different, non-competition assay method.

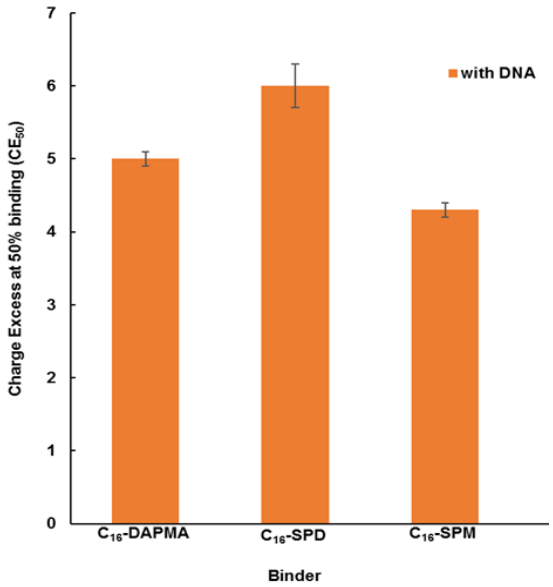

Fig. 3-5 CE_{50} values showing binding selectivity of C_{16}-ligands between different biological polyanions; when binding to DNA: **C_{16}-SPM** > **C_{16}-DAPMA** > **C_{16}-SPD.**

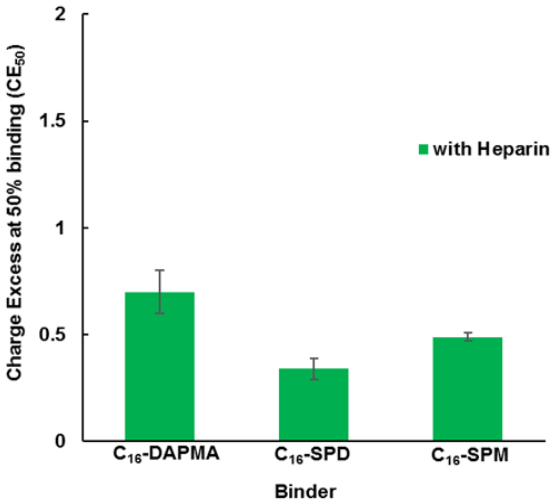

Fig. 3-6 CE_{50} values showing binding selectivity of C_{16}-ligands between different biological polyanions; when binding to heparin: **C_{16}-SPD** > **C_{16}-SPM** > **C_{16}-DAPMA**.

3.4.2 Isothermal Titration Calorimetry

Isothermal Titration Calorimetry (ITC) experiments were conducted using a Nano ITC Technology (TA Instruments, New Castle, DE, USA). ITC is a technique used in quantitative studies of a wide variety of biomolecular interactions.[231,232] It works by directly measuring the heat that is either released or absorbed during a biomolecular binding event. It is the only technique that uses a single experiment to simulate and determine all binding parameters.[233,234] These experiments were performed by our collaborators, Sabrina Pricl and co-workers, in the Molecular Simulation Engineering (MOSE) Laboratory, Department of Engineering and Architectures (DEA), University of Trieste. We have summarized here the key findings.

The thermodynamics of micellization of all SAMul molecules was investigated in Tris HCl/150 mM NaCl buffered solutions using a dilution methodology. The results showed that CACs (Table 3-6) were in very good agreement with those from the Nile Red assay (Table 3-1). In addition, treatment of the ITC data also provided thermodynamic parameters for self-assembly (ΔH_{mic}, $T\Delta S_{mic}$ and ΔG_{mic}) which supported the proposal that **C_{16}-SPM** had the least favourable self-assembly, primarily as a result of the enthalpic term which reflects electronic repulsions between the more highly charged cationic surfaces.

Compound	**C_{16}-DAPMA**	**C_{16}-SPD**	**C_{16}-SPM**
CAC (μM)	34	52	71
ΔH_{mic}/kJ mol^{-1}	-10.81	-8.61	-8.41
$T\Delta S_{mic}$/kJ mol^{-1}	14.72	15.86	15.29
ΔG_{mic}/kJ mol^{-1}	-25.52	-24.47	-23.70

Table 3-6 ITC-derived thermodynamic data of micellisation (CAC) at 298 K. $\Delta G_{mic} = \Delta H_{mic} - T\Delta S_{mic}$, where ΔG_{mic}, ΔH_{mic}, and $T\Delta S_{mic}$ are the free energy, enthalpy and entropy of micellisation, respectively.[217]

Furthermore, they went on to compare the thermodynamics of aggregation of those systems in the presence and absence of polyanion (Table 3-7).[217] The aim of this step was to estimate the difference, which represents the effective binding between the SAMul nanostructures and the polyanion (i.e., $\Delta H_{bind} = \Delta H_{agg} - \Delta H_{mic}$). This simple approach allows extraction and quantification of the effective change in solution thermodynamics induced by the polyanion. Pleasingly, ITC data were in good agreement with the trends recorded from the dye displacement assays; those results were in terms of relative binding affinity.[217] Specifically, for heparin ΔG_{bind} was most favourable with **C_{16}-SPD** while for DNA ΔG_{bind} was most favourable with **C_{16}-SPM**.

Parameter	**Polyanion**	**C_{16}-DAPMA (+2)**	**C_{16}-SPD (+2)**	**C_{16}-SPM (+3)**
CAC (with polyanion)/μM	DNA	6.1	9.8	3.4
	Heparin	13.6	7.2	9.8
ΔH_{agg}/kJ mol^{-1}	DNA	-12.2	-12.5	-15.0
	Heparin	-12.8	-13.5	-11.0
$T\Delta S_{agg}$/kJ mol^{-1}	DNA	17.6	16.2	16.0
	Heparin	15.0	15.9	17.6
ΔG_{agg}/kJ mol^{-1}	DNA	-29.8	-28.7	-31.0
	Heparin	-27.8	-29.4	-28.6
ΔH_{bind}/kJ mol^{-1}	DNA	-1.4	-3.9	-6.6
	Heparin	-1.9	-4.9	-2.6
$T\Delta S_{bind}$/kJ mol^{-1}	DNA	2.9	0.4	0.7
	Heparin	0.3	0.0	2.3
ΔG_{bind}/kJ mol^{-1}	DNA	-4.3	-4.2	-7.3
	Heparin	-2.2	-4.9	-4.9

Table 3-7 Thermodynamic parameters of aggregation (ΔG_{agg}, $T\Delta S_{agg}$ and ΔG_{agg}) and critical aggregation concentrations (CACs) in the presence of polyanion as obtained from ITC measurements at 298 K in a 30 μM solution of DNA or heparin at 150 mM NaCl. Binding parameters ΔH_{bind}, $T\Delta S_{bind}$, and ΔG_{bind} are defined as the difference between parameters for aggregation in the presence and absence of polyanion, respectively (e.g., $\Delta H_{bind} - \Delta H_{agg} - \Delta H_{mic}$).[217]

3.4.3 Multiscale Modelling of Self-Assembly Process

To further understand self-assembly in 150 mM aqueous NaCl, Sabrina Pricl and co-workers at the Molecular Simulation Engineering (MOSE) Laboratory, Department of Engineering and Architectures (DEA), University of Trieste performed multiscale modelling of the self-assembly and polyanion binding process. They employed a well-validated multiscale molecular modelling procedure[102,199,235-237] based on a mesoscopic model. Using the information obtained from atomistic molecular dynamics simulation (MD), they parameterized the dissipative particle dynamics (DPD)[238,239] models that incorporate all essential physics/phenomena observed at the finer level. In outline: i) explicit solvent atomistic MD calculations[240,241] were performed on **C_{16}-DAPMA**, **C_{16}-SPD**, and **C_{16}-SPM** and their assembly; ii) using the information from (i) coarse-grained DPD simulations were carried out at concentrations higher than the experimental CAC and the aggregates were characterized in terms of dimension and aggregation number; iii) the equilibrium configurations of the self-assembled systems obtained using (ii) were mapped back to the corresponding atomistic MD models, and then new atomistic MD simulations conducted to calculate binding energies between the micelle and polyanions. All atomistic simulations and data analysis were performed with the AMBER 14 suite of programs.[242]

In all cases, spherical micelles were obtained (Fig. 3-7 and 3-8). Interestingly, simulation indicated that the compounds formed micelles with different packing densities. The aggregation number (N_{agg}, Table 3-8) suggests that **C_{16}-DAPMA** forms more tightly packed micelles than **C_{16}-SPD**, which in turn is more densely packed than **C_{16}-SPM**. As suggested from experimental results discussed above, the hydrophobic C_{16} chain does indeed have difficulties in bringing together the more highly charged SPM ligands. As a result of the decrease in N_{agg} for **C_{16}-SPM**, the electrostatic potential (ψ_s) also decreases

(Table 3-8), leading to simulated zeta potentials (ζ) in good agreement with the DLS data (Table 3-2), with **C_{16}-DAPMA** > **C_{16}-SPD** > **C_{16}-SPM**.

Compound	N_{agg}	ψ_s (mV)	ζ (mV)
C_{16}-DAPMA	16 ± 2	172.4	50.2
C_{16}-SPD	13 ± 1	153.3	45.1
C_{16}-SPM	10 ± 1	144.6	41.8

Table 3-8 Main characteristics of the spherical SAMul micelles as obtained from multiscale molecular simulations. N_{agg} = aggregation number and ψ_s = surface electrostatic potential.[217]

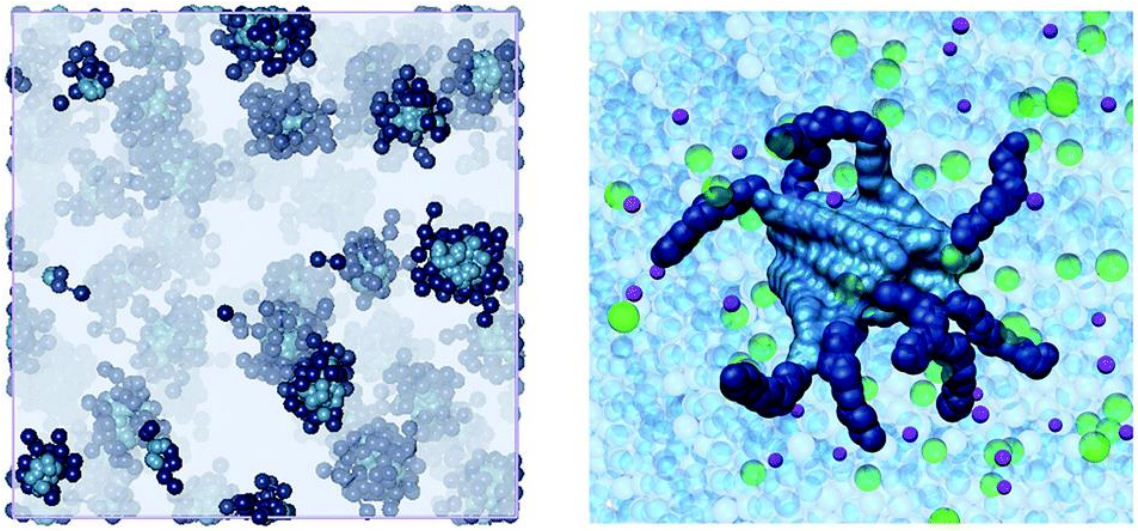

Fig. 3-7 Mesoscopic (left) and atomistic (right) simulations of **C_{16}-SPM** self-assembling into micelles. The C_{16} hydrophobic portion is shown as steel blue spheres whereas the SPM residues are portrayed as navy blue spheres. In the left panel, water, ions and counter-ions are shown as light grey field; in the right panel, water molecules are depicted as transparent light blue spheres, some Na^+ and Cl^- ions are shown as purple and green spheres, respectively.[217]

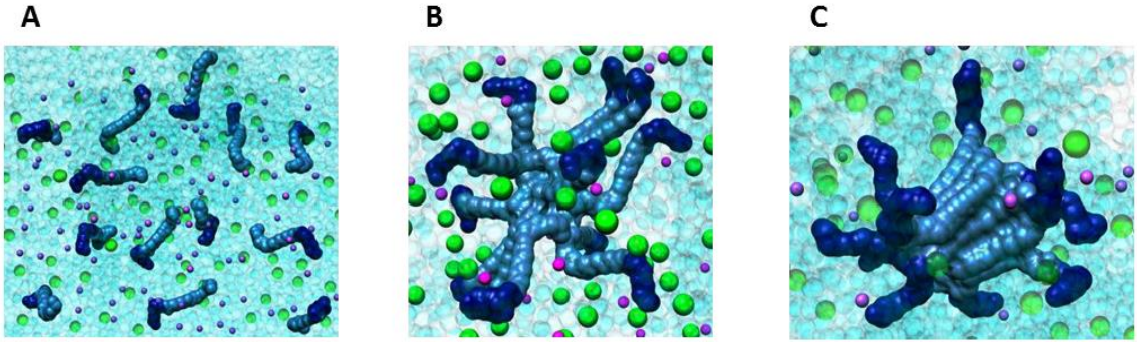

Fig. 3-8 Atomistic simulations of **C_{16}-SPM** self-assembly process into spherical micelles. The panel represent the MD snapshots of the starting point (**A**, 0 ns), an intermediate state (**B**, 10 ns) and the final stage (**C**, 100 ns) of the assembly. The C_{16}- hydrophobic portion is shown as steel blue spheres whereas the SPM residues are portrayed as navy blue spheres. Water molecules are depicted as transparent light blue spheres whereas some Na^+ and Cl^- ions are shown as purple and green spheres, respectively.[217]

As indicated by TEM imaging (Fig. 3-2), the micelles remained significantly intact on polyanion binding. Therefore, a modelling approach which contacts a single micelle with a single polyanion is a valid methodology for obtaining an insight into the fundamental forces responsible for the primary binding event. Clearly, further understanding of the hierarchical assembly and aggregation event is more complex, and was beyond the aim of this study, which was specifically focussed on the differences produced by different ligands at the initial polyanion binding interface.

For DNA binding (Fig. 3-9, top), the **C_{16}-SPM** micelles contain 10 SPM residues, 9 of which effectively contact DNA (a parameter they define as N_{eff}), resulting in a charge-normalized binding free energy (per-effective residue) ΔG^* of -14.32 kJ mol^{-1}. However, **C_{16}-SPD** and **C_{16}-DAPMA** nanostructures only used 7 and 8 (out of 13 and 16) SPM residues, respectively, to bind DNA. For **C_{16}-SPD** and **C_{16}-DAPMA**, the per-effective-residue interactions were lower, with ΔG^* values of -9.76 and -10.80 kJ mol^{-1}, respectively. The simulated ΔG^* values (Fig. 3-6) therefore follow the same trend as the experimental CE_{50} values and ITC data: **C_{16}-SPM** > **C_{16}-DAPMA** > **C_{16}-SPD**.

For heparin binding (Fig. 3-9, bottom), the micelles formed by **C_{16}-SPD** engage 12 out of 13 available ligands in productive binding, resulting in charge normalized ΔG^* of -14.98 kJ mol^{-1}. However, **C_{16}-DAPMA** and **C_{16}-SPM** assemblies only exploit 9/16 and 6/10 ligands, giving ΔG^* values of -8.65 and -11.97 kJ mol^{-1}, respectively. The predicted ΔG^* (Fig. 3-9) values are thus in agreement with the trend of experimental data: **C_{16}-SPD** > **C_{16}-SPM** > **C_{16}-DAPMA**. To understand why polyanions appear to have different selectivities towards SAMul nanostructures, they then broke apart these overall ΔG^* values into enthalpic (ΔH^*) and entropic ($-T\Delta S^*$) components (Fig. 3-10). **C_{16}-SPM** emerges as the optimal DNA binder on enthalpic grounds (Fig. 3-10A), whereas **C_{16}-SPD** emerges as the optimal system for heparin binding, in agreement with ITC (ΔG_{bind}, Fig.

3-10C). This indicated that for DNA, each anionic charge behaves exactly the same as a result of the rigid repetitive nature of the polymer (Fig. 3-10B). However, for heparin this is not the case, and the more flexible, 'adaptive' structure adapts to optimize each individual interaction (Fig. 3-10D).

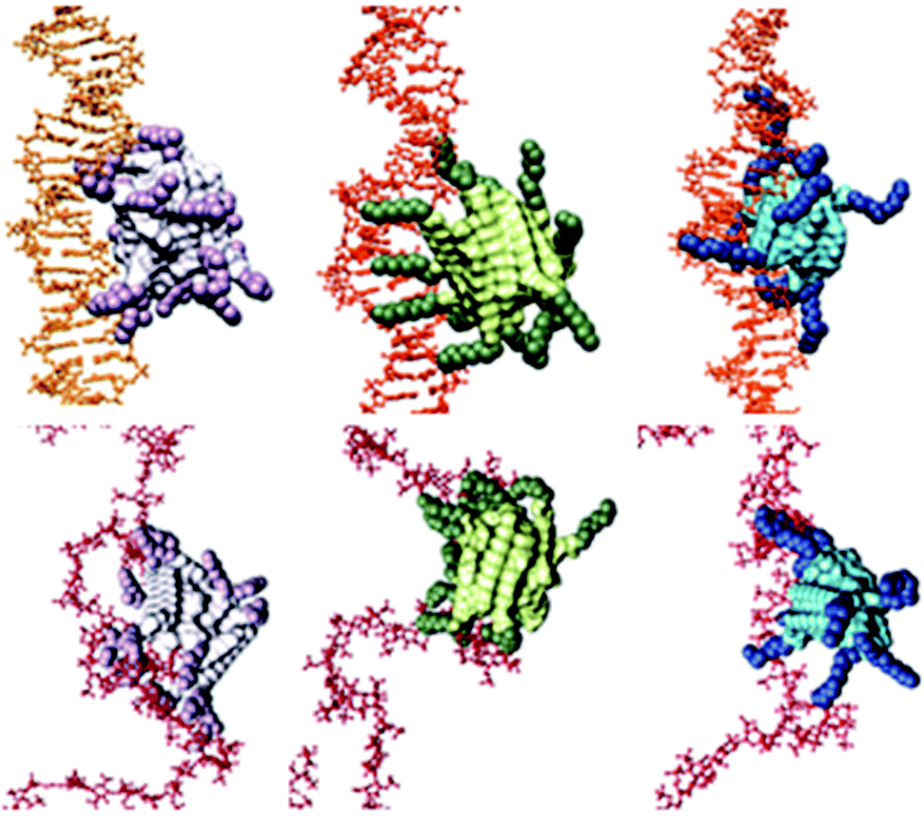

Fig. 3-9 Equilibrated atomistic molecular dynamics (MD) simulation snapshots of SAMul micelles binding DNA (upper panel, orange) and heparin (lower panel, firebrick). In both panels, from left to right: **C_{16}-DAPMA** (light grey (C_{16}) and plum (DAPMA)), **C_{16}-SPD** (lime green (C_{16}) and forest green (SPD)), and **C_{16}-SPM** (steel blue (C_{16}) and navy blue (SPM)). Hydrogen atoms, water molecules, ions and counter-ions are not shown for clarity.[217]

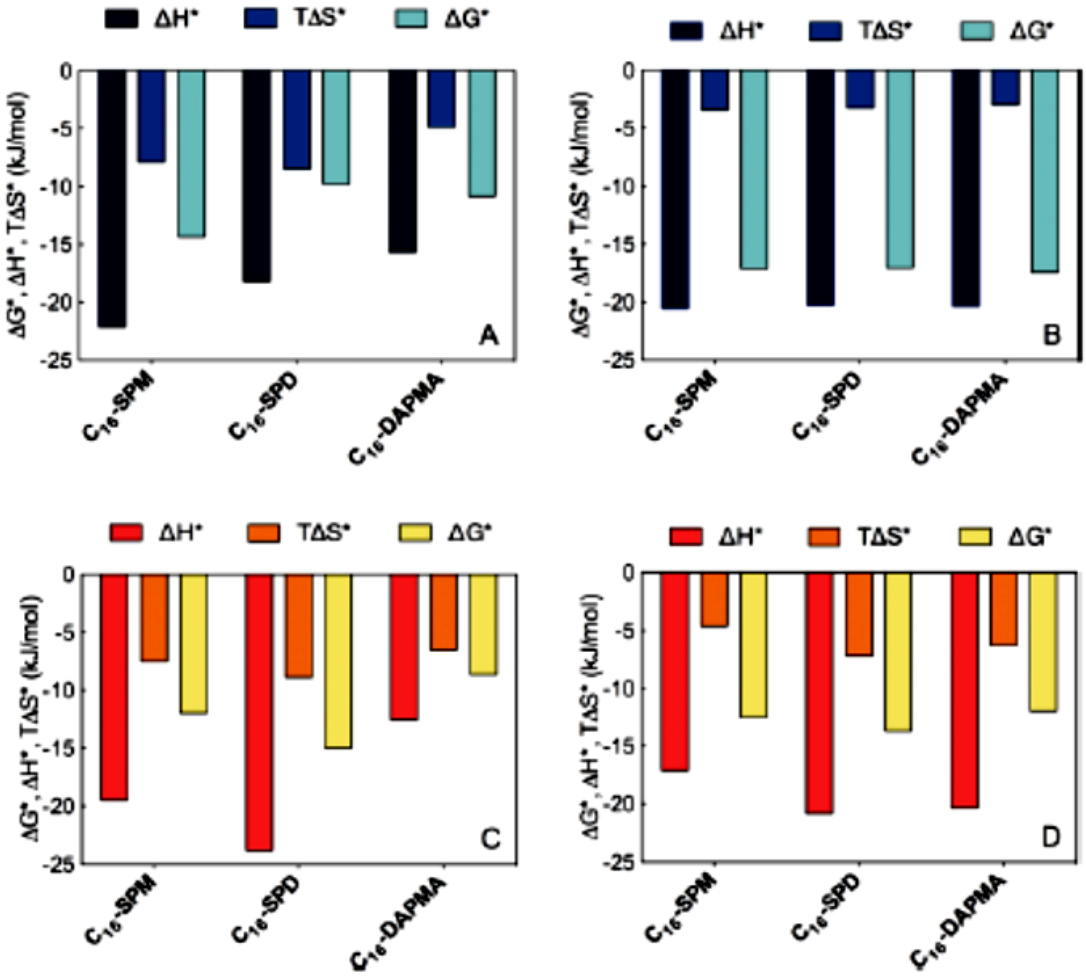

Fig. 3-10 Charge-normalized per-residue effective free energy of binding (Δ*G**), and enthalpic (Δ*H**) and entropic (*T*Δ*S**) components for: **(A)** each SAMul micelle ligand-type complexed with DNA; **(B)** DNA bases complexed with each of the SAMul micelles; **(C)** each SAMul micelle ligand-type complexed with heparin; **(D)** heparin sugars complexed with each of the SAMul micelles.[217]

3.5 Conclusions and Future Work

This chapter reports the results of a highly collaborative project. We demonstrated that the ligand choice in SAMul nanostructures can have an effect in terms of binding selectivity. We found that electrostatic ion–ion binding depends on structural detail, not only charge density – as confirmed by the complementary experimental methods of competition binding assays and isothermal calorimetry. The results showed that, for the compounds studied here, **C_{16}-SPM** is optimal for DNA binding, while **C_{16}-SPD** is optimal for heparin binding. We observed that the polyanions (heparin/DNA) play a role in facilitating self-assembly and hence switching on the multivalent binding, and suggest that specifics of ligand-polyanion interactions help mediate subtle differences in this overall process. In addition, molecular simulation studies lead us to propose that the shape-persistence (DNA), or adaptability (heparin) of the polyanionic targets help mediate the selectivity of interaction with different ligands. These results provide an intriguing insight into molecular recognition processes at nanoscale surfaces and suggest that SAMul nanostructures may deliver some selectivity in addressing the challenging problem of the 'polyanion world'.

For future work, the hydrophobic part of the SAMul systems could be changed to investigate its effect on the performance of the ligands. In addition, different ligands could be used to explore more binding abilities which the different structures might induce.

4 Alternative Approaches to Stabilizing Displays of Heparin-Binding Ligands

4.1 Introduction

So far, all of the synthesized systems (binders) were linear and surfactant-like in nature, consisting of an amine (ligand) polar head group as the positively binding site and a fatty acid as the hydrophobic chain providing the driving force for assembly (in aqueous solution). We noted that in all cases, self-assembly was disrupted in highly competitive serum-containing conditions. In this stage of the work we therefore decided to investigate other options of scaffolds for displaying these ligands. Three different approaches were employed to broaden our understanding of the effects of such modifications on ligand display and heparin binding on the surface of different nanostructures.

The first target compound (**Binder-Dend**) was a branched system containing multiple ligands, but which still had hydrophobic modification and hence the potential to self-assemble. This was selected to compare the effect of head group size and charge density on self-assembly and heparin binding affinity. This system was designed with a branched dendron scaffold[243] displaying three ligands, with a total of 6 positive charges on the periphery. In addition, because the head group was larger than in previous chapters, the hydrophobic tail in this compound was chosen to be longer and saturated (saturated-C_{22}) to encourage self-assembly.

For the second compound (**Binder-NC**) we decided to use gold nanoparticles to stabilize the nanostructured self-assembled system. Gold Nanoparticles (AuNPs) have attracted the attention of researchers due to their unique properties and multi-applications.[69,70] AuNPs are widely used as biomarkers and bio-delivery vehicles in medicine and pharmacy.[71,72] The unique optical properties of AuNPs, their size dependent behaviour and their high chemical stability have made them ideal systems for exploring many

aspects including self-assembly, bio-labelling, catalysis, etc. These nanoparticles when stabilized or protected by a shell of thiolate ligands,[70] display good stability toward aggregation and other modes of decay.[73] Clearly they are well placed to display multiple ligands on their surfaces and can exhibit high stabilities in challenging conditions. Therefore, we decided to display our heparin-binding ligands on AuNP surfaces.

The third compound (**Binder-Poly**) was designed using a polymer as a hydrophobic support able to display multiple heparin-binding ligands on its stable covalent backbone. Researchers in nanomedicine face limitations such as toxicity, instability and lack of disease site selectivity.[244,245] However, in recent years they have often overcome these limitations by attaching drug molecules to biocompatible polymers. Such a combination of nanotechnology and polymer chemistry has been widely employed in the development of cancer therapeutics.[246-248] Indeed, polymers therapeutics are increasingly entering into clinical use and can have wide-ranging potential use. Polymers are usually retained in the bloodstream because of the enhanced permeability and retention (EPR) effect.[249] As such they have appropriate properties for potential application as heparin rescue agents. Therefore, **Binder-Poly** used a polymer scaffold primarily to study the differences between self-assembled systems and polymers in terms of heparin-binding ability.

4.2 C_{22}-Branched SAMul Nanostructure (Binder-Dend)

We constructed this scaffold by initially synthesizing compound **2** (Scheme 4-1) using methods originally developed by Newkome and co-workers[109,250] and refined by Cardona and Gawley.[251] This scaffold was made by dissolving tris(hydroxymethyl)aminoethane in DMSO with KOH, then adding *tert*-butyl acrylate drop-wise. The reaction duration was 24 h and the compound needed purification by column chromatography (SiO_2, 2:1 v/v, EtOAc/Hexane, 0.05% v/v NH_4OH) and was obtained in excellent 80% yield. The

reaction is a Michael addition of each of the three deprotonated alcohols into one equivalents of the conjugated alkene.

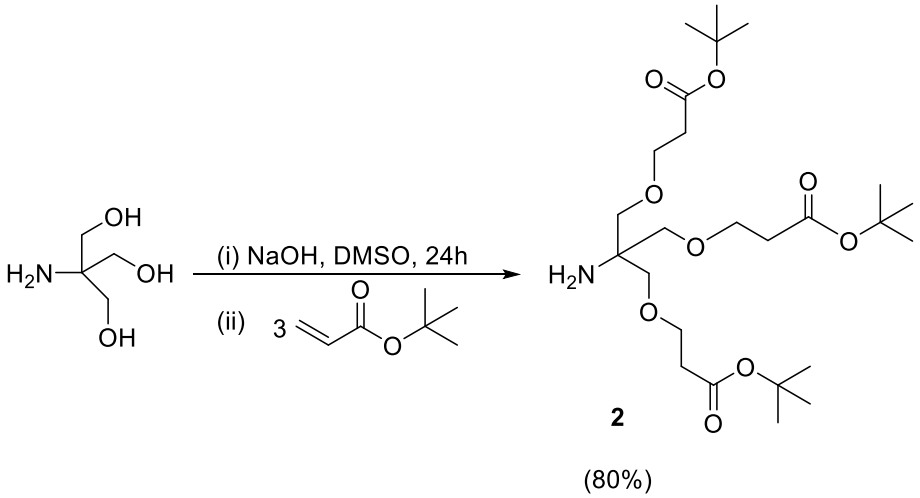

Scheme 4-1 Synthesis of H_2/Newkome-G1/O-*tert*-Butyl Branching (**2**).

The next step consisted of protection of the amine group at the focal point using benzyl chloroformate to give compound **3** (Scheme 4-2). This step took 48 h and the crude product was purified by silica column chromatography to give pure product in a 83% yield. ^{1}H NMR clearly demonstrated the presence of the benzene ring with integration in the correct ratio.

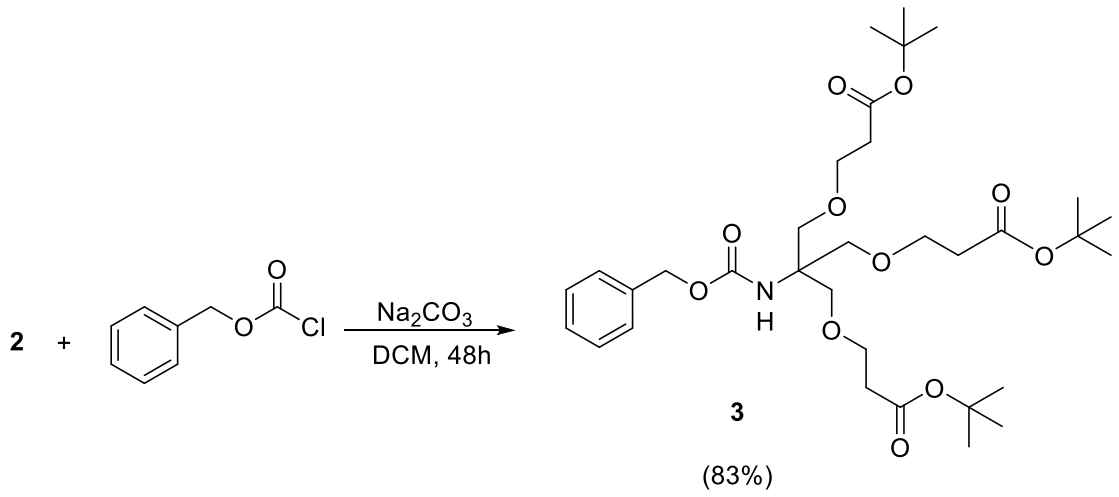

Scheme 4-2 The protection of the amine group by benzyl chloroformate (**3**).

The following step was deprotection of the *tert*-butyl ester-groups[243] from the surface of compound **3** to produce acid-functionalized compound **4** (Scheme 4-3). *tert*-Butyl ester-deprotection was achieved by using formic acid as both reagent and solvent. No further purification was needed for this compound; completion of the reaction was evidenced by the loss of the NMR peak associated with the *tert*-butyl group at 1.4 ppm.

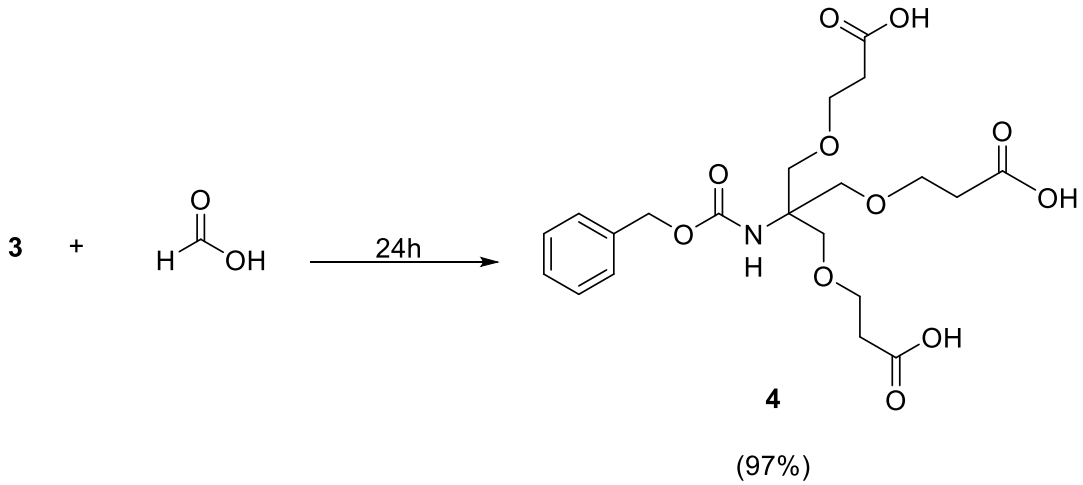

Scheme 4-3 Deprotection of compound **3** Boc-groups to produce compound **4**.

Once compound **3** had been deprotected to produce compound **4**, a coupling reaction between compound **1** (Chapter 2) and compound **4** was made using DCC as the coupling agent. This allowed us to attach the Boc-protected amine ligand to the surface of the dendron. The reaction lasted 3 days (Scheme 4-4). The product was separated using gel permeation chromatography (GPC) column (Bio-beads SX-1, 100% DCM). The yield was 50% and mass spectrometry confirmed the presence of the molecular ion and successful three-fold coupling.

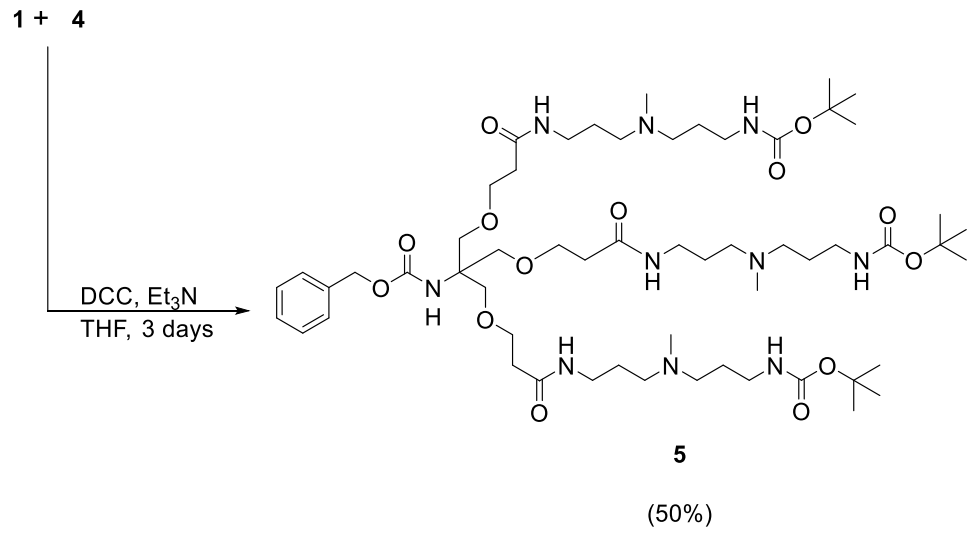

Scheme 4-4 Coupling reaction between compound **1** and compound **4** to give compound **5**.

We next deprotected the Z group (Benzyloxy or benzyl ester) to give compound **6** with an amine group at the focal point in order to allow coupling with the hydrophobic fatty acid in a future step. This was achieved using palladium on carbon (Pd/C, 10%) as the deprotecting agent. This reaction was performed under H_2 for almost four days and was monitored by TLC (Scheme 4-5). The success of the deprotection was determined by the loss of the aromatic signal at 7.26 ppm. The relatively slow nature of this reaction is accounted for by the steric hindrance associated with the location of this benzyloxy carbonyl group at the focal point of a dendritic structure, limiting access to the heterogeneous catalyst surface.

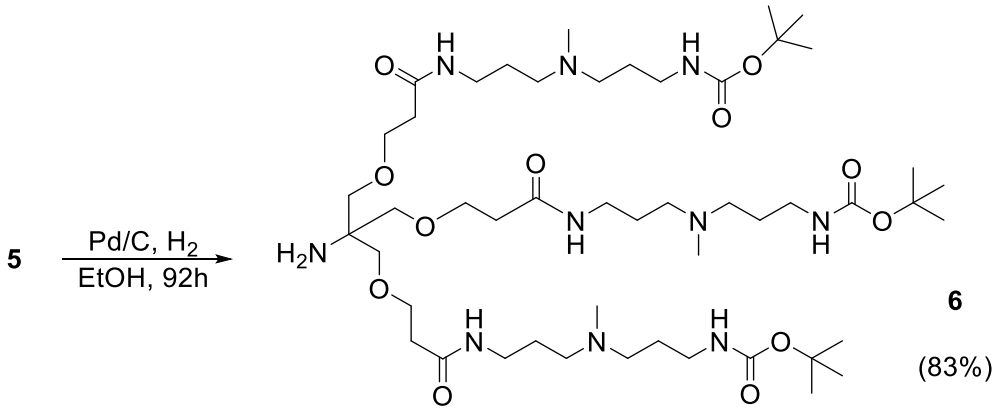

Scheme 4-5 Deprotection of compound 5 Z group to yield compound **6**.

The free amine group at the focal point of the dendron was then coupled with a saturated fatty acid selected to have longer hydrocarbon chain than C_{18}. The saturated fatty acid, docosanoic acid, also known as behenic acid, which consists of C_{22}, was reacted with compound **6** to produce a product (compound **7**) with a yield of 65% (Scheme 4-6). The reaction was performed using TBTU-mediated peptide coupling methods and the product was purified by gel permeation chromatography (GPC) column (Bio-beads SX-1, 100% DCM). The success of the reaction was demonstrated by mass spectrometric molecular ion at HRMS: Calc. $[M+2H]^{2+}$ ($C_{49}H_{100}N_{10}O_{12}$) m/z = 510.3756 Found $[M+2H]^{2+}$ = 510.3760.

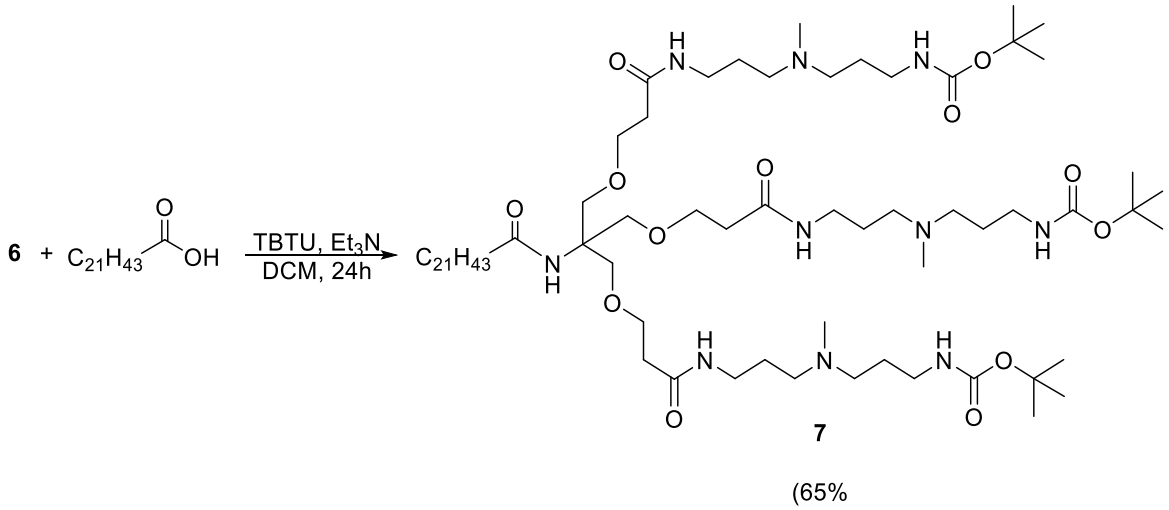

Scheme 4-6 TBTU coupling reaction between behenic acid and compound **6** to produce compound **7**.

The target compound was finally achieved by deprotection of the Boc groups from the three surface ligands. To achieve this, HCl gas was applied for 15-20 seconds to compound **7** and then left to stir for 3 hours (Scheme 4-7). The removal of the Boc group was demonstrated by the loss of CH_3 protons at 1.4 ppm in the ^{1}H NMR. The final product was named **Binder-Dend** and has six positive charges on it three amine ligands. The identity of the product was demonstrated using all key analytical techniques including mass spectrometry (MS); HRMS: Calc. $[M+H]^{3+}$ ($C_{56}H_{119}N_{10}O_7$) m/z = 347.9749 x 3

Found $[M+H]^{3+}$ = 347.9797 x 3 and Calc. $[M+H]^{2+}$ ($C_{56}H_{118}N_{10}O_7$) m/z = 521.4587 x 2

Found $[M+H]^{2+}$ = 521.4598 x 2.

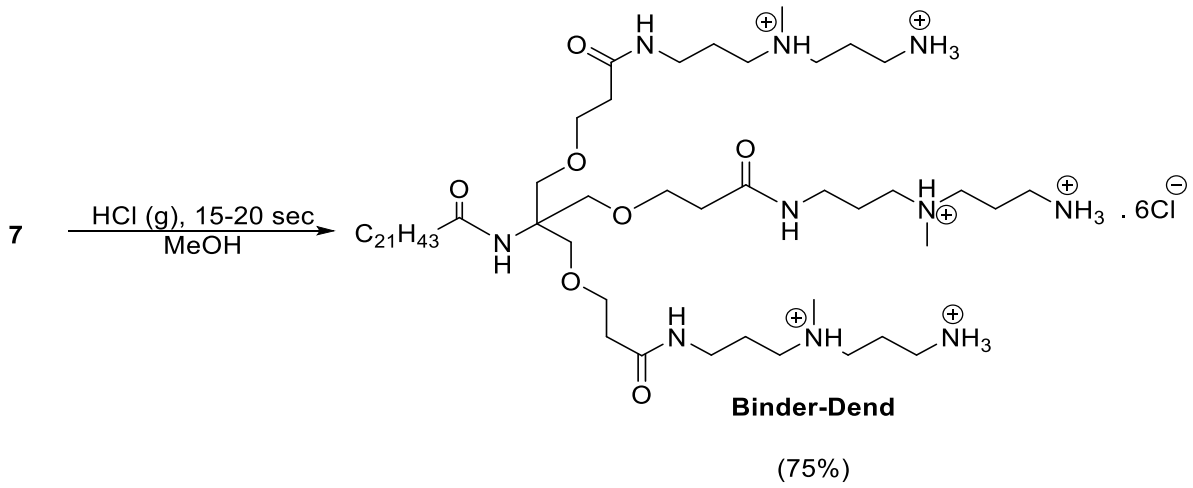

Scheme 4-7 Deprotection of compound **7** Boc groups with HCl gas to produce **Binder-Dend**.

4.2.1 Self-Assembly Studies

4.2.1.1 Nile Red Assay

A Nile Red assay was performed to obtain the CAC of **Binder-Dend** in the same way as described in previous chapters. The CAC for this compound was found to be 117 µM (± 5) (Fig. 4-2). This value shows that self-assembly for such a compound was achieved only at higher concentration than the previously reported compounds. The three amine branches in this compound, holding a total of six positive surface charges, clearly lead to repulsive forces. These charge-chare repulsion forces make it hard for the hydrophobicity of the C_{22} to overcome them and hence for the compound to self-assemble at lower concentrations. However, the self-assembly does occur making this compound a potential nanoscale heparin binder.

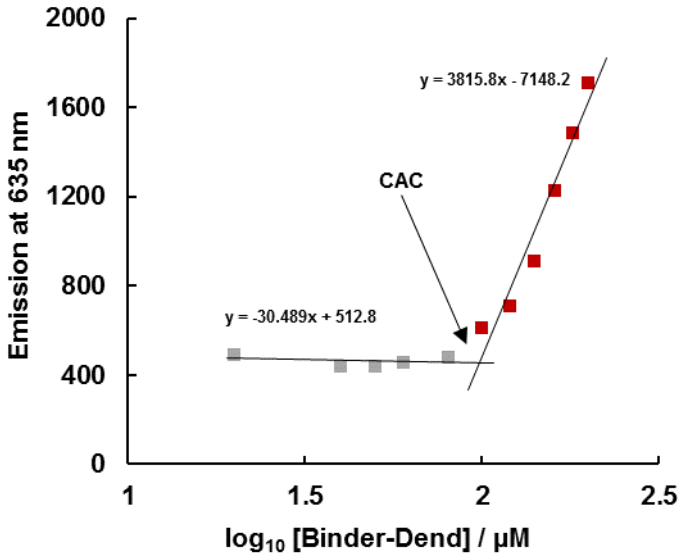

Fig. 4-1 Critical aggregation concentration (CAC) for the branched system (**Binder-Dend**) showing the effect of the density of positive charges on self-assembly.

4.2.1.2 Dynamic Light Scattering (DLS)

DLS analysis of **Binder-Dend** was performed using the same conditions described in previous chapter for other binders. However, **Binder-Dend** assemblies were clearly much larger than the micelles formed by the previous binders. The diameter from the volume distribution was found to be around 138 ± 3 nm (Table 4-1 and Fig. 4-2). Using the intensity distribution gave a diameter of 162 ± 4 nm. This size enhancement is thought to be due to the three amine branches that hold the six positive charges, which give rise to the zeta potential value of 34.1 ± 3.6 mV (Table 4-1). We suggest that the larger repulsive forces between these positive charges led to separation distances in the outer shell of the assemblies. As such the single C_{22} chain in unable to coordinate assembly of the system into a well-defined micelle and instead much larger, less well-defined assemblies – very much larger than the molecular-scale dimensions – are being formed.

Compound	Intensity distribution (nm)	Volume distribution (nm)	PdI	Zeta potential (mV)
Binder-Dend	162 ± 4	138 ± 3	0.20 ± 0.02	34.1 ± 3.6

Table 4-1 DLS analysis of **Binder-Dend** in NaCl (150 mM) / Tris HCl (10 mM).

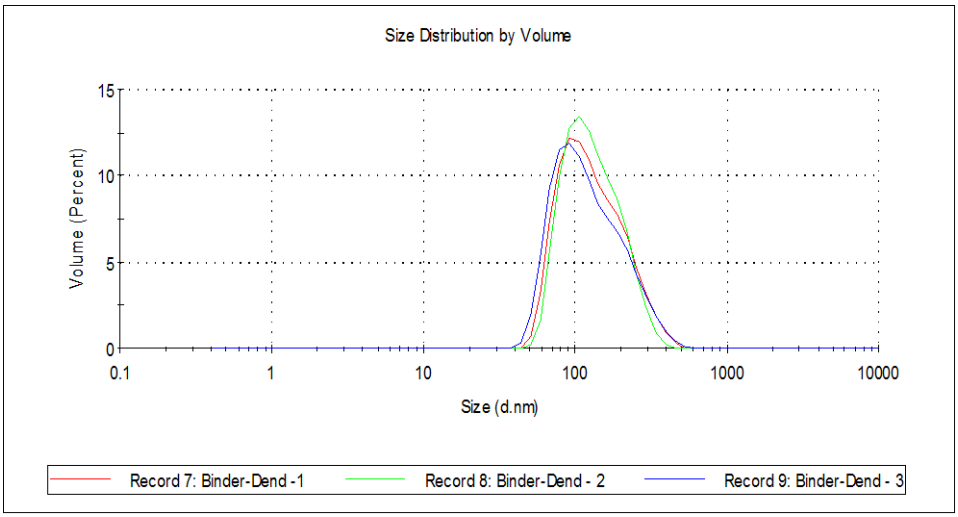

Fig. 4-2 Size distribution by volume from DLS analysis, showing the average size of **Binder-Dend** around 138 ± 3 nm.

4.2.1.3 TEM Images

TEM images of **Binder-Dend** were recorded as described in previous chapter. In the presence of heparin, **Binder-Dend** (Fig. 4-3) showed clear micellar aggregation on the surface of heparin. However, the morphology of these aggregates was less-defined than other compounds reported in previous chapters. These micelles are much smaller than would be suggested by the DLS data in Table 4-1 (≤ 10 nm).

We suggest that the presence of polyanionic heparin helps these compounds to assemble into well-defined micelles because it helps neutralize the cationic surface charge of

Binder-Dend such that the C_{22} hydrophobic chain becomes capable of holding them in close proximity. Indeed, the ability of polyanions to assist the assembly of cationic micelles is a well-known phenomenon.[229,230]

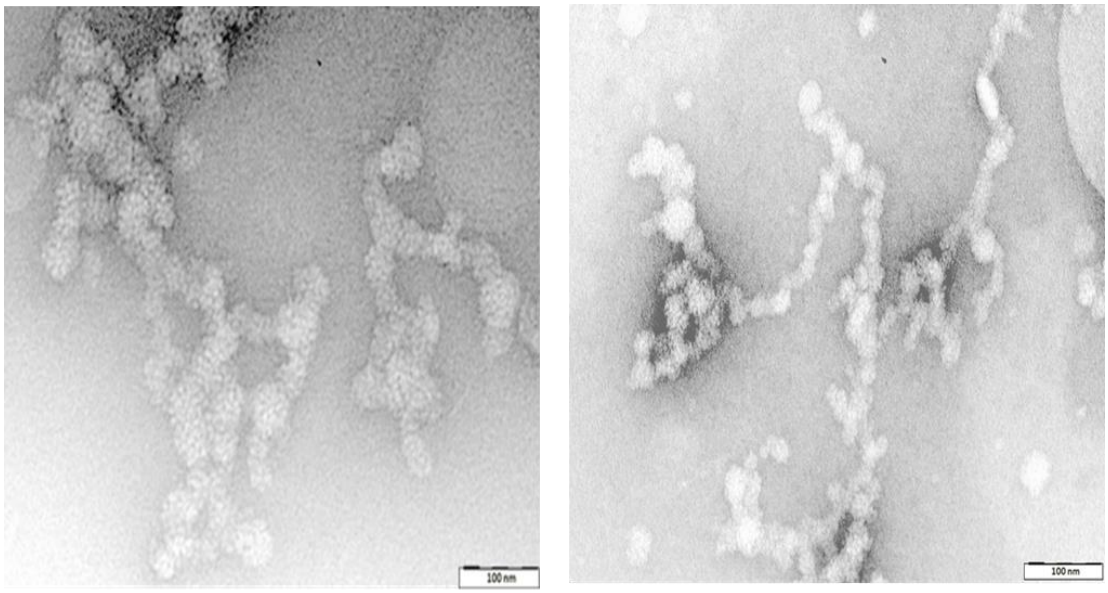

Fig. 4-3 TEM image of **Binder-Dend** dried from aqueous solution (200 µM); in the presence of heparin, showing large connected yet less-defined micellar assemblies on the surface of heparin, scale bar = 100 nm.

4.2.2 Heparin Binding

4.2.2.1 Mallard Blue (MalB) Assay

To gain more insight into the binding behavior of the branched system, we tested the ability of Binder-Dend to bind heparin using MalB assay as described in previous chapters. As expected from Nile Red assay and DLS data, this compound only self-assembled at high concentrations. Therefore, the binding ability of this compound was rather weak in these competitive conditions. Binder-Dend's CE50 values were calculated from the graph below (Fig. 4-4), and found to be 5.7 ± 0.2 (Table 4-2). This gave an EC50 value of 103 µM which suggested that binding was only significantly occurring around the CAC (117 µM) for this compound, suggesting that self-assembly is pre-requisite for effective binding (a SAMul effect). The high value of the charge excess indicated weak binding. We suggest that the poor binding ability of this compound is due to the

difficulties of forming micelles with too many branches and positive charges that causes repulsion effects at micellar surface and gives rise to poorly defined assemblies with relatively low zeta potentials. Unfortunately, due to these unsatisfying results, compared to the previous compounds, we decided not to test this compound in more competitive conditions, such as human serum.

Binder-Dend (in buffer)	
CE_{50}	5.7 ± 0.2
EC_{50} (μM)	103 ± 1.1
Dose (mg) / 100 IU	3.7 ± 0.04

Table 4-2 Calculated CE_{50}, EC_{50} and required dose (in buffer) of **Binder-Dend,** showing the effect of the branched amine groups and positive charges density on the binding abilities.

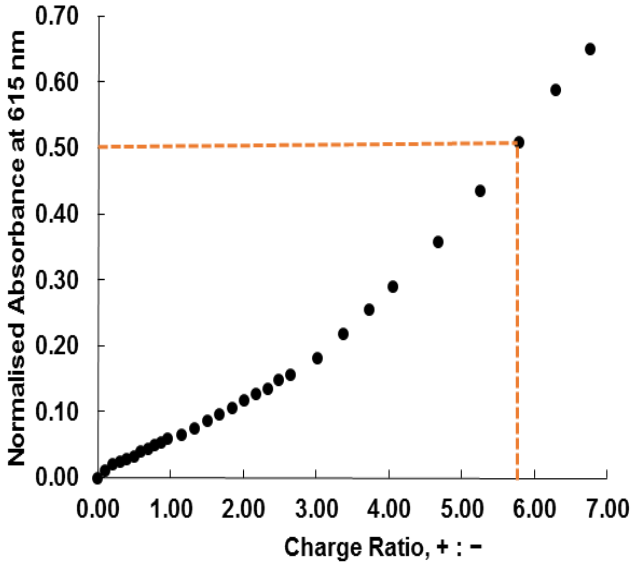

Fig. 4-4 Charge ratio against normalized absorbance at 615 nm in buffer for **Binder-Dend**.

We therefore decided to investigate other methods of displaying multiple ligands on a nanoscale surface to determine how alternative strategies performed in this heparin binding application.

4.3 Thiol Stabilized Gold Nanocomposites; AuNCs-Thiol-DAPMA (Binder-NC)

The search for therapeutic inorganic nanoparticles is growing and becoming an important area of research in the field of nanomedicine.[252-255] For the past couple of decades, gold nanoparticles (AuNPs) have been one of the most studied nanoparticle types for biomedical applications.[256-260] Due to their well-defined nanostructures and unique optical properties, AuNPs have been used as sensors for signaling molecular recognition events such as heparin/protamine aggregation/de-aggregation.[261-263] In addition, upon negative/positive binding of heparin and AuNPs that changes color, in solution, from red to blue has provided a simple and visual approach detecting heparin. Moreover, in cases where gold nanoparticles aggregate, they can be referred to as gold nanocomposites (AuNCs).[261,263-265]

In this work, gold nanoparticles were the original target but their aggregation meant that we obtained gold nanocomposites. AuNCs were stabilized by the thiol group in the new target nanostructure (**Binder-NC**) driving the self-assembly event in solution. The hydrophilic part of the target nanoparticles was the same amine used in the previous compounds with its two positive charges, constituting the binding site to heparin (Fig. 4-5). The stability of metal nanocomposites based on nanoparticles and their ability to display multiple ligands were the main reasons that drew our attention to use them. In addition, the simple agglomeration of these thiolate functionalized AuNCs should allow them to drive the self-assembly in solution, in a controlled way, to secure the heparin binding.

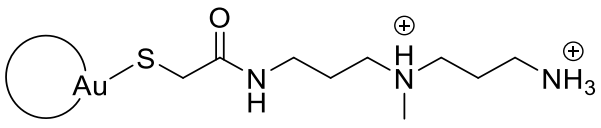

Fig. 4-5 AuNCs-Thiol-DAPMA (**Binder-NC**).

4.3.1 Synthesis of AuNCs-Thiol-DAPMA

The target nanoparticles were produced by coupling protected *N*,*N*-di-(3-aminopropyl)-*N*-methylamine (Boc-DAPMA) or compound **1** (Scheme. 2-1), with thioglycolic acid. The coupling was performed using a standard TBTU coupling reaction as described previously. The product was purified by GPC column (Bio-beads, 100% DCM) and was obtained in 81% yield (Scheme 4-8).

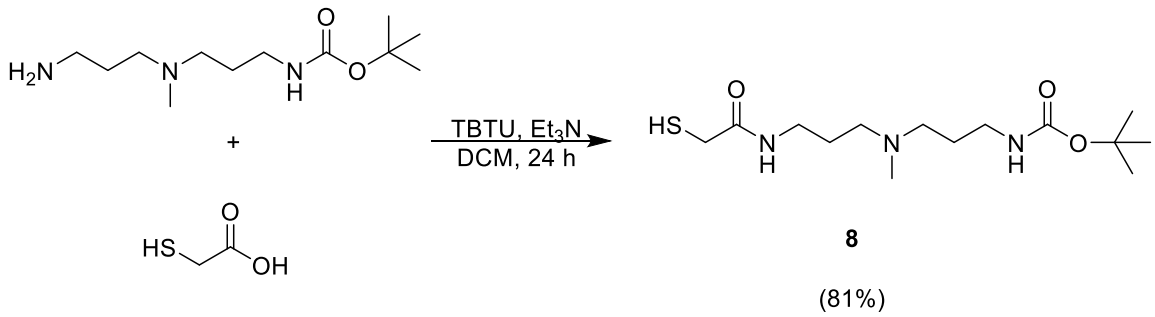

Scheme 4-8 TBTU coupling of compound **1** and thioglycolic acid to produce compound **8**.

The Boc-protected coupled compound (**8**) was then introduced to gold nanocomposites (AuNCs) (Scheme 4-9) in a one pot reaction.[266,267] The AuNCs were synthesized by reducing tetrachloroauric acid ($HAuCl_4$), which has a yellow colour (Fig. 4-6a) using sodium citrate, the colour changed to dark grey/black. The mixture was boiled to 95-100 ^oC for an hour and on prolonged heating the colour changed from black to dark red (ruby) (Fig. 4-6b) indicating the full reduction of the gold nanoparticles (as AuNPs, at around 30 nm in diameter, tend to absorb light in blue-green region, hence reflect it at around 700 nm; the region of red light).[268,269] In this reaction, gold nanoparticles aggregate to form nanocomposites. Synthesis of Au-thiol-DAPMA (**Binder-NC**) was then done by adding compound **8** to the citrate-stabilized AuNCs in the reaction flask. The colour changed to black (Fig. 4-6c) indicating that the AuNCs had bonded to compound **8** to produce Au-Thiol-DAPMA-Boc (**Au-8**) in 91% yield. The mixture was purified using a dialysis membrane 30 (MWCO-12, 1400 Dalton) in ultra-pure water overnight to remove

any excess ligand and citrate (Fig. 4-7). The water was changed (2-3 times/day) and monitored by UV-Vis spectroscopy. The dialysis was stopped when the UV-Vis spectra showed no trace of ligand around 200-300 nm, which meant that the compound was totally purified. The Boc group was then removed by treatment with HCl gas (Scheme 4-9) to produce **Binder-NC** in 92% yield.

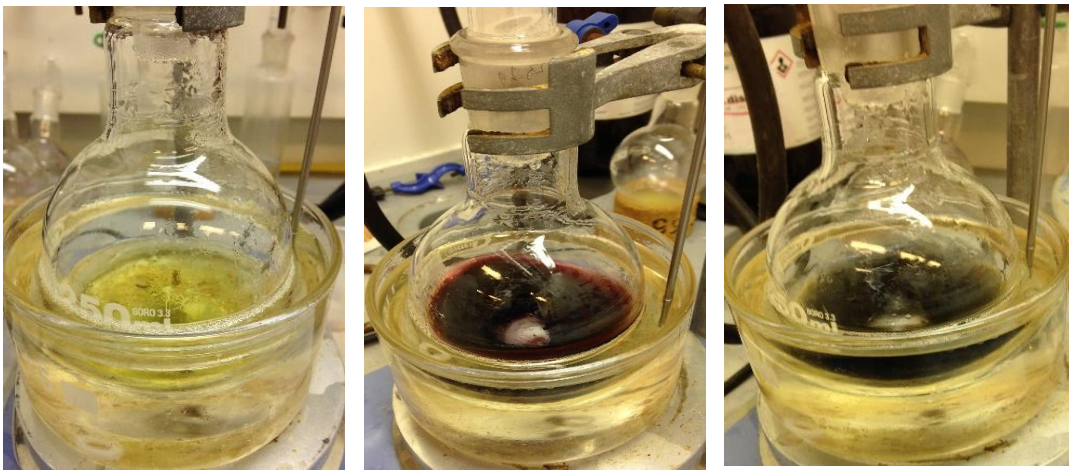

Fig. 4-6 Au-8 synthesis; **(a)** $HAuCl_4$ in water has a yellow colour, **(b)** adding sodium citrate changed the colour to red due to reduction to citrate-stabilized AuNCs and **(c)** adding compound **8** to the reaction flask changed the colour to black as ligand bound to the NCs surface.

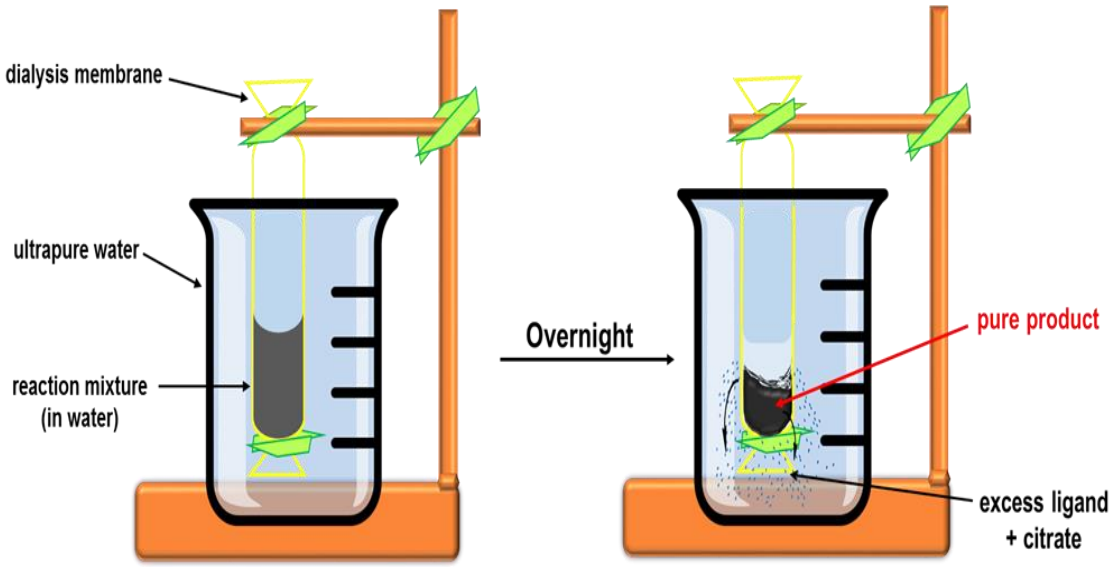

Fig. 4-7 Dialysis of **Au-8** in ultrapure water overnight.

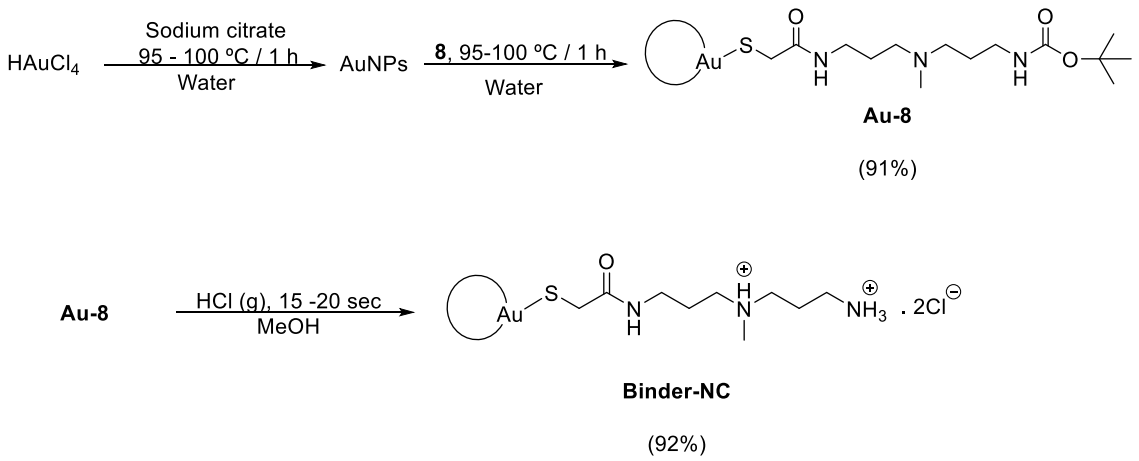

Scheme 4-9 Synthesis of **Binder-NC**.

The removal of the Boc group was successful, as ^{1}H NMR spectra showed the loss of the resonance at 1.4 ppm. Furthermore, UV-Vis measurements before and after removal of the Boc group indicated no major changes in lineshape (around 700 nm) indicating that AuNPs were not significantly affected by the deprotection reaction (Fig. 4-8). However, in these UV-Vis spectra a considerable amount of light scattering was observed – indicated by absorbance across the wavelength range. This led us to conclude that the AuNPs may be aggregating to give AuNCs, with the degree of aggregation increasing after Boc removal.

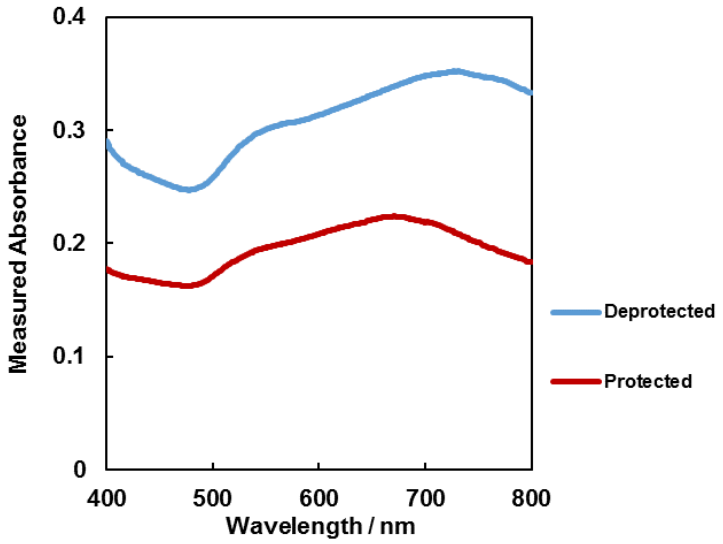

Fig. 4-8 UV.Vis spectra before (red line) and after (blue line) removing the Boc group, showing a considerable amount of light scattering in the absorbance band for AuNPs ($max_{Abs} \approx 700$ nm), in water, indicating that AuNPs aggregated to give AuNCs. The aggregation was higher after Boc removal.

4.3.2 Characterization and Analysis

4.3.2.1 *Energy Dispersive X-Ray (EDX) Analysis*

Energy dispersive X-Ray (EDX)[270] composition analysis can be used to identify the composition of a compound. The method is based on focusing an X-ray beam on a dry sample of the compound (specimen). The scattered electron beam displays the compositional contrast resulting from different atomic number elements as seen in the scanning electron microscopy (SEM) image (Fig. 4-9).

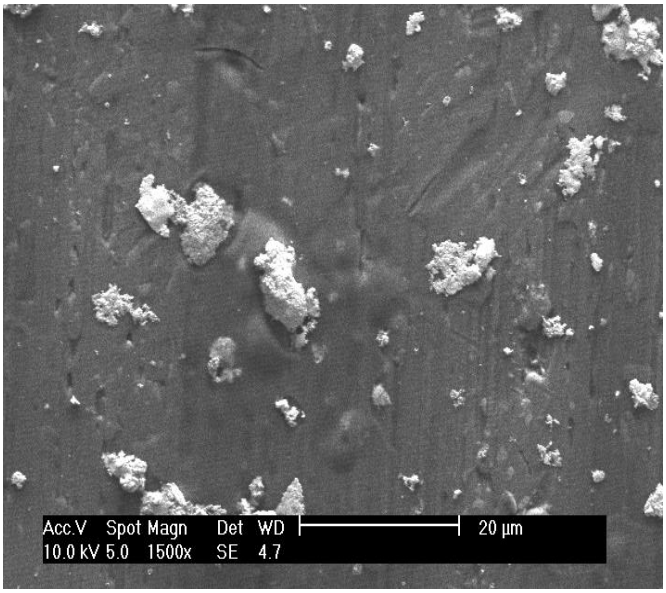

Fig. 4-9 SEM images of **Binder-NC** showing gold nanoparticles charging after exposing to the X-ray beam, scale bar = 20 µm.

The software associates the energy level of the X-rays with the elements and shell levels that generated them, giving Table 4-3 and Fig. 4-10 which show the main elements in the material under analysis. EDX analysis of **Binder-NC** showed the presence of all the main components which would be expected; Au, S, O, N and C (Table 4-3 and Fig. 4-10). As expected the dominant contribution from the metallic gold core, but the ligand shell, containing C/N/O/S could also be detected.

Element Line	*Net Counts*	*Int. Cps/nA*	*Int. Error*	*Atom %*	*Compnd %*	*Norm. Compnd%*
C K*	60687	133.2730	+/- 1.2034	29.129	9.915	9.915
N K*	18988	41.6990	+/- 1.5614	**16.167**	6.417	6.417
O K*	102193	224.4232	+/- 1.6558	33.719	15.288	15.288
Na K*	72354	158.8946	+/- 1.0695	9.220	6.006	6.006
Al K*	1548	3.3995	+/- 0.4480	0.206	0.158	0.158
S K*	2090	4.5898	+/- 0.7818	0.493	0.448	0.448
S L*	7522	16.5189	+/- 0.5227	---	---	---
Au M*	160112	351.6175	+/- 2.2356	**11.066**	61.769	61.769
Total				100.000	100.000	100.000
**** -- Standard Unavailable***						

Table 4-3 EDX analysis of **Binder-NC** showing all its main components; Au, S, O, N and C. (Al is one of the EDX pin stub components).

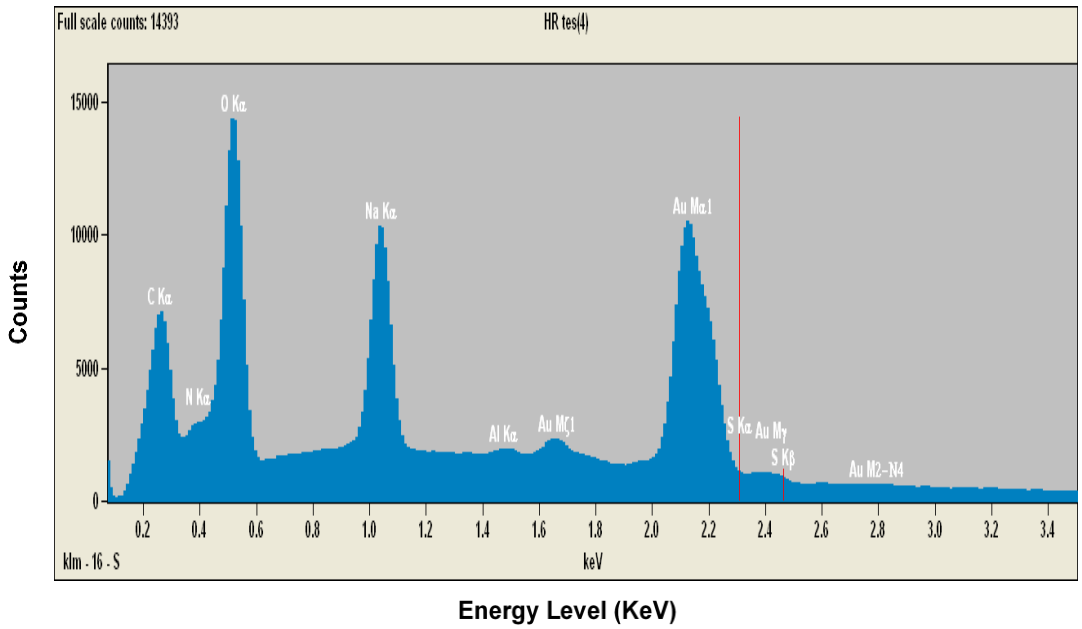

Fig. 4-10 EDX analysis of **Binder-NC** showing all its main components; Au, S, O, N and C. The Y-axis shows the counts (number of X-rays received and processed by the detector) and the X-axis shows the energy level of those counts.

Using the N:Au ratio this allowed us to estimate the ratio of ligand:gold. The ligand contains 3 N atoms, given the atom ratio found by EDX of N:Au is 16.17:11.07 = 1.46. If we assume that there was one ligand per gold atom this value should be 3. Therefore, we can estimate a molecular formula of $Au(ligand)_{1.46/3} = Au(ligand)_{0.49} = Au_{2.05}$ Ligand. However, this should only be considered an estimate of the composition. This is a

relatively small amount of gold and suggest there may be some free ligand presence in the overall system.

4.3.2.2 Dynamic Light Scattering (DLS)

Binder-NC was then characterized in terms of size and charge by dynamic light scattering (DLS). In addition, the precursor, protected AuNCs-Thiol-DAPMA-Boc was also characterized to see the effect of removing the Boc group on the size and/or charge. The samples were prepared as described previously – however, the solvent was methanol. Before removing the Boc group (deprotection), the apparent compound size was bigger, around 300 nm, then it decreased after deprotection to 70 ± 5 nm (Table 4-4). These relatively large diameters are suggestive of aggregation between smaller nanoparticles (see TEM below). Indeed, we can better consider these systems to be nanocomposites. We suspect that most nanoparticle aggregation was probably introduced during the Boc deprotection step, although even with the protected ligand in place, some scattering was seen, so it is likely that replacement of citrate also led to some aggregation. Nonetheless, zeta potential values were negative before removing the protecting group (-7 ± 2.5 mV), but after removing Boc group the resulting nanocomposite gained the required positive charges (+22 ± 0.5 mV), which would allow it to bind electrostatically to heparin.

Compound (in methanol)	**Intensity distribution (nm)**	**Volume distribution (nm)**	**PdI**	**Zeta potential (mV)**
AuNCs-S-DAPMA-Boc	275 ± 53	244 ± 36	0.38 ± 0.04	-7.0 ± 2.5
AuNCs-S-DAPMA (Deprotectd)	72 ± 5	70 ± 5	0.63 ± 0.07	+22.0 ± 0.5

Table 4-4 DLS Analysis of **Binder-NC** (AuNCs-S-DAPMA) before and after removing the Boc group, showing the decrees of size and change of charge.

4.3.2.3 TEM Images

Transmission Electron Microscopy (TEM) images were recorded using standard methods. The images showed that **Binder-NC**, does indeed contain spherical gold nanoparticles (AuNPs) although these are aggregated into an overall nanocomposite (AuNCs). These TEM images (Fig. 4-11) make clear that gold nanoparticles are present in the sample and that they have roughly spherical shapes. We used ImageJ to work out the size distribution of these particles and this is plotted in Fig. 4-12 The average AuNP diameter was 22.5 ± 2.5 nm. The larger size observed by DLS that combines with TEM does suggest that some aggregation of **Binder-NC** takes place. As such, we have formed ligand-modified nanoparticles which aggregated into nanocomposite form.

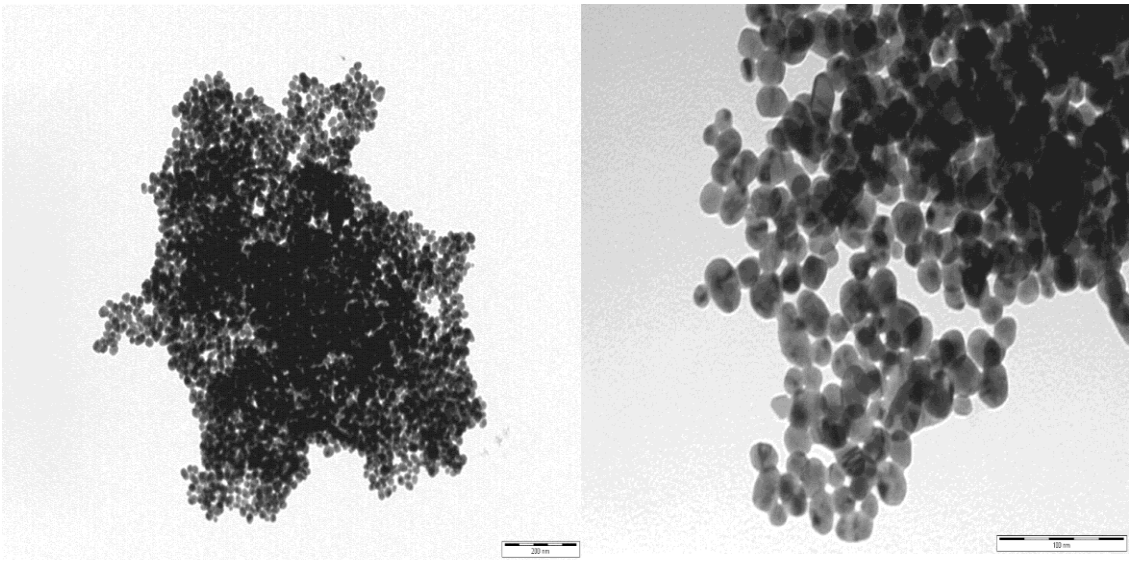

Fig. 4-11 TEM images of **Binder-NC** after dialysis showing spherical particles and a degree of aggregation, scale bar = 200 nm (left) and 100 nm (right).

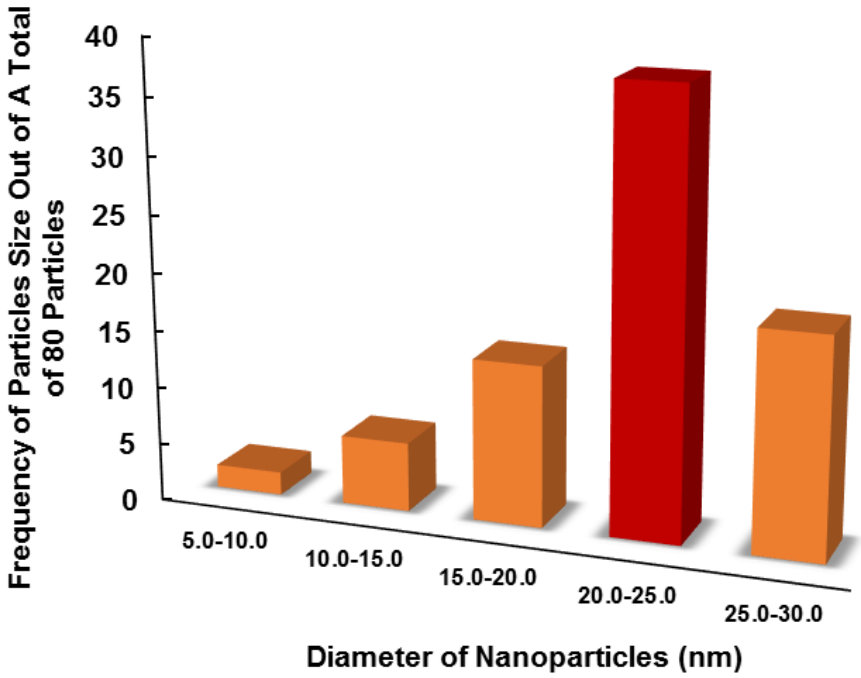

Fig. 4-12 Particle size distribution of **Binder-NC** within the overall nanocomposite; the red bar shows the dominating size between 20-25 nm.

4.3.3 Heparin Binding

4.3.3.1 MalB Assay in Buffer

The heparin binding ability of **Binder-NC** was then determined using the MalB assay. Usually this assay is performed in room temperature, however, due to solubility difficulties we faced with **Binder-NC**, presumably associated with the aggregation observed by DLS and TEM, and made worse in buffer we had to perform the assay at elevated temperatures. The binder precipitated at room temperature (Fig. 13.a), but on increasing temperature, it completely dissolved in the buffer (Fig. 13.b). The assay was performed under heating; being kept in a water bath at 50-55 ºC during the titration (Fig. 14). In addition, the UV-Vis instrument had a thermoelectrically temperature-controlled cell positioner to maintain the same conditions during the assay.

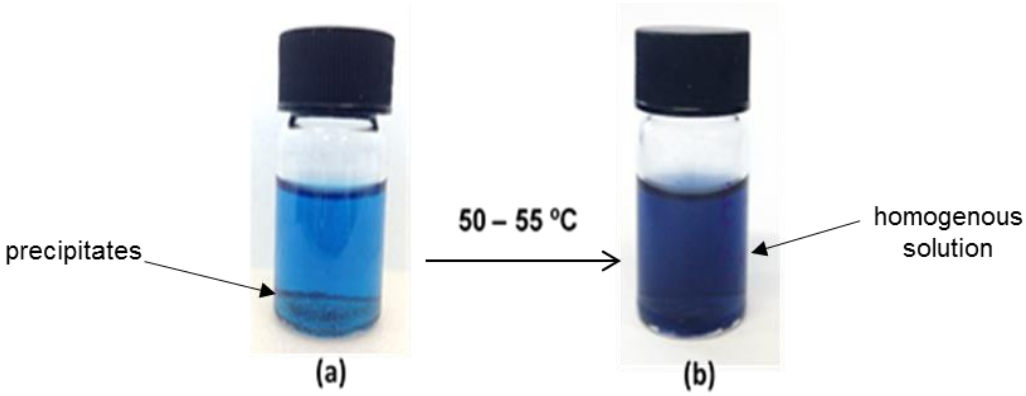

Fig. 4-13 Binder-NC stock solution; precipitating at room temperature (a) and completely dissolving after heating to 50-55 ºC (b).

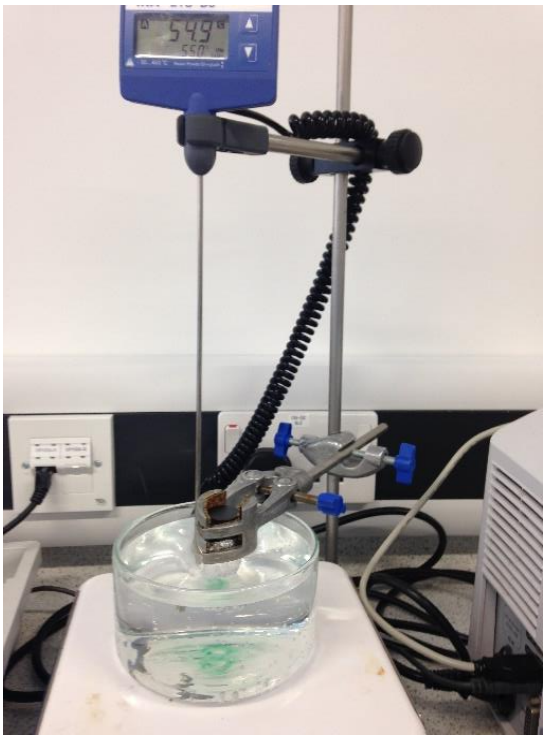

Fig. 4-14 Binder-NC stock solution; kept in water bath at 50 - 55 ºC during MalB assay titration process.

On binding heparin, the MalB peak dropped in intensity and after starting to add **Binder-NC** solution, the peak increased showing a partial replacement of the dye (Fig. 4-15). This demonstrated that **Binder-NC** can bind heparin but not fully replacing the MalB dye, under the titration conditions.

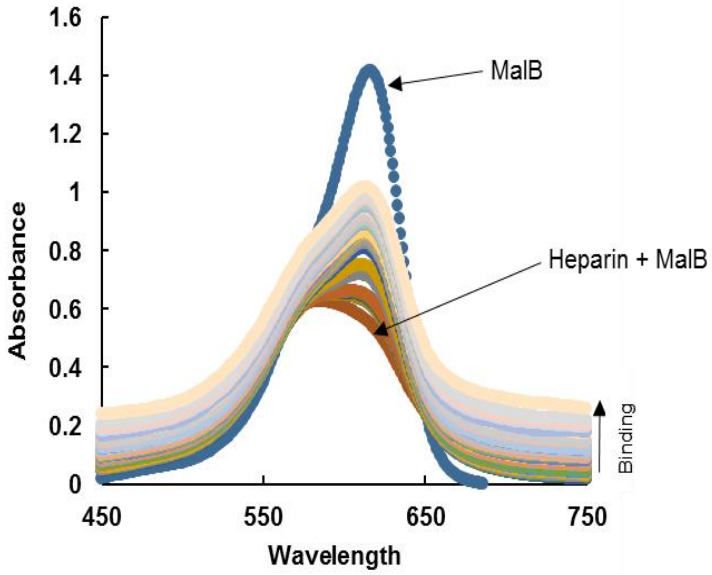

Fig. 4-15 UV-Vis spectra showing **Binder-NC** incomplete replacement of MalB.

Table 4-5 presents the calculated values, from Fig. 4-16, for **Binder-NC**; CE_{50} was 3.8 ± 0.1 and the EC_{50} was 203 ± 7 µM, which are considered high values in terms of heparin binding, comparing to the current commercial heparin binder; protamine. As reported, protamine replacement assay results were; CE_{50} = 0.52 and EC_{50} = 2.34 µM.[173] we suggest that the low observed solubility of this nanocomposite may contribute to the relatively low binding. It is also possible that the optical properties of the AuNPs themselves may be disrupting this assay somewhat.

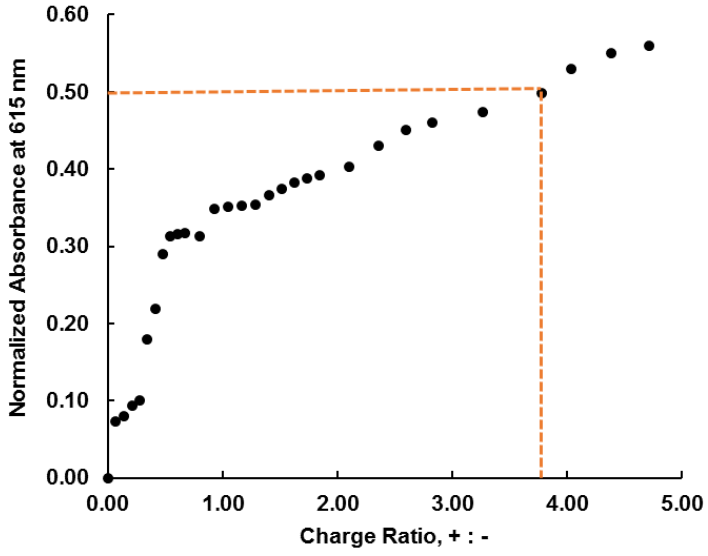

Fig. 4-16 Charge ratio against normalized absorbance at 615 nm in buffer for **Binder-NC** from MalB assay at 50-55 °C.

Binder-NC in buffer (50-55 ºC)	
CE_{50}	3.8 ± 0.1
EC_{50} (µM)	203 ± 7
Dose (mg) / 100 IU	4.1 ± 0.2

Table 4-5 Calculated CE_{50}, EC_{50} and required dose of **Binder-NC** at 50-55 ºC.

In addition, we performed the MalB assay at higher temperature than 55 °C using a heating gun (> 80 °C). The assay under these conditions gave better binding results (Fig. 4-17); CE_{50} was 2.07 ± 0.03 and the EC_{50} was 112 ± 4 µM (Table. 4-6). We suggest that the elevated temperatures improved the solubility hence the binding ability. Clearly, however, such systems would be limited with regards to their use in biologically relevant conditions. As such we turned to other strategies for multivalent ligand display.

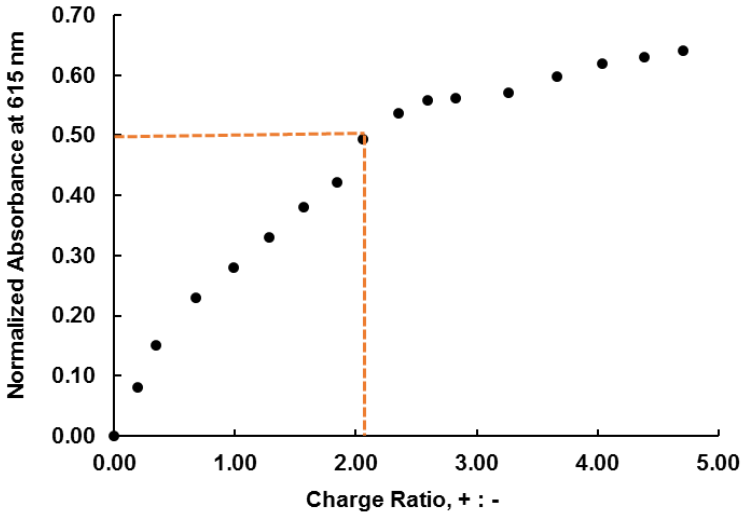

Fig. 4-17 Charge ratio against normalized absorbance at 615 nm in buffer for **Binder-NC** from MalB assay at > 80 °C.

Binder-NC in buffer (> 80 ºC)	
CE_{50}	2.07 ± 0.03
EC_{50} (µM)	112 ± 4
Dose (mg) / 100 IU	2.23 ± 0.02

Table 4-6 Calculated CE_{50}, EC_{50} and required dose of **Binder-NC** at > 80 ºC; improvement of the binding ability due to enhancement in the solubility after heating.

4.4 Polymer Scaffold (Binder-Poly)

The importance of drug polymer conjugates, which was outlined in this chapter's introduction (4-1), lead us to aim to replace the focal group (hydrophobic tail) with a polymer. As a simple first approach, we decided to modify poly(acrylic acid) with the ligands in order to produce **Binder-Poly** (Fig. 4-18).

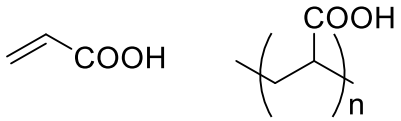

Fig. 4-18 Acrylic acid and poly(acrylic acid).

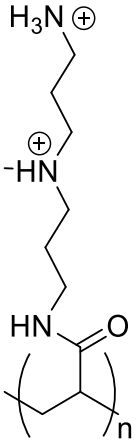

Fig. 4-19 DAPMA-Poly(acrylic acid) **(Binder-Poly)**.

4.4.1 Synthesis of Polymer Stabilized DAPMA

Boc-DAPMA (compound **1**) was reacted with poly(acrylic acid), average MW ≈ 1800 g/mol, n = 25 units, in 1:1 ratio of reactive groups to produce Boc-DAPMA-Poly(acrylic acid). The reaction was done using TBTU as the coupling reagent (Scheme 4-10) to yield Boc-Binder-Poly (54%).

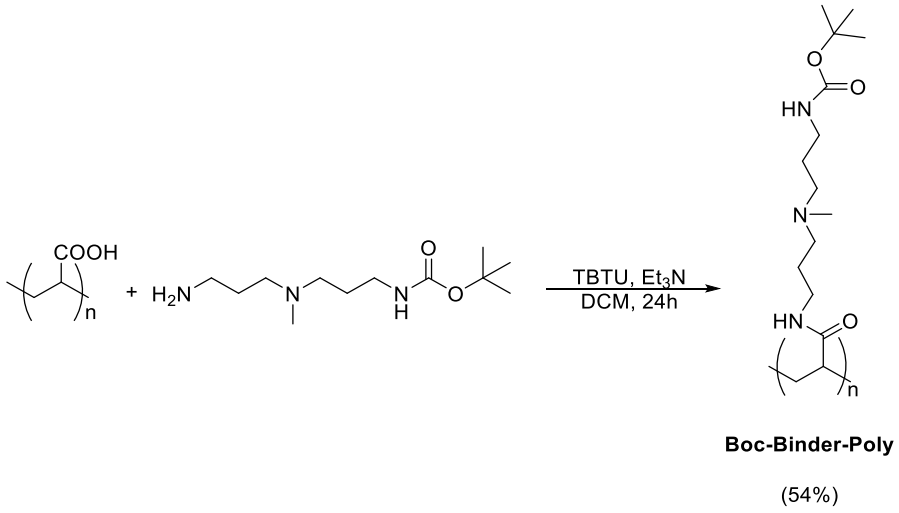

Scheme 4-10 TBTU coupling of compound 1 and poly(acrylic acid), n = 25 units..

This product was then deprotected to produce DAPMA-Poly(acrylic acid) or **Binder-Poly**. The deprotection was performed using HCl gas (Scheme 4-11) to give the desired product in 86% yield. **Binder-Poly** was characterized by MS – however we could not detect the polymer. In addition, ^{1}H NMR spectra showed only some of the ligands protons, and most importantly demonstrated the loss of Boc group after the deprotection reaction at 1.4 ppm (Fig. 4-20). As such we went on to characterize **Binder-Poly** using CHN elemental analysis as described in more detail below. In this way, the actual average molar mass was predicted as 2268.22, calculated from the proposed chemical formula of $C_{103}H_{170}N_{12}O_{46}$.

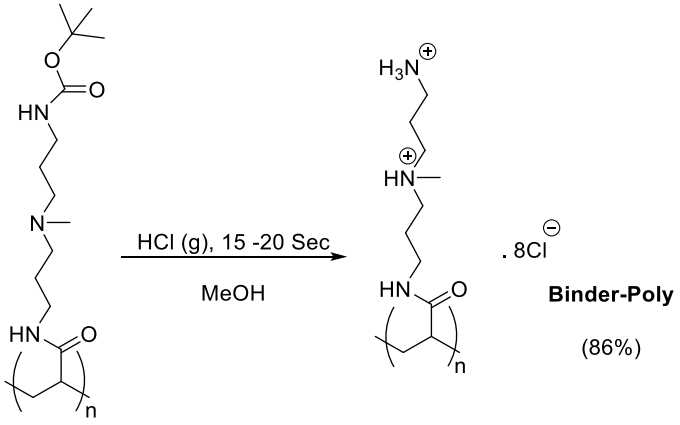

Scheme 4-11 Removal of Boc group by HCl gas to produce **Binder-Poly**.

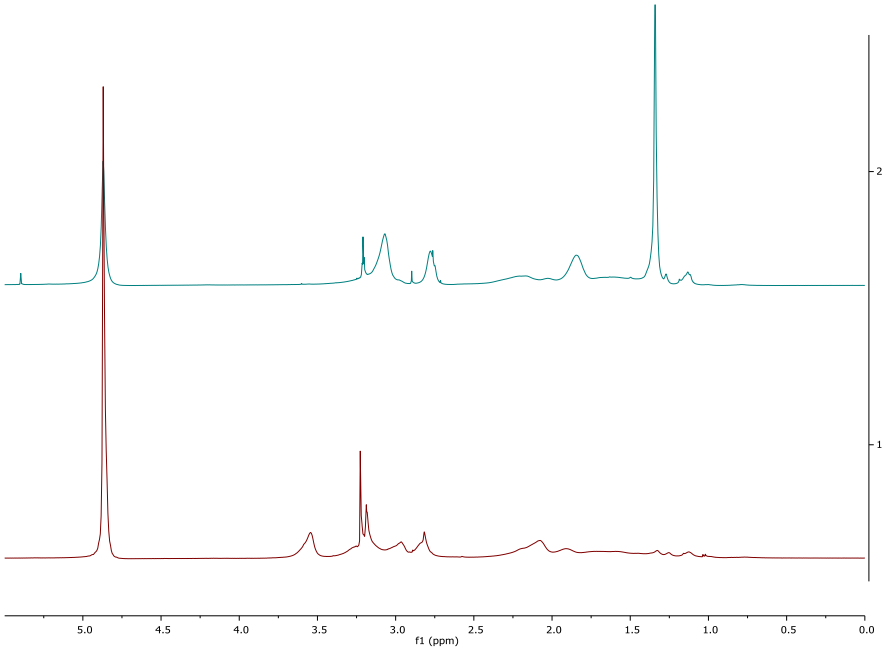

Fig. 4-20 NMR spectra of **Binder-Poly** before Boc deprotection (blue line) and after the deprotection (red line) showing no resonance at 1.4 ppm.

4.4.2 Characterization and Analysis

4.4.2.1 CHN Elemental Analysis

In order to analyse the synthesized compound (**Binder-Poly**) in terms of C, H, and N composition we performed CHN Elemental Analysis. This was performed to calculate each element percentage then the software formed the formula that matched the percentage of each element. The instrument was an Exeter Analytical CE-440 analyzer, used in conjunction with a Sartorius SE2 analytical balance. Samples (~2 mg) were weighed into tin capsules before being sealed and placed in the analyzer. The samples were then burnt in pure oxygen, in a 975 °C furnace, before passing through a cooler furnace containing Cu to remove any traces of O_2 and nitrogen oxides. The combustion products then pass onto the detectors where levels of C, H ad N are calculated (Table 4-7).

The formula of $C_{103}H_{170}N_{12}O_{46}$, gives the suggested structure shown below (Fig. 4-21). This suggested average structure contained four DAPMAs loaded onto the polymer backbone, and would carry 8 positive charges in total after the deprotection reaction.

Symbol	Element	Atomic weight	Atoms	Mass percent
C	Carbon	12.0107	103	53.4962 %
H	Hydrogen	1.00794	170	7.4097 %
N	Nitrogen	14.0067	12	7.2683 %

Table 4-7 Elemental Composition of $C_{103}H_{178}N_{12}O_{46}$; mass composition by element (g/mol), molecular weight: 2312.31g/mol.

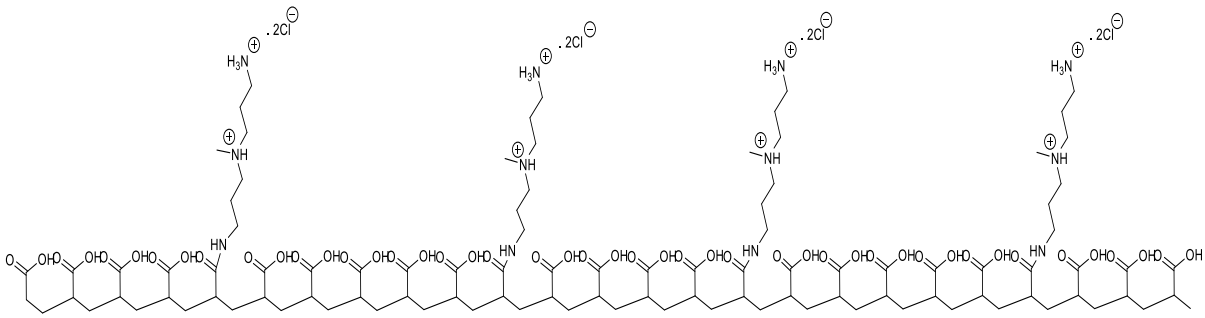

Fig. 4-21 Suggested structure of **Binder-Poly**, generated by ChemDraw software, of the calculated mass from CHN elemental analysis; contained four DAPMA groups carrying 8 positive charges.

4.4.2.2 Dynamic Light Scattering (DLS)

DLS was then performed to measure the size and charge of **Binder-Poly** as described before. Table 4-8 showed that the size, by volume distribution, was 97 ± 8 nm. This is significantly larger than would be expected for a single polymer chain, and is suggestive of aggregation in the solution phase – acrylic acid polymers are well-known to have

aggregation potential in the presence of polycations.[271] The zeta potential was recorded as +25.0 ± 3.0 mV, confirming the required positive charges we aimed to gain after the deprotection reaction.

Compound	**Intensity distribution (nm)**	**Volume distribution (nm)**	**PdI**	**Zeta potential (mV)**
Binder-Poly	148 ± 3	97 ± 8	0.24 ± 0.01	+25 ± 3

Table 4-8 DLS analysis of **Binder-Poly**.

4.4.2.3 TEM Images

TEM images were recorded for **Binder-Poly** as described above. The images (Fig. 4-22b-d) showed very defined spherical aggregations after binding to heparin – however, clearly this is very different to the micellar arrangements seen in previous systems. Once again it is clear that the presence of heparin induces hierarchical assembly of the polycationic system. We suggest that individual polymers can be seen on the surface of these aggregates (Fig. 4-22d) – the estimated diameter of the polymer used should be ca. 5 nm.

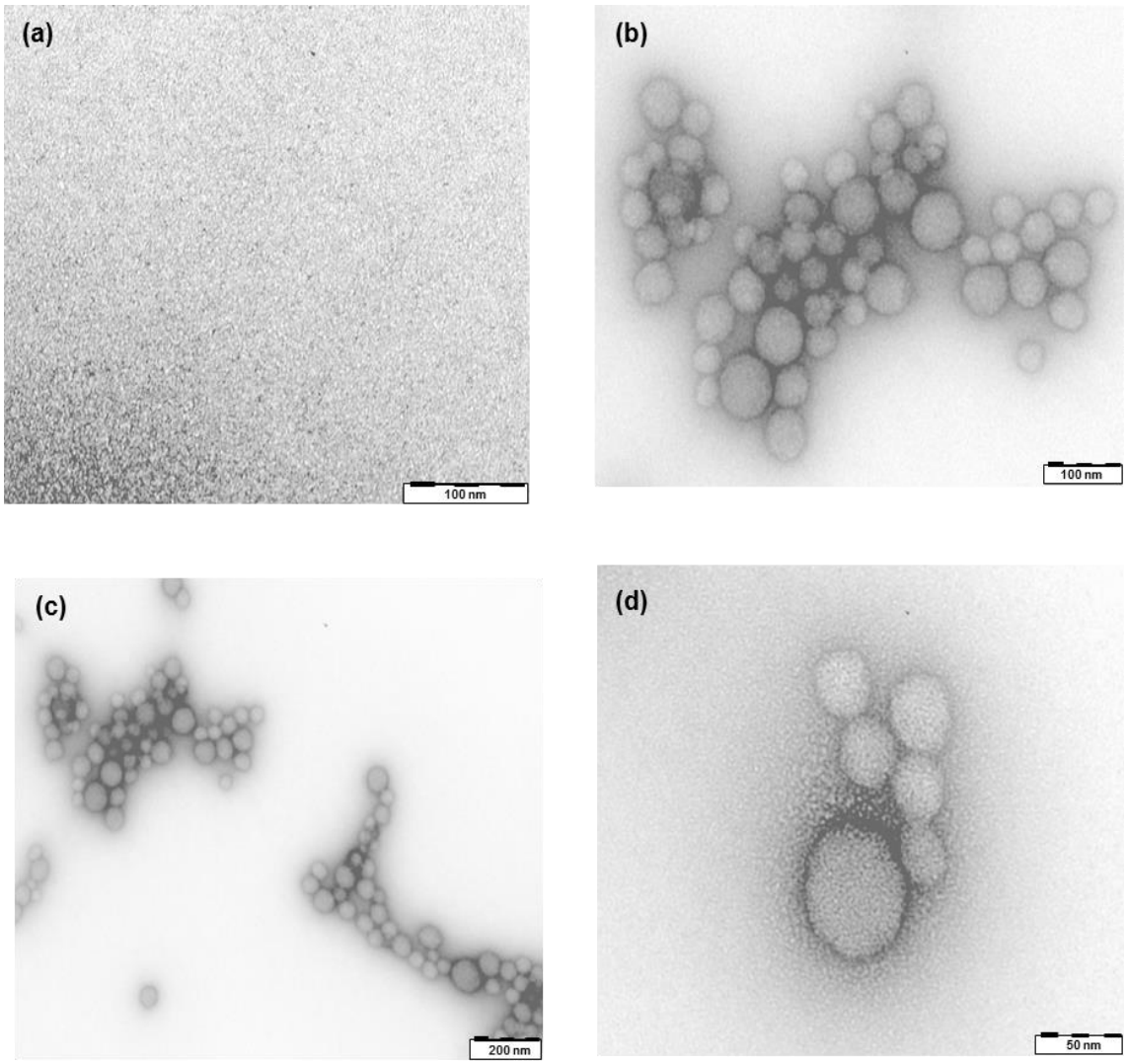

Fig. 4-22 TEM images of **Binder-Poly** before binding to heparin **(a)** showing dispersed nanostructures and after binding to heparin **(b)**, **(c)** and **(d)** the nanostructures were aggregating in an organized spherical shapes on the surface of heparin, scale bar = 100, 200 and 50 respectively.

4.4.3 Heparin Binding

4.4.3.1 MalB Assay in Buffer

To test this compound's (**Binder-Poly**) ability to bind heparin we performed the MalB assay in buffer as described previously. Surprisingly, for a large compound with relatively low loading of ligand, the binding was relatively good (Fig. 4-23). In addition, it was very easy to dissolve in solution. The binding data from Table 4-9 showed that CE_{50} was 2.00

± 0.03, indicating less charge excess, i.e. better binding than either of the two other binders reported in this chapter (**Binder-Dend** and **Binder-NC**). As such, we decided to test its binding to heparin in more biologically relevant competitive conditions, such as human serum.

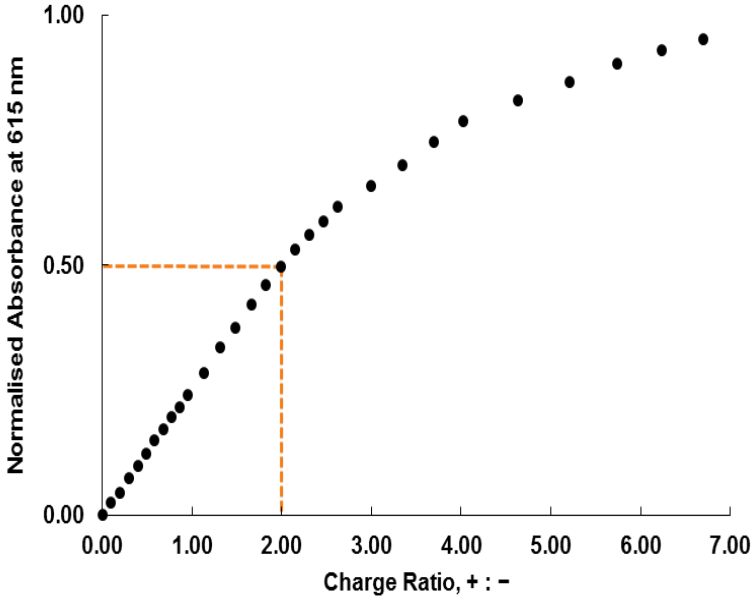

Fig. 4-23 Charge ratio against normalized absorbance at 615 nm in buffer for **Binder-Poly**.

Binder-Poly in Buffer	
CE_{50}	2.0 ± 0.03
EC_{50} (μM)	27 ± 0.4
Dose (mg) / 100 IU	2.1 ± 0.04

Table 4-9 Calculated CE_{50}, EC_{50} and required dose of **Binder-Poly** in buffer.

4.4.3.2 MalB Assay in Human Serum

The binding ability of **Binder-Poly** was then tested in human serum using the MalB assay as described previously. Although the compound showed relatively stable binding to heparin (Fig. 4-24), from Table 4-10, the CE_{50} value was higher than desirable (4.0 ± 0.5).

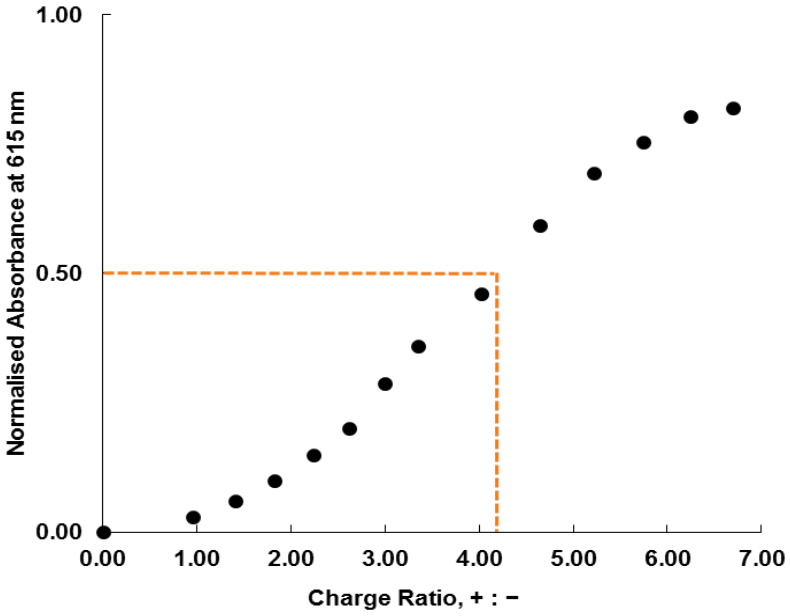

Fig. 4-24 Charge ratio against normalized absorbance at 615 nm in human serum for **Binder-Poly**.

Binder-Poly in Human Serum	
CE_{50}	4.0 ± 0.5
EC_{50} (µM)	57 ± 6
Dose (mg) / 100 IU	4.3 ± 0.4

Table 4-10 Calculated CE_{50}, EC_{50} and required dose of **Binder-Poly** in human serum.

Clearly the presence of serum quite significantly disrupts the binding process – we suggest there may be non-specific binding processes between serum proteins and the poly(acrylic acid) backbone.[272]

4.5 Conclusions and Future Work

Three major modifications to the hydrophobic/hydrophilic units were introduced to the synthesized systems in order to study the effect of such approaches on heparin binding. The first modification was branched system with more charge dense hydrophilic groups and a longer hydrophobic chain (saturated-C_{22}) to produce **Binder-Dend**. The results showed that binding to heparin (in buffer) for **Binder-Dend** was affected due to the poor self-assembly of this system, as measured by the Nile Red assay. Although it had more positive charges (6 +ve) than the previously reported binders, this did not improve the binding as they were not being organized effectively on the nanoscale. For future work, this compound could be enhanced by using more than one hydrophobic group in order to improve the self-assembly or by increasing the dendritic generation so the number of ligands is even greater, to enhance multivalent binding even in the absence of self-assembly.

The second modification was to display the ligands on a gold nanoparticle (AuNPs) core. In all cases aggregation of nanoparticles to give nanocomposites was observed – as characterized by UV-Vis, TEM and DLS. The aim of this step was to stabilize the compound (**Binder-NC**) to obtain better heparin binding. Unfortunately, **Binder-NC** had solubility difficulties in buffer as the nanoparticles were aggregated into a nanocomposite, therefore, performing the binding assay was only possible at elevated temperatures (50-55 °C and >80 °C). Nevertheless, the assay results showed that replacement of MalB was incomplete, we suggest that might be due to AuNCs interfering with the UV-Vis absorbance around $Abs_{max} \approx 700$ nm as well as the lower solubility. We decided then not to proceed with performing more tests on this system. For future work, improving binding to heparin could be achieved if this system was introduced to a different thiol group (longer); with a spacer group to help optimize ligand display, or more positive charges on

the hydrophilic group (binding site). Importantly, in future work, nanoparticles aggregation should be avoided, possibly by using a different, non-citrate, method of synthesis.

The third modification was made by using a polymer to display the ligands. TEM images showed a highly defined spherical aggregation of **Binder-Poly** when binding to heparin. The binding assay data from the MalB assay showed a low CE_{50} (2.0 ± 0.03) which indicated good heparin binding. Therefore, we proceeded to perform the assay in more competitive conditions by using human serum as the medium of the binding process. The result was somewhat promising (CE_{50} = 4.2 ± 0.5) as **Binder-Poly** showed rather more stable binding than the other two systems reported in this chapter. For future work, this compound could be synthesized by using different ratios of the reactants other than the one that was used in this work; polymer:DAPMA (1:1). Changing the ratio by increasing the amount of DAPMA in the reaction would load more ligand onto the polymer, gaining more positive charges along the polymer chain to obtain better heparin binding. Furthermore, different polymer backbones or capping the unpacked sites could be tested to try and avoid any non-specific interactions with serum proteins which may be disrupting the binding process in these highly competitive conditions. For example, ethylene glycol (PEG) units are known to be relatively non-interactive in human serum.[273]

5 Multicomponent SAMul Systems for Multifunctional Binding

5.1 Introduction

The function of a simple micellar system could have limitations of performance. Mixing two or more surfactants has therefore been pursued for over 60 years.[274-278] These studies showed that the surfactants either form mixed micelles or aggregate into separate structures; depending on their chemical nature.[279,280] Structurally similar surfactants tend to aggregate into the same supramolecular structure, whereas chemically different surfactants, for example fluorinated and non- fluorinated surfactants, show de-mixing into separate micelles.[281,282] Synthetic cancer vaccines, have been found to yield a much higher antibody response if they had multiple components, covalently attached in some cases[283,284] but also co-assembled in other cases.[285] The dynamic nature of supramolecular chemistry can therefore be employed to harness enhanced performance and could turn an existing set of amphiphiles into new systems with unique properties. Co-assembly, the assembly of more than one amphiphile into a single supramolecular structure (Fig. 5-1), is therefore a powerful tool that can potentially improve existing properties and even incorporate new functionalities.

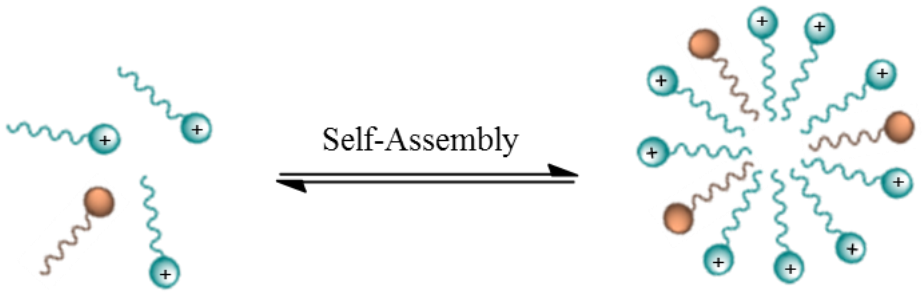

Fig. 5-1 Schematic representation of the aggregation of two amphiphilic components into a single mixed assembly.

A simple example of co-assembly benefits is observed when alkyl sulfate surfactants of different chain lengths are mixed, both amphiphiles assemble into the same micelle but the critical micelle concentration is lower than expected from a linear extrapolation of critical micelle concentration (CMC = CAC) values versus mole fraction (Fig. 5-2).[286] This shows that mixed systems have a stronger driving force to aggregate – an important observation for the development of stable self-assembling systems. In more detail, the curves for the CMC versus mole fraction were quite similar when the difference in the chain lengths was small but dropped significantly when a small amount of longer chain surfactant was added to a solution of shorter chain surfactant.[286] This behaviour was credited to the ineffective penetration of longer surfactant molecules into short-surfactant micelles and lack of mixing.

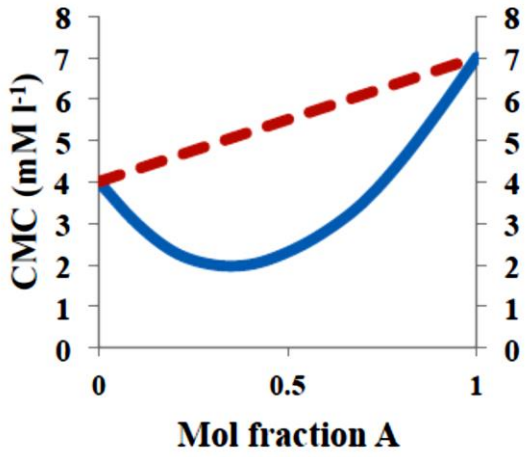

Fig. 5-2 Typical CMC (CAC) versus mol fraction plot of a binary surfactant system. Solid line indicates experimental data, whereas dotted line shows linear extrapolation.[286]

In addition to the fundamental discoveries, which tend to influence aggregation strength, there have been examples of how the co-assembling nature of similar amphiphiles can be used to incorporate additional functionality. Stupp and co-workers have demonstrated beautiful co-assembly of peptide-amphiphilic molecules into nanofibers,[287] as well as co-assembly of opposite peptide polarities into nanofibers where the complementary termini result in the same β-sheet arrangement as the single-component system whilst exhibiting

higher thermal stability compared to the co-assembly of peptide amphiphiles with identical polarity (Fig. 5-3).[288] This strategy is considered to be very powerful as some peptide amphiphiles are epitopes, which have the ability to mimic extracellular matrix proteins hence enhancingcell adhesion or differentiation.[289] By mixing different systems into a co-assembly it is possible to harness their individual advantages.

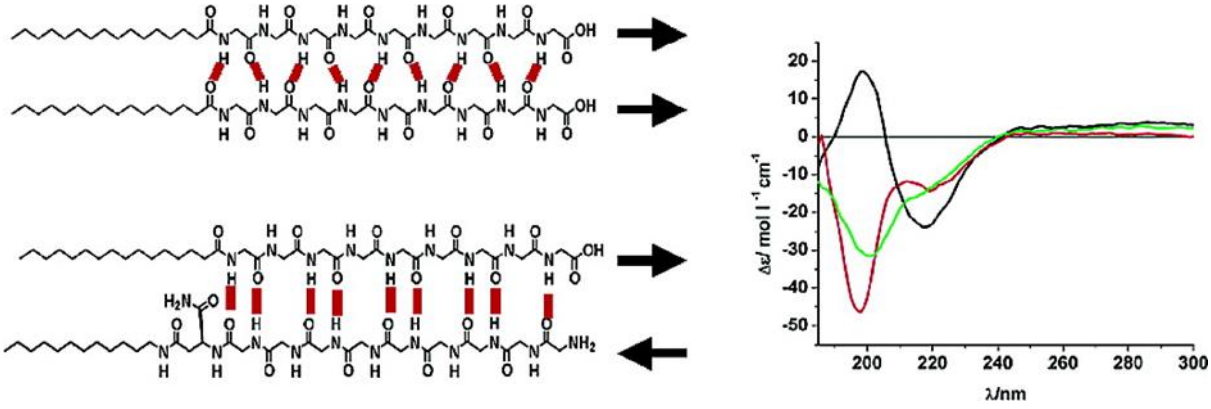

Fig. 5-3 Co-assembly of peptide-amphiphilic molecules with identical polarity (top) and co-assembly of opposite peptide polarities (bottom) into nanofibers. Investigated by circular dichroism (CD); the co-assembly of opposite peptide polarities exhibited higher thermal stability compared to the co-assembly of peptide amphiphiles with identical polarity, Stupp and co-workers, 2005.[288]

PEG lipids are an excellent choice as a second non-ionic amphiphile due to their flexible, non-immunogenic yet hydrophilic nature that sterically stabilises all kinds of colloids and reduces the adsorption to blood components[290,291] (see section 5.2). Therefore, we have chosen them to be inserted to our SAMul nanostructures (Fig. 5-6), employing the co-assembly approach to study its effect on self-assembly and hence binding abilities and selectivities towards polyanionic targets.

5.2 PEGylation and the 'Stealth Effect'

The search for more stable biological systems has led to several approaches on how to protect such systems from being excreted from the blood stream and minimise interactions with non-target sites to maximise efficacy and create a means of regulating

circulation time.[292] One of the strategies to create biocompatibility is to encapsulate active targets into poly(ethylene glycol)-based (PEG-based) micelles, which bury the actives in their interiors,[293] for example, quantum dots were encapsulated in PEG-stabilised phospholipid micelles and used for in vivo imaging.[294] The non-immunogenic and antigenic PEG components essentially mask the highly bio-incompatible nanocrystals and protect them from rapid opsonisation whilst giving them sufficient stability for the imaging to be achieved.[295]

One of the major reasons that drug delivery systems have now entered the mainstream is that the initial problem of rapid removal from the blood stream has been solved, *inter alia*, by 'stealth' systems.[296] In addition to simple stabilisation, superior properties for a variety of applications have been demonstrated. Hanes and co-workers reported[297,298] several examples of block-co-polymeric nanoparticles with low-molecular-weight PEG as the hydrophilic part that facilitates mucus transport for application in gene delivery. They also showed that the PEG chain length can have an effect on adhesive interactions with mucus components limiting them, and enabling delivery.[299]

PEG 'stealth systems' offer a distinctive advantage of increasing stability in biological systems as well as minimizing off-target interactions that maximise efficacy. As such, the 'stealth system' concept can be transferred to self-assembled multivalent systems with potential nanomedical applications. This has been demonstrated by Toft et al., who reported[300] a multicomponent system consisting of membrane-active peptide amphiphiles (PAs) and pegylated peptide amphiphiles designed as a breast cancer antitumor agent. The addition of the pegylated amphiphile delayed the degradation time 8-fold without increasing the cytotoxicity (Fig. 5-4),[300] preventing the unwanted breakdown of the medicinally-active assembly.

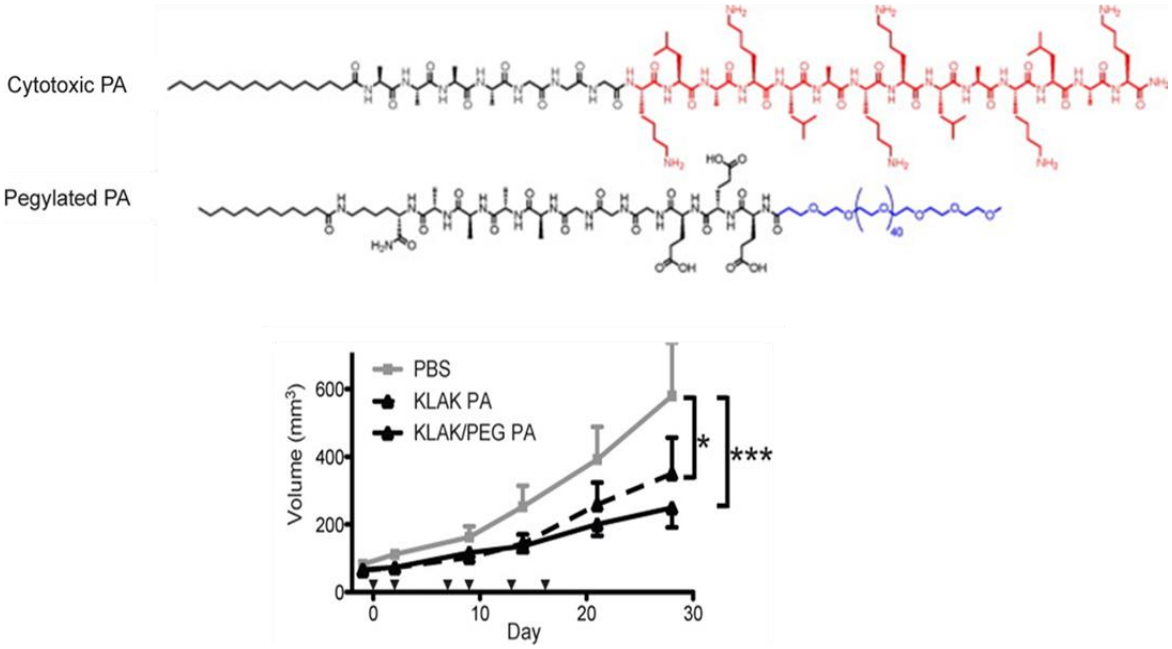

Fig. 5-4 Addition of the pegylated amphiphile delayed the degradation time 8-fold of Pas without increasing the cytotoxicity, Toft et al., 2012.[300]

Barnard et al. demonstrated the effects of co-assembling low-molecular-weight cholesterol-functionalized PEG units of either triethylene glycol (**Chol-PEG-3**) or octaethylene glycol (**Chol-PEG-8**) (Fig. 5-5).[113] In their systems, the addition of **Chol PEG-3** decreased the DNA binding affinity as a consequence of steric crowding and loss of overall solubility. The **Chol-PEG-8** additives, however, not only lowered the surface charge and thereby increased the ability to cross a model mucus layer, but also exhibited a much higher binding affinity towards DNA. It was postulated that longer PEG derivatives enhanced DNA binding due to the higher solubility of the nanostructures and their complexes with DNA.

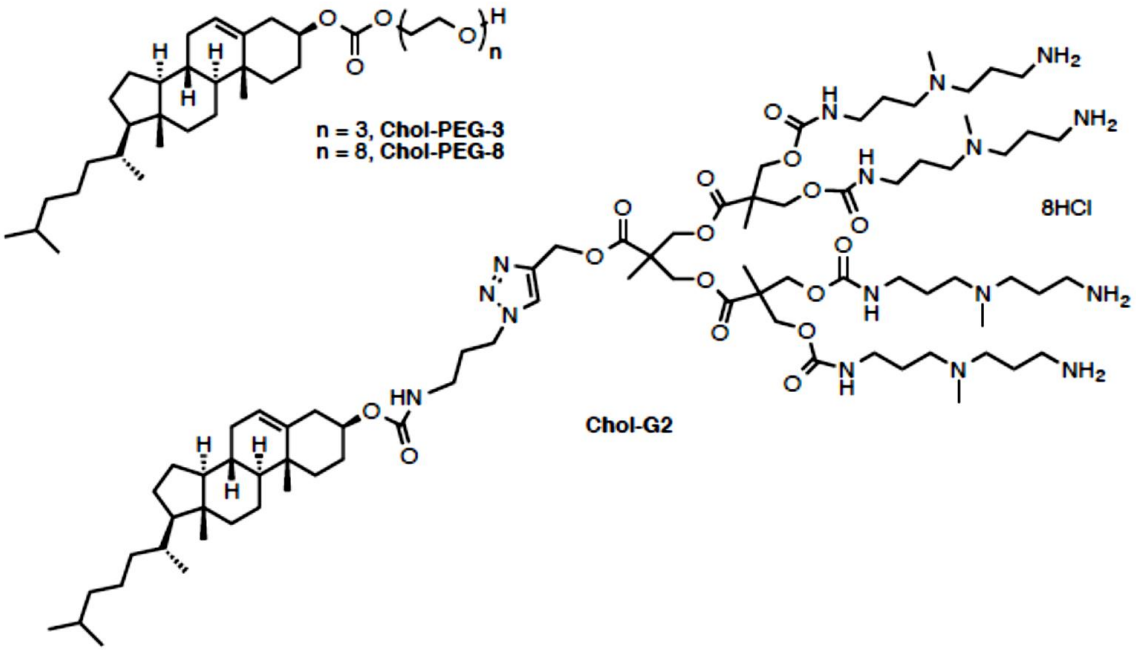

Fig. 5-5 Molecular structures of the SAMul dendron Chol-G2 with cholesterol-functionalised ethylene glycol derivatives (Chol-PEG-3 and Chol-PEG-8) by Barnard et al.[113]

So far, however, the effect of PEGylation towards binding actions of self-assembled multivalent systems remains largely unexplored. In this work we attempt to explore this aspect in terms of self-assembly and binding affinities towards different biological polyanions; heparin and DNA. We recognised that the surface of our micelles reported in previous chapters is highly charge-dense and that repulsions between cationic charges are likely to be significant. Certainly this played a role in limiting the solubility of the amphiphilic synthesised systems reported in Chapter 3. This can also potentially lead to all-target binding and toxicity effects. Co-assembling a second, non-ionic amphiphile was therefore expected to reduce the electrostatic repulsions on the nanostructure surface, as fundamentally demonstrated with simple ionic and non-ionic surfactants that have a lower CMC (CAC) than expected from the linear extrapolation of the CMC (CAC) values versus mole fraction.[301]

5.3 Synthesis of Multicomponent SAMul Systems

This study was performed by MChem student Constantin Voll under my supervision. I helped with advice and training on both the synthesis and the binding assays.

In a previous chapter (Chapter 3), we investigated surface ligand effects on the binding of heparin and DNA using the C_{16} hydrophobic chain. In this chapter we used a longer saturated fatty acid (C_{18}) in an attempt to overcome some of the solubility problems. We selected **C_{18}-SPD** and **C_{18}-SPM**, both consisting of a saturated chain (C_{18}) as the hydrophobic part as well as the previously utilized polyamine; spermidine (SPD) and spermine (SPM) (Fig. 5-6), which exhibited the best binding results for heparin and DNA, respectively. Beyond these simple structural modifications, two PEG lipids, **C_{18}-PEG-3** and **C_{18}-PEG-8** (Fig. 5-5), were then synthesised and co-assembled in 1 and 10 mol% compositions, with the intention of gaining an understanding of the influence of this second component on binding strength, selectivity towards DNA or heparin, and stability and activity in highly competitive biologically relevant conditions such as human serum.

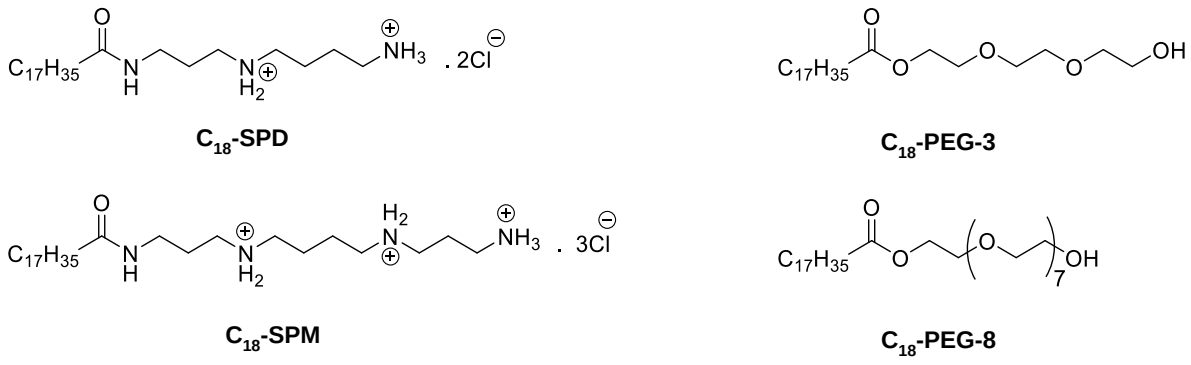

Fig. 5-6 Structures of the investigated binders **C_{18}-SPD** and **C_{18}-SPM** as well as the PEG lipids **C_{18}-PEG-3** and **C_{18}-PEG-8**.

For **C_{18}-SPD** and **C_{18}-SPM**, we used **Boc-SPD** and **Boc-SPM** respectively (previously synthesized in Chapter 3), which were coupled with stearic acid (C_{18} saturated hydrophobic chain).

The coupled compounds were then purified and deprotected by HCl (individually) **C_{18}-SPD** was achieved in overall 36% yield and **C_{18}-SPM** gave 32% yield (Scheme 5-1).

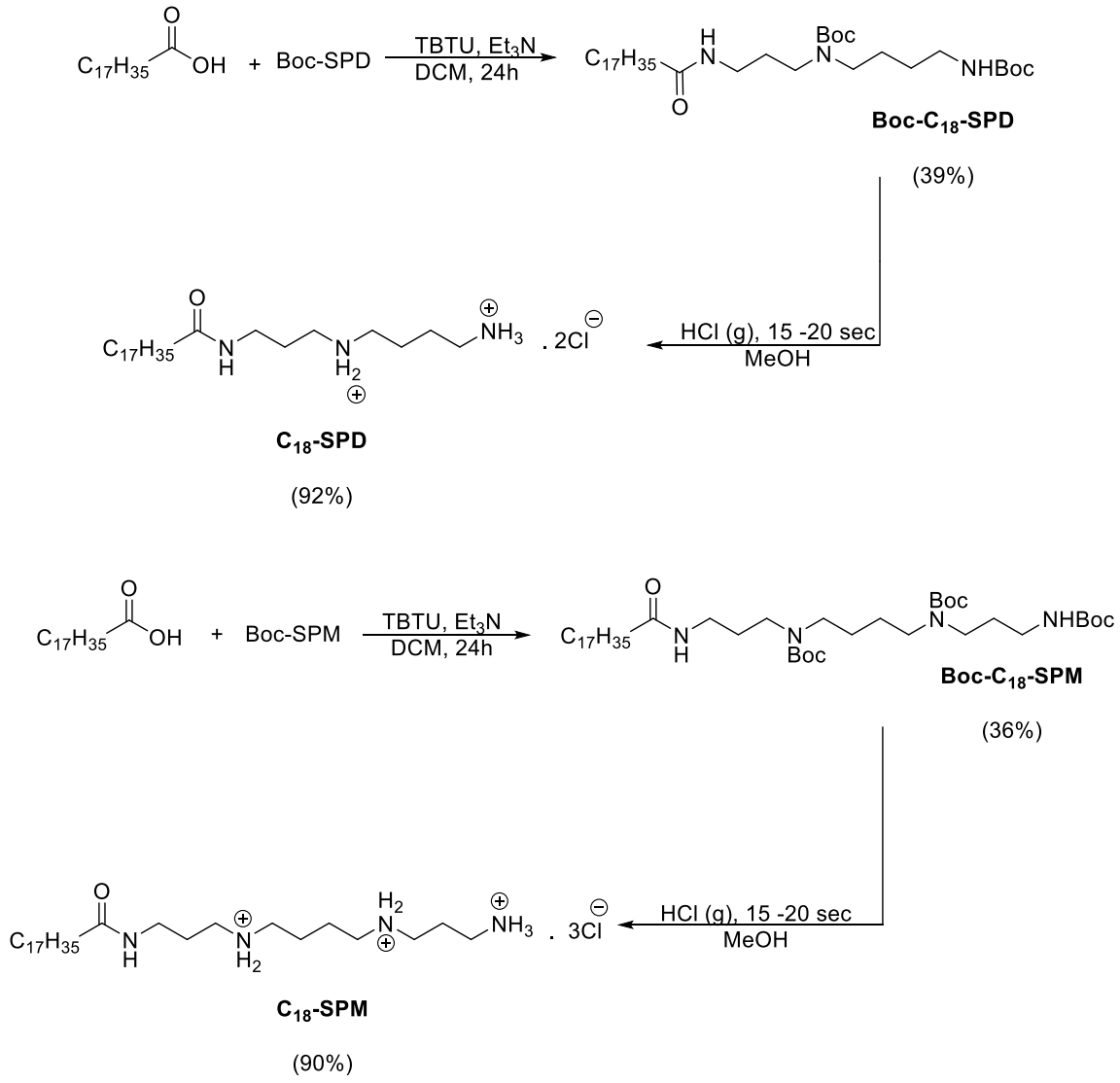

Scheme 5-1 Synthesis of **C_{18}-SPD** and **C_{18}-SPM** SAMul binders.

For the PEG lipids, non-literature based, simple acid-catalysed condensation was chosen for the synthesis of **C_{18}-PEG-3** due to the low cost of the reactants; stearic acid and triethylene glycol (Scheme 5-3). The compound needed purification by column chromatography (SiO_2, 2:1 v/v, hexane/ethyl acetate), and was obtained as yellow powder in 32% yield (Scheme 5-2). The product fully characterized and its high purity confirmed by all available techniques (see experimental section for details).

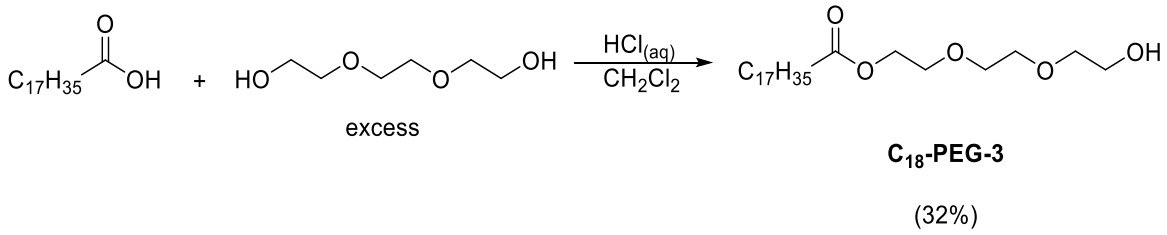

Scheme 5-2 Synthesis of **C_{18}-PEG-3**.

The coupling agent TBTU was used for the synthesis of **C_{18}-PEG-8** from octaethylene glycol and stearic acid in order to minimise the quantities of the more expensive octaethylene glycol. The scale of this non-literature based method could thereby be decreased significantly whilst still producing a sufficient quantity for the desired studies. The mixture was stirred overnight and then dried before it was purified by column chromatography (SiO_2, 1:1 v/v, hexane/ethyl acetate, then 100% ethyl acetate) and was obtained as sticky off-white product in 27% yield (Scheme 5-3). The product was characterised by all available techniques (see experimental section for details) and obtained in high purity.

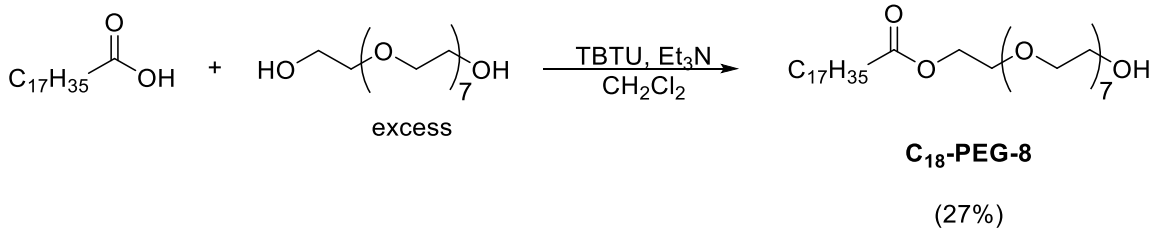

Scheme 5-3 Synthesis of **C_{18}-PEG-8**.

5.4 Self-Assembly Studies

5.4.1 Nile Red Assay

Self-assembly of **C_{18}-SPD** and **C_{18}-SPM** was characterized by the Nile Red assay, as described before, to determine their CAC values. The measurements were done before and after inserting the PEG lipids (Table 5-1).

Compound	PEG lipid	PEG lipid mol%	CAC (μM)
C_{18}-SPD	None	—	48.2 ± 2.1
C_{18}-SPD	C18-PEG–3	10%	52.5 ± 1.7
C_{18}-SPM	None	—	57.6 ± 0.9
C_{18}-SPM	C18-PEG–3	10%	31.6 ± 2.1
C_{18}-SPM	C18-PEG–8	10%	35.9 ± 1.2

Table 5-1 CAC values [μM] for the SAMul binders and mixed aggregates with **C_{18}-PEG–3** or **C_{18}-PEG–8**. **C_{18}-SPD** values measured in PBS buffer, **C_{18}-SPM** values measured in Tris + NaCl buffer.

C_{18}-SPD self-assembled at a concentration of 48.2 ± 2.1 μM in PBS buffer, which is different to the previously reported **C_{16}-SPD** (Chapter 3), which did not dissolve in PBS buffer and had to be examined in Tris-HCl (10 mM) in the presence of NaCl (150 mM). This observation suggests that the longer stearic acid chain provides sufficient hydrophobic force to overcome the electrostatic repulsions on the surface of the nanostructure between the cationic protonated SPD groups and hence enable self-assembly and solubility. It was however necessary to initially encourage the self-assembly by gentle heating, consistent with the self-assembly being entropically driven. **C_{18}-SPM** however, did not dissolve in PBS buffer unless heated vigorously. We therefore

decided to dissolve it in Tris buffer + NaCl. **C_{18}-SPM** (+3 charges) self-assembled at 57.6 ± 0.9 (Table 5-1), although comparison with **C_{18}-SPD** cannot really be made because of the different buffer.

It is worth noting that the different solubility in PBS compared to Tris is probably a result of interactions between the phosphate anions of the buffer and the cationic self-assembled structures lowering the overall solubility. In Tris, the counterions are chloride and will not interact in the same way with the SAMul nanostructures.

The introduction of the second component, **C_{18}-PEG-3** (10 mol%) to **C_{18}-SPD** did not have a major effect on the CAC, which increased slightly from 48.0 ± 2.1 to 53.0 ± 1.7 μM. However, these values are within the error range of one another. The spermidine head group possesses two nominal cationic charges and the incorporation of the PEG lipid was anticipated to reduce those to some extent. However, the PEG lipids somewhat decreased solubility and we suggest this offsets any benefit from the loss of charge-charge interactions in this case. Furthermore, this study was performed in PBS and the phosphate ions will be interacting with **C_{16}-SPD** – potentially lowering the effective CAC. Limited quantities of **C_{18}-SPD** meant that the experiment with 10 mol% **C_{18}-PEG-8** could not be carried out, nor could the buffer be changed to Tri-HCl.

The addition of the second component **C_{18}-PEG-3** or **C_{18}-PEG-8** to **C_{18}-SPM** had a much more significant effect decreasing the CAC from 58 to ca. 35 μM. Both PEG lipids seem to decrease the aggregation concentration to a similar extent. This distinct difference to **C_{18}-SPD** is suggested to result from the more severe charge-charge repulsions on the micellar surface that can be lowered by either PEG lipid. Furthermore, the studies are in Tris buffer and the counterions will not be binding to the SAMul surface – hence the PEG lipid will also have a more significant effect.

5.4.2 Dynamic Light Scattering (DLS)

The effects on surface charge and nanoscale dimensions of co-assembling **C_{18}-PEG-3** or **C_{18}-PEG-8** with **C_{18}-SPD** and **C_{18}-SPM** were then determined by DLS. The size and zeta potential of the nanostructures are important tools in assessing possible effects on polyanion binding capabilities. These studies were all carried out in Tris buffer (10 mM) in the presence of NaCl (150 mM) (Table 5-2) – preventing any possible problems with PBS buffer binding to the micelles.

Compound	PEG lipid	PEG lipid mol%	Volume distribution (nm)	Zeta potential (mV)
C_{18}-SPD	None	—	10.2 ± 0.3	+49.8 ± 1.6
C_{18}-SPD	C_{18}-PEG-3	1%	9.7 ± 0.1	+36.2 ± 4.3
C_{18}-SPD	C_{18}-PEG-3	10%	10.7 ± 0.3	+35.1 ± 3.1
C_{18}-SPD	C_{18}-PEG-8	1%	9.5 ± 0.2	+39.3 ± 6.2
C_{18}-SPD	C_{18}-PEG-8	10%	11.6 ± 0.7	+53.6 ± 2.6
C_{18}-SPM	None	—	9.8 ± 0.4	+33.8 ± 10.5
C_{18}-SPM	C_{18}-PEG-3	1%	10.9 ± 2.0	+45.2 ± 10.1
C_{18}-SPM	C_{18}-PEG-3	10%	*unobtainable*	+45.2 ± 6.3
C_{18}-SPM	C_{18}-PEG-8	1%	*unobtainable*	+45.6 ± 10.1
C_{18}-SPM	C_{18}-PEG-8	10%	19.1 ± 4.5	+37.4 ± 11.6

Table 5-2 Zeta potential (mV) and average diameter (nm) assessed by zeta sizing and intensity distribution in DLS measurements (Tris + NaCl buffer, pH 7.4) at 25 °C.

C_{18}-SPD had a high overall surface charge of +50 mV and a diameter of ca. 10 nm. Conversely, **C_{18}-SPM** had a surface charge of only +34 mV and a diameter of around 10 nm. **C_{18}-SPM** has three positive charges on its surface group and it would be expected to have a higher zeta potential than for **C_{18}-SPD** with two cationic surface charges. We postulated that this reflects the charge-charge repulsions that do not allow the formation of such densely packed nanostructures resulting in a decreased overall surface charge. Similar effects were seen in Chapter 3.

The insertion of uncharged ethylene glycol-type surfactants into cationic assemblies was expected to decrease the overall surface charge density and indeed, this is the case for **C_{18}- SPD** when co-assembled with 1 or 10 mol% **C_{18}-PEG–3** or 1 mol% **C_{18}-PEG-8**. The exception is **C_{18}-SPD** with 10 mol% **C_{18}-PEG-8**, where the overall surface charge slightly increased or, including the error margins, may be unaffected. The average diameter of the assembly with the addition of 1 mol% of either PEG lipid is somewhat decreased, but slightly increased when the lipid is present in 10 mol%, possibly as a result of more molecules being incorporated into each nanostructure.

Surprisingly, the addition of **C_{18}-PEG-3** in 1 or 10 mol% and **C_{18}-PEG-8** in 1 mol% to **C_{18}-SPM** increased the zeta potential. Since the **C_{18}-SPM** solutions remained cloudy without heating, this trend suggest that the insertion of an uncharged amphiphile facilitates self-assembly and thereby increases the surprisingly low starting zeta potential of **C_{18}-SPM**, i.e., the PEG lipid encourages the overall self-assembly process and hence more charged better packed structures can be formed than in its absence. Once 10 mol% of **C_{18}-PEG-8** has been added, the large uncharged moiety may be screening the charge and thereby reduces the zeta potential of the overall micellar nanostructure. The values in Table 5-2 were obtained at 25 °C but the sizes of the **C_{18}-SPM** mol% **C_{18}-PEG–3** as well

as the **C_{18}-SPM** 1 mol% **C_{18}-PEG-8** system were unobtainable under those conditions. Once 10% of PEG lipid was present, the system assembled at room temperature – supporting the view it assists nanostructure formation.

5.5 Binding Data

5.5.1 Heparin Binding

5.5.1.1 MalB Assay in Buffer

The MalB assay was then performed as described previously, on **C_{18}-SPD** and **C_{18}-SPM** before and after of the insertion of the PEG lipids (Table 5-3). It should be noted that under these assay conditions, both **C_{18}-SPD** and **C_{18}-SPM** showed excellent solubility.

Compound	PEG lipid	PEG lipid mol%	CE_{50}	EC_{50} (μM)
C_{18}-SPD	None	—	0.90 ± 0.02	48.7 ± 1.3
C_{18}-SPD	C_{18}-PEG-3	1%	0.76 ± 0.01	41.7 ± 0.6
C_{18}-SPD	C_{18}-PEG-3	10%	0.76 ± 0.03	45.9 ± 1.9
C_{18}-SPD	C_{18}-PEG-8	1%	0.99 ± 0.09	54.3 ± 4.7
C_{18}-SPD	C_{18}-PEG-8	10%	0.98 ± 0.01	49.4 ± 0.9
C_{18}-SPM	None	—	1.93 ± 0.10	69.7 ± 3.6
C_{18}-SPM	C_{18}-PEG-3	1%	2.13 ± 0.20	77.8 ± 7.4
C_{18}-SPM	C_{18}-PEG-8	1%	1.43 ± 0.15	51.9 ± 5.4

Table 5-3 CE_{50} and EC_{50} values (in 150 mM NaCl and 10 mM Tris HCl), for **C_{18}-SPD**, **C_{18}-SPM** and multicomponent systems with 1 or 10 mol% **C_{18}-PEG-3** or **C_{18}-PEG-8**.

From Table 3-5 we can observe that **C_{18}-SPD** showed effective binding for heparin with a CE_{50} value of 0.90 ± 0.02. However, **C_{18}-SPM** with its three cationic charges performed much worse exhibiting a CE_{50} value of 1.93 ± 0.10. This suggests that self-assembly of **C_{18}-SPM** under the assay conditions is incomplete or that the precise structural details are simply not well optimised for heparin binding. This is in agreement with the discussions above about the relatively ineffective packing of **C_{18}-SPM** (as noted by DLS).

Interestingly, the insertion of **C_{18}-PEG-3** (1 or 10 mol%) lowered the CE_{50} value of **C_{18}-SPD** from 0.90 to 0.76 (Table 5-3). It appears that this effect is already induced at 1 mol% and does not scale with a higher concentration (10 mol%), in agreement with prior observations in the binding of DNA by mixed aggregates.[113] We suggest that the increased solubility of the co-assembly enhanced its heparin binding ability. However, mixed aggregates consisting of **C_{18}-SPD** and the larger **C_{18}-PEG-8** (1 or 10 mol%) showed slightly increased CE_{50} values of 0.99 and 0.98, respectively. It is possible that the insertion of **C_{18}-PEG-8** results in partial blockage of the micellar surface owing to the greater length of the uncharged PEG chain. This would suggest that the larger PEG moiety shields charge and the increased solubility does not compensate for the reduction in the surface charge.

The performance of **C_{18}-SPM** was essentially unaffected by **C_{18}-PEG-3** but was improved slightly by **C_{18}-PEG-8**. This is different to the effect of **C_{18}-PEG-8** on **C_{18}-SPD** and may suggest that its role with **C_{18}-SPM** is to facilitate self-assembly and binding – in agreement with the observations above about the ineffective assembly of this compound.

5.5.1.2 MalB Assay in Human Serum

We then wanted to determine whether the improvements in heparin binding are transferable into the biologically more relevant medium of human serum. We reasoned that the PEG additive, by screening the micellar surface charge, may improve stability and hence activity in serum. Therefore, the MalB assay in human serum was performed on **C_{18}-SPD** as it showed more binding ability (in buffer) than **C_{18}-SPM** (Table 5-3).

Compound	**PEG lipid**	**PEG lipid mol%**	**CE_{50}**	**EC_{50} (μM)**
C_{18}-SPD	None	—	1.19 ± 0.01	64.1 ± 0.3
C_{18}-SPD	C_{18}-PEG-8	1%	1.07 ± 0.02	58.3 ± 1.3

Table 5-4 CE_{50} and EC_{50} values (in human serum) for **C_{18}-SPD** and the multicomponent systems consisting of **C_{18}-SPD** with 1 mol% **C_{18}-PEG-8**.

The results from Table 5-4 clearly suggest that the second component **C_{18}-PEG-8** may stabilise the micelles and cause slightly increased binding affinity in human serum. The binding ability of **C_{18}-SPD**, however, appears to be slightly weakened compared to the heparin binding in buffered solution (Table 5-3). This may be due to partial disassembly of the nanostructures. Importantly, the obtained CE_{50} value in the presence of the stabilising PEG lipid of 1.07 ± 0.02 is still good – in particular when the benefits of the SAMul approach are considered. This preliminary result therefore suggests that PEG lipids may have some role to play in stabilizing our SAMul nanostructures in serum, and enhancing performance.

5.5.2 DNA Binding

DNA binding affinities were measured using ethidium bromide displacement assay as described previously. The data from Table 5-5 shows that the CE_{50} values of 0.85 and 6.63 for **C_{18}-SPD** and **C_{18}-SPM**, respectively, demonstrated a very different ability towards DNA for these two systems. **C_{18}-SPD** has a high affinity for DNA, whereas, the very high CE_{50} value for **C_{18}-SPM** suggested that the self-assembly is impeded and the multivalent organisation cannot be fully formed as discussed above.

Compound	PEG lipid	PEG lipid mol%	CE_{50}	EC_{50} (μM)
C_{18}-SPD	None	—	0.85 ± 0.13	1.70 ± 0.25
C_{18}-SPD	C_{18}-PEG-3	1%	0.25 ± 0.01	0.57 ± 0.10
C_{18}-SPD	C_{18}-PEG-3	10%	0.13 ± 0.06	0.30 ± 0.01
C_{18}-SPD	C_{18}-PEG-8	1%	0.39 ± 0.08	0.79 ± 0.02
C_{18}-SPD	C_{18}-PEG-8	10%	0.10 ± 0.07	0.22 ± 0.15
C_{18}-SPM	None	—	4.63 ± 0.98	6.18 ± 1.32
C_{18}-SPM	C_{18}-PEG-3	1%	1.36 ± 0.07	1.83 ± 0.09
C_{18}-SPM	C_{18}-PEG-3	10%	0.91 ± 0.12	1.34 ± 0.19
C_{18}-SPM	C_{18}-PEG-8	1%	0.27 ± 0.03	0.55 ± 0.06
C_{18}-SPM	C_{18}-PEG-8	10%	0.30 ± 0.04	0.67 ± 0.09

Table 5-5 DNA binding efficiency (in buffer); CE_{50} and EC_{50} values for **C_{18}-SPD**, **C_{18}-SPM** and multicomponent systems with 1 or 10 mol% **C_{18}-PEG-3** or **C_{18}-PEG-8**.

Several reports indicate that the structure of spermine is optimised for the binding of DNA[302] and hence stronger binding affinities might be expected. We suggest that the high surface charge of the SPM ligands make it hard for the C_{18} chain to nucleate self-assembly especially at the very low concentrations of this particular assay.

Remarkably, the introduction of the second component **C_{18}-PEG-3** to **C_{18}-SPD** in 1 or 10 mol% has an enormous influence on the binding affinity in this assay, yielding CE_{50} values of 0.25 and 0.13, respectively (Table 5-5). A similar trend is observed for the mixed aggregates with **C_{18}-PEG-8**, where the binding affinity is also greatly increased. In this system, the 10 mol% PEG lipid yields a higher binding affinity than the 1 mol% PEG lipid. In the 10 mol% **C_{18}-PEG-8** to **C_{18}-SPD** system, only 0.10 positive charges are required for each anionic charge on DNA to displace half of the EthBr. As such the presence of PEG lipids very significantly improves DNA binding.

The insertion of just 1 mol% **C_{18}-PEG-3** to **C_{18}-SPM** already has a major influence on the binding affinity; presumably due to increased solubility and reductions in electrostatic repulsions. Increasing to 10 mol% **C_{18}-PEG-3** yields an even lower CE_{50} value. Mixed aggregates with **C_{18}-PEG-8** lower this binding affinity even further to around 0.3 with virtually no difference observable between 1 and 10 mol%. This trend clearly suggests the severe electrostatic repulsions on the head groups and that the insertion of an uncharged second component greatly reduces them (Table 5-5). This enables self-assembly and switches of full SAMul binding towards DNA.

Notably, the EC_{50} values obtained from the DNA assays were much lower than the CAC values obtained in the Nile Red assay (up to 175-fold decrease), suggesting that the presence of DNA assists the aggregation of those poorly assembling binders. Indeed

charge-charge repulsions between the cationic surface charges are very likely to be reduced by the anionic charges present.[229,303] This suggests that multivalent binding can positively influence self-assembly, as well as vice versa. This effect seems to be more noticeable for DNA binding than heparin binding, which may be associated with the lower concentration of the DNA assay making self-assembly the key limitation in terms of activity. It is also worth noting that the impact of PEG lipids on binding DNA here is much more significant than in the example previously reported by Barnard et. al.[113] This may reflect the less effective initial assembly of the ligands in this study.

Overall, the results from this work, performed by Constantin Voll under my supervision, demonstrated that PEG-lipids could be useful additives and significantly improve polyanion binding (DNA) as well as potentially improving serum stability (heparin).

5.6 MalB Assay

We were then interested in other mixtures of self-assembling components and the impact of mixing on polyanion binding. This study was performed in collaboration with postdoctoral researcher Ana Rodrigo who has been developing methodology for screening heparin binding – all the compounds used in these studies were synthesized by me.

We performed a multicomponent MalB assay on some of our synthesized SAMul systems in buffer for heparin binding. In the pharmaceutical industry, screening assays such as high-throughput screening (HTS) assays are common. In general, they involve the process of rapidly differentiating the tested compounds; those that target active vs. those that are inactive.[304] In this step we screened mixtures that consisted of **Binder 2** (Fig 2-

1) which contained unsaturated hydrophobic chain (2 alkene groups), **C_{16}-DAPMA** (Fig. 3-1) which contained shorter saturated hydrophobic chains.

For those mixtures, we performed two assays. Firstly, we varied the charge ratio; the variation of the charge ratio was **C_{16}-DAPMA**:**Binder 2** (50:50), (+: -) = 0.1/, 0.2, 0.25, 0.4, 0.5, 0.75, 1, 1.5, 1.75 and 2. The assay data (Fig. 5-7) showed the effect that alkene groups have on disrupting the binding to heparin by increasing the CE_{50} values. **C_{16}-DAPMA** binds heparin most effectively, whereas **Binder 2** is much less effective because the bent alkene disrupts hydrophobic packing. The 50:50 mixture behaved similarly to **Binder 2**, suggesting that the bent alkene dominates the behaviour of the mixture.

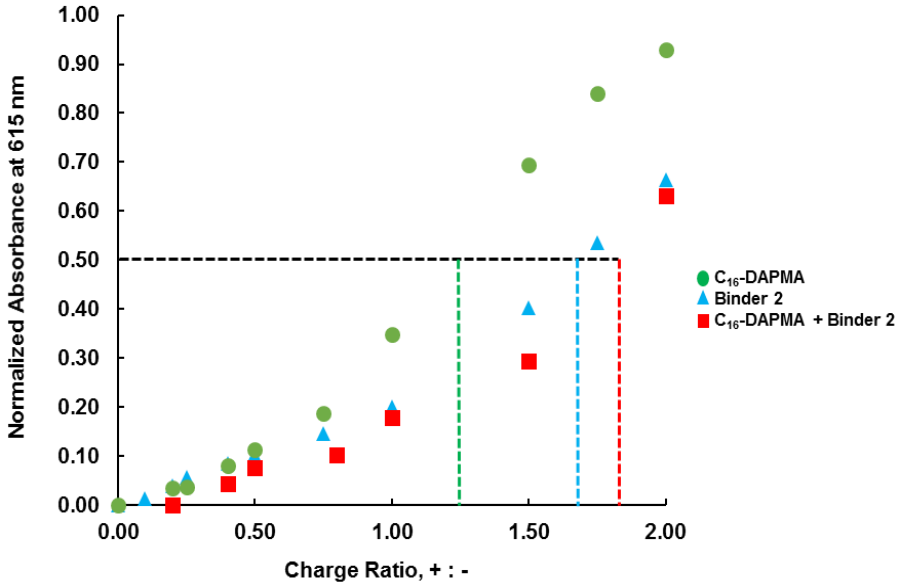

Fig. 5-7 MalB assay (in buffer); charge ratio against normalized absorbance at 615 nm of **Binder 2**, **C_{16}-DAPMA** and mixtures of both binders using variations of charge ratio showing the effect of mixing different SAMul systems on binding heparin.

In the second assay the charge ratio was kept at (+ : -) = 1.0 and the amount of each binder varied as follows; **C_{16}-DAPMA**:**Binder 2** = 0:100, 15:85; 25:75, 40:40, 50:50, 60:40, 75:25, 85:15 and 100:0 (Fig. 5-8). This provides a rapid insight into ability of different binder mixtures to displace MalB from its complex with heparin. The higher the absorbance value, the more MalB displaced and the better the binder is.

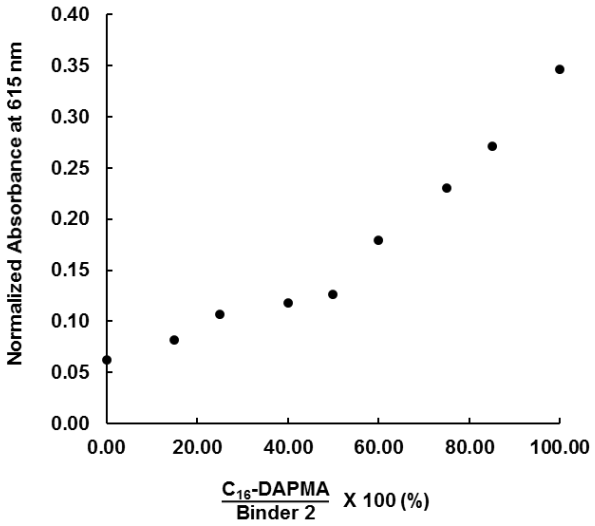

Fig. 5-8 MalB assay (in buffer) for **C_{16}-DAPMA**:**Binder 2** mixture at 0:100, 15:85; 25:75, 40:40, 50:50, 60:40, 75:25, 85:15 and 100:0.

It is clear that with more than 50% of **Binder 2** present, very little MalB is displaced from the complex. However, once less than 50% **Binder 2** is present the binding ability of **C_{16}-DAPMA** begins to exert an influence.

It is apparent that the mixing relationship is non-linear. This indicates that even relatively small amounts of **Binder 2** disrupt the binding quite significantly. This is in agreement with a view that the bent alkene limits self-assembly and hence inhibits effective multivalent binding – even if only small amounts of it are present as an additive.

As such, this assay allows rapid assessment of mixtures of self-assembling components to determine whether they have a neutral influence on one another (linear relationship), a negative influence on one another (concave plot, as here) or a positive synergistic influence when mixed (convex plot).

We anticipate this approach may help identify mixtures of self-assembling components which have positive synergistic effects. Ana Rodrigo is investigating other mixtures of

self-assembling lipids to determine whether this is the case, and results will be reported by her elsewhere.

5.7 Conclusions and Future Work

MChem student Constantin Voll synthesized two novel SAMul binders, **C_{18}-SPD** and **C_{18}-SPM**, and they were analysed in terms of self-assembly, size, surface charge as well as binding affinities towards heparin and DNA. Their mixed aggregates with **C_{18}-PEG-3** and **C_{18}-PEG-8** were investigated to see if the uncharged nature of these lipids can influence self-assembly without effecting binding efficiency to the polyanions heparin and DNA. Both PEG lipids induced observed changes in size and surface charge. **C_{18}-SPD** performed better in binding to heparin and insertion of **C_{18}-PEG-3** in both 1 and 10 mol% increased the binding strength. However, mixed aggregates with **C_{18}-PEG-8** performed worse under those assay conditions. The binding results for **C_{18}-SPD** suggested that this approach of co-assembly may also enhance and inforce heparin binding in human serum. The **C_{18}-SPD** 1 mol% **C_{18}-PEG-8** system outperformed **C_{18}-SPD** binder on its own in human serum indicating that the PEG lipid may stabilize these assemblies somewhat in this competitive environment. These results are promising for the development of clinical heparin reversal agents since the introduction of just 1 mol% of a simple uncharged species may have an influence on binding strength in the clinically relevant medium. Future research may synthesize the corresponding PEG lipid for the **C_{22}-G1** binder, which is an inherently much better heparin binder than **C_{18}–SPD** and may decrease the dose that would be needed to be given to a patient and significantly enhance its serum stability. It may also limit off target interactions *in vivo* – future work will need to probe this.

In addition, mixed SAMul multicomponent systems based on systems synthesized by me were tested in collaboration with Ana Rodrigo using MalB assay. The systems consisted of mixtures of **C_{16}-DAPMA** and **Binder 2**; the components were varied in terms of charge ratio as well as concentration. The results indicated that the alkene disrupts self-assembly and even relatively small amounts limited the performance of a better binder. In the future, this approach may help us rapidly uncover positive synergistic binding effects in mixed lipid systems.

6 Conclusions and Future Work

6.1 Conclusions

In this work we synthesized a number of multivalent systems, most of which were based on a self-assembly approach. These systems were self-assembled multivalent (SAMul) nanostructures with two significant parts; hydrophilic (binding site) and hydrophilic (as driving force for the assembly). All the synthesized systems were designed to have positive surface charges in order to be able to bind, electrostatically, different polyanions such as heparin and DNA. All the compounds/systems in this work were tested in terms of their binding ability towards heparin using the MalB assay, and most of them were tested towards binding DNA using the EthBr assay. Prior to those tests most of these compounds were tested for their self-assembly ability using Nile Red assay (2. 4. 1), to determine their CACs. In addition, DLS characterizations for particle size and zeta potential were performed on all the compounds.

In the first Results and Discussions chapter (Chapter 2) we synthesized three compounds using different unsaturated acids as the hydrophobic part (Fig 2-1). The variation of the alkene group in those compounds, from one to three, induced significant selectivity towards different biological polyanions (heparin and DNA), in addition to different binding ability in competitive conditions such as human serum. We found that human serum disrupted self-assembly and heparin binding. We suggested that the more organized and tightly packed nanostructures are better able to bind heparin while the looser ones are preferentially bound by DNA. The presence of more alkenes disrupts surfactant packing.

Those three systems were also cross-liked in an attempt to stabilize them when binding to heparin or DNA. The cross-linking process was performed using a radical initiator

agent AIBN (Fig 2-29) for the polymerization reaction. However, the cross-linking reaction for the binder with one alkene group (**Binder 1**) was not achieved, while **Binder-3** with the most alkene groups it was the highest conversion. However, cross-linking did not significantly improve polyanion binding or serum stability.

In Chapter 3, we made modifications to the ligands using DAPMA, SPD and SPM, but kept the hydrophobic part unchanged as a saturated C_{16} chain (Fig 3-1). We found that for C_{16} ligands, **C_{16}-SPM** is optimal for DNA binding, while **C_{16}-SPD** is optimal for heparin binding. Also, electrostatic ion–ion binding depends on structural detail, not only charge density – as confirmed by the complementary experimental methods of competition binding assays and isothermal calorimetry. Molecular simulation studies led us to propose that the shape-persistence (DNA), or adaptability (heparin) of the polyanionic targets help mediate the selectivity of interaction with different ligands.

Other alternative approaches to stabilizing multivalent displays of heparin-binding ligands were employed in Chapter 4. Three systems were synthesized based on a branched scaffold (**Binder-Dend**), gold nanoparticles (**Binder-NC**) and a polymer (**Binder-Poly**). For the first system (**Binder-Dend**), although it had more positive charges (6 +ve) than the previously reported binders, did not show improved binding as they were not being organized effectively on the nanoscale. For the second (**Binder-NC**), solubility difficulties in buffer owing to aggregation of nanoparticles into a nanocomposite, meant less binding to heparin, from MalB assay results. We had to perform the assay at elevated temperatures (50-55 °C and >80 °C) – however the assay results showed that replacement of MalB was incomplete. This could be due to AuNPs interfering with the UV-Vis absorbance around $Abs_{max} \approx 700$ nm as well as the solubility difficulties. The third system (**Binder-Poly**), was synthesized using poly(acrylic acid):DAPMA (1:1). TEM images for

this system showed a highly defined spherical aggregation when binding to heparin (Fig. 4-21). The MalB assay results were somewhat promising; $CE_{50} = 2.0 \pm 0.03$ in buffer and $CE_{50} = 4.2 \pm 0.5$ in human serum a rather more stable binding than the other systems reported in the same chapter. There is clearly scope to look at more tailored modified polymers in the future.

In the final results chapter (Chapter 5), a multicomponent approach was tested for binding heparin and DNA. Two compounds; **C_{18}-SPD** and **C_{18}-SPM** were synthesized then introduced to PEG lipids (uncharged species); **PEG-3** and **PEG-8** (Fig. 5-6) to test the effect of mixture on binding heparin and DNA. **C_{18}-SPD** performed better in binding to heparin and insertion of **C_{18}-PEG-3** in both 1 and 10 mol% increased the binding strength. However, mixed aggregates with **C_{18}-PEG-8** performed worse under those assay conditions. The **C_{18}-SPD** 1 mol% **C_{18}-PEG-8** system outperformed **C_{18}-SPD** binder on its own in human serum indicating that the PEG lipid may stabilize these assemblies somewhat in this competitive environment. In addition, mixed SAMul multicomponent systems based on **C_{16}-DAPMA** and **Binder 2** were tested using MalB assay. The results indicated that the alkenes disrupt self-assembly and even relatively small amounts limited the performance of a better binder on mixing. In the future, this assay may also help identify synergistic binding effects on mixing.

Ion-ion binding is often considered as non-directional and as such only depends on the charge density of the species involved – however, these studies clearly demonstrate that under competitive biological conditions, the choice of hydrophobic group and its capacity to display and orientate the ligands has a major role in tuning the binding affinity. Furthermore, the precise choice of ligand and the presence of additives can have significant effects.

Overall, we observed that polyanions (heparin/DNA) play a role in facilitating self-assembly event and hence switching on the multivalent binding effect, and suggest that specifics of ligand-polyanion interactions help mediate subtle differences in this overall process. These results provide an intriguing insight into molecular recognition processes at nanoscale surfaces and suggest that SAMul nanostructures may deliver some selectivity in addressing the challenging problem of the 'polyanion world'.

6.2 Future Work

For future work, the unsaturated hydrophobic tails could be longer, with more alkene groups, to achieve more cross-linking between them. This would allow us to test the effect of more alkene density in such systems. In addition, two tails could be used to enhance the self-assembly hence, ability to bind to heparin. This should encourage the formation of vesicle structures and significantly enhance serum stability. By tuning these head groups and tails, we can modify the binding abilities of the SAMul nanostructures to heparin and DNA; nanoscale biological polyanions.

For the branched system, **Binder-Dend**, binding performance could be enhanced by using more than one hydrophobic group in order to improve the self-assembly or by increasing the dendritic generation so the number of ligands is greater. Also, for the system based on thiol stabilized gold nanoparticles, improved binding to heparin could be achieved if this system was introduced to a different thiol group (longer); with a spacer group to help optimize ligand display, or incorporate more positive charges on the hydrophilic group (binding site). In addition, **Binder-Poly** system, based on a polymer backbone, could be synthesized with different ratios of polymer:DAPMA, other than 1:1 that we used in this

work. These variations could facilitate loading of more ligands onto the polymer, hence more positive charges that would bind heparin/DNA. Moreover, different polymer backbones could also be tested to try and avoid any non-specific interactions with serum proteins which may be disrupting the binding process in these highly competitive conditions.

Future research may synthesize the corresponding PEG lipid for the **C_{22}-G1** binder, which is an inherently much better heparin binder than **C_{18}–SPD** and may decrease the dose that would be needed to be given to a patient and significantly enhance its serum stability. The multicomponent approach may help us uncover positive synergistic binding effects, this will be achieved by investigating other mixtures to determine whether this is the case.

7 Experimental

7.1 Synthetic Materials and Methods

All reagents were purchased from commercial sources and were used directly without any further purification unless stated. Thin layer chromatography (TLC) was performed on Merck aluminium-backed plates coated with 0.25 nm silica gel 60; flash column chromatography was performed on silica gel 60 (35-70 μm) supplied by Fluka Ltd and preparative gel permeation chromatography (GPC) was performed on Biobeads SX-1 supplied by Bio-Rad.

NMR spectra were recorded on a JEOL ECX400 (^{1}H 400 MHz, ^{13}C 100 MHz) spectrometer. HRMS and ESI mass spectra were recorded on a Bruker Daltonics Micro-Tof mass spectrometer. Infrared spectra were recorded on Shimadzu IRPrestige-21 FT-IR spectrometer. Melting points were measured on a Stuart SMP3 melting point apparatus and are uncorrected.

7.1.1 Chapter 2

Synthesis of Mono-Boc DAPMA (Compound 1)[171]

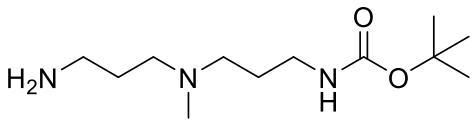

Chemical Formula: $C_{12}H_{27}N_3O_2$
Molecular Weight: 245.37

N,*N*-Di-(3-aminopropyl)-*N*-methylamine (DAPMA) (50 mL, 310 mmol) was dissolved in THF (200 mL) and cooled to 0 °C. Di-(tert-butyl) dicarbonate (Boc_2O) (12.5 g, 57.2 mmol) was dissolved in THF (50 mL) and added dropwise to the amine solution over 2

h. Then the reaction was quenched with water (25 mL). The solvent was dried and the residue was taken up in aqueous NaOH (pH >10, 1 M) and extracted with DCM (80 mL). The organic layer was washed with citrate (citric acid solution) (pH > 4-5, 1 M). The water layers (which contain the product) were combined and basified to pH > 10 with 4 M NaOH. The mono-protected product was then extracted with DCM (80 mL). The organic phases were combined, dried over $MgSO_4$, filtered and the solvent evaporated then the product was dried *in vacuo.* The product was a colorless oil (5.5 g, 39%).

R_f = 0.3 (4:1 MeOH:aqueous ammonia). ^{1}H NMR (DMSO d_6 400 MHz) δ: 6.76 (br t, N*H*, *J* = 5.5 Hz, 1H); 2.88 (app q, C*H*$_2$NHCO, *J* = 6.1 Hz, 2H); 2.50 (t, C*H*$_2$NH$_2$, *J* = 6.7 Hz, 2H); 2.31 (t, C*H*$_2$NCH$_3$, *J* = 7.0 Hz, 2H); 2.27 (t, C*H*$_2$NCH$_3$, *J* = 7.3 Hz, 2H); 2.02 (s, NC*H*$_3$, 3H); 1.47 (app. quin., C*H*$_2$CH$_2$NHCO and C*H*$_2$CH$_2$ NH$_2$, *J* = 6.9 Hz, 4H); 1.38 (s, CC*H*$_3$, 9H). ^{13}C NMR (DMSO d_6 100 MHz) δ: 156.45 (*C*=O); 77.21 (*C*CH$_3$); 55.03, 54.90 (*C*H$_2$NCH$_3$); 41.76 (NC*H*$_3$); 39.73 (*C*H$_2$NHCO); 38.34 (*C*H$_2$NH$_2$); 30.20 (*C*H$_2$CH$_2$NHCO); 28.14 (C*C*H$_3$); 27.21 (*C*H$_2$CH$_2$NH$_2$). HRMS: Calc. $[M+H]^+$ ($C_{12}H_{28}N_3O_2$) m/z = 246.2176, found $[M+H]^+$ = 246.2173 (100%). IR: ν_{max} (cm^{-1}): 3350.3*m* (N-H); 2975*w*, 2931*s*, 2797*s* (all CH); 1795*s* 1621*s* (C=O); 1454*w*, 1391*w*, 1367*s*, 1277*w*, 1250*m*, 1173*w*.

Coupling of Boc-DAPMA and Oleic Acid (Mono-Unsaturated-C$_{18}$-Boc-DAPMA)

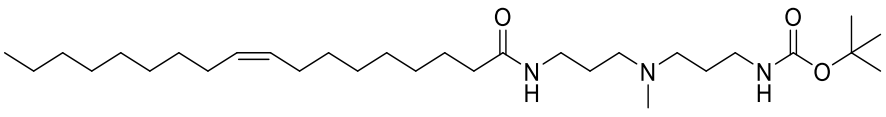

Chemical Formula: $C_{30}H_{59}N_3O_3$
Molecular Weight: 509.82

Oleic acid (1.00 g, 3.54 mmol) was dissolved in DCM (65 mL) then TBTU (1.25 g, 3.89 mmol) and Et_3N (5.4 mL) were added respectively. The mixture was stirred for 5 minutes

at room temperature. Compound **1** (0.87 g, 3.54 mmol) was dissolved in DCM (65 mL) then was added to the reaction flask. The reaction was stirred overnight, then the mixture was concentrated *in vacuo* and the residue was dissolved in EtOAc (50 mL) and washed with $NaHSO_4$ (2 x 15 mL, 1.33 M), $NaHCO_3$ (2 x 15 mL, saturated), deionized water (3 x 15 mL) and brine (15 mL, saturated). The organic layer was collected, dried over $MgSO_4$ and filtered (filter paper, 90 mm) then dried *in vacuo.* The product was concentrated and purified by gel permeation chromatography (GPC) column (Bio-beads, 100% DCM). The solvent was dried *in vacuo* and the product was a gluey oil (700 mg, 40%).

R_f = 0.3 (90:10:1 DCM/MeOH/Et_3N). ^{1}H NMR ($CDCl_3$, 400 MHz) δ: 6.85 (br s, N*H*, 1H); 5.34 (br s, N*H*Boc, 1H); 5.33-5.30 (m, C*H*CH, 2H); 3.33 (app q, CH_2NHCO, *J* = 6.0 Hz, 2H); 3.22 (app q, *CH*$_2$NCH$_3$, *J* = 6.0 Hz, 2H); 3.14 .58 (t, CH_2NCH$_3$, *J* = 6.4 Hz, 4H); 3.09 (q, CH$_2$CH_2CH, *J* = 7.2 Hz, 4H); 2.78 (s, NCH_3, 3H); 2.26 (t, CH$_2$CH_2CO, *J* = 7.6 Hz, 2H); 1.99-1.92 (m, CH_2CH$_2$NH, 4H); 11.41 (s, C(CH_3)$_3$, 9H); 1.27-1.29 (m, CH$_2$CH_2CH$_2$, 20H); 0.87 (t, CH_3CH$_2$, *J* = 6.4 Hz, 3H). ^{13}C NMR ($CDCl_3$, 100 MHz) δ: 176.15(*C*ONH); 156.16 (O*C*ONH); 129.82 (2 x *C*H=CH); 79.84 (*C*CH$_3$); 53.79 (*C*H$_2$NCH$_3$); 46.41 (N*C*H$_3$); 39.20 (*C*H$_2$NH); 37.25 (*C*H$_2$NHCO); 35.72 (*C*H$_2$CO); 34,68 (CH$_2$*C*H$_2$CO); 31.94 (*C*H$_2$CH); 29.80 (*C*H$_2$CH$_2$CH$_2$); 28.36 (C(*C*H$_3$)$_3$); 27.26 (*C*H$_2$CH$_2$NCH$_3$); 24.85 (*C*H$_2$CH$_2$NH); 22.72 (*C*H$_2$CH$_3$); 14.18 (*C*H$_3$CH$_2$). HRMS: Calc. $[M+H]^+$ ($C_{30}H_{60}N_3O_3$) m/z = 510.4629, found $[M+H]^+$ = 510.4647 (100%). IR: ν_{max} (cm^{-1}): 3287*m* (N-H); 3009*w*, 2926*s*, 2855*s* (all CH); 1638*s* (C=O); 1542*s* (C=O); 1464*m*, 1299*m*, 1272*m*, 1250*s*, 1171*s*, 1056m 1049*s*, 867*w*, 723*w*.

Deprotection of Mono-Unsaturated-C_{18}-Boc-DAPMA (Binder 1)

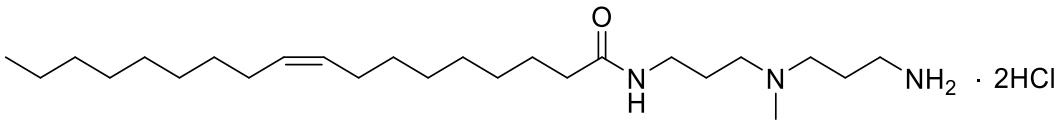

Chemical Formula: $C_{25}H_{53}Cl_2N_3O$
Molecular Weight: 482.62

Mono-unsaturated-C_{18}-Boc-DAPMA (700 mg, 1.37 mmol) was dissolved in methanol (25 mL) then HCl gas was applied for 15-20 seconds then the mixture was stirred for 3 hours and monitored by TLC. The solvent was dried *in vacuo* and the product was a gummy orange solid (600 mg, 91%).

R_f = 0.3 (90:10:1 DCM/MeOH/Et_3N). ^{1}H NMR (CD_3OD, 400 MHz) δ: 7.25 (br s, N*H*, 2H); 6.78 (br s, N*H*, 2H); 5.38-5.22 (m, C*H*CH, 2H); 5.16 (br s, N*H*, 1H); 3.27 (app q, C*H*$_2$NHCO, *J* = 12 Hz, 2H); 3.14 (app q, CH_2CH_2NH, *J* = 4.1 Hz, 2H); 2.72 (t, C*H*$_2$CH, *J* = 12.0 Hz, 2H); 2.37 (t, C*H*$_2$$NCH_3$, *J* = 12.0 Hz, 4H); 2.17 (s, NC*H*$_3$, 3H); 2.12 (t, CH_2CH_2CO, *J* = 8.0 Hz, 2H); 2.01 (q, C*H*$_2$CH, *J* = 8.0 Hz, 4H); 1.60 (m, C*H*$_2$$CH_2$NH, 4H); 1.32-1.22 (m, CH_2(C*H*$_2$)$_{10}$$CH_2$, 20H); 0.84 (t, C*H*$_3$$CH_2$, *J* = 8.0 Hz, 3H). ^{13}C NMR (CD_3OD, 100 MHz) δ: 172.55 (*C*ONH); 130.61 (2 x *C*H=CH); 56.51 (*C*H_2NCH_3); 47.23 (N*C*H_3); 40.70 (*C*H_2NH); 39.70 (*C*H_2NH_2); 36.82 (*C*H_2CO); 32.52 (*C*H_2CH_2CO); 31.91 (*C*$H_2CH_2CH_3$); 29.11 (*C*$H_2CH_2CH_2$); 27.15 (*C*H_2CH); 26.23 (*C*$H_2CH_2NCH_3$); 24.34 (*C*H_2CH_2NH); 22.62 (*C*H_2CH_3); 14.16 (*C*H_3CH_2). HRMS: Calc. $[M+H]^+$ ($C_{25}H_{52}N_3O$) m/z = 410.4105, found $[M+H]^+$ = 410.4097 (100%). IR: ν_{max} (cm^{-1}): 3285*w* (N-H); 3011*w*, 2924*s*, 2854*s* (all CH); 1634*s* (C=O); 1542*s* (C=O); 1465*m*, 1377*m*, 1248*m*, 1056*m*, 835*s*, 739m, 557*s*, 478*w*.

Coupling of Linoleic Acid and Boc-DAPMA (Di-Unsaturated-C_{18}-Boc-DAPMA)

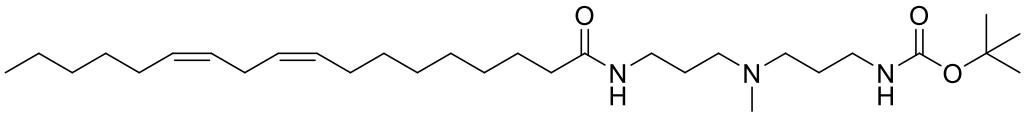

Chemical Formula: $C_{30}H_{57}N_3O_3$
Molecular Weight: 507.80

Linoleic acid (1.00 g, 3.56 mmol) was dissolved in DCM (65 mL) then TBTU (1.25 g, 3.89 mmol) and Et_3N (5.4 mL) were added. The mixture was stirred for 5 minutes at room temperature. Compound **1** (0.875 g, 3.56 mmol) was dissolved in DCM (65 mL) then was added to the reaction flask. The reaction was stirred overnight, then the mixture was concentrated *in vacuo* and the residue was dissolved in EtOAc (50 mL) and washed with $NaHSO_4$ (2 x 15 mL, 1.33 M), $NaHCO_3$ (2 x 15 mL, saturated), deionised water (3 x 15 mL) and brine (15 mL, saturated). The organic layer was collected, dried over $MgSO_4$ and filtered (filter paper, 90 mm) then dried *in vacuo.* The product was concentrated and purified by gel permeation chromatography (GPC) column (Bio-beads, 100% DCM). The product was a gluey orange solid (600 mg, 33%).

R_f = 0.3 (90:10:1 DCM/MeOH/Et_3N). ^{1}H NMR ($CDCl_3$, 400 MHz) δ: 6.78 (br s, N*H*, 1H); 5.38-5.22 (m, C*H*CH, 4H); 5.16 (br s, N*H*Boc, 1H); 3.27 (app q, CH_2NHCO, *J* = 12.0 Hz, 2H); 3.14 (app q, CH_2CH_2NH, *J* = 4.0 Hz, 2H); 2.72 (t, CHCH_2CH, *J* = 10.2 Hz, 2H); 2.37 (t, CH_2NCH_3, *J* = 7.8 Hz, 4 H); 2.17 (s, NCH_3, 3H); 2.12 (t, CH_2CH_2CO, *J* = 8.0 Hz, 2H); 2.01 (q, CH_2CH_2CH, *J* = 8.0 Hz, 4H); 1.60-1.58 (m, CH_2CH_2NH, 4H); 1.39 (s, C(CH_3)$_3$, 9H); 1.32-1.22 (m, $CH_2CH_2CH_2$, 16H); 1.25 (sxt, CH_2CH_3, *J* = 8.4 Hz, 2H), 0.84 (t, CH_3CH_2, *J* = 6.4 Hz, 3H). ^{13}C NMR ($CDCl_3$, 100 MHz) δ: 173.41 (*C*ONH); 156.16 (O*C*ONH); 130.23 (2 x *C*H=CH); 128.02 (2 x *C*H=CH); 79.06 (*C*CH_3); 55.69 (2 x *C*H_2NCH_3); 41.63 (N*C*H_3); 39.11 (*C*H_2NH); 38.12 (*C*H_2NHCO); 36.82 (*C*H_2CO); 31.55 (*C*H_2CH); 29.68 (7 x *C*$H_2CH_2CH_2$); 28.47 (C(*C*H_3)$_3$); 27.23 (*C*H_2CH_2NCH_3);

26.18 (*C*H_2CH_2NH); 25.91 (*C*H_2); 22.61 (*C*H_2CH_3); 20 14.13 (*C*H_3CH_2). HRMS: Calc. $[M+H]^+$ ($C_{30}H_{58}N_3O_3$) m/z = 508.4473, found $[M+H]^+$ = 508.4456 (100%). IR: ν_{max} (cm^{-1}): 3300*w* (N-H); 3009*w*, 2926*s*, 2855*s* (all CH); 1692*s*, 1647*s* (C=O); 1538*m*, 1456*m*, 1390*m*, 1272*m*, 1250*s*, 1171*s*, 1046*s*, 867*w*, 723*w*.

Deprotection of Di-Unsaturated-C_{18}-Boc-DAPMA (**Binder 2**)

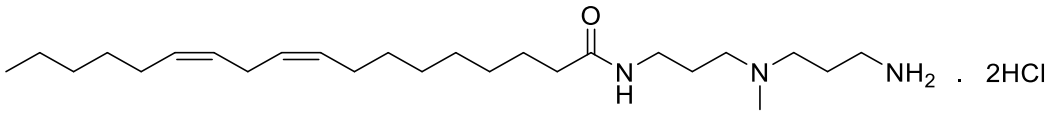

Chemical Formula: $C_{25}H_{51}Cl_2N_3O$
Molecular Weight: 480.60

Di-unsaturated-C_{18}-Boc-DAPMA (600 mg, 1.182 mmol) was dissolved in MeOH (25 mL) then HCl gas was applied for 15-20 seconds then the mixture was stirred for 3 hours and monitored by TLC. The product was a gummy orange solid (0.455 g, 80%).

R_f = 0.3 (90:10:1 DCM/MeOH/Et_3N). ^{1}H NMR ($CDCl_3$, 400 MHz) δ: 6.78 (br s, N*H*, 2H); 5.38-5.22 (m, C*H*CH, 4H); 5.16 (br s, N*H*, 1H); 3.27 (app q, C*H*$_2$NHCO, *J* = 12Hz, 2H); 3.14 (app q, CH_2CH_2NH, *J* = 4Hz, 2H); 2.72 (t, CHC*H*$_2$CH, *J* = 4.0 Hz, 2H); 2.37 (t, C*H*$_2$$NCH_3$, *J* = 6.2 Hz, 4H); 2.17 (s, NC*H*$_3$, 3H); 2.12 (t, CH_2CH_2CO, *J* = 8.0 Hz, 2H); 2.01 (q, C*H*$_2$CH, *J* = 8.0 Hz, 4H); 1.62-1.57 (m, C*H*$_2$$CH_2NH$, 4H); 1.32-1.22 (m, $CH_2CH_2CH_2$, 16H); 0.84 (t, C*H*$_3$$CH_2$, *J* = 7.0 Hz, 3H). ^{13}C NMR ($CDCl_3$, 100 MHz) δ: 173.41 (*C*ONH); 135.17, 133.34, 131.56, 130.23 (4 x *C*HCH); 128.02 (*C*H_2CH); 55.69 (2 x *C*$H_2$$NCH_3$); 41.63 (N*C*$H_3$); 39.11 (*C*$H_2$NH); 38.12 (*C*$H_2$NHCO); 36.82 (*C*$H_2$CO); 33.52 (*C*$H_2$CH); 31.43, 31.02, 30.98, 30.52, 30.19, 29.68, 29.45 (7 x *C*$H_2CH_2CH_2$); 27.23 (*C*$H_2CH_2NCH_3$); 26.18 (*C*H_2CH_2NH); 25.91 (CH_2*C*H_2CH); 22.61 (*C*H_2CH_3); 14.13 (*C*H_3CH_2). HRMS: Calc. $[M+H]^+$ ($C_{25}H_{50}N_3O$) m/z = 408.3948, found $[M+H]^+$ =

408.3931 (100%). IR: ν_{max} (cm^{-1}): 3315*w* (N-H); 3007*w*, 2923*s*, 2785*s* (all CH); 1682*s* (C=O); 1646*s* (C=O); 1552*m*, 1452*m*, 1380*m*, 1262*m*, 1245*s*, 1143*s*, 1016*s*, 867*w*, 723*w*.

Coupling of Boc-DAPMA and Linolenic Acid (Tri-Unsaturated-C_{18}-Boc-DAPMA)

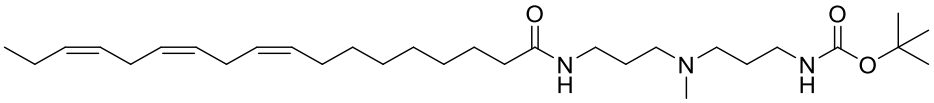

Chemical Formula: $C_{30}H_{55}N_3O_3$
Molecular Weight: 505.79

Linolenic acid (1.00 g, 3.56 mmol) was dissolved in DCM (65 mL) then TBTU (1.25 g, 3.95 mmol) and Et_3N (5.4 mL) were added. The mixture was stirred for 5 minutes at room temperature. Compound **1** (0.87 g, 3.56 mmol) was dissolved in DCM (65 mL) then was added to the reaction flask. The reaction was stirred overnight, then the mixture was concentrated *in vacuo* and the residue was dissolved in EtOAc (50 mL) and washed with $NaHSO_4$ (2 x 15 mL, 1.33 M), $NaHCO_3$ (2 x 15 mL, saturated), deionised water (3 x 15 mL) and brine (15 mL, saturated). The organic layer was collected, dried over $MgSO_4$ and filtered (filter paper 90 mm) then dried *in vacuo.* The product was concentrated and purified by gel permeation chromatography (GPC) column (Bio-beads, 100% DCM). The product was a gluey brown oil (620 mg, 34%).

R_f = 0.3 (90:10:1 DCM/MeOH/Et_3N). ^{1}H NMR ($CDCl_3$, 400 MHz) δ: 7.24 (br s, N*H*, 1H); 5.41 (br s, N*H*Boc, 1H); 5.31-5.25 (m, C*H*CH, 6H); 3.24 (app q, CH_2NHCO, *J* = 6.2 Hz, 2H); 3.22 (app q, *CH*$_2$NHBoc, *J* = 6.1 Hz, 2H); 3.09 (t, CHCH_2CH, *J* = 7.2 Hz, 4H); 2.48 (t, CH_2NCH_3, *J* = 6.4 Hz, 4H);2.19 (s, NCH_3, 3H); 2.06 (t, CH_2CH_2CO, *J* = 7.6 Hz, 2H); 2.02 (q, CH_2CH_2CH *J* = 6.0 Hz, 2H); 1.99-1.92 (m, CH_2CH_2NH, 4H); 1.41 (s, C(CH_3)$_3$, 9H); 1.27-1.29 (m, CH_2(CH_2)$_5CH_2$, 10H); 0.87 (t, CH_3CH_2, *J* = 6.4 Hz, 3H). ^{13}C NMR ($CDCl_3$, 100 MHz) δ: 175.40 (*C*ONH); 154.13 (O*C*ONH); 133.19, 132.87,

132.43, 131.65, 131.26, 130.72 (6 x *C*H=CH); 81.34 (*C*CH_3); 56.24 (2 x *C*H_2NCH_3); 47.31 (N*C*H_3); 39.80 (*C*H_2NH); 37.42 (*C*H_2NHCO); 34.89 (*C*H_2CO); 32.43 (2 x *C*H_2CH); 29.92 (5 x *C*$H_2CH_2CH_2$); 28.46 (C(*C*$H_3)_3$); 26.98 (*C*$H_2CH_2NCH_3$); 24.76 (*C*H_2CH_2NH); 23.76 (CH_2*C*H_2CO); 21.82 (*C*H_2CH_3); 14.34 (*C*H_3CH_2). HRMS: Calc. $[M+H]^+$ ($C_{30}H_{56}N_3O_3$) m/z = 506.4316, found $[M+H]^+$ = 506.4322 (100%). IR: ν_{max} (cm^{-1}): 3300*w* (N-H); 3009*w*, 2926s, 2855*s*, (all CH); 1692*s* (C=O); 1647*s* (C=O); 1538*m* (C=O); 1456*m*, 1389*m*, 1275*m*, 1254*s*, 1165*s*, 1048*s*, 850*w*, 733*w*.

Deprotection of Tri-Unsaturated-C_{18}-Boc-DAPMA (Binder 3)

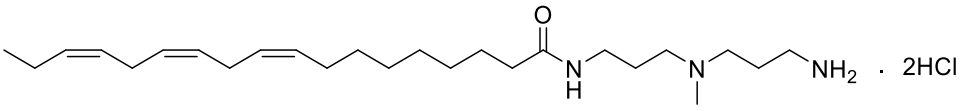

Chemical Formula: $C_{25}H_{49}Cl_2N_3O$
Molecular Weight: 478.59

Tri-unsaturated-C_{18}-Boc-DAPMA (400 mg, 0.791 mmol) was dissolved in MeOH (25 mL) then HCl gas was applied for 15-20 seconds then the mixture was stirred for 3 hours and monitored by TLC. The solvent was dried *in vacuo* product was a gummy brown solid (295 mg, 92%).

R_f = 0.3 (90:10:1 DCM/MeOH/Et_3N). ^{1}H NMR ($CDCl_3$, 400 MHz) δ: 6.97 (br s, N*H*, 1H); 5.34 (br s, NH_2, 2H); 5.33-5.30 (m, C*H*CH, 6H); 3.33 (app q, CH_2NHCO, *J* = 6.1 Hz, 2H); 3.14 (app q, CH_2CH_2NH, *J* = 6.1 Hz, 2H); 3.09 (q, CH_2CH, *J* = 7.2 Hz, 4H); 2.78 (s, NCH_3, 3H); 2.58 (t, CH_2NCH_3, *J* = 6.3 Hz, 4H); 2.26 (t, CH_2CH_2CO, *J* = 7.6 Hz, 2H); 1.99-1.92 (m, CH_2CH_2NH, 4H); 1.27-1.29 (m, CH_2(C$H_2)_5CH_2$, 10H); 0.87 (t, CH_3CH_2, *J* = 6.3 Hz, 3H. ^{13}C NMR (CD_3OD, 100 MHz) δ: 172.55 (*C*ONH); 134.35, 134.13, 133.45, 132.85, 130.61, 130.23 (6 x *C*H=CH); 56.51 (2 x *C*H_2NCH_3); 47.23 (N*C*H_3); 40.70 (*C*H_2NH); 39.70 (*C*H_2NH_2); 36.82 (*C*H_2CO); 31.91 (5 x *C*$H_2CH_2CH_2$); 29.11 (CH_2*C*H_2CH); 27.15 (2 x *C*H_2CH); 26.23 (*C*$H_2CH_2NCH_3$); 24.34 (*C*H_2CH_2NH);

22.62 (*C*H_2CH_3); 14.16 (*C*H_3CH_2). HRMS: Calc. $[M+H]^+$ ($C_{25}H_{52}N_3O$) m/z = 406.3792, found $[M+H]^+$ = 406.3783 (100%). IR: ν_{max} (cm^{-1}): 3284*w* (N-H); 3008*w*, 2927*s*, 2855*s*, (all CH); 1716*s* (C=O); 1642*s* (C=O); 1547*m*, 1460*s*, 1367*m*, 1196*m*, 1065*s*, 844*w*, 747*s*, 596*s*.

Cross-linking Alkene Groups (Polymerization) of Binder 1[175]

Binder 1 (40 mg, 0.083 mmol) was dissolved in methanol (4 mL). The mixture was sonicated for 5 minutes to ensure homogeneity. The solvent was evaporated under a flow of nitrogen. The resultant film was hydrated (water, 10 mL) then sonicated for 10 minutes. The resultant was centrifuged at 4000 rpm for 15 minutes, then filtered (0.22 µm nylon filter). The solution was deoxygenated by bubbling with nitrogen for 1 hour. A solution of 2,2-azo-bis(isobutyronitrile) (AIBN) (10 wt % of **Binder 1** = 4 mg, 0.024 mmol) in THF (1 mL) was added then the mixture was stirred for 2 hours before the temperature was raised to 70 °C for 24 h under nitrogen. The solution was washed with DCM (10 mL) to remove excess AIBN and the product was collected from the water layer by vacuum distillation (50 °C). The product was a yellowish sticky solid (31 mg 77%).

R_f = 0.3 (90:10:1 DCM/MeOH/Et_3N). ^{1}H NMR data showed similar spectra comparing to **Binder 1**. ^{13}C NMR could not be obtained due the weak sample. HRMS: Calc. $[M+H]^+$ ($C_{25}H_{52}N_3O$) m/z = 410.4105, found $[M+H]^+$ = 410.4097 (100%). IR: ν_{max} (cm^{-1}): 3286*w* (N-H); 2927*w*, 2853*s* (all CH); 1545*s* (C=O); 1257*m*, 1052*w*, 865*s*, 734*w*, 554*s*.

Cross-linking Alkene Groups (Polymerization) of Binder 2[175]

Binder 2 (40 mg, 0.083 mmol) was dissolved in methanol (4 mL). The mixture was sonicated for 5 minutes to ensure homogeneity. The solvent was evaporated under a flow of nitrogen. The resultant film was hydrated (water, 10 mL) then sonicated for 10 minutes.

The resultant was centrifuged at 4000 rpm for 15 minutes, then filtered (0.22 µm nylon filter). The solution was deoxygenated by bubbling with nitrogen for 1 hour. A solution of 2,2-azo-bis(isobutyronitrile) (AIBN) (10 wt % of **Binder 2** = 4 mg, 0.024 mmol) in THF (1 mL) was added then the mixture was stirred for 2 hours before the temperature was raised to 70 °C for 24 h under nitrogen. The solution was washed with DCM (10 mL) to remove excess AIBN and the product was collected from the water layer by vacuum distillation (50 °C). The product was an orange sticky solid (26 mg 65%).

R_f = 0.3 (90:10:1 DCM/MeOH/Et_3N). ^{1}H NMR (CD_3OD, 400 MHz) δ: 5.62 (br s, N*H*, 1H); 4.84 (br s, NH_2, 2H); 3.25 (q, CH_2NHCO, *J* = 1.6 Hz, 2H); 3.22 (t, CH_2NH_2, *J* = 6.0 Hz, 2H) 3.14 (q, $CH_2CH_2NH_2$, *J* = 6.0 Hz, 2H); 2.78 (s, NCH_3, 3H); 2.52 (t, CH_2NCH_3, *J* = 6.4 Hz, 4H); 2.26 (t, CH_2CH_2CO, *J* = 7.6 Hz, 2H); 1.99-1.92 (m, CH_2CH_2NH, 4H); 1.27-1.29 (m, $CH_2CH_2CH_2$, 12H); 0.87 (t, CH_3CH_2, *J* = 6.4 Hz, 3H). The rest of ^{1}H NMR spectra was not clear although some unreacted alkenes were observed at 5.32 ppm ca. 24%. ^{13}C NMR could not be obtained due the weak sample. MS spectra were not obtained as the product is a cross-linked nanostructure. IR: ν_{max} (cm^{-1}): 3286*w* (N-H); 3154*s*, 2924*m*, 2854*s* (all CH); 1638*s*, 1543*s* (C=O); 1258*m*, 1056*w*, 863*s*, 739*w*, 557*s*.

Cross-linking Alkene Groups (Polymerization) of Binder 3[175]

Binder **3** (60 mg, 0.125 mmol) was dissolved in methanol (6 mL). The mixture was sonicated for 5 minutes to ensure homogeneity. The solvent was evaporated under a flow of nitrogen. The resultant film was hydrated (water, 10 mL) then sonicated for 10 minutes. The resultant was centrifuged at 4000 rpm for 15 minutes, then filtered (0.22 µm nylon filter). The solution was deoxygenated by bubbling with nitrogen for 1 hour. A solution of 2,2-azo-bis(isobutyronitrile) (AIBN) (10 wt % of **Binder 3** = 6 mg, 0.024 mmol) in THF (1 mL) was added then the mixture was stirred for 2 hours before the temperature

was raised to 70 °C for 24 h under nitrogen. The solution was washed with DCM (10 mL) to remove excess AIBN and the product was collected from the water layer by vacuum distillation (50 °C). The product was a yellowish sticky solid (38 mg 63%).

R_f = 0.3 (90:10:1 DCM/MeOH/Et_3N). ^1H NMR (CD_3OD, 400 MHz) δ: 5.75 (br s, N*H*, 1H); 4.84 (br s, NH_2, 2H); 3.26 (q, CH_2NHCO, *J* = 1.6 Hz, 2H); 3.21 (t, CH_2NH_2, *J* = 6.0 Hz, 2H) 3.17 (q, $CH_2CH_2NH_2$, *J* = 6.0 Hz, 2H); 2.73 (s, NCH_3, 3H); 2.31 (t, CH_2CH_2CO, *J* = 7.6 Hz, 2H); 2.01-1.93 (m, CH_2CH_2NH, 4H); 1.54 (t, CH_2NCH_3, *J* = 6.4 Hz, 4H); 0.87 (t, CH_3CH_2, *J* = 6.4 Hz, 3H). The rest of ^1H NMR spectra was not clear (some unreacted alkenes were observed at 5.34 ppm ca. 19%.). ^{13}C NMR could not be obtained due the weak sample. MS spectra were not obtained as the product is a cross-linked nanostructure. IR: ν_{max} (cm^{-1}): 3286*w* (N-H); 2924*w*, 2854*s* (all CH); 1543*s* (C=O); 1258*m*, 1056*w*, 863*s*, 739*w*, 557*s*.

7.1.2 Chapter 3

Synthesis of Mono-Boc-DAP

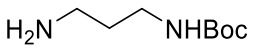

Chemical Formula: $C_8H_{18}N_2O_2$
Molecular Weight: 174.24

Di-aminopropane (22.2 ml, 335 mmol) was dissolved in absolute EtOH (80 ml) then Boc_2O (14.6 g, 67 mmol) was dissolved in EtOH (8 ml) and added to the mixture dropwise over a period of one hour. Afterwards the mixture was quenched with water (10 ml) and the solvent was evaporated *in vacuo*. The product was dissolved in $NaOH_{aq}$ (50 ml, 1M), so that the pH >10, and the mixture was extracted three times with DCM (50 ml). The combined organic layers were washed with citrate (1M) until the pH was 3-4.

The aqueous layer was then basified with $NaOH_{aq}$ (5M) (pH >10) and the product was extracted three times with DCM (50 ml). The solution was dried over $MgSO_4$, filtered and dried *in vacuo* resulting in a white oily liquid (4.0 g, 34%).

R_f = 0.13 (DCM/MeOH =1:1). ^{1}H NMR (400 MHz, $CDCl_3$) δ: 4.93 (s, N*H*, 1H); 3.20 (app q, C*H*$_2$NHCO, *J* = 5.2 Hz, 2H); 2.75 (t, H_2NCH_2, *J* = 6.0 Hz 2H); 1.60 (app quint, $CH_2CH_2CH_2$, *J* = 6.4 Hz, 4H); 1.42 (s, C(C*H*$_3$)$_3$, 9 H). ^{13}C NMR (100 MHz, $CDCl_3$) δ: 153.27 (NH*C*OO*t*Bu); 79.17(*C*(CH$_3$)$_3$); 39.77(*C*H$_2$NH); 38.54 (NH$_2$*C*H$_2$); 33.41 (CH$_2$*C*H$_2$CH$_2$); 28.54 (C(*C*H$_3$)$_3$). HRMS: Calc. $[M+H]^+$ ($C_8H_{18}N_2O_2$) m/z = 175.1368, found $[M+H]^+$ = 175.1447 (100%). IR: ν_{max} (cm^{-1}): 3340*w* (N-H); 2975*w*, 2928*s*, 2868*s*, (all CH); 1689*s* (C=O); 1538*s* (C=O); 1454*m*, 1391*m*, 1364*m*, 1327*m*, 1273*m*, 1250*s*, 1170*m*, 1049*m*, 868*w*, 818*w*, 781*w*, 620*w*.

Synthesis of Boc-C$_{16}$-DAP

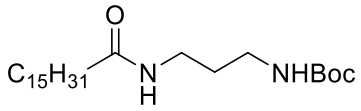

Chemical Formula: $C_{24}H_{48}N_2O_3$
Molecular Weight: 412.66

Palmitic acid (1.00 g, 3.9 mmol) was dissolved in DCM (65 ml) then TBTU (1.25 g, 3.9 mmol) and Et_3N (approx. 5 ml) were added. The mixture was stirred for 5 minutes and mono-Boc-DAP (683 mg, 3.9 mmol) was dissolved in DCM (65 ml) and added. The solution was left stirring overnight. The solvent was evaporated *in vacuo.* After that the product was purified by column chromatography (DCM to DCM/MeOH (9:1)). The product was isolated as a white powder (1.50 g, 93%).

R_f = 0.43 (DCM/MeOH, 9:1). ^{1}H NMR (400 MHz, $CDCl_3$) δ: 6.22 (br s, N*H*, 1H); 4.93 (br s, N*H*Boc, 1H); 3.29 (q, C*H*$_2$NHCO, *J* = 6.2, 6.4 Hz, 2H); 3.16 (app q, C*H*$_2$NBoc, *J* = 6.0, 5.6 Hz, 2H); 2.18 (t, C*H*$_2$CONH, *J* = 7.6 Hz, 2H); 1.60 (m, C*H*$_2$CH$_2$CONH + CH$_2$C*H*$_2$CH$_2$, 4H); 1.43 (s, C(C*H*$_3$)$_3$, 9H); 1.32-1.24 (m, CH$_3$(C*H*$_2$)$_{12}$CH$_2$, 24H); 0.87 (t,

C*H*$_3$CH$_2$, *J* = 7.0 Hz, 3H). ^{13}C NMR (100 MHz, $CDCl_3$) δ: 173.85 (*C*=O); 153.15 (O*C*ONH); 79.52 (*C*$(CH_3)_3$); 37.02 (*C*H_2NHCO); 32.07 (NH*C*H_2CH$_2$*C*H_2NH); 30.44, 29.83, 29.8, 29.65, 29.51, 29.45, 28.53, 25.95 (NH*C*H_2*C*H_2CH$_2$NH + (*C*H_2)$_{12}$CO); 22.84 (*C*H_2CH$_3$); 14.28 (*C*H$_3$CH$_2$). HRMS: Calc. $[M+H]^+$ ($C_{24}H_{50}N_2O_3$) m/z = 413.3738, found $[M+H]^+$ = 413.3719 (33%,); Calc. $[M+Na]^+$ ($C_{24}H_{48}N_2NaO_3$) m/z = 435.3571, found $[M+Na]^+$ = 435.3565 (100%). IR: ν_{max} (cm^{-1}): 3360*m* (N-H); 3310*m*, 2918*s*, 2851*s* (all CH); 1685*s* (C=O); 1639*s* (C=O); 1538*m*, 1468*w*, 1444*w*, 1391*w*, 1364*w*, 1280*m*, 1253*w*, 1173*m*, 1133*w*, 721*w*.

Deprotection of Boc-C_{16}-DAP (C_{16}-DAP)

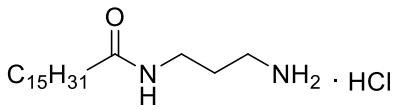

Chemical Formula: $C_{19}H_{41}ClN_2O$
Molecular Weight: 349.00

Boc-Protected C_{16}-DAP (1.3 g, 3.15 mmol) was dissolved in MeOH (25 mL) and HCl gas was applied for approx.15-20 seconds. The mixture was stirred for 3 hours and the solvent was removed *in vacuo*., and after drying in vacuum, the product was obtained as a white solid (1.1 g, 85%).

R_f = 0.1 (90:10:1 DCM/MeOH/Et_3N). ^{1}H NMR (400 MHz, CD_3OD) δ: 3.24 (t, C*H*$_2$NHCO, *J* = 6.8 Hz, 2H); 2.89 (t, C*H*$_2$NH$_2$, *J* = 7.2 Hz, 2H); 2.11 (t, C*H*$_2$CO *J* = 6.8 Hz, 2H); 1.80 (app quint, C*H*$_2$CH$_2$NH$_2$, *J* = 7.0 Hz, 2H); 1.57 (app quint, C*H*$_2$CH$_2$CONH, *J* = 6.6 Hz, 2H); 1.25 (br s, (C*H*$_2$)$_{12}$, 24 H); 0.87 (t, C*H*$_3$CH$_2$, J = 7.0 Hz, 3H). ^{13}C NMR (100 MHz, CD_3OD) δ: 38.19 (*C*H_2NH$_2$); 36.96 (*C*H_2NHCO); 36.80 (*C*H_2CONH); 33.08 (*C*H_2CH$_2$NH$_2$); 30.79 (*C*H$_3$*C*H$_2$*C*H$_2$); 30.63, 30.48, 30.36 (C$_3$H$_7$(*C*H$_2$)$_{10}$); 28.84 ((*C*H$_2$)$_2$CH$_2$CH$_2$CONH); 27.00 (*C*H$_2$CH$_2$CONH); 23.74 (*C*H$_2$CH$_3$); 14.44 (*C*H$_3$) (C=O peak was not observed owing to low intensity spectrum). HRMS: Calc. $[M+H]^+$

($C_{19}H_{41}N_2O$) m/z = 313.3213; found $[M+H]^+$ = 313.3215 (100%). IR: ν_{max} (cm^{-1}): 3287*m* (N-H); 2955*m*, 2918*s*, 2848*s* (all CH); 1642*s* (C=O); 1616*w*, 1555*m*, 1525*w*, 1468*w*, 1438*w*, 1267*w*, 1163*w*, 1009*w*, 721*w*.

Synthesis of Boc-Protected C_{16}-DAPMA

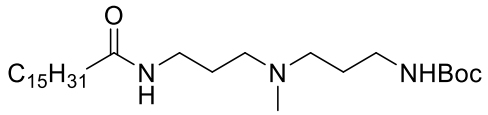

Chemical Formula: $C_{28}H_{57}N_3O_3$
Molecular Weight: 483.78

Palmitic acid (1.00 g, 3.9 mmol) was dissolved in DCM (65 ml) then TBTU (1.25 g, 3.9 mmol) and Et_3N (approx. 5 ml) were added. The mixture was stirred for 5 minutes and mono-Boc-DAPMA (compound **1**) (950 mg, 3.9 mmol) was added. The solution was left stirring overnight. The solvent was evaporated *in vacuo.* After evaporation of solvent, the product was dissolved again in EtOAc (50 ml) and washed two times with sat. $NaHSO_4$ (15 ml), two times with sat. $NaHCO_3$ (15 ml), three times with H_2O (15 ml) and once with sat. NaCl (15 ml). After GPC on Bio-beads SX-1 (100%, DCM), the product was obtained as a white solid (1.70 g, 90 %).

R_f = 0.08 (DCM:MeOH:Et_3N, 90:10:0.1). ^1H NMR (400 MHz, $CDCl_3$) δ: 6.82 (br s, N*H*, 1H), 5.1 (br s, N*H*Boc, 1H); 3.34 (td, C*H*$_2$NHCO, *J* = 5.9, 6.0 Hz, 2H); 3.20 (td, C*H*$_2$NHBoc, *J* = 5.6, 5.5 Hz, 2H); 2.73 (br, C*H*$_2$N(CH_3), 4H); 2.47 (s, N(C*H*$_3$), 3H); 2.18 (t, C*H*$_2$CONH, *J* = 7.2 Hz, 2H); 1.83-1.75 (m, C*H*$_2$CH$_2$N(CH_3), 4H); 1.60 (t, C*H*$_2$CH$_2$CONH, *J* = 7.2 Hz, 2H); 1.43 (s, C(C*H*$_3$)$_3$, 9H); 1.32-1.24 (m, CH_3(C*H*$_2$)$_{12}$CH$_2$, 24H); 0.87 (t, C*H*$_3$CH$_2$, *J* = 6.8 Hz, 3H). ^{13}C NMR (100 MHz, $CDCl_3$) δ: 173.99 (*C*=O); 156.31 (*C*=*O*Boc); 79.12 (*C*CH_3); 36.83 (*C*H$_2$NHCO); 31.87 (*C*H$_2$); 29.60 (2 x *C*H$_2$); 29.39 (2 x *C*H$_2$); 28.24 (C(*C*H$_3$)$_3$); 26.23 (2 x *C*H$_2$); 25.84 (2 x *C*H$_2$); 24.51 (*C*H$_2$); 22.57 (*C*H$_2$CH$_3$); 13.98 (*C*H$_3$CH$_2$). HRMS: Calc. $[M+H]^+$ ($C_{28}H_{58}N_3O_3$) m/z = 484.4473, found

$[M+H]^+$ = 484.4474 (100%). IR: ν_{max} (cm^{-1}): 3300*w* (N-H); 3017*w*, 2936*s*, 2845*s* (all CH); 1671*s* (C=O); 1647*s* (C=O); 1538*m* (C=O); 1456*m*, 1390*m*, 1272*m*, 1250*s*, 1171*s*, 1046*s*, 867*w*, 723*w*.

Deprotection of Boc-C16-DAPMA (C16-DAPMA)

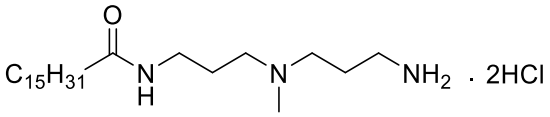

Chemical Formula: $C_{23}H_{51}Cl_2N_3O$
Molecular Weight: 456.58

Boc-Protected C_{16}-DAPMA (1.79 g 3.70 mmol) was dissolved in MeOH (25 mL) and HCl gas was applied for approx.15-20 seconds. The mixture was stirred for 3 hours and the solvent was removed *in vacuo*, and after drying in vacuum, the product was obtained as slightly orange solid (1.70 g, 95%.).

R_f = 0.1 (90:10:1 DCM/MeOH/Et_3N). ^{1}H-NMR (400 MHz, CD_3OD) δ: 3.05-3.29 (m, C*H*$_2$NH$_2$ + C*H*$_2$NHCO, 4H); 3.04 (t, C*H*$_2$N(CH$_3$), *J* = 7.4 Hz, 4H); 2.43 (s, N(C*H*$_3$), 3H); 2.22 (t, C*H*$_2$CONH, *J* = 8.0 Hz, 2H); 2.12 (app. quint., C*H*$_2$CH$_2$*N(CH$_3$)*, *J* = 7.8 Hz, 2H); 1.95 (quint., C*H*$_2$CH$_2$*NH*$_2$, *J* = 6.8 Hz, 2H); 1.56 (app. quint., C*H*$_2$CH$_2$CONH, *J* = 6.0 Hz, 2H); 1.24-1.19 (m, CH$_3$(C*H*$_2$)$_{12}$, 24H); 0.86 (t, C*H*$_3$CH$_2$, *J* = 5.4 Hz, 3H). ^{13}C NMR (100 MHz, CD_3OD) δ: 177.42 (*C*ONH); 55.24, 54.22 (*C*H$_2$N(CH$_3$)); 40.30 (N(*C*H$_3$)); 37.77 (*C*H$_2$CO); 37.16 (*C*H$_2$NHCO); 36.80 (*C*H$_2$NH$_2$); 32.99 (*C*H$_2$); 30.71 (*C*H$_2$); 30.39 (*C*H$_2$); 26.91 (2 x *C*H$_2$); 26.71 (2 x *C*H$_2$); 25.48 (2 x *C*H$_2$); 23.65 (2 x *C*H$_2$); 23.43(*C*H$_2$CH$_3$); 14.37 (*C*H$_3$CH$_2$). HRMS: Calc. $[M+H]^+$ ($C_{23}H_{50}N_3O$) m/z = 384.3948, found $[M+H]^+$ = 384.3961 (100%). IR: ν_{max} (cm^{-1}): 3370*m* (N-H); 2955*m*, 2922*s*, 2851*s*, 2254*m* (all CH); 1642*m* (C=O); 1612*m*, 1542*m*, 1468*s*, 1378*m*, 1260*w*, 1234*w*, 1160*w*, 1070*w*, 738*s*.

Synthesis of Mono-Boc-DAB[226]

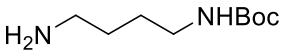

Chemical Formula: $C_9H_{20}N_2O_2$
Molecular Weight: 188.27

1,4-Diaminobutane (25 g, 284 mmol) was dissolved in THF (200 ml) and Boc_2O (12.37 g, 56.7 mmol) dissolved in THF was added dropwise over two hours. The mixture was then left stirring overnight, then the solvent was evaporated and the residue was dissolved again in water. The bis-protected water-insoluble side product was separated by filtration and the product was extracted from the filtrate three times with DCM (100 ml). The product was dried over $MgSO_4$, filtered and dried in vacuum resulting in an oil (6.2 g, 58 %).

R_f = 0.1 (DCM/MeOH/Et_3N, 90:10:1). ^{1}H NMR (400 MHz, $CDCl_3$): δ = 4.77 (br s, N*H*, 1H); 3.07 (t, CH_2NH, *J* = 6.2 Hz, 2H); 2.67 (t, CH_2NH_2, *J* = 6.6 Hz, 2H); 1.52-1.39 (m, $CH_2(CH_2)_2CH_2$ + $C(CH_3)_3$, 13H). ^{13}C NMR (100 MHz, $CDCl_3$) δ: 156.10 (*C*=O); 79.05 ($C(CH_3)_3$); 41.85 (H_2NCH_2); 40.48 (CH_2NH); 28.49 ($C(CH_3)_3$ + $CH_2CH_2NH_2$); 27.54 (CH_2CH_2NH). HRMS: Calc. $[M+H]^+$ ($C_9H_{21}N_2O_2$) m/z = 189.1598, found $[M+H]^+$ = 189.1595 (46%); Calc. $[M+Na]^+$ ($C_9H_{20}N_2NaO_2$) m/z = 211.1417, found $[M+Na]^+$ = 211.1414 (100%). IR: ν_{max} (cm^{-1}): 3343*m* (N-H); 2975s, 2931*s*, 2864*m* (all C-H); 1686*s* (C=O); 1521*s*, 1481*m*, 1451*w*, 1310*w*, 1277*m*, 1170.0*w*, 1046w, 1006*m*, 818*m*, 778*w*, 747, 614*w*.

Cyanoethyl-mono-Boc-DAB[225]

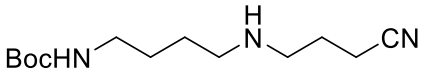

Chemical Formula: $C_{13}H_{25}N_3O_2$
Molecular Weight: 255.36

Mono-Boc-DAB (5.0 g, 26.5 mmol) was dissolved in THF (15 ml) and cooled to 0 °C. Freshly distilled acrylonitrile (1.84 ml, 27.8 mmol) was added dropwise via syringe to the solution. The mixture was stirred at 0 °C for 20 min and then at 45 °C for 1.5 hour, afterwards the solvent was evaporated. Because mass spectrum and ^{1}H-NMR indicated that the reaction was not complete, another portion of acrylonitrile (0.87 ml, 13.25 mmol) was added to the mixture at 0 °C. The solution was stirred for 30 min at 0 °C, for 1 h at 45 °C and then for 2 h at 100 °C. After drying in vacuum the product was obtained as a yellow oil (5.35 g, 84 %).

R_f = 0.01 (DCM/MeOH/Et_3N, 90:10:1). ^{1}H NMR (400 MHz, $CDCl_3$) δ: 4.77 (br s, N*H*); 3.10 (br t, C*H*$_2$NHCO, *J* = 6.2 Hz, 2H); 2.90 (t, C*H*$_2$CN, *J* = 6.8 Hz, 2H); 2.63 (t, C*H*$_2$CH$_2$CN, *J* = 8.2 Hz, 2H); 2.51 (t, C*H*$_2$NH(CH$_2$)$_2$CN, *J* = 5.5 Hz, 2H); 2.48 (q, C*H*$_2$NH *J* = 6.8 Hz, 2H); 1.56-1.50 (m, CH$_2$C*H*$_2$C*H*$_2$CH$_2$, 4H); 1.41 (br s, C(C*H*$_3$)$_3$, 9 H). ^{13}C NMR (100 MHz, $CDCl_3$) δ: 153.11 (*C*=O); 118.81 (*C*N); 79.16 (*C*(CH$_3$)$_3$); 48.81 (*C*H$_2$NH(CH$_2$)$_2$CN); 45.09 (*C*H$_2$CH$_2$CN); 40.42 (*C*H$_2$NHCO); 28.51 (C(*C*H$_3$)$_3$); 27.85 (*C*H$_2$); 25.70 (*C*H$_2$); 18.79 (*C*H$_2$). HRMS: Calc. $[M+H]^+$ ($C_{13}H_{26}N_3O_2$) m/z = 256.1790, found $[M+H]^+$ = 256.1861 (85%); Calc. $[M+Na]^+$ ($C_{13}H_{25}N_3NaO_2$) m/z = 287.1863, found $[M+Na]^+$ 287.1673 (100%). IR: ν_{max} (cm^{-1}): 3343*s* (N-H); 2978*s*, 2935*m*, 2864*s* (all CH); 2245 (CN); 1689*s* (C=O); 1518*s*, 1478*w*, 1454*m*, 1391*m*, 1364*m*, 1273*w*, 1250*w*, 1170*s*, 1046*s*, 1009*w*, 865*w*, 778*w*, 758*m*.

Cyanoethyl-Di-Boc-DAB[225]

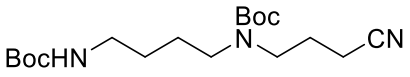

Chemical Formula: $C_{18}H_{33}N_3O_4$
Molecular Weight: 355.48

Cyanethyl-mono-Boc-DAB **(**5.44 g, 22.5 mmol) was dissolved in THF (25 ml) then a solution of Boc_2O (5.41 g, 24.8 mmol) in THF (40 ml) was added at 0 °C. The reaction was allowed to reach r.t. while stirring for 4 h. Afterwards, water (5 ml) was added and the solvent evaporated. After drying in vacuum, the product was obtained in quant. yield (7.8 g, 97%).

R_f = 0.02 (DCM/MeOH/Et_3N, 90:10:1). ^{1}HNMR (400 MHz, $CDCl_3$) δ: 4.69 (br s, N*H*); 3.42 (t, J = 6.6 Hz, C*H*$_2$CH$_2$CN, 2H); 3.24 (t, C*H*$_2$NHBoc, *J* = 7.2 Hz, 2H); 3.10 (br t, C*H*$_2$CN, *J* = 5.4 Hz, 2H); 2.60 (br t, C*H*$_2$NBoc(CH$_2$)$_2$CN, *J* = 5.6 Hz, 2H); 2.01 (br s, NH); 1.50- 1.39 (m, CH$_2$C*H*$_2$C*H*$_2$CH$_2$ + C(C*H*$_3$)$_3$, 22H). ^{13}C NMR (100 MHz, $CDCl_3$) δ: 146.78 (CONBoc); 136.12 (*C*ONHBoc); 118.38 (*C*N); 80.48 (*C*(CH$_3$)$_3$); 79.16 (*C*(CH$_3$)$_3$); 48.25 (*C*H$_2$NBoc); 43.90 (*C*H$_2$NBoc); 40.05 (*C*H$_2$NHBoc); 28.39 (C(*C*H$_3$)$_3$); 27.44 (C(*C*H$_3$)$_3$); 26.02 (*C*H$_2$CH$_2$CH$_2$NBoc); 25.51 (*C*H$_2$CH$_2$NBoc); 17.02 (*C*H$_2$). HRMS: Calc. $[M+H]^+$ ($C_{18}H_{34}N_3O_4$) m/z = 356.2315, found $[M+H]^+$ = 356.2208 (100%). IR: ν_{max} (cm^{-1}): 3363*m* (N-H); 2975*s*, 2935*s*, 2868*s* (all C-H); 2251 (CΞN); 1689 (C=O); 1518*m*, 1478*w*, 1451*w*, 1414*m*, 1391*w*, 1267*m*, 1250*w*, 1093*w*, 1006*w*, 932*m*, 865*m*, 774*w*.

Synthesis of N^1,N^2-Bis-Boc-spermidine (Boc-SPD)[226]

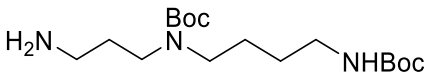

Chemical Formula: $C_{17}H_{35}N_3O_4$
Molecular Weight: 345.48

Lithium aluminium hydride (0.389 g, 10.25 mmol) was suspended in dry ether (20 ml) then cyanoethyl-di-Boc-DAB (1.03 g) (2.98 mmol) dissolved in dry ether (30 ml) was added dropwise over 35 min at 0 °C. The mixture was stirred at 0 °C for 1 h and then carefully quenched with MeOH (30 ml) and water (10 ml). The resulting reaction mixture was strongly basic (pH > 10). The product was extracted three times with diethyl ether (30-40 ml). Afterwards the combined organic layers were acidified with citrate (1 M) until the pH was around 3-4. The product was extracted twice with water and the combined aqueous layers (just from second extraction) were washed with Et_2O (30 ml) twice. The aqueous layer was basified with NaOH (1 M, ca. 200 ml) and the product was extracted with DCM (3 x 50 ml). The combined DCM layers were dried over $MgSO_4$, filtered and the solvent was evaporated *in vacuo*. After drying, the product was obtained as a slightly yellow oil (0.63 g, 62 %).

^{1}H NMR (400 MHz, $CDCl_3$) δ: 4.64 (br s, N*H*); 3.25-3.11 (m, C*H*$_2$NBoc + C*H*$_2$NHBoc, 6H); 2.67 (t, C*H*$_2$NH$_2$, *J* = 6.6 Hz, 2H); 1.62 (quint., C*H*$_2$CH$_2$NH$_2$, *J* = 6.9 Hz, 2H); 1.55-1.36 (m, CH$_2$C*H*$_2$C*H*$_2$CH$_2$ + C(C*H*$_3$)$_3$, 22H). ^{13}C NMR (100 MHz, $CDCl_3$) δ: 145.83 (*C*=O); 136.11 (*C*=ONH); 81.32 (*C*(CH$_3$)$_3$); 79.48 (*C*(CH$_3$)$_3$); 46.62 (*C*H$_2$NBoc); 40.33 (*C*H$_2$NHBoc + *C*H$_2$NH$_2$); 29.53 (C(*C*H$_3$)$_3$); 28.60 (C(*C*H$_3$)$_3$); 27.73 (*C*H$_2$); 27.56 ((*C*H$_2$)$_2$CH$_2$NBoc). HRMS: Calc. $[M+H]^+$ ($C_{17}H_{36}N_3O_4$) m/z = 346.2628, found $[M+H]^+$ = 346.2691 (100%). IR: ν_{max} (cm^{-1}): 3708*m* (N-H); 3665*m* (N-H); 3350*w* (N-H); 2971*m*, 2935*s*, 2868*s* (all CH); 1679*s* (C=O); 1525*s*, 1478*w*, 1454*w*, 1421*m*, 1391*w*, 1364*w*, 1300*s*, 1273*m*, 1250*s*, 1166*m*, 1170*w*, 868*m*, 818*w*, 771*w*.

Boc-Protected C_{16}-Spermidine (Boc-C_{16}-SPD)

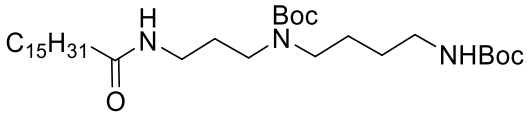

Chemical Formula: $C_{33}H_{65}N_3O_5$
Molecular Weight: 583.90

Palmitic acid (0.472 g, 1.84 mmol, 1.04 eq.), N^1,N^5-bis-Boc-spermidine (0.61 g, 1.76 mmol), TBTU (0.585 g, 1.82 mmol) and Et_3N (3.5 ml) were dissolved in DCM (65 ml). After the solvent was evaporated, some of the crude product (700 mg from 2.10 g) was purified, first by GPC in DCM and second by column chromatography (SiO_2 in Hex/EtOAc 1:1). The product was obtained as a white powder (258 mg, purified material, equivalent to 76% if all was purified).

R_f = 0.23 (Hex:EtOAc, 1:1). ^{1}H NMR (400 MHz, $CDCl_3$) δ: 6.72 (br s, N*H*, 1H); 4.55 (br s, N*H*Boc, 1H); 3.27-3.13 (m, C*H*$_2$NHCO, 8H); 2.17 (t, C*H*$_2$CONH, *J* = 7.6 Hz, 2H); 1.68-1.52 (m, C*H*$_2$CH$_2$NBoc + (C*H*$_2$)$_2$CH$_2$NHBoc + C*H*$_2$CH$_2$CONH, 8H); 1.45 + 1.43 (2 s, C(C*H*$_3$)$_3$, 18H); 1.32-1.24 (m, CH$_3$(C*H*$_2$)$_{12}$CH$_2$, 24H); 0.87 (t, C*H*$_3$CH$_2$, *J* = 6.8 Hz, 3H). ^{13}C NMR (100 MHz, $CDCl_3$) δ: 172.11 (*C*=O); 156.14, 152.54 (2 x *C*=OBoc); 81.43, 79.88 (2 x *C*(CH$_3$)$_3$); 46.65 ((*C*H$_2$)$_2$NCO); 37.15 (*C*H$_2$NHCO); 32.07 (*C*H$_2$NHCOBoc); 29.83, 29.80, 29.66, 29.53 (C(*C*H$_3$)$_3$); 29.50, 29.47, 28.55 (C(*C*H$_3$)$_3$); 29.50 (*C*H$_2$); 29.47 (*C*H$_2$); 28.55 (*C*H$_2$); 27.61 (*C*H$_2$); 25.96 (*C*H$_2$CH$_2$CO); 24.76 (*C*H$_2$); 23.03 (*C*H$_2$); 22.83 (*C*H$_2$CH$_3$); 14.27 (*C*H$_3$CH$_2$). HRMS: Calc. $[M+Na]^+$ ($C_{33}H_{65}N_3NaO_5$) m/z = 606.4831, found $[M+Na]^+$ = 606.4829 (100%); Calc. $[M+H]^+$ ($C_{33}H_{66}N_3O_5$) m/z = 584.4997, found = 584.4986 (24%). IR: ν_{max} (cm^{-1}): 3819*m* (N-H); 3765*m* (N-H); 2965*m*, 2943*s*, 2875*s* (all CH); 1682*s*, 1544*s* (C=O); 1525*s*, 1478*w*, 1454*w*, 1421*m*, 1393*w*, 1361*w*, 1317*s*, 1265*m*, 1254*s*, 1132*m*, 1112*w*, 862*m*, 834*w*, 761*w*.

Deprotection of Boc-C_{16}-SPD (C_{16}-SPD)

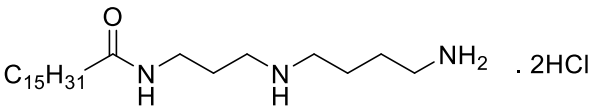

Chemical Formula: $C_{23}H_{51}Cl_2N_3O$
Molecular Weight: 456.58

Boc-Protected Spermidine (258 mg, 0.44 mmol) was dissolved in MeOH (25 mL) and HCl gas was applied for ca. 15-20 seconds. The mixture was stirred for 3 hours and the solvent was removed *in vacuo*, and after drying in vacuum, product was obtained as a white solid (209 mg, 81%).

R_f = 0.2 (90:10:1 DCM/MeOH/Et_3N). ^{1}H NMR (400 MHz, CD_3OD) δ: 3.25 (t, C*H*$_2$NHCO *J* = 6.6 Hz, 2H); 3.12-3.03 (m, C*H*$_2$NH + C*H*$_2$NH$_2$, 6H); 2.22 (t, C*H*$_2$CONH, *J* = 7.6 Hz, 2H); 1.92 (app quint, C*H*$_2$CH$_2$NHCO *J* = 7.6 Hz, 2H); 1.78 (app. quint, C*H*$_2$CH$_2$NH$_2$ + C*H*$_2$CH$_2$CONH, *J* = 4.0 Hz, 4H); 1.55 (br quint, C*H*$_2$CH$_2$CH$_2$NH$_2$, 2H); 1.24 (br app s, CH$_3$(C*H*$_2$)$_{12}$CH$_2$, 24H); 0.84 (t, C*H*$_3$CH$_2$, *J* = 6.8 Hz, 3H). Solubility problems prevented the measurement of ^{13}C NMR. HRMS: Calc. $[M+H]^+$ ($C_{23}H_{50}N_3O$) m/z = 384.3948, found $[M+H]^+$ = 384.3948 (100%). IR: ν_{max} (cm^{-1}): 3308*m* (N-H); 2954*m*, 2916*s*, 2849*s*, 2788*m* (all CH); 2746*m*, 1644*s*, 1613*m* (C=O); 1543*s* (N-H); 1526*s*, 1464*s*, 1439*w*, 1360*m*, 1344*m*, 1269*m*, 1204, 1172*m*, 1090*m*, 1059*m*, 1015*m*, 757*m*, 728*m*, 680*m*, 600*w*, 550*m*, 458*w*.

Boc-Spermine (Boc-SPM)[227]

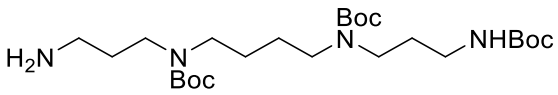

Chemical Formula: $C_{25}H_{50}N_4O_6$
Molecular Weight: 502.70

Under a N_2-atmosphere, spermine (4.92 g, 23.58 mmol) was dissolved in MeOH (100 ml) and cooled to -78 °C. Ethyl tri-fluoroacetate (2.45 ml, 23.58 mmol) was added gradually

and the mixture was stirred for 1 h at -78 °C and for 75 minutes at 0 °C. Afterwards, Boc_2O (20.58 g, 95.32 mmol) was added, the solution was stirred for 1 h at 0 °C, then for 105 min at r.t. and subsequently quenched with water (10 ml). NH_{3aq} (concentrated) was added until the pH was higher than 10 and the mixture was stirred overnight. The solvent was evaporated and the crude product was dried in vacuum as a very sticky colourless yellow oil. Mass spectrometry suggested the ratio of desired product and tetra-Boc-spermine as ca. 3:1. The crude product was used in the following coupling reaction without further purification.

R_f = 0.18 (Hex:EtOAc, 1:1). ^{1}H NMR (400 MHz, $CDCl_3$) δ: 8.29 (br s, N*H*, 1H); 4.45 (br s, NH_2, 2H); 3.30-3.08 (m, CH_2NHBoc + CH_2NBoc, 10H); 2.90 (m, $CH_2CH_2NH_2$, 2H); 1.87 (m, C$H_2CH_2NH_2$, 2H); 1.65 (m, CH_2CH_2NHBoc, 2H); 1.45-1.42 (m, CH_2NHBoc + C(CH_3)$_3$, 31H). Solubility problems prevented the measurement of ^{13}C NMR. HRMS: Calc. $[M+H]^+$ ($C_{25}H_{52}N_4O_6$) m/z = 502.688, found $[M+H]^+$ = 503.3794 (100%); Calc. $[M+Na]^+$ ($C_{25}H_{50}N_4NaO_6$) m/z = 525.3803, found $[M+Na]^+$ = 625.4136 (54%). IR: ν_{max} (cm^{-1}): 3340*w* (N-H); 2971*m*, 2935*s* (all CH); 2871*m*, 1679*s* (C=O); 1531*m*, 1478*w*, 1391*m*,1304*w*, 1200*w*, 1160*m*, 871*w*, 835*w*, 801*m*, 771*w*, 721*w*.

Boc-Protected C_{16}-Spermine (Boc-C_{16}-SPM)

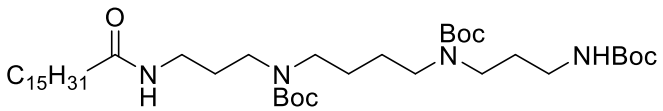

Chemical Formula: $C_{41}H_{80}N_4O_7$
Molecular Weight: 741.11

Palmitic acid (0.76 g, 2.98 mmol) was dissolved in DCM (65 ml) then TBTU (1.25 g, 3.9 mmol) and Et_3N (approx. 5 ml) were added. The mixture was stirred for 5 minutes and

tri-Boc-spermidine (1.50 g, 2.98 mmol) was dissolved in DCM (65 ml) and added. The solution was left stirring overnight. After the solvent was evaporated, product was purified first by silica column in DCM/MeOH (1:0 to 9:1). Two fractions were combined (2.5 g) and purified again by a second column in Hex/EtOAc 2:1. The product was obtained as a colourless oil (448 mg, 28 %). After 72 h some white crystals formed in the oil.

R_f = 0.22 (Hex:EtOAc, 1:1). ^{1}H NMR (400 MHz, $CDCl_3$) δ: 8.29 (br s, N*H*, 1H); 5.27 (br s, N*H*Boc, 1H); 3.13-3.25 (m, C*H*$_2$NHCO + C*H*$_2$NBoc + C*H*$_2$NHBoc, 12H); 2.17 (t, C*H*$_2$CONH, *J* = 7.6 Hz, 2H); 1.69-1.60 (m, C*H*$_2$CH$_2$NBoc + (C*H*$_2$)$_2$CH$_2$NHBoc, 8H); 1.45 (s, C(C*H*$_3$)$_3$, 27H); 1.32-1.24 (m, CH$_3$(C*H*$_2$)$_{12}$CH$_2$ + C*H*$_2$CH$_2$CONH, 26H); 0.87 (t, C*H*$_3$CH$_2$, *J* = 7.0 Hz, 3H). Solubility problems prevented the measurement of ^{13}C NMR. HRMS: Calc. $[M+H]^+$ ($C_{41}H_{81}N_4O_7$) m/z = 742.6100, found $[M+H]^+$ = 742.6095 (25%); Calc. $[M+Na]^+$ ($C_{41}H_{80}N_4NaO_7$) m/z = 763.5921, found $[M+Na]^+$ = 763.5914 (100%). IR: ν_{max} (cm^{-1}): 3352*w* (N-H); 2998*m*, 2945*s* (all CH); 2887*m*, 1673*s*, 1561*m* (C=O); 1478*w*, 1398*m*,1317*w*, 1246*w*, 1187*m*, 894*w*, 865*w*, 823*m*, 745*w*, 721*w*.

Deprotection of Boc-C$_{16}$-SPM (C$_{16}$-SPM)

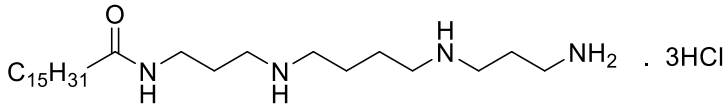

Chemical Formula: $C_{26}H_{59}Cl_3N_4O$
Molecular Weight: 550.14

Boc-Protected Spermine (448 mg), was dissolved in MeOH (25 mL) and HCl gas was applied for approx.15-20 seconds. The mixture was stirred for 3 hours and the solvent was removed *in vacuo*., and after drying in vacuum, the product was obtained as a white solid (323 mg, 97 %). ^{1}H NMR (400 MHz, $CDCl_3$) δ: 5.65 (br s, N*H*); 3.25 (t, C*H*$_2$NHCO

J = 6.8 Hz, 2H); 3.17-3.03 (m, C*H*$_2$NH + C*H*$_2$NH$_2$, 10H); 2.22 (t, C*H*$_2$CONH, *J* = 7.4 Hz, 2H); 2.08 (app. quint., C*H*$_2$CH$_2$NH$_2$, *J* = 7.9 Hz, 2H); 1.89 (approx. quint., C*H*$_2$CH$_2$NHCO, *J* = 7.0 Hz, 2H); 1.78 (m, CH$_2$(C*H*$_2$)$_2$CH$_2$, 4H); 1.55 (approx. quint, C*H*$_2$CH$_2$CONH, *J* = 6.0 Hz, 2H); 1.24 (s, CH$_3$(C*H*$_2$)$_{12}$CH$_2$, 24H); 0.84 (t, C*H*$_3$CH$_2$, *J* = 6.6 Hz, 3H). Solubility problems prevented the measurement of ^{13}C NMR. HRMS: Calc. $[M+H]^+$ ($C_{26}H_{58}N_4O$) m/z= 441.4527, found $[M+H]^+$ = 441.4541 (100%). IR: ν_{max} (cm^{-1}): 3317*m*, 2954*s* (N-H); 2918*s*, 2849*s*, 2782*s*, 2750*s*, 1703*s* (all CH); 1645*s* (C=O); 1531*s*, 1488*m*, 1464*s*, 1444*m*, 1411*w*, 1388*m*, 1349*m*, 1269*m*, 1250*m*, 1209*m*, 1182*s*, 1164*s*, 1087*w*, 1058*m*, 979*w*, 872*w*, 761*m*, 724*m*, 678*m*, 550*w*.

7.1.3 Chapter 4

Synthesis of H$_2$/Newkome-G1/O-*tert*-Butyl Branching (Compound 2)[109,250]

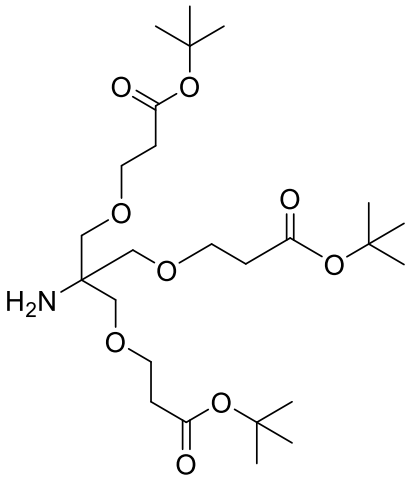

Chemical Formula: $C_{25}H_{47}NO_9$
Molecular Weight: 505.65

Tris (hydroxymethyl) aminoethane (6.01 g, 49.52 mmol) and DMSO (10 mL) were mixed and cooled to 15 °C under N_2. NaOH (1 mL, 5 M) was added to the reaction flask. Then *tert*-butyl acrylate (25 mL, 34 mmol) was added dropwise (40 mL/h, 37.5 min). The reaction was cooled to room temperature and stirred for 24 h. The solvent was removed

in vacuo (30-40 °C). The product was purified by column chromatography (SiO_2, 2:1 v/v, EtOAc/Hexane, 0.05% v/v NH_4OH). A colorless oil was recovered (4.80 g, 80%).

R_f = 0.25 (2:1, EtOAc/Hexane, drops of NH_4OH). ^1H NMR ($CDCl_3$, 400 MHz) δ: 3.64 (t, OCH_2CH_2, *J* = 6.0 Hz, 6H); 3.41 (s, CCH_2O, 6H); 2.43 (t, CH_2CH_2O, *J* = 6.0 Hz, 6H); 1.81 (s, NH_2, 2H); 1.38 (s, $(CH_3)_3C$, 27H). ^{13}C NMR ($CDCl_3$, 100 MHz) δ: 170.15 (COO^t-Bu); 79.59 ($C(CH_3)_3$); 72.37 (CCH_2O); 66.64 (OCH_2CH_2); 55.54 (CCH_2O); 35.78 (CH_2CH_2O); 27.62 ($(CH_3)_3C$). HRMS: Calc. $[M+H]^+$ **(**$C_{25}H_{48}NO_9$**)** m/z = 506.3324, found $[M+H]^+$ = 506.3320 (100%). IR: ν_{max} (cm^{-1}): 3412*w* (N-H); 2998*m*, 2945*s* (all CH); 2857*m*, 1673*s*, 1561*m*, 1498*w*, 1496*m*,1317*w*, 1246*w*, 1152*s*, 1132*s*, 1112*s*, 1048*s*, 865*w*, 823*m*, 670*w*, 543*w*.

Synthesis of Z/Newkome-G1/O-*tert*-Butyl (Compound 3)[251]

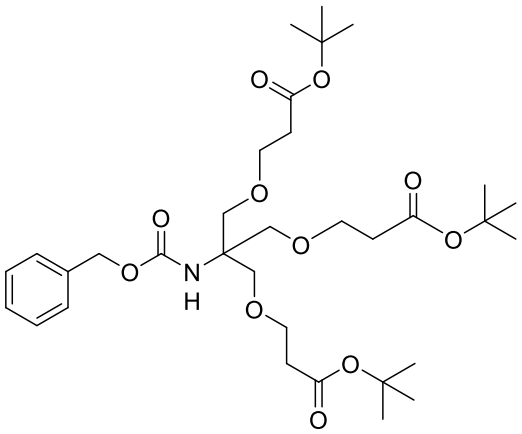

Chemical Formula: $C_{33}H_{53}NO_{11}$
Molecular Weight: 639.78

Compound **2** (1.33 g, 2.62 mmol) was dissolved in DCM (21 mL), Na_2CO_3 (25 mL, 25% by mass in water) was added while stirring, then benzyl chloroformate (1.17 mL, 6.8 mmol) was added (rapidly), and the mixture was left to stir for 48 h. The product was extracted with DCM (40 mL) then dried over $MgSO_4$ and the solvent was removed *in*

vacuo. The crude product was purified by column chromatography (SiO_2, 2:1 v/v, Cyclohexane/EtOAc). The product was a colorless oil (1.40 g, 83%).

R_f = 0.65 (2:1 Cyclohexane/EtOAc). ^{1}H NMR ($CDCl_3$, 400 MHz) δ: 7.23-7.19 (m, C*H* aromatic, 5H); 5.16 (s, N*H*, 1H); 4.91 (s, CH_2 benzylic, 2H); 3.55 (s, CCH_2O, 6H); 3.54 (t, OCH_2CH$_2$, *J* = 6.0 Hz, 6H); 2.33 (t, CH_2CH$_2$O, *J* = 6.0 Hz, 6H); 1.31 (s, (CH_3)$_3$C, 27H). ^{13}C NMR ($CDCl_3$, 100 MHz) δ: 171.14 (*C*OO^t-Bu); 155.53 (*C*ONH); 137.03, 128.69.128.26, 128.18 (*C*H aromatic); 80.76 (*C*(CH$_3$)$_3$); 73.65 (*C*CH$_2$O); 69.66 (*C*H$_2$O); 67.37 (CH$_2$*C*H$_2$O); 66.39 (*C*H$_2$ benzylic); 59.00 (*C*H$_2$O); 36.51 (*C*H$_2$CH$_2$O); 28.37 ((*C*H$_3$)$_3$C). HRMS: Calc. $[M+H]^+$ ($C_{33}H_{54}NO_{11}$) m/z = 640.3691, found $[M+H]^+$ = 640.3724 (100%). IR: ν_{max} (cm^{-1}): 3097*m* (CH, aromatic); 2987*w* (N-H); 2963*m*, 2927*s*, 2851*s*, 2254*m* (all CH); 1751*m*, 1665*s* (C=O); 1652*s* (C=O); 1612*m* (C=C); 1542*m*, 1468*s*, 1378*m*, 1260*w*, 1234*w*, 1160*w*, 1070*w*, 748*s*, 561*w*.

Synthesis of Z/Newkome-G1/OH (Compound 4)[251]

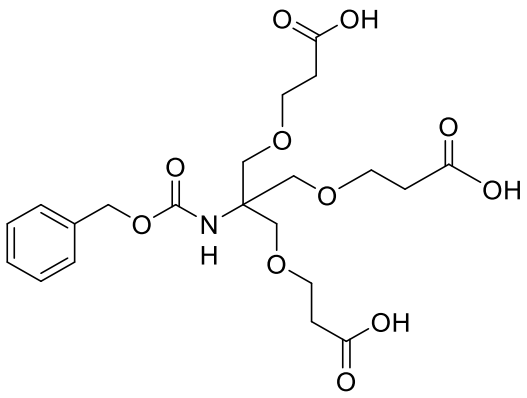

Chemical Formula: $C_{21}H_{29}NO_{11}$
Molecular Weight: 471.46

Compound **3** (1.30 g, 2.03 mmol) was mixed with formic acid (7.5 mL) and stirred for 24 h at room temperature. Formic acid was removed *in vacuo* at 50 °C; the product was a colorless oil (950 mg, 99%).

R_f = 0.25 (90:10 DCM/MeOH). ^{1}H NMR (Acetone-d_6, 400 MHz) δ: 8.2 (s, COO*H*, 3H); 7.37-7.29 (m, C*H* aromatic, 5H); 5.78 (s, N*H*, 1H); 5.02 (s, CH_2 benzylic, 2H); 3.70 (s, CCH_2O, 6H); 3.67 (t, OCH_2CH$_2$, *J* = 6.0 Hz, 6H); 2.54 (t, CH_2CH$_2$O, *J* = 6.0 Hz, 6H). ^{13}C NMR (Acetone-d_6, 100 MHz) δ: 173.01 (*C*OOH); 158.17 (*C*ONH); 128.50, 128.54, 129.16, 138.39 (*C*H aromatic); 69.91 (C*C*H$_2$O); 67.67 (CH$_2$*C*H$_2$O); 66.12 (*C*H$_2$ benzylic); 59.81 (*C*CH$_2$O); 35.11 (*C*H$_2$CH$_2$O). HRMS: Calc. $[M+H]^+$ ($C_{21}H_{30}NO_{11}$) m/z = 472.1813, found $[M+H]^+$ = 472.1807 (100%). IR: ν_{max} (cm^{-1}): 3065*m* (CH, aromatic); 3002*w* (N-H); 2956*m*, 2945*s*, 2875*s*, 2456*m* (all CH); 1745*s* (C=O); 1664*s* (C=O); 1635*s* (C=O); 1623*m* (C=C); 1534*m*, 1476*s*, 1340*m*, 1284*w*, 1245*w*, 1178*w*, 1082*w*, 734*s*, 585*w*.

Synthesis of Z/G1/mono-Boc DAPMA (Compound 5)[251]

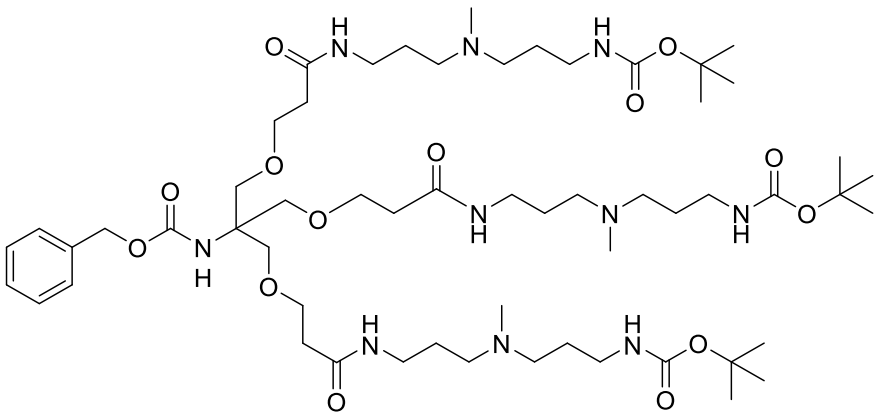

Chemical Formula: $C_{57}H_{104}N_{10}O_{14}$
Molecular Weight: 1153.52

Compound **4** (800 g, 1.7 mmol) was dissolved in THF (40 mL), DCC (2.30 g, 11.5 mmol) and Et_3N (1.20 g, (1.10 mL), 11.5 mmol) were added. The mixture was cooled to 0 °C. Compound **1** (1.30 g, 3.7 mmol) was dissolved in THF (40 mL) then the solution was added dropwise to the reaction flask. The reaction was left to stir for 3 days then it was filtered to remove the precipitate. The filtrate was collected and the solvent dried *in vacuo*. In order to remove the formed DCU (*N*,*N*'-Dicyclohexylurea), the residue was dissolved

in DCM (80 mL), filtered over Celite then dried *in vacuo*. The crude product was dissolved in chloroform (80 mL), filtered over Celite and dried *in vacuo*. The product at this stage was an oil-like that needed purification by GPC column (Bio-beads, 100% DCM). The compound was the first fraction to be collected; it was a yellowish orange (amber) oil. The yield was (980 mg, 50%).

R_f = 0.1 (100% MeOH). ^{1}H NMR ($CDCl_3$, 400 MHz) δ: 7.26-7.24 (m, C*H* aromatic, 5H); 7.22-7.15 (br m, N*H* amides, 3H); 5.26 (s, N*H*, 1H); 5.25 (br m, N*H*Boc, 3H); 5.23 (s, CH_2 benzylic, 2H); 3.61 (s, CCH_2O, 6H); 3.60 (t, OCH_2CH$_2$, *J* = 6.0 Hz, 6H); 3.38 (d, NHCH_2CH$_2$CH$_2$, *J* = 5.8 Hz 6H); 3.19 (d, CH_2NHCOO^t-Bu, *J* = 5.8 Hz, 6H); 2.32-2.13 (CH_2CH$_2$O, CH_2N(CH$_3$)CH$_2$ and CH$_2$N(CH$_3$)CH_2, 18H); 2.18 (s, NCH_3, 9H); 1.60 (m, CH$_2$CH_2CH_2, 12H); 1.35 (s, C(CH_3)$_3$, 27H). ^{13}C NMR ($CDCl_3$, 100 MHz) δ: 176.21 (*C*ONH); 156.02, 154.22 (*C*=O); 154.22 137.22, 128.19, 127.30, 127.11 (*C*H aromatic); 72.01 (NH$_2$*C*CH$_2$O); 67.91 (O*C*H$_2$CH$_2$O); 55.90 (CH$_2$*C*H$_2$NCH$_3$); 41.80 (N*C*H$_3$); 39.30 (NH*C*H$_2$CH$_2$); 38.10 (OCNH*C*H$_2$); 36.88 (OCH$_2$*C*H$_2$CO); 28.10 (OC(*C*H$_3$)$_3$); 26.90 (*C*H$_2$CH$_2$NCH$_3$); 26.30 (*C*H$_2$CH$_2$NH). HRMS: Calc. $[M+2H]^{2+}$ ($C_{57}H_{106}N_{10}O_{14}$) m/z = 577.3940, found $[M+2H]^{2+}$ = 577.3887 (100%). IR: ν_{max} (cm^{-1}): 3037*w* (CH, aromatic); 3190*m (*N-H); 2963*m*, 2927*s*, 2851*s*, 2254*m* (all CH); 1772*s* (C=O); 1665*s* (C=O); 1652*s* (C=O); 1615*m* (C=C); 1554*m*, 1448*s*, 1338*m*, 1256*w*, 1214*w*, 1120*w*, 875*w*, 564*s***,** 451*w*.

Removing Compound 5's Z Group (Deprotection) (Compound 6)[251]

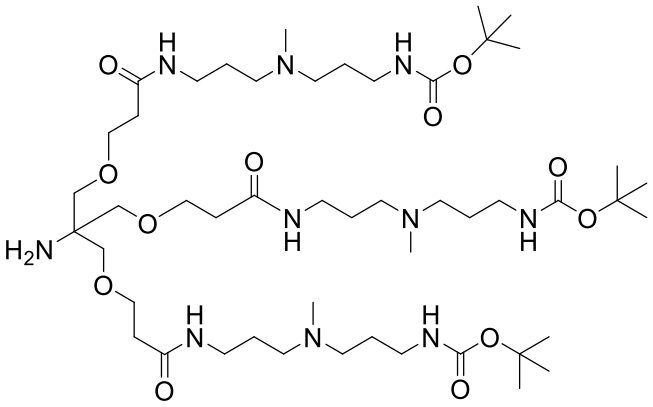

Chemical Formula: $C_{49}H_{98}N_{10}O_{12}$
Molecular Weight: 1019.38

Compound **5** (950 mg, 0.823 mmol) was dissolved in EtOH (7.5 mL) then Pd/C (10%, 65 mg) was added as the catalyst. The reaction was left stirring under H_2 for 72 h and monitored by TLC. The mixture was filtered over Celite to remove the catalyst. The solvent was dried *in vacuo* and the product was concentrated and purified by gel permeation chromatography (GPC) column (Bio-beads, 100% DCM). The product was a gluey orange solid (700 mg, 83%).

R_f = 0.01 (90:10:1 DCM/MeOH/Et_3N). ^{1}H NMR ($CDCl_3$, 400 MHz) δ: 7.31-7.26 (br m, N*H* amides, 3H); 5.32 (s, N*H*, 2H); 5.32 (br m, N*H*Boc, 3H); 3.68 (s, CCH_2O, 6H); 3.66 (t, OCH_2CH$_2$, *J* = 6.0 Hz, 6H); 3.43 (d, NHCH_2CH$_2$CH$_2$, *J* = 5.8 Hz 6H); 3.14 (d, CH_2NHCOO^t-Bu, *J* = 5.8 Hz, 6H); 2.39-2.35 (m, CH_2CH$_2$O, CH_2N(CH$_3$)CH$_2$ and CH$_2$N(CH$_3$)CH_2, 18H); 2.17 (s, NCH_3, 9H); 1.67 (m, CH$_2$CH_2CH_2, 12H); 1.43 (s, C(CH_3)$_3$, 27H). ^{13}C NMR ($CDCl_3$, 100 MHz) δ: 171.03 (*C*=O); 154.98 (*C*=O); 72.60 (NH$_2$*C*CH$_2$O); 67.91 (O*C*H$_2$CH$_2$O); 55.92 (CH$_2$*C*H$_2$NCH$_3$); 41.80 (N*C*H$_3$); 39.30 (NH*C*H$_2$CH$_2$); 38.10 (OCNH*C*H$_2$); 36.88 (OCH2*C*H$_2$CO); 28.15 (OC(*C*H$_3$)$_3$); 26.97 (*C*H$_2$CH$_2$NCH$_3$); 26.30 (*C*H$_2$CH$_2$NH). HRMS: Calc. $[M+2H]^{2+}$ ($C_{49}H_{100}N_{10}O_{12}$) m/z = 510.3756, found $[M+2H]^{2+}$ = 510.3760 (100%). IR: ν_{max} (cm^{-1}): 3112*m (*N-H); 2976*m*, 2935*s*, 2764*s*, 2388*m* (all CH); 1745*s* (C=O); 1675*s* (C=O); 1657*s* (C=O); 1519*m*, 1439*s*, 1348*m*, 1276*w*, 1226*w*, 1174*w*, 765*w*, 536*s*.

Coupling of Compound 6 and Behenic Acid (Compound 7)

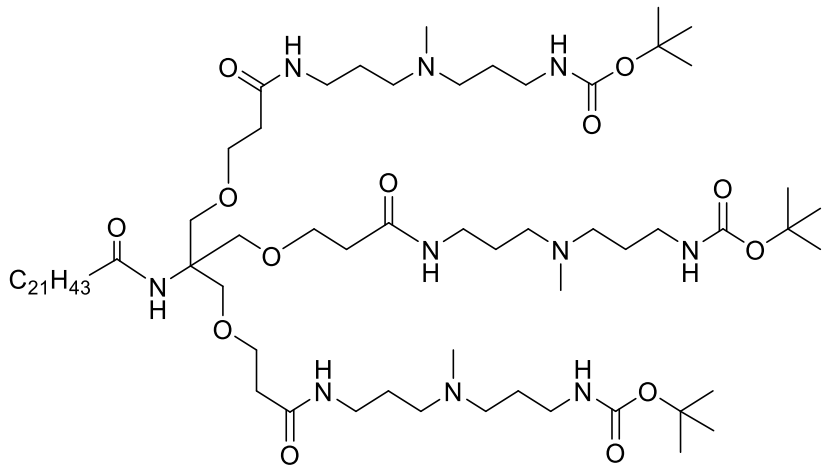

Chemical Formula: $C_{71}H_{140}N_{10}O_{13}$
Molecular Weight: 1341.96

Behenic acid (1.00 g, 3 mmol) was dissolved in DCM (65 mL). TBTU (1.25 g, 3.95 mmol) and Et_3N (5.4 mL) were added. The mixture was stirred for 5 minutes at room temperature. Compound **6** (680 mg, 0.66 mmol) was dissolved in DCM (65 mL) then was added to the reaction flask. The reaction was stirred overnight, then the mixture was concentrated *in vacuo*. The product was concentrated and purified by gel permeation chromatography (GPC) column (Bio-beads, 100% DCM). The product was a gluey orange solid (840 mg, 95%).

R_f = 0.01 (90:10:1 DCM/MeOH/Et_3N). ^{1}H NMR ($CDCl_3$, 400 MHz) δ: 7.28-7.23 (br m, N*H* amides, 3H); 5.30 (s, N*H*, 1H); 5.24 (br m, N*H*Boc, 3H); 3.68 (s, CC*H*$_2$O, 6H); 3.66 (t, OC*H*$_2$CH$_2$, *J* = 6.0 Hz, 6H); 3.43 (d, NHC*H*$_2$CH$_2$CH$_2$, *J* = 5.8 Hz 6H); 3.14 (d, C*H*$_2$NHCOO^t-Bu, *J* = 5.8 Hz, 6H); 2.72 (t, CHC*H*$_2$CH, 2H); 2.39-2.35 (m, C*H*$_2$CH$_2$O, C*H*$_2$N(CH$_3$)CH$_2$ and CH$_2$N(CH$_3$)C*H*$_2$, 18H); 2.17 (s, NC*H*$_3$, 9H); 2.12 (t, CH$_2$C*H*$_2$CO, *J* = 8 Hz, 2H); 1.67-1.62 (m, CH$_2$C*H*$_2$CH$_2$, 34H); 1.43 (s, C(C*H*$_3$)$_3$, 27H); 0.84 (t, C*H*$_3$CH$_2$, *J* = 8 Hz, 3H). ^{13}C NMR ($CDCl_3$, 100 MHz) δ: 174.43 (CHNHCO); 144.80 (*C*ONH);

77.24 (*C*CH_3); 67.68 (O*C*H_2CH_2O); 54.15 (CH_2*C*H_2NCH_3); 51.54 (*C*H_2NCH_3); 42.04 (N*C*H_3); 40.10 (NH*C*H_2CH_2); 34.19 (OCNH*C*H_2); 33.26 (OCH_2*C*H_2CO); 31.60 (*C*H_2CO); 29.43 (OC(*C*$H_3)_3$); 29.23 (*C*$H_2CH_2NCH_3$); 29.19 (*C*H_2CH_2NH) 29.17 (CH_2*C*H_2CO); 28.49 (*C*H_2CH_3); 28.11 (*C*H_2); 27.62 (*C*H_2); 26.23 (*C*H_2); 25.54 (*C*H_2); 14.16 (*C*H_3CH_2). HRMS: Calc. $[M+2H]^{2+}$ ($C_{71}H_{142}N_{10}O_{13}$) m/z = 671.4904, found $[M+2H]^{2+}$ = 671.4917 (100%). IR: ν_{max} (cm^{-1}): 3290*w* (N-H); 2928*s*, 2857*s* (all CH); 1694*s* (C=O); 1652*s* (C=O); 1532*m*, 1250*s*, 1168*s*, 1094*s*, 864*m*, 745*m*.

De-protection of Compound 7 (Binder-Dend)

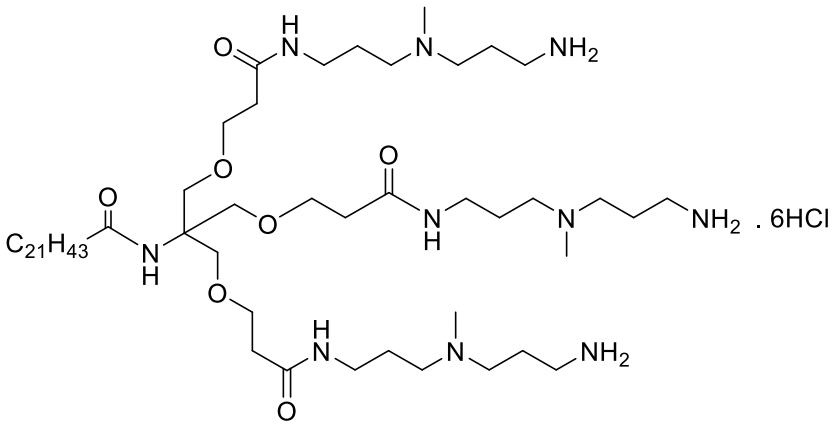

Chemical Formula: $C_{56}H_{122}Cl_6N_{10}O_7$
Molecular Weight: 1260.36

Compound **7** (800 mg, 0.6 mmol) was dissolved in methanol (25 mL) then HCl gas was applied for 15-20 seconds then the mixture was stirred for 3 hours and monitored by TLC. The solvent was dried *in vacuo* and the product was a gummy orange solid (680 mg, 90%).

R_f = 0.03 (90:10:1 DCM/MeOH/Et_3N). ^{1}H NMR ($CDCl_3$, 400 MHz) δ: 7.31-7.26 (br m, N*H* amides, 3H); 6.34-6.12 (br m, NH_2, 6H); 5.20 (s, N*H*, 1H); 3.63 (s, CCH_2O, 6H); 3.60 (t, OCH_2CH_2, *J* = 6.0 Hz, 6H); 3.55 (d, NHC$H_2CH_2CH_2$, *J* = 5.8 Hz 6H); 3.27 (d,

C*H*$_2$NHCOO^t-Bu, *J* = 5.8 Hz, 6H);3.66 (t, OC*H*$_2$CH$_2$, *J* = 6.0 Hz, 6H); 3.43 (d, NHC*H*$_2$CH$_2$CH$_2$, *J* = 5.8 Hz, 6H); 3.14 (d, C*H*$_2$NHCOO^t-Bu, *J* = 5.8 Hz, 6H); 2.72 (t, CHC*H*$_2$CH, *J* = 5.4 Hz, 2H); 2.39-2.35 (m, C*H*$_2$CH$_2$O, C*H*$_2$N(CH$_3$)CH$_2$ and CH$_2$N(CH$_3$)C*H*$_2$, 18H); 2.17 (s, NC*H*$_3$, 9H); 2.12 (t, CH$_2$C*H*$_2$CO, *J* = 8.0 Hz, 2H); 1.67-1.59 (m, CH$_2$C*H*$_2$CH$_2$, 34H); 0.84 (t, C*H*$_3$CH$_2$, *J* = 8.0 Hz, 3H). ^{13}C NMR (CDCl$_3$, 100 MHz) δ: 174.43 (CHNH*C*O); 164.82 (*C*ONH); 67.68 (O*C*H$_2$CH$_2$O); 54.15 (CH$_2$*C*H$_2$NCH$_3$); 51.54 (*C*H$_2$NCH$_3$); 42.04 (N*C*H$_3$); 40.10 (NH*C*H$_2$CH$_2$); 34.19 (OCNH*C*H$_2$); 33.26 (OCH$_2$*C*H$_2$CO); 31.60 (*C*H$_2$CO); 29.43 (OC(*C*H$_3$)$_3$); 29.23 (*C*H$_2$CH$_2$NCH$_3$); 29.19 (*C*H$_2$CH$_2$NH) 29.17 (CH$_2$*C*H$_2$CO); 28.49 (*C*H$_2$CH$_3$); 26.75 (*C*H$_2$); 25.73 (*C*H$_2$); 24.31 (*C*H$_2$); 22.17 (*C*H$_2$); 20.98 (*C*H$_2$); 14.16 (*C*H$_3$CH$_2$). HRMS: Calc. [M+3H]$^{3+}$ (C$_{56}$H$_{119}$N$_{10}$O$_7$) m/z = 347.9749, found [M+3H]$^{3+}$ = 347.9797 (100%); Calc. [M+2H]$^{2+}$ (C$_{56}$H$_{118}$N$_{10}$O$_7$) m/z = 521.4587, found [M+2H]$^{2+}$ = 521.4598 (45%). IR: ν_{max} (cm^{-1}): 3290*w* (N-H); 2928*s*, 2857*s* (C-H); 1694*s* (C=O); 1574*s*, 1250*s*, 1170*s*, 1092*s*, 862*m*, 668*m*, 580*w*.

Coupling of Thioglycolic acid and Compound 1 (Compound 8)

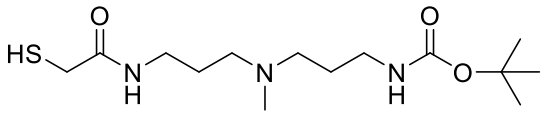

Chemical Formula: $C_{14}H_{29}N_3O_3S$
Molecular Weight: 319.46

Thioglycolic acid (1.0 g, 0.76 mL, 10.86) was dissolved in DCM (65 mL), then TBTU (3.7 g, 11.50 mmol) and Et$_3$N (5.4 mL, 38.72 mmol) were added respectively. The mixture was stirred for 5 minutes at room temperature. The mixture was stirred for 5 minutes then compound **1** (2.66 g, 10.86 mmol) was dissolved in DCM (65 mL) and added to the reaction flask. The reaction was stirred overnight then the mixture was

concentrated in *vacuo* and the residue purified by GPC column chromatography (Bio-beads, 100% DCM). The product was a sticky orange solid with a distinct sulfur smell (2.80 g, 81%).

R_f = 0.15 (90:10:1 DCM/MeOH/Et_3N). ^{1}H NMR ($CDCl_3$, 400 MHz) δ: 7.45 (br t, N*H* amides, *J* = 6.2 Hz, 2H); 3.45 (d, C*H*$_2$SH, *J* = 5.8 Hz, 2H); 3.42 (q C*H*$_2$NHCO, J = 5.6 Hz, 2H); 3.18 (q, CH_2C*H*$_2$NH, *J* = 6.8 Hz, 2H); 2.45 (t, C*H*$_2$N(CH_3), *J* = 6.4 Hz, 4H); 2.26 (s, CH_2N(C*H*$_3$), 3H); 1.70 (m, CH_2C*H*$_2$NH, 4H); 1.51 (t, CH_2S*H*, *J* = 5.8 Hz, 1H). ^{13}C NMR ($CDCl_3$, 100 MHz) δ: 165.76 (*C*ONH); 162.37 (O*C*ONH); 81.15 (*C*CH_3); 59.34 (*C*H_2NCH_3); 48.43 (N*C*H_3); 37.86 (*C*H_2NH); 36.98 (*C*H_2NHCO); 35.74 (*C*H_2CO); 32.05 (*C*H_2SH); 27.65 (C(*C*H_3)$_3$); 26.07 (*C*$H_2$$CH_2NCH_3$); 25.11 (*C*$H_2$$CH_2$NH). HRMS: Calcd. $[M+H]^+$ ($C_{14}H_{29}N_3O_3S$) m/z = 319.1924, found $[M+H]^+$ = 319.1921 (100%). ν_{max} (solid): 3287*w* (N-H); 3009*w*, 2926*s*, 2855*s*, (all CH); 2603*m*, 2586*m* (S-H); 1638*s* (C=O); 1542*s* (C=O); 1464*m*, 1299*m*, 1272*m*, 1250*s*, 1171*s*, 1056m 1049*s*, 867*w*, 723*w*.

Synthesis of Au-Thiol-DAPMA-Boc (Au-8)

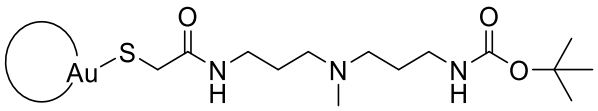

Chemical Formula: $C_{14}H_{28}Au_{2.05}N_3O_3S$
Molecular Weight: 723.24

Tetrachloroauric acid (210 mg. 0.6 mmol) was diluted by ultra-pure water (50 ml) to give a yellow soulution. Sodium citrate (3 mL, 50 mg/mL) was added to the solution, boiled at > 97 °C and the colour changed to dark grey/black indicating the success of the reduction. The mixture was boiled for a further hour, and on prolonged heating the colour changed from black to dark red (ruby). Compound **8** (192 mg, 0.6 mmol) was dissolved

in ultra-pure water (50 mL) then added to the reaction flask and left to boil for another hour; the colour changed to black indicating the coupling of compound **8** and the citrate-stabilized AuNPs. Once the reaction flask reached room temperature, the mixture was purified using a dialysis membrane 30 (MWCO-12, 1400 Dalton), the dialysis process took place overnight (water was replaced twice). The pure product was collected from the dialysis membrane and solvent was dried *in vacuo* and the product was obtained in 91% yield (280 mg).

R_f = 0.01 (MeOH). ^{1}H NMR (CD_3OD, 400 MHz) δ: 6.85 (br s, N*H*, 1H); 5.34 (br s, N*H*Boc, 1H); 3.48 (br s, C*H*$_2$S, 2H); 3.32 (q, C*H*$_2$NHCO, *J* = 6.0 Hz, 2H); 3.21 (q, *CH*$_2$NHBoc, *J* = 6.0 Hz, 2H); 2.54 (m, CH_2*CH*$_2$NH, 4H); 2.23 (s, NC*H*$_3$, 3H); 1.62 (t, C*H*$_2$$CH_2NCH_3$, *J* = 6.4 Hz, 4H); 1.41 (s, C(C*H*$_3$)$_3$, 9H). ^{13}C NMR ($CDCl_3$, 100 MHz) δ: 169.27 (*C*ONH); 158.32 (O*C*ONH); 80.04 (*C*CH_3); 58.42 (*C*H_2NCH_3); 46.65 (N*C*H_3); 38.91 (*C*H_2NH); 37.76 (*C*H_2NHCO); 34.92 (*C*H_2CO); 31.65 (*C*H_2S); 27.93 (C(*C*H_3)$_3$); 25.98 (*C*$H_2CH_2NCH_3$); 24.21 (*C*H_2CH_2NH). IR: ν_{max} (cm^{-1}): 3107*w* (N-H); 2981*w*, 2942*s* (all CH); 1683*s* (C=O); 1532*s* (C=O); 1443*w*, 1397*w*, 1361*s*, 1278*w*, 1245*m*, 1109*w*.

UV-Vis, TEM and DLS indicated aggregation of the nanoparticles into nanocomposite.

Deprotection of Au-8 (Binder-NC)

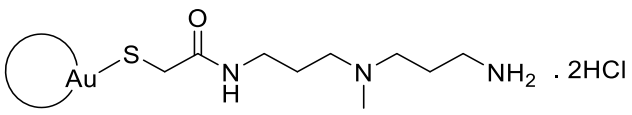

Chemical Formula: $C_9H_{22}Au_{2.05}Cl_2N_3OS$
Molecular Weight: 695.05

Au-8 (260 mg, 0.51 mmol) was dissolved in methanol (20 mL) then HCl gas was applied for 15-20 seconds and the mixture was stirred for 3 hours and monitored by TLC. The solvent was dried *in vacuo* and the product was a gummy orange solid (680 mg, 90%).

Characterizing this product was achieved by energy dispersive X-Ray (EDX) analysis as described in Chapter 4. ^{1}H NMR ($CDCl_3$, 400 MHz) showed the loss of the Boc group at 1.4 ppm. MS spectra could not be obtained. ^{1}H NMR (CD_3OD, 400 MHz) δ: 7.02 (br s, N*H*, 1H); 6.76 (br s, NH_2, 2H); 4.12 (br s, CH_2S, 2H); 3.35 (q, CH_2NHCO, *J* = 6.0 Hz, 2H); 3.26 (q, CH_2NH_2, *J* = 6.0 Hz, 2H); 2.67 (m, CH_2CH_2NH, 4H); 2.29 (s, NCH_3, 3H); 1.71 (t, C$H_2CH_2NCH_3$, *J* = 6.4 Hz, 4H). ^{13}C NMR ($CDCl_3$, 100 MHz) δ: 170.06 (*C*ONH); 78.61 (*C*CH_3); 61.34 (*C*H_2NCH_3); 47.71 (N*C*H_3); 39.64 (*C*H_2NH); 37.22 (*C*H_2NH_2); 35.37 (*C*H_2CO); 32.09 (*C*H_2S); 24.67 (*C*$H_2CH_2NCH_3$); 23.82 (*C*H_2CH_2NH). IR: ν_{max} (cm^{-1}): 3350*w* (N-H); 2975*w*, 2931*s*, 2797*s* (all CH); 1695*s* (C=O); 1521*s* (C=O); 1454.7*w*, 1391*w*, 1367*s*, 1277*w*, 1250*m*, 1173*w*.

UV-Vis, TEM and DLS indicated aggregation of the nanoparticles into nanocomposite.

Coupling Poly(acrylic acid) and Compound 1 (Boc-Binder-Poly)

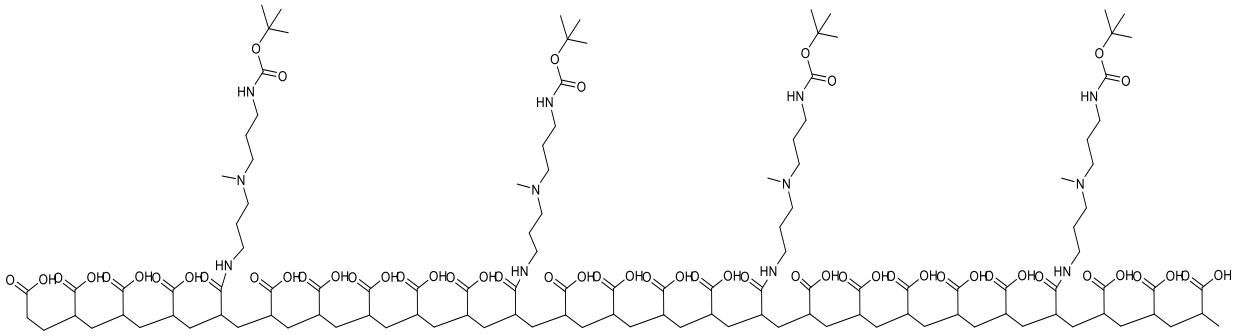

Chemical Formula: $C_{123}H_{202}N_{12}O_{54}$
Molecular Weight: 2713.00

Poly(acrylic acid) (2.50 g, 1.4 mmol) was dissolved in DCM (65 mL) then TBTU (1.25 g, 3.95 mmol) and Et_3N (4.5 mL, 38.72 mmol) were added. The mixture was stirred for 5 minutes, then compound **1** (0.34 g, 1.4 mmol) was dissolved in DCM (65 mL) and

added to the reaction flask. The reaction was stirred overnight then the mixture was concentrated in *vacuo* and the residue was purified by GPC column (Bio-beads, 100% DCM). The product was a white powder (1.80 g, 54%). This system could not be analyzed by MS or NMR, therefore it was characterized after deprotection by CHN elemental analysis (section 4. 4. 2), C = 53%, H = 7% and N = 7%.

Deprotection of Boc-Binder-Poly (Binder-Poly)

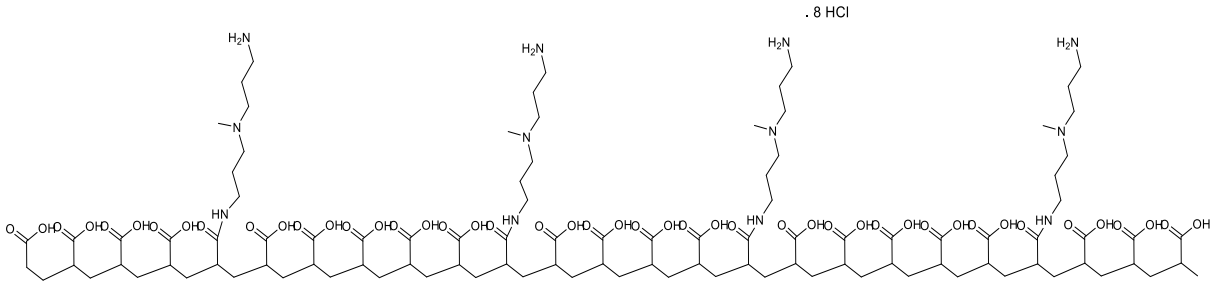

Chemical Formula: $C_{103}H_{170}N_{12}O_{46}$
Molecular Weight: 2312.53

Boc-Binder-Poly (1.50 g, 0.63 mmol) was dissolved in MeOH (45 mL) then HCl gas was applied for 15-20 seconds then the mixture was stirred for 3 hours and monitored by TLC. The solvent was dried *in vacuo* product was a gummy brown solid (1.23 g, 86%).

The product was characterized by MS – however we could not detect the polymer due to its polydispersity. In addition, ^{1}H NMR spectra showed only some of the ligand protons although importantly demonstrated the loss of Boc group, after the deprotection reaction, at 1.4 ppm. CHN elemental analysis; C (53.49%), H (7.40%) and N (7.26%), allowed molar mass to be predicted as 2604.20 (+ 8HCl), calculated from the proposed chemical formula of $C_{103}H_{170}N_{12}O_{46;}$ molar mass = 2312.31. IR: ν_{max} (cm^{-1}): 3012*w* (N-H); 2951*w* (CH); 1642*s* (C=O); 1626*s* (C=O); 1531*w* (CONH); 1454*w*, 1391*w*, 1367*s* 1277*w*, 1250*m*, 1173*w*. 687*m*, 544*w*.

7.1.4 Chapter 5

Synthesis of C_{18}-di-Boc-SPD

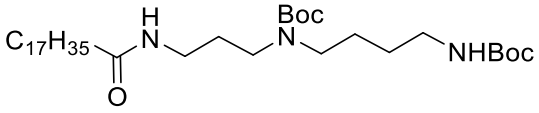

Chemical Formula: $C_{35}H_{69}N_3O_5$
Molecular Weight: 611.95

Stearic acid (334 mg, 1.17 mmol) was dissolved in CH_2Cl_2 (23 mL), and TBTU (373 mg, 1.16 mmol) and triethylamine (ca. 2.3 mL) were added. The reaction mixture was stirred for 5 min before di-boc-spermidine (390 mg, 1.13 mmol) in CH_2Cl_2 (19 mL) was added. The solution was stirred overnight and the solvent removed *in vacuo* to give an orange oil as the crude, which was purified by gel permeation chromatography (GPC) column (Bio-beads, 100% DCM) and secondly on silica gel using hexane/ethyl acetate (1:1) to give a white solid product (0.345 g, 49%).

R_f = 0.69 (1:1 hexane/ethyl acetate). ^{1}H NMR (400 MHz, CD_3OD) δ: 6.72 (br s, N*H*, 1H); 4.55 (br s, N*H*Boc, 1H); 3.27-3.13 (m, C*H*$_2$NHCO, 8H); 2.17 (t, C*H*$_2$CONH, *J* = 7.6 Hz, 2H); 1.68-1.52 (m, C*H*$_2$CH$_2$NBoc + (C*H*$_2$)$_2$CH$_2$NHBoc + C*H*$_2$CH$_2$CONH, 8H); 1.45 + 1.43 (2 s, C(C*H*$_3$)$_3$, 18H); 1.32-1.24 (m, CH$_3$(C*H*$_2$)$_{12}$CH$_2$, 24H); 0.87 (t, C*H*$_3$CH$_2$, *J* = 6.8 Hz, 3H). ^{13}C NMR (100 MHz, $CDCl_3$) δ: 172.11 (*C*=O); 156.14, 152.54 (2 x *C*=OBoc); 81.43, 79.88 (2 x *C*(CH$_3$)$_3$); 46.65 ((*C*H$_2$)$_2$NCO); 37.15 (*C*H$_2$NHCO); 32.07 (*C*H$_2$NHCOBoc); 29.53, 29.50(C(*C*H$_3$)$_3$); 29.47, 28.55 (C(*C*H$_3$)$_3$); 27.61 (*C*H$_2$CH$_2$CO); 25.96 (*C*H$_2$); 24.23 (*C*H$_2$); 23.16 (*C*H$_2$); 22.97 (*C*H$_2$); 22.63 (*C*H$_2$CH$_3$); 14.27 (*C*H$_3$CH$_2$). HRMS: Calc. $[M+H]^+$ ($C_{35}H_{70}N_3O_5$) m/z = 612.5315, found $[M+H]^+$ = 612.5304 (65%); Calc. $[M+Na]^+$ ($C_{35}H_{69}N_3$ NaO_5) m/z = 634.5135, found $[M+Na]^+$ = 634.5126 (100%). IR: ν_{max} (cm^{-1}): 3819*m* (N-H); 3765*m* (N-H); 2965*m*, 2943*s*, 2875*s* (all CH); 1682*s*, 1544*s*

(C=O); 1525*s*, 1478*w*, 1454*w*, 1421*m*, 1393*w*, 1361*w*, 1317*s*, 1265*m*, 1254*s*, 1132*m*, 1112*w*, 862*m*, 834*w*, 761*w*.

Synthesis of C_{18}-SPD

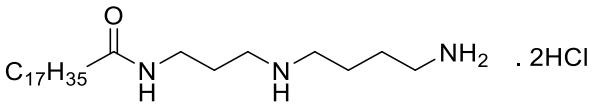

Chemical Formula: $C_{25}H_{55}Cl_2N_3O$
Molecular Weight: 484.64

C_{18}-di-boc-SPD (345 mg, 0.563 mmol) was dissolved in methanol (25 mL) and HCl gas was applied for approx. 15-20 seconds. The reaction mixture was stirred for 3 h and the solvent removed in vacuo to yield a white solid. MS indicated incomplete deprotection, so the same HCl gas cycle was repeated to yield a white product (67 mg, 92%).

R_f = 0.2 (90:10:1 DCM/MeOH/Et_3N). ^{1}H NMR (400 MHz, CD_3OD) δ: 3.24 (t, CH_2NHCO *J* = 6.4 Hz, 2H); 3.15-3.07 (m, CH_2NH + CH_2NH_2, 6H); 2.25 (t, CH_2CONH, *J* = 7.2 Hz, 2H); 1.92 (app quint, CH_2CH_2NHCO *J* = 7.6 Hz, 2H); 1.78 (app. quint, C$H_2CH_2NH_2$ + CH_2CH_2CONH, *J* = 4.0 Hz, 4H); 1.55 (br quint, C$H_2CH_2CH_2NH_2$, 2H); 1.25 (br app s, CH_3(CH_2)$_{12}CH_2$, 24H); 0.82 (t, CH_3CH_2, *J* = 6.5 Hz, 3H). HRMS: Calcd. $[M+H]^+$ ($C_{25}H_{54}N_3O$) m/z = 412.4267, found $[M+H]^+$ = 412.4250 (100%). IR: ν_{max} (cm^{-1}): 3309*w* (N-H); 2956*m*, 2917*s*, 2848*s*, 2787*w*, 2746*w* (all CH); 1642.6*m* (C=O); 1526.0*m* (C=O); 1464*m*, 1435*w*, 1365*w*, 1259.2*w*, 1170.1*m*, 1014.8*w*, 720.0*m*. Decomposition point: 211 °C. It was not possible to obtain a ^{13}C NMR spectrum due to the low solubility of the compound – even when run overnight on a 500 MHz instrument.

Synthesis of C_{18}-tri-Boc-SPM

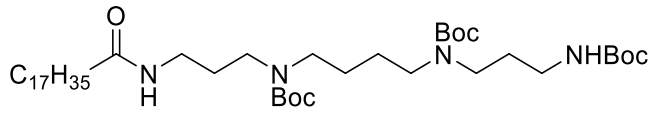

Chemical Formula: $C_{43}H_{84}N_4O_7$
Molecular Weight: 769.17

Stearic acid (0.85 g, 3.0 mmol) was dissolved in DCM (65 mL), and TBTU (1.05 g, 3.3 mmol) and triethylamine (ca. 5 mL) were added. The reaction mixture was stirred for 5 min before tri-Boc-spermine (Boc-SPM) (1.50 g, 3.0 mmol) in DCM (80 mL) was added. The solution was stirred overnight and the solvent removed *in vacuo* to give a cream solid as the crude, which was chromatographed on silica gel using pure DCM and hexane/ethyl acetate (2:1) as the second silica column to give the product as a white powder (0.844 g, 37%).

R_f = 0.68 (DCM), 0.22 (1:1 hexane/ethyl acetate). ^{1}H NMR (400 MHz, CD_3OD) δ: 6.29 (br s, N*H*, 1H); 5.54 (br s, N*H*Boc, 1H); 3.87-3.58 (m, C*H*$_2$NHCO + C*H*$_2$NBoc + C*H*$_2$NHBoc, 12H); 2.21 (t, C*H*$_2$CONH, *J* = 7.6 Hz, 2H); 1.68-1.64 (m, C*H*$_2$CH$_2$NBoc + (C*H*$_2$)$_2$CH$_2$NHBoc, 8H); 1.42 (s, C(C*H*$_3$)$_3$, 27H); 1.30-1.23 (m, CH$_3$(C*H*$_2$)$_{14}$CH$_2$ + C*H*$_2$CH$_2$CONH, 30H); 0.85 (t, C*H*$_3$CH$_2$, *J* = 7.0 Hz, 3H). Solubility problems prevented the measurement of ^{13}C NMR. HRMS: Calc. $[M+H]^+$ ($C_{43}H_{85}N_4O_7$) m/z = 770.6340, found $[M+H]^+$ = 770.6213 (56%); Calc. $[M+Na]^+$ ($C_{43}H_{84}N_4NaO_7$) m/z = 791.6238, found $[M+Na]^+$ = 791.6213 (100%). IR: ν_{max} (cm^{-1}): 3316*w* (N-H); 2986*m*, 2976*s* (all CH); 2869*m*, 1665*s*, 1523*m* (C=O); 1490*w*, 1378*m*,1317*w*, 1248*w*, 1174*m*, 837*w*, 820*w*, 723*m*, 616*w*, 523*w*.

Synthesis of C_{18}-SPM

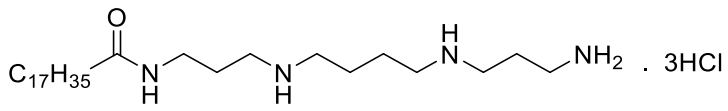

Chemical Formula: $C_{28}H_{63}Cl_3N_4O$
Molecular Weight: 578.19

C_{18}-tri-boc-SPM (844 mg, 1.1 mmol) was dissolved in methanol (25 mL) and HCl gas was applied for approx. 15-20 seconds. The reaction mixture was stirred for 3 h and the solvent removed in vacuo to yield a white solid (138.8 mg, 90%).

R_f = 0.65 (DCM). ^{1}HNMR (400 MHz, CD_3OD) δ: 5.65 (br s, N*H*); 3.25 (t, C*H*$_2$NHCO *J* = 6.8 Hz, 2H); 3.17-3.03 (m, C*H*$_2$NH + C*H*$_2$NH$_2$, 10H); 2.22 (t, C*H*$_2$CONH, *J* = 7.4 Hz, 2H); 2.08 (app. quint., C*H*$_2$CH$_2$NH$_2$, *J* = 7.9 Hz, 2H); 1.89 (approx. quint., C*H*$_2$CH$_2$NHCO, *J* = 7.0 Hz, 2H); 1.78 (m, CH$_2$(C*H*$_2$)$_2$CH$_2$, 4H); 1.55 (approx. quint, C*H*$_2$CH$_2$CONH, *J* = 6.0 Hz, 2H); 1.24 (s, CH$_3$(C*H*$_2$)$_{12}$CH$_2$, 24H); 0.84 (t, C*H*$_3$CH$_2$, *J* = 6.6 Hz, 3H). HRMS: Calc. $[M+H]^+$ ($C_{28}H_{60}N_4O$) m/z = 468.4767, found $[M+H]^+$ = 469.4824 (100%). IR: ν_{max} (cm^{-1}): 3339.7*w* (N-H); 2954*m*, 2918*s*, 2848*s*, 2782*s*, 2747*m*, 2689*w* (all CH); 1702*m* (C=O); 1643*m* (C=O); 1529*m* (CONH); 1463*m*, 1439*w*, 1348*w*, 1265*w*, 1249*w*, 1208*m*, 1182*m*, 1165*m*, 1058*m*, 721*m*, 677*w*. It was not possible to obtain a ^{13}C NMR spectrum due to the low solubility of the compound – even when run overnight on a 500 MHz instrument.

Synthesis C_{18}-PEG-3

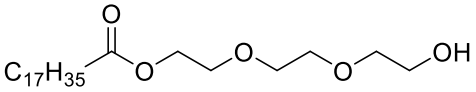

Chemical Formula: $C_{24}H_{48}O_5$
Molecular Weight: 416.64

Stearic acid (1.50 g, 5.3 mmol) and concentrated HCl (aq) (ca. 2 mL) were added to a solution of triethylene glycol (3.52 mL, 26.4 mmol) in dry DCM (50 mL). The reaction was stirred overnight, dried over $MgSO_4$, filtered and dried *in vacuo* to yield a white sticky solid that was chromatographed using hexane/ethyl acetate (2:1) to yield a yellow powder (704 mg, 32%).

R_f = 0.05 (2:1 hexane/ethyl acetate). ^{1}H NMR (400 MHz, CD_3OD) δ: 4.18 (t, C*H*$_2$OCO, *J* = 4.8 Hz, 2H); 3.67 (t, CH_2CH_2O, *J* = 4.8 Hz, 4H); 3.64 (t, C*H*$_2$OH, *J* = 4.7 Hz, 2H); 3.63-3.58 (t, CH_2CH_2O, *J* = 5.2 Hz, 4H); 3.53 (t, C*H*$_2$CO, *J* = 5.7 Hz, 2H); 2.26 (t, CH_2CH_2CO, *J* = 7.6 Hz, 2H); 1.65-1.55, 1.38-1.25, 1.22-1.17 (m, $CH_2CH_2CH_2$, 28H); 0.86 (t, C*H*$_3$CH$_2$, *J* = 6.9 Hz, 3H). HRMS: Calc. $[M+H]^+$ ($C_{24}H_{49}O_5$) m/z = 417.3580, found $[M+H]^+$ = 417.3572 (44%); Calc. $[M+Na]^+$ ($C_{24}H_{48}NaO_5$) m/z = 439.3399, found $[M+Na]^+$ = 439.3388 (100%). IR: ν_{max} (cm^{-1}): 3319*w* (N-H); 2954*m*, 2916*s*, 2870*m*, 2848*s* (all CH); 1740*s* (C=O); 1462*m*, 1325*w*, 1174*m*, 1138*s*, 1104*m*, 1058*s*, 1038*s*, 895*m*, 861*w*, 730*w*, 719*m*, 558*w*. mp: 39.3-39.9 °C.

Synthesis of C_{18}-PEG-8

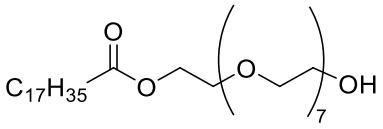

Chemical Formula: $C_{34}H_{68}O_{10}$
Molecular Weight: 636.91

Stearic acid (155 mg, 0.5 mmol) was dissolved in DCM and Et_3N (ca. 1.5 mL) and TBTU (184 mg, 0.6 mmol) were added. After 5 min of stirring, octaethylene glycol (500 mg, 1.4 mmol) was added and the reaction mixture stirred overnight and chromatographed using hexane/ethyl acetate (1:1, then pure ethyl acetate) to give a sticky off-white product (80 mg, 27%).

R_f = 0.02 (2:1 hexane/ethyl acetate). ^{1}H NMR (400 MHz, CD_3OD) δ: 4.21 (t, C*H*$_2$OCO, *J* = 4.8 Hz, 2H); 3.76-3.68 (t, CH_2CH_2O, *J* = 4.8 Hz, 14H); 3.64 (t, C*H*$_2$OH, *J* = 4.6 Hz, 2H); 3.62-3.58 (CH_2CH_2O, *J* = 5.6 Hz, 14H); 3.56 (t, C*H*$_2$CO, *J* = 5.2 Hz, 2H); 2.34 (t, *J* = 7.4 Hz, 2H); 2.26 (t, CH_2CH_2CO, *J* = 7.6 Hz, 2H); 1.36-1.21 (m, $CH_2CH_2CH_2$, 28H); 0.90 (t, C*H*$_3$CH$_2$, *J* = 6.9 Hz, 3H). IR: ν_{max} (cm^{-1}): 3025*w* (CH); 2916*m* (CH); 2848*m* (CH); 1723*m* (C=O); 1492*m*, 1452*m*, 1363*w*, 1260*m*, 1185*m*, 1080*m*, 1028*m*, 954*m*, 802*w*, 758*m*, 696*s*, 539*m*. Decomposition point: 218 °C.

7.2 Assay and Analysis Materials and Methods

All materials, except Mallard Blue (MalB) dye, which was synthesized in the DKS group laboratory, employed in spectroscopic assays were obtained from commercial sources and used without further purification unless stated. Sodium salt heparin from porcine intestinal mucosa with a molecular weight between 15,000 ± 2,000 Da (1 KU = 1000 units) was obtained from Calbiochem®. Ammonium carbonate, deoxyribonucleic acid sodium salt from calf thymus (DNA), ethylenediaminetetraacetic acid trisodium salt hydrate (EDTA), ethidium bromide (EthBr), *N*-(2-hydroxyethyl)piperazine-*N*′-(2-ethanesulfonic acid) (HEPES), human serum (from human male AB plasma), Nile Red, phosphate buffered saline (PBS), and Trizma® hydrochloride (Tris HCl) were obtained from Sigma Aldrich.

UV/Vis absorbance was measured on a Shimadzu UV-2401PC spectrophotometer and fluorescence on a Hitachi F-4500 spectrofluorimeter. All MalB solutions were incubated at 50°C for 24 hours prior to use and stored in the dark. Unless stated, all experiments were performed in triplicate and data are reported as a mean value plus or minus one standard deviation. TEM images were obtained by an FEI Tecnai 12 BioTWIN operated at 120 kV. Dynamic Light Scattering (DLS) was carried out using a Zetasizer Nano (Malvern Instruments). The EDX system is a Thermo Ultra Dry detector and Noran software which produces the spectral peak graphs. The SEM is an FEI Sirion XL30. CHN analysis were performed with Exeter Analytical CE-440 analyser, used in conjunction with a Sartorius SE2 analytical balance. Isothermal Titration Calorimetry (ITC) experiments were conducted using a Nano ITC Technology (TA Instruments, New Castle, DE, USA) and performed by our collaborators in the Molecular Simulation Engineering (MOSE) Laboratory, Department of Engineering and Architectures (DEA), University of Trieste; Erik Laurini, Paola Posocco and Sabrina Pricl.

Nile Red Assay[183]

This assay aims to determine the critical aggregation concentration (CAC) for the binders. A Nile Red (2.5 mM) stock solution was made in EtOH. Solutions of binder were prepared at a variety of concentrations starting from (200 µM) in disposable cuvettes. Samples of the stock solution were diluted by PBS buffer to the required concentration in a 1 mL assay volume. Nile Red (1 µL) was applied to each sample to give a concentration of (2.5 µM). The fluorescence emission was measured using an excitation wavelength of 550 nm. Fluorescence intensity was recorded at 635 nm. This procedure was performed in triplicate.

Dynamic Light Scattering (DLS)

The measurements were made of the back-scattered light fluctuations at an angle of 173° with the calculation of an autocorrelation function. The samples were measured at 25 °C, adjusted to the temperature for 1 minute prior to the measurement. The autocorrelation functions were analysed using the DTS v5.1 software provided by Malvern. Measurements were done in triplicate with 10-15 runs per single measurement and the calculated mean values (based on intensity and volume distribution) were used. The samples were measured in 10 mM Tris HCl buffer and in ultrapure water. The samples were measured after filtering through nylon filters (0.45µm) to remove all dust from them.

Transmission Electron Microscopy (TEM)

10 µL of compound (200 µM) in H_2O was placed on a copper grid (standard) with Formvar and carbon support film and allowed to set for 5 minutes. A stain (1% uranyl acetate) was applied to the grid while wet (1% in water, pH 4.5) to allow the stain to run across the grid, then the majority of it was wiped off with a filter paper. The grid was left to rest for 20 minutes before taking the images.

Mallard Blue (MalB) Assay in Buffer[123]

MalB (25 µM) solution was incubated at 50 °C for 24 hours (to prevent aggregation) prior to use and was wrapped with foil to ensure that the dye was not exposed to direct light. 2 mL of MalB (25 µM), heparin (27 µM) and NaCl (150 mM) in Tris HCl (10 mM) was placed in a cuvette then titrated with binder stock solution to give a suitable charge ratio for the binder and heparin in the cuvette. Binder stock solution consisted of the original solution of MalB/Heparin/NaCl/Tris HCl stock solution, then a concentration of the binder, depending on the charge of the binder, was added so that, after 10 µL binder stock, the cuvette charge ratio (+:-) is 0.1. After each addition, the mixture in the cuvette was stirred (with a clean plastic pipette) to ensure total mixing and the absorbance was recorded at 615 nm against the baseline of the Tris HCl (10 mM). The normalization of the absorbance was made between two solutions, the first one was MalB (25 µM) and NaCl (150 mM) in Tris HCl (10 mM) and the other contained MalB (25 µM), heparin (27 µM) and NaCl (150 mM) in Tris HCl (10 mM). This procedure was performed in triplicate.

Mallard Blue (MalB) Assay in Human Serum[123]

MalB (25 µM) solution was incubated at 50 °C for 24 hours prior to use and was wrapped with foil to ensure that the dye was not exposed to direct light. 14 disposable cuvettes were charged with 1.75 mL of MalB (28.53 µM) in Tris HCl (10 mM) and a certain volume of the binder stock solution to maintain a suitable charge ratio between binder and heparin. The binder stock solution consisted of the binder and also MalB (25 µM), heparin (27 µM) and Tris HCl (10 mM). Another heparin (80 µM) solution was made separately in human serum (100%). Each cuvette was titrated sequentially with 0.25 mL of the heparin-in-serum solution and was mixed fully (with a clean plastic pipette). The absorbance was recorded at 615 nm against the baseline of 1.75 mL Tris HCl (10 mM)

and 0.25 mL human serum (100%). Normalization of the absorbance was made between two solutions, the first is MalB (25 μM) and the second containing MalB (25 μM) and heparin (27 μM). This procedure was performed in triplicate.

Energy dispersive X-Ray (EDX) Analysis

The EDX system is a Thermo Ultra Dry detector and Noran software which produces the spectra peak graphs. The SEM is an FEI Sirion XL30. Samples were dissolved in MeOH, applied on metal pin stub and allowed to dry prior to analysis.

Ethidium Bromide Displacement (DNA Assay)[208,305]

A solution of Calf Thymus DNA (8.0 μM) was prepared in SHE buffer (2 mM HEPES, 0.05 mM EDTA, 150mM NaCl) at pH 7.5. Ethidium bromide was diluted with SHE Buffer to give a final concentration of 10.14 μM. Background ethidium bromide fluorescence was measured at 5.07 μM. The binder stock solution, at varying concentration depending on the charge of the binder, was prepared in a 50:50 solution of the ethidium bromide and DNA solutions to give a final EthBr concentration of 5.07 μM and DNA at 4.0 μM with respect to one DNA base (*Mr* 330 $gmol^{-1}$). Appropriate amounts of the binder solution were added to 2 ml of a stock solution containing EthBr (5.07 μM) and DNA (4.0 μM) to achieve the desired charge ratio (+:-). The fluorescence was measured on a Hitachi F-4500 spectrofluorimeter using an excitation wavelength of 540 nm. Fluorescence intensity was recorded at 595 nm. The fluorescence values were normalised to a solution containing only DNA (4.0 μM) and EthBr (5.07 μM). This procedure was performed in triplicate.

Isothermal Titration Calorimetry (ITC)[217]

Isothermal Titration Calorimetry (ITC) experiments were carried out by Pricl and co-workers at University of Trieste. Full details of the methodology can be found in reference.[217] The experiments were conducted using a Nano ITC Technology (TA Instruments, New Castle, DE, USA). Binding conditions were optimized for each SAMul ligand. The thermodynamics of micellization of all SAMul molecules were investigated in Tris HCl/150 mM NaCl buffered solutions. The same solution conditions were employed to obtain the thermodynamic parameters for heparin/SAMul ligand binding, while for DNA binding SHE/150 mM NaCl buffered solutions were used. In the binding assays, DNA and heparin initial concentration in the corresponding buffered solutions was 30 μM. All solutions and buffers used in the experiments were degassed for 30 min at room temperature under stirring at 350 rpm prior to experiment. Upon filling the cell and syringe, stirring was turned on and each system was allowed to thermally equilibrate for 30 minutes. The enthalpy change caused by DNA/heparin dilution, measured under the same circumstances by titration buffer/NaCl solutions into the corresponding solutions, was found to be very small and therefore was neglected. Raw data curves were integrated with Microcal Origin Software, as described in the instrument manual. Statistics were performed on the thermodynamic parameters with a desired confidence interval of 95%. Each experiment was repeated in duplicate, and showed excellent reproducibility.

Multiscale Modelling Methods[217]

Multiscale modelling of self-assembly process was carried out by Pricl and co-workers at University of Trieste. Full details of the methodology can be found in reference.[217]

In summary, they used their well-validated multiscale molecular modelling procedure[102,199,235-237] based on the systematic elimination of computationally expensive degrees of freedom while retaining implicitly their influence on the remaining degrees freedom.

The outline of the general strategy of the multiscale modeling approach may be summarized as follows: i) explicit solvent atomistic MD calculations[240,241] were performed on **C_{16}-DAPMA**, **C_{16}-SPD**, and **C_{16}-SPM** and their assembly; using the AMBER program[306] and the GAFF force field,[307,308] solvated in a TIP3P[309] water box; ii) coarse-grained DPD simulations[238,239] were carried out at concentrations higher than the experimental CAC and the aggregates were characterized in terms of dimension and aggregation number; the mesoscale model parameters were calculated exploiting the conformational properties and energetic values obtained from MD simulation at point (i)[306] using an explicit solvent model in which each molecule was represented as single force centers (beads) and solvent was treated explicitly in the presence of ions and counterions. Langevin dynamics were then conducted using the DPD representation of the system; iii) the equilibrium configurations of the self-assembled systems obtained at point (ii) were mapped back to the corresponding atomistic MD models, and then new atomistic MD simulations were conducted to calculate binding energies between each micelle and DNA as well as the heparin molecule.

Abbreviations

AIBN	2-2'-azobis(2-methylpropionitrile)
app	Apparent (NMR)
ATIII	Antithrombin III
AuNCs	Gold Nanocomposites
AuNPs	Gold Nanoparticles
br	Broad (NMR)
Boc	tert-Butyl Dicarbonate
Boc_2O	di-tert-butyl dicarbonate
CAC	Critical Aggregation Concentration
Calc	Calculated
CD_3OD	Deuterated Methanol
CD	Circular Dichroism
CE_{50}	Charge Excess at 50% Binding
Chol	Cholesterol
C-L	Cross-linking
CMC	Critical Micelle Concentration
d	Doublet (NMR)
DAB	1,4-Diaminobutane
DAP	Diaminopropane
DAPMA	*N*,*N*-Di-(3-aminopropyl)-*N*-methylamine
DCM	Dichloromethane
DCC	*N*,*N*'-dicyclohexylcarbodiimide
DCU	*N*,*N'*-Dicyclohexylurea
DLS	Dynamic Light Scattering
DNA	Deoxyribonucleic Acid
DPD	Dissipative Particle Dynamics
EC_{50}	Effective Concentration at 50% Binding
EDX	Energy Dispersive X-Ray
EPR	Enhanced Permeability and Retention
ESI	Electrospray Ionization
EtBr	Ethidium Bromide
Et_3N	Triethylamine
EtOAc	Ethyl Acetate

FDA	Food and Drug Administration
G1	First Generation
GPC	Gel Permeation Chromatography
HCl(g)	Gaseous Hydrogen Chloride
HEPES	*N*-(2-hydroxyethyl)piperazine-*N*'-(2-ethanesulfonic acid)
HIV	Human Immunodeficiency Virus
HRMS	High Resolution Mass Spectrometry
HTS	High-Throughput Screening
HSA	Human Serum Albumin
Hz	Hertz
IR	Infrared
ITC	Isothermal Titration Calorimetry
IU	International Unit
J	Coupling frequency, Hz
kDa	1000 Dalton (Atomic mass unit)
LMWHs	Low Molecular Weight Heparins
m	medium (IR)
m	Multiplet (NMR)
M	Molar Concentration
m/z	Mass/charge ratio (Mass spectrometry)
MalB	Mallard Blue (Dye)
max_{Abs}	Maximum Absorbance
MD	Multiscale Modelling
mg	Milligram
MHz	Megahertz
mL	Milliliter
µM	Micro Molar
µm	Micro Millimeter
mp	Melting Point
MS	Mass Spectrometry
mV	Millivolts
MW	Molecular Weight
MWCO	Molecular Weight Cut-Off
nm	Nanometer
NMR	Nuclear Magnetic Resonance

NPs	Nanoparticles
ns	Nano second
PA	Peptide Amphiphile
PAMAM	Poly(amidoamine)
PBS	Phosphate-buffered Saline
PDI	Poly-Dispersity Index
PEG	Poly(ethylene) glycol
ppm	Parts per million (NMR)
q	Quartet (NMR)
quint	Quintet (NMR)
R_f	Retention factor
r.t	Room Temperature
s	strong (IR)
s	Singlet (NMR)
SAMul	Self-Assembled Multivalency
SEM	Scanning Electron Microscopy
SPD	Spermidine
SPM	Spermine
t	Triplet (NMR)
TBTU	O-(Benzotriazol-1-yl)-*N*,*N*,*N′*,*N′*-tetramethyluronium tetrafluoroborate
TEM	Transmission Electron Microscopy
THF	Tetrahydrofuran
TLC	Thin Layer Chromatography
UV	Ultraviolet (spectroscopy)
+ve	Positive charge
Vis	Visible light (spectroscopy)
ν_{max}	Infrared Maximum Spectra
w	weak (IR)
Z	Benzyloxy or benzyl ester protecting group

References

1. C. Toumey, *Nat Nano*, 2009, **4**, 783-784.
2. S. Lindsay, *Introduction to Nanoscience*, Oxford University Press, Oxford, 2010.
3. O. C. Farokhzad and R. Langer, *ACS Nano*, 2009, **3**, 16-20.
4. H. G. Craighead, *Science*, 2000, **290**, 1532-1535.
5. A. P. Nikalje, *Med. Chem.*, 2015, **5**, 81-89.
6. A. Bao, B. Goins, R. Klipper, G. Negrete and W. T. Phillips, *J. Pharmacol. Exp. Ther.*, 2004, **308**, 419-425.
7. K.-H. Chuang, H.-E. Wang, F.-M. Chen, S.-C. Tzou, C.-M. Cheng, Y.-C. Chang, W.-L. Tseng, J. Shiea, S.-R. Lin and J.-Y. Wang, *Mol. Cancer Ther.*, 2010, **9**, 1903-1912.
8. Y. C. Barenholz, *J. Control. Release*, 2012, **160**, 117-134.
9. Y. Barenholz, *Handbook of Harnessing Biomaterials in Nanomedicine, Pan Standford Publishing Pte. Ltd., Singapure*, 2012, **2012**, 335-398.
10. Y. Barenholz, *J. Control. Release*, 2012, **160**, 117-134.
11. C. Loo, A. Lin, L. Hirsch, M.-H. Lee, J. Barton, N. Halas, J. West and R. Drezek, *Technol. Cancer Res. Treat.*, 2004, **3**, 33-40.
12. K. Sokolov, M. Follen, J. Aaron, I. Pavlova, A. Malpica, R. Lotan and R. Richards-Kortum, *Cancer Res.*, 2003, **63**, 1999-2004.
13. L. Laurent, J. Villain, P. Boisseau and B. Loubaton, *Comp. Rend. Phys.*, 2011, **12**, 620-636.
14. M. D. Wang, D. M. Shin, J. W. Simons and S. Nie, *Exp. Rev. Anticancer Ther.*, 2007, **7**, 833-837.
15. Y. Xin, Q. Huang, J.-Q. Tang, X.-Y. Hou, P. Zhang, L. Z. Zhang and G. Jiang, *Cancer Lett.*, 2016, **379**, 24-31.
16. A. Samad, Y. Sultana and M. Aqil, *Curr. Drug Del.*, 2007, **4**, 297-305.
17. E. Marin, M. I. Briceño and C. Caballero-George, *Int. J. Nanomedicine*, 2013, **8**, 3071-3091.
18. L. S. Nair and C. T. Laurencin, in *Tissue Engineering I*, Springer, 2005, pp. 47-90.
19. J. Park, M. Ye and K. Park, *Molecules*, 2005, **10**, 146-161.
20. V. Mohanraj and Y. Chen, *Trop. J. Pharm. Res.*, 2006, **5**, 561-573.
21. A. O. Elzoghby, W. M. Samy and N. A. Elgindy, *J. Control. Release*, 2012, **157**, 168-182.
22. G. Modi, V. Pillay and Y. E. Choonara, *Ann. N.Y. Acad. Sci.*, 2010, **1184**, 154-172.
23. B. Godin, J. H. Sakamoto, R. E. Serda, A. Grattoni, A. Bouamrani and M. Ferrari, *Trends Pharmacol. Sci.*, 2010, **31**, 199-205.
24. H. Liu, E. B. Slamovich and T. J. Webster, *Int. J. Nanomedicine*, 2006, **1**, 541.
25. S. Svenson and D. A. Tomalia, *Adv. Drug Deliv. Rev.*, 2012, **64**, S102-115.
26. D. A. Tomalia, *Sci. Am.*, 1995, **272**, 62-66.
27. D. A. Tomalia, *Prog. Polym. Sci.*, 2005, **30**, 294-324.
28. A.-M. Caminade, S. Fruchon, C.-O. Turrin, M. Poupot, A. Ouali, A. Maraval, M. Garzoni, M. Maly, V. Furer and V. Kovalenko, *Nature commun.*, 2015, **6**, 7722-7732.
29. D. A. Tomalia, L. Reyna and S. Svenson, *Biochem. Soc. Trans.*, 2007, **35**, 61-67.
30. C. Dufes, I. F. Uchegbu and A. G. Schatzlein, *Adv. Drug. Deliv. Rev.*, 2005, **57**, 2177-2202.
31. A. Wei, J. G. Mehtala and A. K. Patri, *J. Control. Release*, 2012, **164**, 236-246.

32. M. Mammen, S.-K. Choi and G. M. Whitesides, *Angew. Chem. Int. Ed.*, 1998, **37**, 2754-2794.
33. J. Huskens, *Curr. Opin. Chem. Biol.*, 2006, **10**, 537-543.
34. A. Mulder, J. Huskens and D. N. Reinhoudt, *Org. Biomol. Chem.*, 2004, **2**, 3409-3424.
35. C. Fasting, C. A. Schalley, M. Weber, O. Seitz, S. Hecht, B. Koksch, J. Dernedde, C. Graf, E. W. Knapp and R. Haag, *Angew. Chem. Int. Ed.*, 2012, **51**, 10472-10498.
36. C. Fasting, C. A. Schalley, M. Weber, O. Seitz, S. Hecht, B. Koksch, J. Dernedde, C. Graf, E.-W. Knapp and R. Haag, *Angew. Chem. Int. Ed.*, 2012, **124**, 10622-10650.
37. L. L. Kiessling, J. E. Gestwicki and L. E. Strong, *Angew. Chem. Int. Ed.*, 2006, **45**, 2348-2368.
38. R. S. Kane, *Langmuir*, 2010, **26**, 8636-8640.
39. S. P. Jones, G. M. Pavan, A. Danani, S. Pricl and D. K. Smith, *Chem. Eur. J.*, 2010, **16**, 4519-4532.
40. J. Huskens, A. Mulder, T. Auletta, C. A. Nijhuis, M. J. Ludden and D. N. Reinhoudt, *J. Am. Chem. Soc.*, 2004, **126**, 6784-6797.
41. M. Marsh and A. Helenius, *Cell*, 2006, **124**, 729-740.
42. M. Vlasak, I. Goesler and D. Blaas, *J. Virol.*, 2005, **79**, 5963-5970.
43. J. Grove and M. Marsh, *J. Cell Biol.*, 2011, **195**, 1071-1082.
44. D. V. Rakhuba, E. I. Kolomiets, E. S. Dey and G. I. Novik, *Pol. J. Microbiol.*, 2010, **59**, 145-155.
45. D. A. Tomalia, H. Baker, J. Dewald, M. Hall, G. Kallos, S. Martin, J. Roeck, J. Ryder and P. Smith, *Polym. J.*, 1985, **17**, 117-132.
46. P. T. Wong, K. Tang, A. Coulter, S. Tang, J. R. Baker and S. K. Choi, *Biomacromolecules*, 2014, **15**, 4134-4145.
47. M. X. Tang, C. T. Redemann and F. C. Szoka, *Bioconjugate Chem.*, 1996, **7**, 703-714.
48. K. Madaan, S. Kumar, N. Poonia, V. Lather and D. Pandita, *J. Pharm. Bioallied Sci.*, 2014, **6**, 139.
49. T. Honda, S. Yoshida, M. Arai, T. Masuda and M. Yamashita, *Bioorg. Med. Chem. Lett.*, 2002, **12**, 1929-1932.
50. H. Kamitakahara, T. Suzuki, N. Nishigori, Y. Suzuki, O. Kanie and C. H. Wong, *Angew. Chem. Int. Ed.*, 1998, **37**, 1524-1528.
51. M. Mammen, G. Dahmann and G. M. Whitesides, *J. Med. Chem.*, 1995, **38**, 4179-4190.
52. M. Matrosovich, L. Mochalova, V. Marinina, N. Byramova and N. Bovin, *FEBS Lett.*, 1990, **272**, 209-212.
53. E. Fan, Z. Zhang, W. E. Minke, Z. Hou, C. L. Verlinde and W. G. Hol, *J. Am. Chem. Soc.*, 2000, **122**, 2663-2664.
54. S. Basha, P. Rai, V. Poon, A. Saraph, K. Gujraty, M. Y. Go, S. Sadacharan, M. Frost, J. Mogridge and R. S. Kane, *Proc. Natl. Acad. Sci. USA*, 2006, **103**, 13509-13513.
55. B. D. Polizzotti, R. Maheshwari, J. Vinkenborg and K. L. Kiick, *Macromolecules*, 2007, **40**, 7103-7110.
56. J. E. Gestwicki and L. L. Kiessling, *Nature*, 2002, **415**, 81-84.
57. G. Maheshwari, G. Brown, D. A. Lauffenburger, A. Wells and L. G. Griffith, *J. Cell Sci.*, 2000, **113**, 1677-1686.
58. M. M. Santore, J. Zhang, S. Srivastava and V. M. Rotello, *Langmuir*, 2008, **25**, 84-96.

59. J. Dernedde, A. Rausch, M. Weinhart, S. Enders, R. Tauber, K. Licha, M. Schirner, U. Zügel, A. von Bonin and R. Haag, *Proc. Natl. Acad. Sci. USA*, 2010, **107**, 19679-19684.
60. M. Mammen, K. Helmerson, R. Kishore, S.-K. Choi, W. D. Phillips and G. M. Whitesides, *Chem. Biol.*, 1996, **3**, 757-763.
61. P. I. Kitov, J. M. Sadowska, G. Mulvey, G. D. Armstrong, H. Ling, N. S. Pannu, R. J. Read and D. R. Bundle, *Nature*, 2000, **403**, 669-672.
62. P. L. Felgner, T. R. Gadek, M. Holm, R. Roman, H. W. Chan, M. Wenz, J. P. Northrop, G. M. Ringold and M. Danielsen, *Proc. Natl. Acad. Sci. USA*, 1987, **84**, 7413-7417.
63. R. W. Malone, P. L. Felgner and I. M. Verma, *Proc. Natl. Acad. Sci. USA*, 1989, **86**, 6077-6081.
64. P. L. Felgner and G. Ringold, *Nature*, 1989, **337**, 387.
65. J. H. Felgner, R. Kumar, C. Sridhar, C. J. Wheeler, Y. J. Tsai, R. Border, P. Ramsey, M. Martin and P. L. Felgner, *J. Biol. Chem.*, 1994, **269**, 2550-2561.
66. G. Gebeyehu, J. A. Jessee, V. C. Ciccarone, P. Hawley-Nelson and A. Chytil, *U.S. Patent 5334761*, 1994.
67. L. Stamatatos, R. Leventis, M. J. Zuckermann and J. R. Silvius, *Biochemistry*, 1988, **27**, 3917-3925.
68. J.-P. Behr, B. Demeneix, J.-P. Loeffler and J. Perez-Mutul, *Proc. Natl. Acad. Sci. USA*, 1989, **86**, 6982-6986.
69. M.-C. Daniel and D. Astruc, *Chem. Rev.*, 2004, **104**, 293-346.
70. R. Sardar, A. M. Funston, P. Mulvaney and R. W. Murray, *Langmuir*, 2009, **25**, 13840-13851.
71. E. Boisselier and D. Astruc, *Chem. Soc. Rev.*, 2009, **38**, 1759-1782.
72. W. Zhao, Y. Gao, S. A. Kandadai, M. A. Brook and Y. Li, *Angew. Chem. Int. Ed.*, 2006, **45**, 2409-2413.
73. A. C. Templeton, W. P. Wuelfing and R. W. Murray, *Acc. Chem. Res.*, 2000, **33**, 27-36.
74. G. Schmid, R. Pfeil, R. Boese, F. Bandermann, S. Meyer, G. H. M. Calis and J. W. A. van der Velden, *Chem. Ber.*, 1981, **114**, 3634-3642.
75. M. Brust, M. Walker, D. Bethell, D. J. Schiffrin and R. Whyman, *J. Chem. Soc., Chem. Commun.*, 1994, 801-802.
76. S. R. K. Perala and S. Kumar, *Langmuir*, 2013, **29**, 9863-9873.
77. J. C. Love, L. A. Estroff, J. K. Kriebel, R. G. Nuzzo and G. M. Whitesides, *Chem. Rev.*, 2005, **105**, 1103-1170.
78. D. V. Leff, P. C. Ohara, J. R. Heath and W. M. Gelbart, *J. Phys. Chem.*, 1995, **99**, 7036-7041.
79. J. Turkevich, P. C. Stevenson and J. Hillier, *Disc. Faraday Soc.*, 1951, **11**, 55-75.
80. B. V. Enustun and J. Turkevich, *J. Am. Chem. Soc.*, 1963, **85**, 3317-3328.
81. J. Kimling, M. Maier, B. Okenve, V. Kotaidis, H. Ballot and A. Plech, *J. Phys. Chem. B*, 2006, **110**, 15700-15707.
82. G. Frens, *Nature-Phys. Sci.*, 1973, **241**, 20-22.
83. M. K. Chow and C. F. Zukoski, *J. Colloid Interface Sci.*, 1994, **165**, 97-109.
84. M.-C. Bowman, T. E. Ballard, C. J. Ackerson, D. L. Feldheim, D. M. Margolis and C. Melander, *J. Am. Chem. Soc.*, 2008, **130**, 6896-6897.
85. M. Marradi, F. Chiodo, I. Garcia and S. Penadés, *Chem. Soc. Rev.*, 2013, **42**, 4728-4745.
86. A. K. Adak, H.-J. Lin and C.-C. Lin, *Org. Biomol. Chem.*, 2014, **12**, 5563-5573.
87. C.-C. Lin, Y.-C. Yeh, C.-Y. Yang, C.-L. Chen, G.-F. Chen, C.-C. Chen and Y.-C. Wu, *J. Am. Chem. Soc.*, 2002, **124**, 3508-3509.

88. Y. J. Chen, S. H. Chen, Y. Y. Chien, Y. W. Chang, H. K. Liao, C. Y. Chang, M. D. Jan, K. T. Wang and C. C. Lin, *ChemBioChem*, 2005, **6**, 1169-1173.
89. K. Sakurai, Y. Hatai and A. Okada, *Chem. Sci.*, 2016, **7**, 702-706.
90. H. Shelanski and M. Shelanski, *J. Int. Coll. Surg.*, 1956, **25**, 727-734.
91. H. A. Ravin, A. M. Seligman and J. Fine, *N. Engl. J. Med.*, 1952, **247**, 921-929.
92. H. Ringsdorf, *J. Polym. Sci., Polym. Symp.*, 1975, **51**, 135-153.
93. N. Larson and H. Ghandehari, *Chem. Mater.*, 2012, **24**, 840-853.
94. L. L. Kiessling, J. E. Gestwicki and L. E. Strong, *Curr. Opin. Chem. Biol.*, 2000, **4**, 696-703.
95. J. D. Reuter, A. Myc, M. M. Hayes, Z. Gan, R. Roy, D. Qin, R. Yin, L. T. Piehler, R. Esfand, D. A. Tomalia and J. R. Baker, *Bioconjugate Chem.*, 1999, **10**, 271-278.
96. A. Conway, T. Vazin, D. P. Spelke, N. A. Rode, K. E. Healy, R. S. Kane and D. V. Schaffer, *Nat. Nano*, 2013, **8**, 831-838.
97. G. M. Whitesides, J. P. Mathias and C. T. Seto, *Science*, 1991, **254**, 1312-1319.
98. D. Chandler, *Nature*, 2005, **437**, 640-647.
99. X. Chi, A. J. Guerin, R. A. Haycock, C. A. Hunter and L. D. Sarson, *J. Chem. Soc., Chem. Commun.*, 1995, 2563-2565.
100. J. N. Israelachvili, D. J. Mitchell and B. W. Ninham, *J. Chem. Soc., Faraday Trans. 2*, 1976, **72**, 1525-1568.
101. A. Barnard and D. K. Smith, *Angew. Chem. Int. Ed.*, 2012, **51**, 6572-6581.
102. S. P. Jones, N. P. Gabrielson, C. H. Wong, H. F. Chow, D. W. Pack, P. Posocco, M. Fermeglia, S. Pricl and D. K. Smith, *Mol. Pharm.*, 2011, **8**, 416-429.
103. U. Griesenbach, D. M. Geddes and E. Alton, *Gene Ther.*, 2006, **13**, 1061-1067.
104. B. Fang and J. A. Roth, *Cancer Biol. Ther.*, 2003, **2**, 114-120.
105. S. Yadav, M. Mahato, R. Pathak, D. Jha, B. Kumar, S. R. Deka, H. K. Gautam and A. K. Sharma, *J. Mater. Chem. B*, 2014, **2**, 4848-4861.
106. N. P. Gabrielson and J. Cheng, *Biomaterials*, 2010, **31**, 9117-9127.
107. S. P. Jones, N. P. Gabrielson, D. W. Pack and D. K. Smith, *Chem. Commun.*, 2008, 4700-4702.
108. G. R. Newkome, Z. Yao, G. R. Baker and V. K. Gupta, *J. Org. Chem.*, 1985, **50**, 2003-2004.
109. G. R. Newkome and X. Lin, *Macromolecules*, 1991, **24**, 1443-1444.
110. A. Barnard, P. Posocco, S. Pricl, M. Calderon, R. Haag, M. E. Hwang, V. W. Shum, D. W. Pack and D. K. Smith, *J. Am. Chem. Soc.*, 2011, **133**, 20288-20300.
111. D. J. Welsh, S. P. Jones and D. K. Smith, *Angew. Chem. Int. Ed.*, 2009, **48**, 4047-4051.
112. A. Barnard, P. Posocco, M. Fermeglia, A. Tschiche, M. Calderon, S. Pricl and D. K. Smith, *Org. Biomol. Chem.*, 2014, **12**, 446-455.
113. A. Barnard, M. Calderon, A. Tschiche, R. Haag and D. K. Smith, *Org. Biomol. Chem.*, 2012, **10**, 8403-8409.
114. A. Tschiche, A. M. Staedtler, S. Malhotra, H. Bauer, C. Bottcher, S. Sharbati, M. Calderon, M. Koch, T. M. Zollner, A. Barnard, D. K. Smith, R. Einspanier, N. Schmidt and R. Haag, *J. Mater. Chem. B*, 2014, **2**, 2153-2167.
115. G. Sephel, K. Tashiro, M. Sasaki, D. Greatorex, G. Martin, Y. Yamada and H. Kleinman, *Biochem. Biophys. Res. Commun.*, 1989, **162**, 821-829.
116. K.-i. Tashiro, G. C. Sephel, B. Weeks, M. Sasaki, G. Martin, H. K. Kleinman and Y. Yamada, *J. Biol. Chem.*, 1989, **264**, 16174-16182.
117. H. Cui, M. J. Webber and S. I. Stupp, *Biopolymers*, 2010, **94**, 1-18.
118. G. A. Silva, C. Czeisler, K. L. Niece, E. Beniash, D. A. Harrington, J. A. Kessler and S. I. Stupp, *Science*, 2004, **303**, 1352-1355.

119. R. C. Claussen, B. M. Rabatic and S. I. Stupp, *J. Am. Chem. Soc.*, 2003, **125**, 12680-12681.
120. V. M. Tysseling-Mattiace, V. Sahni, K. L. Niece, D. Birch, C. Czeisler, M. G. Fehlings, S. I. Stupp and J. A. Kessler, *J. Neurosci.*, 2008, **28**, 3814-3823.
121. S. K. M. Nalluri, J. Voskuhl, J. B. Bultema, E. J. Boekema and B. J. Ravoo, *Angew. Chem. Int. Ed.*, 2011, **50**, 9747-9751.
122. D. L. Rabenstein, *Nat. Prod. Rep.*, 2002, **19**, 312-331.
123. S. M. Bromfield, P. Posocco, M. Fermeglia, S. Pricl, J. Rodriguez-Lopez and D. K. Smith, *Chem. Commun.*, 2013, **49**, 4830-4832.
124. A. Shvarev and E. Bakker, *J. Am. Chem. Soc.*, 2003, **125**, 11192-11193.
125. C. Oschatz, C. Maas, B. Lecher, T. Jansen, J. Björkqvist, T. Tradler, R. Sedlmeier, P. Burfeind, S. Cichon, S. Hammerschmidt, W. Müller-Esterl, Walter A. Wuillemin, G. Nilsson and T. Renné, *Immunity*, **34**, 258-268.
126. S. M. Bromfield, E. Wilde and D. K. Smith, *Chem. Soc. Rev.*, 2013, **42**, 9184-9195.
127. D. A. Garcia, T. P. Baglin, J. I. Weitz and M. M. Samama, *Chest*, 2012, **141**, e24S-e43S.
128. B. P. Schick, D. Maslow, A. Moshinski and J. D. S. Antonio, *Blood*, 2004, **103**, 1356-1363.
129. L. Jin, J. P. Abrahams, R. Skinner, M. Petitou, R. N. Pike and R. W. Carrell, *Proc. Natl. Acad. Sci. USA*, 1997, **94**, 14683-14688.
130. H. Miyasaka, B. K. Choudhury, E. W. Hou and S. S. L. Li, *Eur. J. Biochem.*, 1993, **216**, 343-352.
131. A. I. De Agostini, S. C. Watkins, H. S. Slayter, H. Youssoufian and R. D. Rosenberg, *J. Cell Biol.*, 1990, **111**, 1293-1304.
132. A. F. Charles and D. A. Scott, *Biochem. J*, 1936, **30**, 1927-1933.
133. E. Jorpes, *Biochem. J*, 1942, **36**, 203-213.
134. T. E. Warkentin and J. G. Kelton, *Am. J. Med.*, 1996, **101**, 502-507.
135. M. J. M. F. Griffin, H. M. M. D. Rinder, B. R. M. D. Smith, J. B. Tracey, N. S. Kriz, C. K. P. Li and C. S. M. D. Rinder, *Anesth. Analg.*, 2001, **93**, 20-27.
136. S. Middeldorp, *Thromb. Res.*, 2008, **122**, 753-762.
137. L. Jaques, *Pharmacol. Rev.*, 1979, **31**, 99-166.
138. P. G. Hattersley, *JAMA*, 1966, **196**, 436-440.
139. J. Wippermann, J. M. Albes, M. Hartrumpf, M. Kaluza, R. Vollandt, R. Bruhin and T. Wahlers, *Eur. J. Cardiothorac. Surg.*, 2005, **28**, 127-132.
140. J. Hirsh, J. E. Dalen, D. R. Anderson, L. Poller, H. Bussey, J. Ansell, D. Deykin and J. T. Brandt, *Chest*, 1998, **114**, 445S-469S.
141. J. Hirsh, V. Fuster, J. Ansell and J. L. Halperin, *Circulation*, 2003, **107**, 1692-1711.
142. J. Hirsh, J. E. Dalen, D. R. Anderson, L. Poller, H. Bussey, J. Ansell and D. Deykin, *Chest*, 2001, **119**, 8S-21S.
143. S. V. Pizzo, M. L. Schwartz, R. L. Hill and P. A. McKee, *J. Clin. Invest.*, 1972, **51**, 2841-2850.
144. D. E. Levy, J. Trammel and W. W. Wasiewski, *J. Stroke Cerebrovasc. Dis.*, 2009, **18**, 23-27.
145. A. Greinacher and N. Lubenow, *Circulation*, 2001, **103**, 1479-1484.
146. S. Petros, *Biologics: Targets and Therapy*, 2008, **2**, 481-490.
147. E. P. Bianchini, J. Fazavana, V. Picard and D. Borgel, *Blood*, 2011, **117**, 2054-2060.
148. F. Ottensmeyer, R. Whiting and A. Korn, *Proc. Natl. Acad. Sci. USA*, 1975, **72**, 4953-4955.
149. M. Nybo and J. S. Madsen, *Basic Clin. Pharmacol. Toxicol.*, 2008, **103**, 192-196.

150. D. H. Stone, B. W. Nolan, A. Schanzer, P. P. Goodney, R. A. Cambria, D. S. Likosky, D. B. Walsh and J. L. Cronenwett, *J. Vasc. Surg.*, 2010, **51**, 559-564.e551.
151. C. Ja and J. A. Silverman, *J. Cardiovasc. Surg.*, 1999, **40**, 659-666.
152. S. E. Kimmel, M. Sekeres, J. A. Berlin and N. Ellison, *Anesth. Analg.*, 2002, **94**, 1402-1408.
153. S. E. Kimmel, M. A. Sekeres, J. A. Berlin, N. Ellison, V. J. DiSesa and B. L. Strom, *J. Am. Coll. Cardiol.*, 1998, **32**, 1916-1922.
154. R. J. Cobel-Geard and H. I. Hassouna, *Am. J. Hematol.*, 1983, **14**, 227-233.
155. A. S. Brecher and A. R. Roland, *Blood Coagul. Fibrinolysis*, 2008, **19**, 591-596.
156. V. G. Nielsen and S. N. Malayaman, *Anesth. Analg.*, 2010, **111**, 593-594.
157. N. D. Kien, D. D. Quam, J. A. Reitan and D. A. White, *J. Cardiothorac. Vasc. Anesth.*, 1992, **6**, 143-147.
158. A. Koster, J. Borgermann, J. Gummert, M. Rudloff, A. Zittermann and U. Schirmer, *Clin. Appl. Thromb. -Hemost.*, 2014, **20**, 290-295.
159. I. J. Welsby, M. F. Newman, B. Phillips-Bute, R. H. Messier, E. D. Kakkis and M. Stafford-Smith, *Anesthesiology*, 2005, **102**, 308-314.
160. W. A. Weiss, J. S. Gilman, A. J. Catenacci and A. E. Osterberg, *J. Am. Med. Assoc.*, 1958, **166**, 603-607.
161. C. W. Lillehei, L. P. Sterns, D. M. Long and D. Lepley, *Ann. Surg.*, 1960, **151**, 11-16.
162. B. J. Oberhardt, P. Lalezari and A. F. Jiang, *Immunology*, 1973, **24**, 445-453.
163. P. V. Nash and T. D. Bjornsson, *Anal. Biochem.*, 1984, **138**, 319-323.
164. G. Montalescot, W. M. Zapol, A. Carvalho, D. R. Robinson, A. Torres and E. Lowenstein, *Circulation*, 1990, **82**, 1754-1764.
165. L. D'Ilario, I. Francolini, A. Martinelli and A. Piozzi, *Dyes and Pigments*, 2009, **80**, 343-348.
166. M. Junaid, M. M. Choudhary, Z. A. Sobani, G. Murtaza, S. Qadeer, N. S. Ali, M. J. Khan and A. Suhail, *World J. Surg. Oncol.*, 2012, **10**, 1-5.
167. V. C. Yang, H. Bernstein, C. L. Cooney, J. C. Kadam and R. Langer, *Thromb. Res.*, 1986, **44**, 599-610.
168. H. Bernstein, V. C. Yang, D. Lund, M. Randhawa, W. Harmon and R. Langer, *Kidney Int.*, 1987, **32**, 452-463.
169. K. Kaminski, B. Kalaska, P. Koczurkiewicz, M. Michalik, K. Szczubialka, A. Mogielnicki, W. Buczko and M. Nowakowska, *MedChemComm*, 2014, **5**, 489-495.
170. J. Kuziej, E. Litinas, D. A. Hoppensteadt, D. Liu, J. M. Walenga, J. Fareed and W. Jeske, *Clin. Appl. Thromb. -Hemost.*, 2010, **16**, 377-386.
171. A. C. Rodrigo, A. Barnard, J. Cooper and D. K. Smith, *Angew. Chem. Int. Ed.*, 2011, **50**, 4675-4679.
172. J. Gapinski, J. D. Szymański, A. Wilk, J. Kohlbrecher, A. Patkowski and R. Hołyst, *Langmuir*, 2010, **26**, 9304-9314.
173. S. M. Bromfield, P. Posocco, C. W. Chan, M. Calderon, S. E. Guimond, J. E. Turnbull, S. Pricl and D. K. Smith, *Chem. Sci.*, 2014, **5**, 1484-1492.
174. R. K. O'Reilly, *Philos. Trans. R. Soc. A*, 2007, **365**, 2863-2878.
175. M. Danquah, T. Fujiwara and R. I. Mahato, *J. Polym. Sci., Part A: Polym. Chem.*, 2013, **51**, 347-362.
176. V. Percec, C.-H. Ahn and B. Barboiu, *J. Am. Chem. Soc.*, 1997, **119**, 12978-12979.
177. C. G. Clark Jr and K. L. Wooley, *Current opinion in colloid & interface science*, 1999, **4**, 122-129.
178. E. R. Zubarev, M. U. Pralle, L. Li and S. I. Stupp, *Science*, 1999, **283**, 523-526.

179. K. B. Thurmond, T. Kowalewski and K. L. Wooley, *J. Am. Chem. Soc.*, 1996, **118**, 7239-7240.
180. K. Procházka, M. K. Baloch and Z. Tuzar, *Macromol. Chem. Phys.*, 1979, **180**, 2521-2523.
181. S. Balalaie, M. Mahdidoust and R. Eshaghi-Najafabadi, *J. Iran. Chem. Soc.*, 2007, **4**, 364-369.
182. P. Greenspan, E. P. Mayer and S. D. Fowler, *J. Cell Biol.*, 1985, **100**, 965-973.
183. M. C. A. Stuart, J. C. van de Pas and J. B. F. N. Engberts, *J. Phys. Org. Chem.*, 2005, **18**, 929-934.
184. I. R. Sitepu, L. Ignatia, A. K. Franz, D. M. Wong, S. A. Faulina, M. Tsui, A. Kanti and K. Boundy-Mills, *J. Microbiol. Methods*, 2012, **91**, 321-328.
185. F. A. Carey and R. J. Sundberg, *Advanced Organic Chemistry: Part A: Structure and Mechanisms*, Springer Science & Business Media, 2007.
186. N. Murata and D. A. Los, *Plant Physiol.*, 1997, **115**, 875-879.
187. G. Lenaz, *Biosci. Rep.*, 1987, **7**, 823-837.
188. M. Pasenkiewicz-Gierula, W. K. Subczynski and A. Kusumi, *Biochemistry*, 1990, **29**, 4059-4069.
189. D. A. Los and N. Murata, *Biochim. Biophys. Acta*, 2004, **1666**, 142-157.
190. L. E. Drain, *Chichester, Sussex, England and New York, Wiley-Interscience, 1980. 250 p.*, 1980, **1**.
191. B. Chu, in *Soft Matter Characterization*, eds. R. Borsali and R. Pecora, Springer Netherlands, Dordrecht, 2008, pp. 335-372.
192. C. C. Miller, *Proceedings of the Royal Society of London. Series A, Containing Papers of a Mathematical and Physical Character*, 1924, **106**, 724-749.
193. R. J. Young and P. A. Lovell, *Introduction to polymers*, CRC press, 2011.
194. U. Nobbmann and A. Morfesis, *Mater. Today*, 2009, **12**, 52-54.
195. E. Seyrek, P. L. Dubin and J. Henriksen, *Biopolymers*, 2007, **86**, 249-259.
196. E. M. Muñoz and R. J. Linhardt, *Arterioscler. Thromb. Vasc. Biol.*, 2004, **24**, 1549-1557.
197. B. Michen, C. Geers, D. Vanhecke, C. Endes, B. Rothen-Rutishauser, S. Balog and A. Petri-Fink, *Sci. Rep.*, 2015, **5**, 9793.
198. H. Wong, J.-M. Victor and J. Mozziconacci, *PLoS One*, 2007, **2**, e877.
199. S. M. Bromfield, A. Barnard, P. Posocco, M. Fermeglia, S. Pricl and D. K. Smith, *J. Am. Chem. Soc.*, 2013, **135**, 2911-2914.
200. M. D. Klein, R. A. Drongowski, R. J. Linhardt and R. S. Langer, *Anal. Biochem.*, 1982, **124**, 59-64.
201. M. Dockal, D. C. Carter and F. Ruker, *J. Biol. Chem.*, 1999, **274**, 29303-29310.
202. A. Fernández-San Millán, A. Mingo-Castel, M. Miller and H. Daniell, *Plant Biotechnol. J.*, 2003, **1**, 71-79.
203. M. Fasano, S. Curry, E. Terreno, M. Galliano, G. Fanali, P. Narciso, S. Notari and P. Ascenzi, *IUBMB Life*, 2005, **57**, 787-796.
204. M. V. Lizenko, T. G. Regerand, A. M. Bakhirev, V. I. Petrovskii and E. I. Lizenko, *J. Evol. Biochem. Physiol.*, **43**, 183-190.
205. D. C. Carter and J. X. Ho, *Adv. Protein Chem.*, 1994, **45**, 153-203.
206. V. Arroyo, R. García-Martinez and X. Salvatella, *J. Hepatol.*, 2014, **61**, 396-407.
207. S. E. Halford and J. F. Marko, *Nucleic Acids Res.*, 2004, **32**, 3040-3052.
208. B. Cain, B. Baguley and W. Denny, *J. Med. Chem.*, 1978, **21**, 658-668.
209. R. G. H. Gershon, S. B. Guttman and A. Minsky, *Biochemistry*, 1993, **32**, 7143-7151.
210. R. F. Pasternack, E. J. Gibbs and J. J. Villafranca, *Biochemistry*, 1983, **22**, 2406-2414.

211. M. Anjomshoa, H. Hadadzadeh, S. J. Fatemi and M. Torkzadeh-Mahani, *Spectrochim. Acta. A Mol. Biomol. Spectrosc.*, 2015, **136 Pt B**, 205-215.
212. R. P. Paitandi, R. K. Gupta, R. S. Singh, G. Sharma, B. Koch and D. S. Pandey, *Eur. J. Med. Chem.*, 2014, **84**, 17-29.
213. E. Pedziwiatr, D. Shcharbin, L. Chonco, P. Ortega, F. Javier de la Mata, R. Gómez, B. Klajnert, M. Bryszewska and M. A. Muñoz-Fernandez, *J. Fluorescence*, 2008, **19**, 267-275.
214. O. G. Mouritsen, *Eur. J. Lipid Sci. Technol.*, 2011, **113**, 1174-1187.
215. C. J. Hawker and K. L. Wooley, *Science*, 2005, **309**, 1200-1205.
216. R. Srinivas, S. Samanta and A. Chaudhuri, *Chem. Soc. Rev.*, 2009, **38**, 3326-3338.
217. L. E. Fechner, B. Albanyan, V. M. P. Vieira, E. Laurini, P. Posocco, S. Pricl and D. K. Smith, *Chem. Sci.*, 2016, **7**, 4653-4659.
218. D. Joester, M. Losson, R. Pugin, H. Heinzelmann, E. Walter, H. P. Merkle and F. Diederich, *Angew. Chem. Int. Ed.*, 2003, **42**, 1486-1490.
219. X. Liu, J. Zhou, T. Yu, C. Chen, Q. Cheng, K. Sengupta, Y. Huang, H. Li, C. Liu, Y. Wang, P. Posocco, M. Wang, Q. Cui, S. Giorgio, M. Fermeglia, F. Qu, S. Pricl, Y. Shi, Z. Liang, P. Rocchi, J. J. Rossi and L. Peng, *Angew. Chem. Int. Ed. Engl.*, 2014, **53**, 11822-11827.
220. S. K. Nalluri, J. Voskuhl, J. B. Bultema, E. J. Boekema and B. J. Ravoo, *Angew. Chem. Int. Ed. Engl.*, 2011, **50**, 9747-9751.
221. S. M. Bromfield and D. K. Smith, *J. Am. Chem. Soc.*, 2015, **137**, 10056-10059.
222. D. Li and N. J. Wagner, *J. Am. Chem. Soc.*, 2013, **135**, 17547-17555.
223. A. Perico and A. Ciferri, *Chemistry - A European Journal*, 2009, **15**, 6312-6320.
224. M. S. Sulatha and U. Natarajan, *J Phys Chem B*, 2015, **119**, 12526-12539.
225. M. Israel, J. S. Rosenfield and E. J. Modest, *J. Med. Chem.*, 1964, **7**, 710-716.
226. R. Andruszkiewicz, M. Radowski and Z. Czajgucki, *Synth. Commun.*, 2005, **35**, 1085-1094.
227. I. S. Blagbrough and A. J. Geall, *Tetrahedron Lett.*, 1998, **39**, 439-442.
228. K. Esumi and M. Ueno, *Structure-performance relationships in surfactants*, Marcel Dekker, New York, 2003.
229. A. J. Konop and R. H. Colby, *Langmuir*, 1999, **15**, 58-65.
230. H. Schiessel, M. D. Correa-Rodriguez, S. Rudiuk, D. Baigl and K. Yoshikawa, *Soft Matter*, 2012, **8**, 9406-9411.
231. E. Freire, O. L. Mayorga and M. Straume, *Anal. Chem.*, 1990, **62**, 950A-959A.
232. M. M. Pierce, C. S. Raman and B. T. Nall, *Methods*, 1999, **19**, 213-221.
233. M. R. Duff, J. Grubbs and E. E. Howell, *J. Vis. Exp.*, 2011, 2796.
234. T. Wiseman, S. Williston, J. F. Brandts and L.-N. Lin, *Anal. Biochem.*, 1989, **179**, 131-137.
235. P. Posocco, E. Laurini, V. Dal Col, D. Marson, K. Karatasos, M. Fermeglia and S. Pricl, *Curr. Med. Chem.*, 2012, **19**, 5062-5087.
236. X. Liu, J. Wu, M. Yammine, J. Zhou, P. Posocco, S. Viel, C. Liu, F. Ziarelli, M. Fermeglia, S. Pricl, G. Victorero, C. Nguyen, P. Erbacher, J. P. Behr and L. Peng, *Bioconjugate Chem.*, 2011, **22**, 2461-2473.
237. P. Posocco, S. Pricl, S. Jones, A. Barnard and D. K. Smith, *Chem. Sci.*, 2010, **1**, 393-404.
238. R. D. Groot and P. B. Warren, *J. Chem. Phys.*, 1997, **107**, 4423.
239. P. Hoogerbrugge and J. Koelman, *Europhys. Lett.*, 1992, **19**, 155.
240. X. Liu, C. Liu, E. Laurini, P. Posocco, S. Pricl, F. Qu, P. Rocchi and L. Peng, *Mol. Pharm.*, 2012, **9**, 470-481.
241. K. Karatasos, P. Posocco, E. Laurini and S. Pricl, *Macromol. Biosci.*, 2012, **12**, 225-240.

242. D. A. Case, V. Babin, J. T. Berryman, R. M. Betz, Q. Cai, D. S. Cerutti, T. E. Cheatham, T. A. I. Darden, R. E. Duke, H. Gohlke, A. W. Goetz, S. Gusarov, N. Homeyer, P. Janowski, J. Kaus, I. Kolossváry, A. Kovalenko, T. S. Lee, S. LeGrand, T. Luchko, R. Luo, B. Madej, K. M. Merz, F. Paesani, D. R. Roe, A. Roitberg, C. Sagui, R. Salomon-Ferrer, G. Seabra, C.L. Simmerling, J. S. W. Smith, J. W. R. C. Walker, X. W. R. M. Wolf and P. A. Kollman, 2014, AMBER 14, University of California, San Francisco.
243. C. M. Cardona and R. E. Gawley, *J. Org. Chem.*, 2002, **67**, 1411-1413.
244. M. Mikhaylova, D. K. Kim, N. Bobrysheva, M. Osmolowsky, V. Semenov, T. Tsakalakos and M. Muhammed, *Langmuir*, 2004, **20**, 2472-2477.
245. W. B. Tan and Y. Zhang, *J. Biomed. Mater. Res. A*, 2005, **75**, 56-62.
246. R. Duncan, *Nat. Rev. Drug Discov.*, 2003, **2**, 347-360.
247. J. H. Park, S. Kwon, J. O. Nam, R. W. Park, H. Chung, S. B. Seo, I. S. Kim, I. C. Kwon and S. Y. Jeong, *J. Control. Release*, 2004, **95**, 579-588.
248. M. J. Vicent, *AAPS J.*, 2007, **9**, E200-E207.
249. H. Maeda, K. Greish and J. Fang, in *Polymer therapeutics II*, Springer, 2006, pp. 103-121.
250. J. K. Young, G. R. Baker, G. R. Newkome, K. F. Morris and C. S. Johnson Jr, *Macromolecules*, 1994, **27**, 3464-3471.
251. C. M. Cardona and R. E. Gawley, *J. Org. Chem.*, 2002, **67**, 1411-1413.
252. R. R. Arvizo, S. Rana, O. R. Miranda, R. Bhattacharya, V. M. Rotello and P. Mukherjee, *Nanomed. Nanotechnol. Biol. Med.*, 2011, **7**, 580-587.
253. P. Ghosh, G. Han, M. De, C. K. Kim and V. M. Rotello, *Adv Drug Deliv Rev*, 2008, **60**, 1307-1315.
254. C. M. Niemeyer, *Angew. Chem. Int. Ed.*, 2001, **40**, 4128-4158.
255. M. C. Daniel and D. Astruc, *Chem. Rev.*, 2004, **104**, 293-346.
256. Z. P. Aguilar, *Nanomaterials for medical applications*, Newnes, 2013.
257. R. Arvizo, R. Bhattacharya and P. Mukherjee, *Expert opinion on drug delivery*, 2010, **7**, 753-763.
258. A. Liu and B. Ye, *Clin. Lab.*, 2013, **59**, 23-36.
259. X. Zhang, *Cell Biochem. Biophys.*, 2015, **72**, 771-775.
260. M. S. Khan, G. D. Vishakante and H. Siddaramaiah, *Adv. Colloid Interface Sci.*, 2013, **199–200**, 44-58.
261. B. K. Jena and C. R. Raj, *Biosens. Bioelectron.*, 2008, **23**, 1285-1290.
262. N. L. Rosi and C. A. Mirkin, *Chem. Rev.*, 2005, **105**, 1547-1562.
263. R. Cao and B. Li, *Chem. Commun.*, 2011, **47**, 2865-2867.
264. X. Fu, L. Chen and J. Li, *Analyst*, 2012, **137**, 3653-3658.
265. X. Fu, L. Chen, J. Li, M. Lin, H. You and W. Wang, *Biosens. Bioelectron.*, 2012, **34**, 227-231.
266. C. Li, D. Li, G. Wan, J. Xu and W. Hou, *Nanoscale Res. Lett.*, 2011, **6**, 440.
267. J. Ohyama, Y. Hitomi, Y. Higuchi, M. Shinagawa, H. Mukai, M. Kodera, K. Teramura, T. Shishido and T. Tanaka, *Chem. Commun.*, 2008, 6300-6302.
268. R. Brown, *J. Mod. Opt.*, 1984, **31**, 3-3.
269. Y. Q. He, S. P. Liu, L. Kong and Z. F. Liu, *Spectrochim. Acta. A Mol. Biomol. Spectrosc.*, 2005, **61**, 2861-2866.
270. J. J. Friel, *X-Ray and Image Analysis in Electron Microscopy*, Princeton Gamma-Tech, Incorporated, 1994.
271. R. Chollakup, W. Smitthipong, C. D. Eisenbach and M. Tirrell, *Macromolecules*, 2010, **43**, 2518-2528.
272. S. Yu, X. Xu, C. Yigit, M. van der Giet, W. Zidek, J. Jankowski, J. Dzubiella and M. Ballauff, *Soft Matter*, 2015, **11**, 4630-4639.

273. C. Ragi, M. R. Sedaghat-Herati, A. A. Ouameur and H. A. Tajmir-Riahi, *Biopolymers*, 2005, **78**, 231-236.
274. A. D. Bangham, M. M. Standish and J. C. Watkins, *J. Mol. Biol.*, 1965, **13**, 238-252.
275. J. Salager, M. Bourrel, R. Schechter and W. Wade, *Soc. Petrol. Eng. J.*, 1979, **19**, 271-278.
276. P. M. Holland, *Adv. Colloid Interface Sci.*, 1986, **26**, 111-129.
277. J. F. Rathman and J. F. Scamehorn, *Langmuir*, 1986, **2**, 354-361.
278. K. Ogino and M. Abe, *Mixed Surfactant Systems*, CRC Press, 1992.
279. E. W. Kaler, K. L. Herrington, A. K. Murthy and J. A. N. Zasadzinski, *J. Phys. Chem.*, 1992, **96**, 6698-6707.
280. H. Endo, M. Mihailescu, M. Monkenbusch, J. Allgaier, G. Gompper, D. Richter, B. Jakobs, T. Sottmann, R. Strey and I. Grillo, *J. Chem. Phys.*, 2001, **115**, 580-600.
281. H. Wennerström and B. Lindman, *Phys. Rep.*, 1979, **52**, 1-86.
282. N. Funasaki and S. Hada, *J. Phys. Chem.*, 1983, **87**, 342-347.
283. S. Ingale, M. A. Wolfert, J. Gaekwad, T. Buskas and G.-J. Boons, *Nat. Chem. Biol.*, 2007, **3**, 663-667.
284. A. Kaiser, N. Gaidzik, T. Becker, C. Menge, K. Groh, H. Cai, Y. M. Li, B. Gerlitzki, E. Schmitt and H. Kunz, *Angew. Chem. Int. Ed.*, 2010, **49**, 3688-3692.
285. Z. H. Huang, L. Shi, J. W. Ma, Z. Y. Sun, H. Cai, Y. X. Chen, Y. F. Zhao and Y. M. Li, *J. Am. Chem. Soc.*, 2012, **134**, 8730-8733.
286. K. Shinoda, *J. Phys. Chem.*, 1954, **58**, 541-544.
287. K. L. Niece, J. D. Hartgerink, J. J. Donners and S. I. Stupp, *J. Am. Chem. Soc.*, 2003, **125**, 7146-7147.
288. H. A. Behanna, J. J. Donners, A. C. Gordon and S. I. Stupp, *J. Am. Chem. Soc.*, 2005, **127**, 1193-1200.
289. G. A. Silva, C. Czeisler, K. L. Niece, E. Beniash, D. A. Harrington, J. A. Kessler and S. I. Stupp, *Science*, 2004, **303**, 1352-1355.
290. D. E. Owens and N. A. Peppas, *Int. J. Pharm.*, 2006, **307**, 93-102.
291. D. D. Lasic and D. Needham, *Chem. Rev.*, 1995, **95**, 2601-2628.
292. C. Monfardini and F. M. Veronese, *Bioconjugate Chem.*, 1998, **9**, 418-450.
293. V. P. Torchilin, *Adv. Drug Deliv. Rev.*, 2002, **54**, 235-252.
294. B. Dubertret, P. Skourides, D. J. Norris, V. Noireaux, A. H. Brivanlou and A. Libchaber, *Science*, 2002, **298**, 1759-1762.
295. Y. Zhang and A. Clapp, *Sensors*, 2011, **11**, 11036-11055.
296. T. M. Allen and P. R. Cullis, *Science*, 2004, **303**, 1818-1822.
297. S. K. Lai, D. E. O'Hanlon, S. Harrold, S. T. Man, Y.-Y. Wang, R. Cone and J. Hanes, *Proc. Natl. Acad. Sci. USA*, 2007, **104**, 1482-1487.
298. N. J. Boylan, J. S. Suk, S. K. Lai, R. Jelinek, M. P. Boyle, M. J. Cooper and J. Hanes, *J. Control. Release*, 2012, **157**, 72-79.
299. O. Mert, S. K. Lai, L. Ensign, M. Yang, Y.-Y. Wang, J. Wood and J. Hanes, *J. Control. Release*, 2012, **157**, 455-460.
300. D. J. Toft, T. J. Moyer, S. M. Standley, Y. Ruff, A. Ugolkov, S. I. Stupp and V. L. Cryns, *ACS Nano*, 2012, **6**, 7956-7965.
301. N. Nishikido, *J. Colloid Interface Sci.*, 1977, **60**, 242-251.
302. I. Blagbrough, A. Geall and A. Neal, *Biochem. Soc. Trans.*, 2003, **31**, 397-406.
303. L. Chiappisi, I. Hoffmann and M. Gradzielski, *Soft Matter*, 2013, **9**, 3896-3909.
304. J. Inglese, R. L. Johnson, A. Simeonov, M. Xia, W. Zheng, C. P. Austin and D. S. Auld, *Nat. Chem. Biol.*, 2007, **3**, 466-479.
305. D. L. Boger, B. E. Fink, S. R. Brunette, W. C. Tse and M. P. Hedrick, *J. Am. Chem. Soc.*, 2001, **123**, 5878-5891.

306. P. Posocco, C. Gentilini, S. Bidoggia, A. Pace, P. Franchi, M. Lucarini, M. Fermeglia, S. Pricl and L. Pasquato, *ACS Nano*, 2012, **6**, 7243-7253.
307. J. Wang, R. M. Wolf, J. W. Caldwell, P. A. Kollman and D. A. Case, *J. Comput. Chem.*, 2004, **25**, 1157-1174.
308. J. Wang, W. Wang, P. A. Kollman and D. A. Case, *J. Mol. Graphics Modell.*, 2006, **25**, 247-260.
309. W. L. Jorgensen, J. Chandrasekhar, J. D. Madura, R. W. Impey and M. L. Klein, *J. Chem. Phys.*, 1983, **79**, 926-935.